

Spatio-Temporal Non-Linear Dynamics of Lasing in Micro-Cavities Full Vectorial Maxwell-Bloch FDTD Simulations

Von der Fakultät für Mathematik und Physik der Universität Stuttgart
zur Erlangung der Würde eines
Doktors der Naturwissenschaften (Dr. rer. nat.)
genehmigte Abhandlung

von

Andreas Klaedtke

aus Stuttgart-Degerloch

Hauptberichter: Prof. Dr. O. Hess
Mitberichter: Prof. Dr. H. Herrmann
Tag der mündlichen Prüfung: 21. Dezember 2004

Theoretische Quantenelektronik
Institut für Technische Physik, DLR
Pfaffenwaldring 38-40
D-70569 Stuttgart

2004

Zusammenfassung

Klaedtke, Andreas:

Spatio-Temporal Non-Linear Dynamics of Lasing in Micro-Cavities **Full Vectorial Maxwell-Bloch FDTD Simulations**

Der Fokus dieser Arbeit ruht auf extrem schnellen und nichtlinearen Effekten in dielektrischen Mikrokavitäten für kohärente Strahlungsquellen. Dieser Kavitätstyp verspricht niedrige Pumpschwellen für den Laserbetrieb und ultra schnelle Modulierbarkeit. Mikrokavitäten mit niedrigen Pumpschwellen stellen mögliche Einzelphotonenquellen dar, die in quantenoptischer Datenverarbeitung ihre Anwendungen finden sollen. Diese Arbeit stellt zum ersten Mal die komplette dreidimensionale Beschreibung der vollständigen Polarisationsdynamik während des Einschwingvorgangs eines Laserprozesses in einer Mikrokavität vor. Als Kavitätsgeometrien wurden sogenannte dielektrische “Microdisks” und “Microgears” ausgewählt.

Zur Simulation der nichtlinearen, ultrakurzen Effekte in Mikrokavitäten wurde im Rahmen dieser Doktorarbeit ein auf dem Finite Elemente im Zeitraum (FDTD) basierendes Programm für dreidimensionale räumliche Geometrien entwickelt, an verschiedene Rechnerarchitekturen angepasst und getestet. Der FDTD Algorithmus beschreibt die zeitliche Entwicklung des elektromagnetischen Feldes auf einem numerischen Gitter vom Yee Typ indem er mit Hilfe der Faradayschen und der generalisierten Ampèreschen Gleichung die Felder des nächsten aus den Feldern des vorhergehenden Zeitpunktes berechnet. Dieser Algorithmus ist vom “Leap-frog” Typ und seine Genauigkeit ist von zweiter Ordnung. Durch die Materialgleichung wird die mikroskopische Polarisation, beschrieben in einem semiklassischen Formalismus durch die optischen Bloch-Gleichungen, als zusätzliche reelle Differenzgleichung in den FDTD Algorithmus eingebettet.

Resonatoren mit verteilter Rückführung (DFB Resonatoren), mit eindimensionaler oder zweidimensionaler Korrugation, stellen die erste Art von Mikroresonator dar auf die die numerische Methode angewandt wird. Dieser Resonatortyp findet Anwendung in sogenannten Plastiklasern die vollständig aus organischen Materialien bestehen um extrem flexible und formbare, grossflächige Lichtquellen zu bilden. Die numerischen Rechnungen in dieser Arbeit resultieren in qualitativen Ergebnissen die Aufschluss über die Art des DFB Mechanismus geben, und quantitativen Resultaten zu DFB Strukturen wie sie in Experimenten verwendet wurden.

Die letzten zwei Kapitel der Arbeit befassen sich mit Scheibenlasern, die Abmessungen

im Bereich der Lichtwellenlänge besitzen. Ausgehend von glatten dielektrischen Zylindern werden die kalten Kavitätsmoden vermessen und den Ergebnissen anderer Arbeiten gegenübergestellt. Die Auswirkungen von periodischen Modulationen des Zylinderradius mit unterschiedlicher Stärke auf die Eigenschaften von kalten Resonatormoden werden umrissen und quantitativ an einzelnen Moden untersucht. Diese dielektrischen Scheiben mit periodischer Modulation des Radius werden Mikrozahlräder genannt.

Die Simulationen des transienten Verhaltens während der Relaxationsoszillationen des aktiven Materials in Scheibenlasern zeigen stationäres räumliches Lochbrennen. Dieses stationäre Verhalten wird allerdings sehr schnell durch eine Rotationsbewegung des elektromagnetischen Feldes abgelöst. Wir führen dies auf die kontinuierliche azimuthale Entartung der Eigenmoden der kalten Kavität und dem nichtlinearen Typ der kombinierten optischen Maxwell-Bloch Gleichungen zurück. Durch den Übergang zur Zahnradgeometrie wird die kontinuierliche azimuthale Entartung der Moden aufgehoben. Wie zu erwarten zeigen die Simulationen ein stationäres räumliches Lochbrennen, demnach in diesem Resonatortyp, auch noch während des eingeschwungenen statischen Verhaltens des Laserprozesses.

Es zeigt sich, dass die Modenbeschreibung einer kalten dielektrischen Kavität zwar einen Eindruck der zu erwartenden Eigenschaften des um eine nicht-lineare Materialgleichung erweiterten Resonators gestattet aber nicht ausreichend ist nicht lineare Effekte vorherzusagen.

Abstract

Klaedtke, Andreas:

Spatio-Temporal Non-Linear Dynamics of Lasing in Micro-Cavities **Full Vectorial Maxwell-Bloch FDTD Simulations**

This work explores the ultra fast and non-linear effects in dielectric micro-cavities and micro-cavity lasers on the basis of full vectorial Maxwell-Bloch finite difference in time domain simulations. Micro-cavity lasers promise low lasing pump thresholds and ultra fast amplitude modulations. Micro-cavities with low pump thresholds may function as single photon sources which are required for quantum optic data processing. For the first time the full three dimensional complete polarisation dynamics during the initial transient of a lasing process in a micro-cavity are calculated and discussed. So called microdisks and microgears were chosen as the cavity geometries.

In order to simulate the non-linear, ultra short effects in micro cavities, a three dimensional finite element in time domain (FDTD) code was set up, adapted to different types of computer architectures and verified. The FDTD algorithm describes the temporal evolution of the electromagnetic fields on a Yee type numerical grid by using the Faraday and the generalised Ampère law to calculate the fields at a new time step from the former time step in a leap frog like, second order accurate scheme. The Maxwell material equations introduce the polarisation into the FDTD algorithm. It is described for the first time in a semi-classical, self consistent three dimensional formalism by the discretised optical Bloch equations as separate difference equations.

Resonators with distributed feedback (DFB resonators), including one or two dimensional corrugations, pose the first type of micro-resonator for which the numerical method is applied. This type of resonator is used in so called “plastic lasers” which are entirely made from organics in order to form extremely flexible and shapeable, large area light sources. The simulations in this work lead to qualitative results which give insight in the type of DFB mechanism, and they give quantitative results for DFB structures which are used in experiments.

The last two chapters of this work deal with disk type lasers with length scales in the range of a few wavelengths. Starting with smooth shaped dielectric cylinders, cold cavity modes are computed and measured. The results are then compared to experiments and different theoretical computations from literature.

Subsequently, the influence of a periodic modulation of the cylinder radius – which characterises the microgear laser – with variable depth on the properties of cold cavity

modes in smooth shaped disks is studied. Quantitative investigations are performed on selected modes. These dielectric disks with a periodic modulation of the radius are called microgears.

The simulations of the initial transient relaxation oscillation of the active material in microdisk lasers visualise the quasi stationary spatial hole burning process. But this initially static behaviour is immediately replaced by a rotational movement of the electromagnetic mode. We ascribe this effect to the continuous azimuthal degeneracy of the eigenmodes of the cold cavity and the non-linearity of the combined optical Maxwell-Bloch equations. The continuous azimuthal degeneracy is removed by the transition to the microgear geometry. The simulations of lasing in this kind of resonator shows a spatially static hole burning of the inversion from the first relaxation oscillations to the steady state lasing process.

It is thereby demonstrated that the mode decomposition of a cold dielectric cavity is an indication of the properties which are to be expected of a lasing resonator, but proves to be insufficient to predict non-linear effects in micro and macro lasers.

Contents

1. Introduction, Overview and Outlook	11
2. Micro-Cavity Lasers	15
3. Finite Difference in Time Domain Method	21
3.1. Introduction	21
3.1.1. Unit Systems	22
3.2. Core Algorithm	23
3.2.1. Discretisation Scheme	23
3.2.2. One-Dimensional Practice	24
3.2.3. Generic Three Dimensional	25
3.2.4. Stability and Accuracy	26
3.2.5. Aliasing of Material Parameters	27
3.3. Boundary Conditions	28
3.3.1. Metallic Boundary Condition	28
3.3.2. Using Symmetries to Create Boundary Conditions	29
3.3.3. Periodic Boundaries	29
3.3.4. Mur Open Boundary Condition	30
3.3.5. PML and UPML	31
3.4. Simulation Setups	38
3.4.1. Ho's Method and Band Structure calculations	38
3.4.2. One Dimensional Plane-Wave Simulations	41
3.4.3. Three Dimensional Micro-Cavity Simulations	42
3.4.4. Discrete Poynting Theorem	43
4. Nonlinear, Active Materials	45
4.1. Full Vectorial Maxwell-Bloch Equations	46
4.1.1. Quantum Mechanics, Semi-Classical Approach	46
4.1.2. Relation between Maxwell-Bloch and Oscillator Differential Equation	49
4.1.3. Phenomenological Terms	53
4.1.4. Discrete Full-Vectorial Maxwell-Bloch Equations	54
4.2. Absorption and Phase Shift in a Linear Material	55
4.2.1. Theoretical Description	56

4.2.2. Simulation	57
4.3. Ultra-Fast Pulse Interaction	60
4.3.1. Rabi Flopping	61
4.3.2. Rabi Flopping with Detuned Excitation	63
4.3.3. Pi-Pulse Propagation	63
4.4. Normal Mode Coupling	64
4.5. Stimulated Systems	68
4.5.1. Laser Cavity Equations	68
4.5.2. Spiking and Relaxation Oscillations	72
5. Plane DFB Structures	75
5.1. Guided Modes in Thin Dielectric Slabs	75
5.2. One Dimensional Patterned Organic DFB Lasers	79
5.2.1. The Distributed Feedback Mechanism	81
5.2.2. FDTD Simulations	84
5.2.3. Band Structure	86
5.2.4. Mode Structure	88
5.2.5. Tunability	90
5.3. Two Dimensional Corrugation	92
6. Microdisk	95
6.1. Whispering Gallery Modes	97
6.1.1. Product Ansatz	99
6.1.2. Different Analytical Methods	106
6.2. Cold Cavity FDTD Simulations	107
6.2.1. Resonance Frequencies and Mode Structure	109
6.2.2. Mode Volume	112
6.2.3. Quality Factor	112
6.2.4. Discussion	114
6.3. Pumped Non-Linear Dynamics	115
6.3.1. Fast Time Dynamics	118
6.3.2. Ultra-Fast Time Dynamics	120
7. Microgear	123
7.1. Properties of Cold Cavity Microgears	124
7.1.1. Pedestal	125
7.1.2. Corrugation and Mode Degeneracy	126
7.1.3. Resonant Wavelength Shift	127
7.1.4. Mode Structure	128
7.1.5. Quality Factors	132
7.1.6. Mode Volume	132
7.2. Pumped Non-Linear Dynamics	133
7.2.1. Initial Relaxation Oscillation	133
7.2.2. Steady State Dynamics of Gear compared to Disk	137

A. Matrix	143
B. Discretised PML Equations	145
C. Software	147

Contents

1. Introduction, Overview and Outlook

Since the 1960s the technical ability to generate coherent high-frequency electromagnetic radiation has established the broad field of laser physics which influenced nearly every other field of physical science and even other disciplines like medicine or biology. In the 1980s the use of lasers in communication technology and the entertainment industry to transmit and process information created a huge market for coherent light generating sources. The market necessity to manufacture cheap but reliable radiation sources leads compulsorily to a miniaturisation of these optoelectronic devices.

Another driving force besides the cost factor, for the creation of lasers with cavities of wavelength size is, the prospect of using and investigating so called cavity quantum electrodynamic effects (cavity QED). Probably the most intriguing physical phenomenon is the Purcell effect which was first proposed in 1946 by E. M. Purcell in proceedings of the American Physical Society [1]. The Purcell effect describes the alteration of the spontaneous decay factor due to the dielectric surroundings in which the emitter is embedded. The suppression of spontaneous emission into non-lasing frequencies reduces the lasing threshold. It has been shown that low lasing thresholds can be achieved in microdisk cavities [2] and the threshold-less laser has been predicted. Very low output power is a requirement for the generation of number-state light and non-classical photon statistics which are desirable to generate light sources for quantum computing. Other benefits of micro-cavities are the possibility to modify the spatial emission characteristics and the spectral line shape (see for an early overview from 1992, Yokoyama [3]). The short photon lifetimes in these very small cavities are ideal for ever faster modulation of the laser emission which is quite important to information and communication technologies.

All these effects require the cavity to be especially tailored to the light emission of the active material. A profound breakdown of the electromagnetic field behaviour in the laser system is therefore mandatory. Mathematical models which describe laser systems combine the physics of the light field with the quantum electronic properties of the laser active material. Common continuous wave (cw) type lasers with large resonator cavities can be well described by a rough sketch of the electrodynamic properties of the cavity with sufficient accuracy. This is due to the fact that the cavities are much larger than the lasing wavelength and the plane wave or Gaussian approximation of the light field inside the resonator is a good approximation, as well as the linear regime of the coupled light matter equations in which the laser operates. But with decreasing size of the cavities to the wavelength range of the generated light, the exact description of the electromagnetic radiation is of increasing importance. The much more refined modelling of today's micro sized lasers requires the full set of the Maxwell equations to describe

1. Introduction, Overview and Outlook

the complex vectorial nature of the electromagnetic radiation. In addition to the now indispensable significance of the vectorial nature, the interest in the ultra-fast dynamics of the lasing process renders many approximation techniques inadequate.

This work discusses the modelling of the laser process in a semi-classical framework where the classical electromagnetic field is described by the Maxwell equations, and quantum mechanics governs the behaviour of the active material. Due to the inherent computational complexity of the problem, the most simple set of equations is favoured. The finite differences in time-domain (FDTD) based Yee algorithm proved to be accurate (a second order accurate leap-frog scheme) and highly efficient in solving the curl part of the Maxwell equations. In the calculation of cold cavity spectra it is superior to frequency domain techniques as it allows for a faster calculation of the resonator spectrum (see [4]). This algorithm with all the necessary accompanying boundary conditions and discretisation difficulties are outlined in chapter 3. A first application of this method is the cold cavity investigation of a thin film distributed feedback cavity with one- or two-dimensionally corrugated surfaces. This micro-cavity type is employed in so called plastic lasers [5]. The results of the simulations will be set into context with experimental measurements in chapter 5. This chapter serves also as an introduction to the idea of the distributed feedback mechanism and the mode picture in slab waveguides which will turn up again in the following chapters.

Several approaches have been made since the introduction of the FDTD method to include the non-linear behaviour of materials interacting with the electromagnetic fields. The approach which is used in this work is presented in chapter 4. It is based on the transformation of the two-level Bloch equations of complex values to a set of differential equations of real values. This allows us to use real valued physical entities which are favourable, because complex values would mean a doubling in computer memory requirements and processing time. In addition to the size advantages of the second order differential equation approach with real variables over the first order differential equations with complex variables, it turned out that the leap-frog type second order algorithm is much more stable. The accuracy is compared to theoretical results in simple one dimensional systems at the end of chapter 4. The set of comparisons starts with a linear susceptibility analysis of the light matter interaction and the reproduction of the Rabi flopping behaviour which is predicted by quantum mechanics. In the following, the interaction of the cavity with the active material is studied and the normal mode coupling phenomenon is simulated. Last but not least, a transient relaxation oscillation behaviour in a non-radiatively pumped Bragg mirror cavity is simulated.

The last two chapters investigate two types of micro-cavities. Chapter 6 is investigating a microdisk laser and chapter 7 the so called microgear cavity system which is essentially a microdisk with a circumferential corrugation. Several cold cavity properties of the microdisk are first investigated. A sketch of the mode structure inside cylindrical cavities is outlined and a labelling of the highly confined whispering gallery modes is introduced. It is found that the modes share a continuous azimuthal degeneracy. In order to fit the emission characteristic of the active material to the cavity resonances, the highly confined modes are determined and measured. These results are also compared to other reported calculations in referenced literature. At the end of chapter 6, a certain

cold cavity mode is selected and the two-level system is tuned to its eigenfrequency and the transient relaxation oscillation behaviour inside this micro-cavity is simulated. The stunning effect of a rotating electromagnetic mode is found after the first initial relaxations. It is assumed that this is caused by the non-linear effect of spatial hole burning and the azimuthal degeneracy of the cold cavity modes. Evidence for the spatial hole burning and the inversion density pinning effect is presented.

The introduction of a corrugation at the circumference of the cylindrical cavity reduces the continuous azimuthal to a discrete degeneracy, therefore pinning the cold cavity mode in place. This idea is investigated in chapter 7. It is also put into relation to experimental and theoretical work by Fujita and Baba [6]. They claim that the lower threshold current which is measured in microgear lasers, in contrast to microdisk lasers, is due to the higher Q factor of the associated modes and the existence of so called non-radiating modes. A slight increase in the quality factor of the weakly corrugated resonator can be found in the calculations, although it rapidly decreases for deep corrugated surfaces. It is shown that the continuous degeneracy of the modes is broken with the introduction of the corrugation. Finally, the transient initial relaxation oscillation behaviour of the microgear is compared to the microdisk. The pinning of the mode is successfully obtained during the simulation time.

The basic work for further simulations which take an in depth look at such phenomena as normal mode coupling in micro-cavities and the ultra-fast modulation of micro-cavity lasing devices is presented in this work. The derived and implemented algorithm has proven to be stable and accurate in the simulations. Some long time instabilities which occurred in the calculations presented in chapter 5 could be traced to the combination of periodic and open boundary conditions. The precise source mechanism which leads to these instabilities could not be investigated in time. This is open to future work. Some minor influence of the UPML boundary conditions on the electromagnetic field structure, in the simulations of chapters 6 and 7, are also waiting to be tackled. The vectorial coupling between the dielectric dipole transition and the field can only handle π -type transitions so far. An extension of the algorithm to σ -type electric dipole transitions would be highly desirable. The extension of the optical two-level Bloch equations to semiconductor Bloch equations has already been done in a one dimensional simulation and is under current investigation by K. Böhringer.

The microdisk, microgear and related dielectric cavities are ideal geometries for this real space and time approach due to their tiny sizes. Such phenomena as the spatial hole burning effect or the mode competition during the lasing process are awaiting further detailed investigation. The dependence of the rotation speed of the electromagnetic field during the steady state lasing in microdisks is just one of the unknown features. Of special interest would also be the experimental verification of the rotating electromagnetic modes in ultra fast time-resolved near-field measurements.

1. *Introduction, Overview and Outlook*

2. Micro-Cavity Lasers

Every musical instrument, guitars, pianos, flutes, organs, etc., use oscillating structures to create a size dependent resonant frequency spectrum of sound waves. The cavity or resonator in optics defines its electromagnetic frequency spectrum. In contrast to the scalar nature of the acoustic wave however, the electromagnetic field is of vectorial nature which makes the investigations more complicated. As the size of the instrument gets smaller, for example shorter flutes, organ pipes or strings in pianos or harps, their frequency spectrum shifts to higher tunes and the resonant frequencies are more sparsely distributed. The relative frequency range where only one resonance is found gets larger for smaller resonator sizes. In a one dimensional Fabry-Perot cavity of length L for example, the lateral mode spacing would be

$$\Delta\omega = \frac{\pi c}{L}. \quad (2.1)$$

Smaller cavity lengths will therefore result in a larger frequency spacing. This is important in order to achieve single frequency operation.

A perfectly lossless optical cavity would confine the electromagnetic energy infinitely and would then have spectral resonances at precise values. These frequencies are the eigenvalues to the eigensolutions of the wave equation for the cavity geometry. Another term for eigensolution is eigenmode or mode and the spatial pattern of the mode is called the mode structure. But naturally these modes would not emit any radiation and therefore be totally useless in light sources. Emission of electromagnetic radiation requires a coupling of the electromagnetic field inside the resonator to the surrounding field outside the cavity. The coupling strength is measured by a decay coefficient which is specific for each resonance. A frequency spectrum of a lossless cavity has infinitely thin peaks at the eigenfrequencies of the dielectric cavity. If the modes are coupled to the outside and lose energy in time, the emission spectrum of the cavity will show peaks with a certain finite line width. This line width is related to the decay coefficient of the resonance. The loss and the frequency of the resonance can also be combined to give a quality factor. This quality factor is proportional to the confinement time which is the inverse of the decay coefficient, in units of the optical period of the resonance frequency.

The eigenvalues to the eigensolutions of the wave equation of a lossy cavity become complex, with the imaginary part being a measure of the energy flux out of the cavity. A second quantisation of the electromagnetic field on behalf of such a complex pseudo mode basis system is not possible. In a strict way modes are something which is independent of time. The complex eigenvalue on the other hand is similar to a mode with

2. Micro-Cavity Lasers

a decreasing amplitude over time. Electromagnetic resonances which are lossy should therefore be called pseudo modes, although this is normally not considered in cavities with low loss. Usually the cavity is considered without loss and the eigenmodes of this perfect cavity form the basis system. The equations of motion of the system are then expanded with decay terms which couple the cavity to the surrounding free space modes. These dissipative terms have to be counteracted by Langevin noise terms in quantum mechanical evolution equations to satisfy the commutator relations of the operators. The noise terms must then obey certain correlation function relations.

It should be obvious that there are two domains of cavity types classified by their loss. Cavities with modes of high quality factors can be described by a closed cavity picture which is then coupled weakly to the surrounding electromagnetic fields by loss channels. On the other end of the scale are cavities with pseudo modes of low quality factors. A calculation of their idealised lossless cavity modes results in eigenfrequencies and mode structures which strongly differ from the electromagnetic fields at the resonance of the real cavity. The separation of the modes into the cavity modes and the surrounding free space mode continuum is misleading.

But besides the larger resonance frequency separation, why is it interesting to create small cavity volumes and high quality factors? The main physical reason is related to the change of the spontaneous emission rate. This is a bit awkward at first glance. Why should the spontaneous emission of matter be related to its surroundings and to be more precise to the electromagnetic field properties? But the change of the spontaneous emission rate by different cavity types has been shown. The spontaneous emission rate in free space is given by Einstein's A factor (see also "Optical Processes in Micro-cavities" [7]). Fermi's golden rule which gives the transition rate (the A factor) of a quantum mechanical two-level system which is coupled by a dipole Hamiltonian to an electromagnetic field is proportional to an effective mode density $g(\omega)$ of the system. This mode density in free space is

$$g_{\text{fs}}(\omega) d\omega = \frac{\omega^2 d\omega}{\pi^2 c^3}. \quad (2.2)$$

By putting the active medium in a cavity we change the mode density of the electromagnetic field. This mode density is not only defined by the cavity type but also depends on the position of the active medium (local mode density).

The atom cannot radiate if the mode density of the electromagnetic field at the frequency and position of the material's dipole transition is zero. The material's radiative lifetime for this dipole transition would be infinitely long. This is called "inhibited spontaneous emission". On the other hand, if the transition frequency is equal to the eigenmode of a cavity, then the lifetime will be shorter than the lifetime of this transition in free space. This effect is called "enhanced spontaneous emission".

This has been shown in many experiments starting with the work of Purcell [1] who predicted this effect in 1946. The change of the spontaneous emission rate or lifetime is given by the Purcell or enhancement factor

$$F(\omega) := \frac{g_{\text{cavity}}(\omega)}{g_{\text{fs}}(\omega)}. \quad (2.3)$$

Table 2.1.: Overview of different micro-cavity types and their most extreme experimentally established properties [8].

Name	Volume	Quality Factor
Photonic crystal	$1 (\lambda/n)^3$	10^4
Fabry-Perot or Bragg mirror	$5 (\lambda/n)^3$	10^3
Microdisk	$6 (\lambda/n)^3$	10^4
Microsphere	$1,000 (\lambda/n)^3$	10^8

It is related to the local density of electromagnetic states in relation to the density of states in free space. Purcell [1] derived the following expression which relates the enhancement factor to the quality factor Q of the cavity mode and the cavity volume V

$$F(\lambda) \sim \frac{Q \lambda^3}{V}. \quad (2.4)$$

The quality factor Q is a measure of the line width of the cavity mode.

The important thing here is that the enhancement factor is proportional to the quality factor and inversely proportional to the cavity volume. The lower the cavity loss and the smaller the cavity volume, the larger the enhancement factor. Exemplary quality factors and volumes of micro cavity resonances which were reported in publications are sampled in table 2.1.

Several different types of cavities for optical applications were manufactured and investigated, driven by different interests, needs and motives. Most of the cavities try to achieve a good optical confinement by means of photonic band gap structures in one or more dimensions, or by using total internal reflection under shallow angles. Cavities with long photon lifetimes, that is ultra high quality factors, play an important role in strong coupling experiments. Weak coupling limit phenomena like spontaneous emission enhancement are found in cavities with lower quality factors but very small cavity volumes [8]. The cavity types which are found in literature include:

DFB micro-cavity [9] DFB micro-cavities are a combination of waveguide type resonators and photonic crystal type structures to achieve a feedback by Bragg reflection from the photonic crystal structure. They are called micro-cavities as the thickness of the waveguide is around the wavelength of the guided light.

These structures have been applied to organic materials to allow highly flexible, large area coherent light emitters.

Bragg mirror or Fabry-Perot type cavity Planar metallic mirrors or dielectric Bragg mirrors form longitudinal mesoscopic laser cavities. The confinement of light is only along the normal direction of the mirror surfaces. But metallic mirrors or a large number of Bragg-layers can lead to high quality factors.

2. *Micro-Cavity Lasers*

VCSEL [10], Micropost, Micropillar [11] A special type of Bragg mirror cavity with additional transverse confinement of electromagnetic radiation is the vertical cavity surface emitting laser (VCSEL). The dielectric material – air interface creates a kind of cylindrical waveguide with the Bragg layers on both ends of the cavity in longitudinal direction. Another possibility for transverse mode confinement is a oxide aperture which directs the pumping current to a small optical gain region. The central cavity itself can be of very small volume as in micropost or micropillar resonators which are just very VCSEL structures with small diameters and sometimes a metallic surface.

Photonic crystal cavities [12, 13] The smallest reported cavity volumes so far are photonic crystal based cavities. They consist of a thin layer of dielectric material which confines the modes in two dimensions. This thin layer is then patterned to create a two dimensional photonic band gap structure. Defects (omissions or) inside the periodic structure are used as small cavities.

Microdisk [14, 15, 16] Microgear [6], Microtoroid [17] All those cavities rely on a special type of electromagnetic field mode which has its field maxima near the circumference of the dielectric cylinder. The quality factor is strongly dependent on the curvature of the cylinder with respect to the wavelength of the resonance. Higher quality factors are achieved if this relative curvature is small. Microdisks are perfectly cylindric structures. Microtoroids have a somewhat donut like, smooth outer shape and microgears are disk like cavities with a periodic corrugation of the radius. Common techniques from semiconductor manufacturing, like lithography and etching processes, can be used to create these devices which make them especially interesting for integrated optical systems.

Zeolites [18] Zeolite micro-lasers are a nanoporous guest host system where organic dyes are inserted into channel pores of zeolite crystals. These crystals have a usually hexagonal cross section and are very long in relation to the diameter. The diameter of the structure gets smaller towards the tip of the crystal. Very small hexagonal cross sections near the tip have shown to be of the size of the lasing wavelength [19]. The confinement mechanism of the lasing mode is similar to the microdisk.

Microsphere [20], Microdroplet [9] Microspheres and microdroplets use a similar confinement method as the disk type cavities. Due to the generally larger ratio of radius to resonance wavelength, their quality factors are much higher.

Microring [21] Microrings are rings of higher refractive index material than its surroundings. They work as the microdisk cavities. The discrete frequency spectrum is used in filter applications where the microring is attached to two tangential waveguides which act as input and output from the filter device. The microring resonator only transmits resonant frequencies from the input to the output channel. High Q factors for these resonators have been reported.

From the large number of different micro-cavities we have chosen the DFB micro-waveguide which are used in “plastic lasers” and the microdisk, microgear cavities. The microdisk and microgear are an especially good natured object for FDTD simulations because of their small size.

2. *Micro-Cavity Lasers*

3. Finite Difference in Time Domain Method

The finite difference in time domain (FDTD) era started when in 1966 Yee [22] presented a scheme to arrange the spatial and temporal positions of the discretised electric and magnetic fields in space and time. This arrangement allowed for a straight forward discretisation of the two curl Maxwell equations, leading to a highly efficient and accurate algorithm to compute the evolution of the electromagnetic fields. Since then, a huge amount of publications has demonstrated the successful application of this FDTD method to countless problems in electromagnetics. Good sources of references are Tafloves excellent review books [23] and [24], or the Internet site <http://www.fDTD.org> with an up to date database of publications related to the FDTD method.

In the next sections of this chapter, the basic parts of the FDTD algorithm will be introduced. It is only concerned with the electromagnetic field and the optical phenomena arising from the Maxwell equations without free charges or currents. The extension to FDTD simulations with active materials is presented in the next chapter. An overview of the different types of simulations which are then used in subsequent chapters is finally given.

3.1. Introduction

Optical phenomena are described in classical electrodynamics by four fields. Those are the electric field \mathbf{E} , the dielectric displacement \mathbf{D} , the magnetic field \mathbf{H} and finally the magnetic induction \mathbf{B} . All four fields are three dimensional vectors in three dimensional space.

The Maxwell equations (see for example [25])

$$\begin{aligned}\operatorname{div} \mathbf{D} &= \rho \\ \operatorname{curl} \mathbf{E} &= - \frac{\partial \mathbf{B}}{\partial t} \\ \operatorname{curl} \mathbf{H} &= \frac{\partial \mathbf{D}}{\partial t} + \mathbf{J} \\ \operatorname{div} \mathbf{B} &= 0,\end{aligned}\tag{3.1}$$

which are given in full vectorial notation in the SI unit system are linking these four fields to the scalar charge density ρ and the current density \mathbf{J} . To fully determine this

3. Finite Difference in Time Domain Method

set of equations, two additional material functional dependencies

$$\begin{aligned} \mathbf{D} &= f[\mathbf{E}, \mathbf{p}] \\ \mathbf{B} &= f[\mathbf{H}, \mathbf{M}], \end{aligned} \tag{3.2}$$

are relating the dielectric displacement to the electric field and the magnetic induction to the magnetic field. The macroscopic polarisation \mathbf{p} and the macroscopic magnetisation \mathbf{M} are fields which are introduced to model this interrelationship.

For our purposes, we can ignore free charges and free currents. The material properties in our simulations can be modelled by the functional dependences of \mathbf{D} to \mathbf{E} and \mathbf{B} to \mathbf{H} . We further restrict the functional dependence to linear behaviour so that we can write equations (3.2) in terms of the linear dielectric material tensor ϵ and the linear permeability tensor μ .

$$\begin{aligned} \mathbf{D} &= \epsilon \cdot \mathbf{E} \\ \mathbf{B} &= \mu \cdot \mathbf{H}. \end{aligned} \tag{3.3}$$

In several simulations, the material properties are not only linear but also isotropic. The functional dependency then reduces to simple scalar proportionality factors ϵ and μ . The material properties of free space should be linear and isotropic with the material constants ϵ_0 and μ_0 .

Furthermore, we will only treat non magnetic materials so that $\mu = \mu_0$ can always be applied. For passive (cold cavity) simulations, ϵ is only a function of space, not of time.

3.1.1. Unit Systems

The SI system of physical units is normally not utilised in FDTD type algorithms. This is due to the imbalance in the magnitudes of the dielectric constant $\epsilon_0 \approx 8.85 \times 10^{-12} \text{ A}^2 \text{ s}^4 \text{ kg}^{-1} \text{ m}^{-3}$) and the permeability $\mu_0 \approx 1.26 \times 10^{-6} \text{ kg m s}^{-2} \text{ A}^{-2}$ of vacuum. This is the reason why most publications are using the Heaviside-Lorentz (HL) system of units. The Maxwell equations then take on the form

$$\begin{aligned} \text{div } \mathbf{D} &= \rho \\ \text{curl } \mathbf{H} &= c^{-1} \left(\frac{\partial \mathbf{D}}{\partial t} + \mathbf{J} \right) \\ \text{curl } \mathbf{E} &= -c^{-1} \frac{\partial \mathbf{B}}{\partial t} \\ \text{div } \mathbf{B} &= 0. \end{aligned} \tag{3.4}$$

This system is much better suited to equalise the magnitude of the numerical values of the electric and magnetic field, allowing higher precision when additions are performed on digital microprocessors using floating point numbers. The multiplication with the constant speed of light in vacuum c can also be avoided by setting $c = 1$ (normalised HL, or nHL).

In the SI unit system the two material parameters ϵ and μ were physical entities with units. When changing the system of units to HL these two parameters get unit-less. They are just numbers. Associated with this change to unit-less quantities is the modification of the electric field unit for example. This changes from V m^{-1} in the SI system to A s m^{-2} in the HL unit system. In a later chapter we will use SI units for the Bloch equations. To connect the calculations of the Bloch equations (SI) and the Maxwell equations (nHL), we have to translate the values of the physical entities. It can be easily deduced that the electric field value E_{SI} in the SI unit system, is the electric field value E_{nHL} in the nHL unit system divided by ϵ_0 in the SI unit system.

3.2. Core Algorithm

The Maxwell equations (3.4) are differential equations which pose a well defined boundary value problem. An algorithm for the core region of the simulation space must be bounded as computer memory is a limited quantity. The field values inside the core of the simulation region are updated by the FDTD core algorithm which will be presented in this sections. The boundary condition algorithm completes the calculation at the surfaces of the central simulation region. For different problems like open space simulations, there exist different boundary region algorithms. Calculating the Maxwell equations numerically requires them to be in a discretised form. This will be discussed in the next section.

3.2.1. Discretisation Scheme

In order to make the appearance of the discretised equations short and concise, a special notation for the fields F at certain positions \mathbf{r} in Cartesian space, at x, y, z and time t , is introduced. Space should be discretised on an evenly spaced, rectangular grid with a spatial stepping of δs , and time should be discretised with a stepping of δt . The relation between the position \mathbf{r} on the grid at the integer coordinates (i, j, k) and at the point in time m is therefore $x_i = i \cdot \delta s + o_x$, $y_j = j \cdot \delta s + o_y$ and $z_k = k \cdot \delta s + o_z$.

$$\mathbf{r}(i, j, k) = x_i \mathbf{e}_x + y_j \mathbf{e}_y + z_k \mathbf{e}_z \quad (3.5)$$

A point m in discretised time is related to $t = m \cdot \delta t + o_t$.

The offsets o_x, o_y, o_z and o_t are constant values describing the position of the origin in space and time which can be adapted as the need arises. Instead of defining the position in brackets like $F(x_i, y_j, z_k)$, the following short form is used

$$F(x_i, y_j, z_k) = F|_{i,j,k}. \quad (3.6)$$

In a similar way, the point in time is given by a special notation (this time superscripted)

$$G(x_i, y_j, z_k, t_m) = G|_{i,j,k}^m. \quad (3.7)$$

When discretising the equations, differentials have to be translated to differences which sometimes depend on averaging to get the correct centring of the positions on

3. Finite Difference in Time Domain Method

the grid. A differential operation \hat{d} on the function F of s at the position p should be represented by a difference quotient as given in

$$\left. \frac{\partial F(s)}{\partial s} \right|_{s=p} \rightarrow \lim_{\delta s \rightarrow 0} \frac{F(p + \delta s/2) - F(p - \delta s/2)}{\delta s} =: \hat{d}|_{s=p} F. \quad (3.8)$$

Averaging operations \hat{m} of a function F of t to the position T in their simplest form are of similar type

$$F(t) \Big|_{t=T} \rightarrow \lim_{\delta t \rightarrow 0} \frac{F(T + \delta t/2) + F(T - \delta t/2)}{2} =: \hat{m}|_{t=T} F. \quad (3.9)$$

This operator will be necessary if F is only defined at $T - \delta t/2$ and $T + \delta t/2$ but not at T .

3.2.2. One-Dimensional Practice

As an example, the discretisation of the Maxwell equations (3.4) for plane waves travelling parallel to the x axis is investigated. The electric field $\mathbf{E}(x)$ should be polarised along the z direction. For simplicity we will concentrate on free space. Maxwell's equations then simplify to

$$\begin{aligned} \frac{\partial E_z}{\partial z} &= 0 \\ \frac{\partial H_y}{\partial x} &= c^{-1} \left(J_z + \frac{\partial D_z}{\partial t} \right) \\ \frac{\partial E_z}{\partial x} &= c^{-1} \frac{\partial B_y}{\partial t} \\ \frac{\partial H_y}{\partial y} &= 0. \end{aligned} \quad (3.10)$$

As for a plane wave which is travelling along the x direction, the electric and magnetic fields are only functions of x , the first and the last (divergence) equation are already satisfied. So we do not have to compute them. The remaining equations that we have to take into account are

$$\begin{aligned} \frac{\partial H_y}{\partial x} &= c^{-1} \left(J_z + \frac{\partial E_z}{\partial t} \right) \\ \frac{\partial E_z}{\partial x} &= c^{-1} \frac{\partial H_y}{\partial t}. \end{aligned} \quad (3.11)$$

If we write these two equations, employing the operator notation

$$\begin{aligned} \hat{d}|_x H_y &= c^{-1} \left(J_z + \hat{d}|_t E_z \right) \\ \hat{d}|_x E_z &= c^{-1} \hat{d}|_t H_y, \end{aligned} \quad (3.12)$$

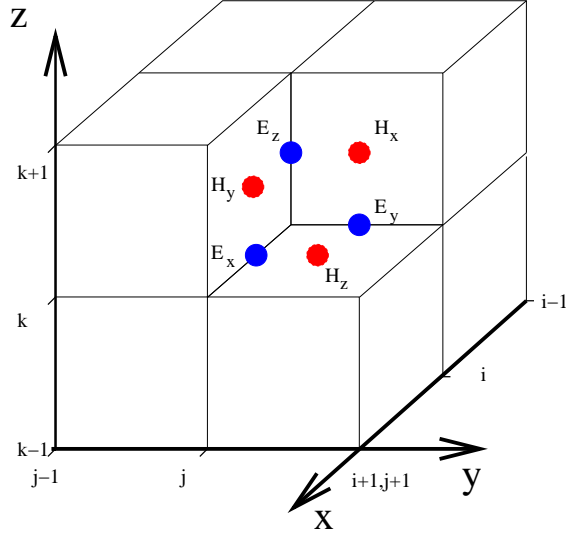


Figure 3.1.: The “Yee cube” showing the distribution of the field-vector components in one grid cell at space point i, j, k . Shown are the Cartesian components of the electric (E) and the magnetic (H) fields.

the transformation to a discrete form with rule (3.8) is straight forward. It becomes apparent, that the system of two equations is only compatible if the spatial grid as well as the temporal grid for the magnetic and the electric fields are shifted by half a step

$$\begin{aligned} c \frac{1}{\delta x} \left(H_y|_{i+\frac{1}{2}}^m - H_y|_{i-\frac{1}{2}}^m \right) &= J_z|_i^m + \frac{1}{\delta t} \left(E_z|_i^{m+\frac{1}{2}} - E_z|_i^{m-\frac{1}{2}} \right) \\ c \frac{1}{\delta x} \left(E_z|_{i+1}^{m-\frac{1}{2}} - E_z|_i^{m-\frac{1}{2}} \right) &= \frac{1}{\delta t} \left(H_y|_{i+\frac{1}{2}}^m - H_y|_{i-\frac{1}{2}}^m \right). \end{aligned} \quad (3.13)$$

The resulting distribution of electromagnetic field components in space is called the Yee scheme. It is of leap-frog type. Yee proposed it in 1966 in a paper [22] as an efficient and second order accurate algorithm to calculate electrodynamic scattering and antenna problems.

3.2.3. Generic Three Dimensional

Figure 3.1 shows the peculiar positioning of the field components in one grid cell which is the spatial part of the Yee scheme. This cubic grid cell with the field components pinned at the spatial positions on which they are defined is called a Yee cube or Yee cell. The components of the dielectric displacement \mathbf{D} and the magnetic induction \mathbf{B} are defined at the same positions as their appertaining field components \mathbf{E} and \mathbf{H} . The polarisation vector \mathbf{p} and the dielectric constant ϵ are placed at the same positions as the electric field components.

In full complexity, discretised and ordered to match the numerical algorithm the

3. Finite Difference in Time Domain Method

Maxwell curl equations are shown in equation (3.14) and equation (3.15).

$$\begin{aligned}
D_x|_{i+\frac{1}{2},j,k}^{m+\frac{1}{2}} &= D_x|_{i+\frac{1}{2},j,k}^{m-\frac{1}{2}} + \left[\frac{c \delta t}{\delta y} \cdot \left(H_z|_{i+\frac{1}{2},j+\frac{1}{2},k}^m - H_z|_{i+\frac{1}{2},j-\frac{1}{2},k}^m \right) \right. \\
&\quad \left. - \frac{c \delta t}{\delta z} \cdot \left(H_y|_{i+\frac{1}{2},j,k+\frac{1}{2}}^m - H_y|_{i+\frac{1}{2},j,k-\frac{1}{2}}^m \right) \right] \\
&\quad - \delta t \cdot J_x|_{i+\frac{1}{2},j,k}^m \\
D_y|_{i,j+\frac{1}{2},k}^{m+\frac{1}{2}} &= D_y|_{i,j+\frac{1}{2},k}^{m-\frac{1}{2}} + \left[\frac{c \delta t}{\delta z} \cdot \left(H_x|_{i,j+\frac{1}{2},k+\frac{1}{2}}^m - H_x|_{i,j+\frac{1}{2},k-\frac{1}{2}}^m \right) \right. \\
&\quad \left. - \frac{c \delta t}{\delta x} \cdot \left(H_z|_{i+\frac{1}{2},j+\frac{1}{2},k}^m - H_z|_{i-\frac{1}{2},j+\frac{1}{2},k}^m \right) \right] \\
&\quad - \delta t \cdot J_y|_{i,j+\frac{1}{2},k}^m \\
D_z|_{i,j,k+\frac{1}{2}}^{m+\frac{1}{2}} &= D_z|_{i,j,k+\frac{1}{2}}^{m-\frac{1}{2}} + \left[\frac{c \delta t}{\delta x} \cdot \left(H_y|_{i+\frac{1}{2},j,k+\frac{1}{2}}^m - H_y|_{i-\frac{1}{2},j,k+\frac{1}{2}}^m \right) \right. \\
&\quad \left. - \frac{c \delta t}{\delta y} \cdot \left(H_x|_{i,j+\frac{1}{2},k+\frac{1}{2}}^m - H_x|_{i,j-\frac{1}{2},k+\frac{1}{2}}^m \right) \right] \\
&\quad - \delta t \cdot J_z|_{i,j,k+\frac{1}{2}}^m
\end{aligned} \tag{3.14}$$

$$\begin{aligned}
B_x|_{i,j+\frac{1}{2},k+\frac{1}{2}}^{m+1} &= B_x|_{i,j+\frac{1}{2},k+\frac{1}{2}}^m - \left[\frac{c \delta t}{\delta y} \cdot \left(E_z|_{i,j+1,k+\frac{1}{2}}^{m+\frac{1}{2}} - E_z|_{i,j,k+\frac{1}{2}}^{m+\frac{1}{2}} \right) \right. \\
&\quad \left. - \frac{c \delta t}{\delta z} \cdot \left(E_y|_{i,j+\frac{1}{2},k+1}^{m+\frac{1}{2}} - E_y|_{i,j+\frac{1}{2},k}^{m+\frac{1}{2}} \right) \right] \\
B_y|_{i+\frac{1}{2},j,k+\frac{1}{2}}^{m+1} &= B_y|_{i+\frac{1}{2},j,k+\frac{1}{2}}^m - \left[\frac{c \delta t}{\delta z} \cdot \left(E_x|_{i+\frac{1}{2},j,k+1}^{m+\frac{1}{2}} - E_x|_{i+\frac{1}{2},j,k}^{m+\frac{1}{2}} \right) \right. \\
&\quad \left. - \frac{c \delta t}{\delta x} \cdot \left(E_z|_{i+1,j,k+\frac{1}{2}}^{m+\frac{1}{2}} - E_z|_{i,j,k+\frac{1}{2}}^{m+\frac{1}{2}} \right) \right] \\
B_z|_{i+\frac{1}{2},j+\frac{1}{2},k}^{m+1} &= B_z|_{i+\frac{1}{2},j+\frac{1}{2},k}^m - \left[\frac{c \delta t}{\delta x} \cdot \left(E_y|_{i+1,j+\frac{1}{2},k}^{m+\frac{1}{2}} - E_y|_{i,j+\frac{1}{2},k}^{m+\frac{1}{2}} \right) \right. \\
&\quad \left. - \frac{c \delta t}{\delta y} \cdot \left(E_x|_{i+\frac{1}{2},j+1,k}^{m+\frac{1}{2}} - E_x|_{i+\frac{1}{2},j,k}^{m+\frac{1}{2}} \right) \right]
\end{aligned} \tag{3.15}$$

3.2.4. Stability and Accuracy

Discretisation schemes like the Yee scheme are often called “leap frog” methods. The name should visualise two frogs separate by a half jump length, alternatively jumping or leaping forward. Maybe the one in front is waiting for the other to overtake. These kinds of schemes often have improved accuracy and stability over other differencing schemes of the same order. Despite being just of second order, the Yee scheme is of nearly the same accuracy as a fourth order discretising method and highly stable whilst being simple to compute with just a few multiplications and additions.

It can be shown (see for example [26]) that in d spatial dimensions the algorithm in order to be stable requires the Courant condition to be satisfied

$$c \cdot \delta t \leq d^{-\frac{1}{2}} \cdot \delta s. \quad (3.16)$$

Another restriction has to be made for the spatial stepping δs . The wavelengths in the material with the highest diffraction index, which are to be investigated, should be represented by at least 12 grid points. This is a more strict application of the Nyquist criterion which has proven to be a good rule of thumb.

It should be mentioned here that there is a drawback associated with this method. Energy should be conserved by the basic Maxwell equations in free space but it turns out that the Yee algorithm is only energy conserving when looking at averaged values over longer times [23]. If this is a problem, higher orders of approximation for the differentials are possible and have been applied in simulations (see Taflove [24]).

3.2.5. Aliasing of Material Parameters

In most simulations, the material parameter ϵ is a non-smooth function of the position with step discontinuities. The stair-casing method is usually applied in FDTD simulations. Stair-casing describes dielectric constant setups, if the value is either set or not set to the objects dielectric constant for certain conditions. Conditions might be fully occupied cells, or cells where the object is present at all. This way to set up the material grid is very easy for the programmer to implement. Holland [27] investigated the errors of the stair-casing method for the dielectric constant and Cangellaris and Wright [28] rigorously determined the errors of the stair-casing method for conducting boundaries in FDTD simulations. Schneider and Shlager [29] published a rule of thumb which they derived from their work on horn antennas. The rule states that stair-casing errors are small when the staircase diagonal is smaller than half a wavelength at the smallest significant wavelength in the simulation.

A more accurate but complicated approach is the alias or regularisation(1) method (as seen in fig. 3.2). For higher accuracy the dielectric constant should be a weighted average of every dielectric structure in its surrounding cube, or in other words the normalised integral over the surrounding cell. This leads to a faster convergence with grid resolution in band structure calculations [30].

The weights have to be determined by the fraction of cell space that the epsilon occupies. In three dimensions and for arbitrary shape of objects, this can be done by using a much finer grid and the stair-casing method to set up a intermediate grid which is then numerically integrated to form the coarse grid for the FDTD simulation. Simple objects like the cylinder of the microdisk resonators can be analytically described.

In the calculation of the fields, the dielectric constant ϵ is accessed at three positions in each grid cell. We should point out that the use of three different grids for the inverse ϵ field is not mandatory for the stair-case setup. Only one grid is of real significance and the values of ϵ at the half-step points in space can be calculated by interpolating adjacent points as needed by still preserving the second order accuracy (see Hwang and Cangellaris [31]).

3. Finite Difference in Time Domain Method

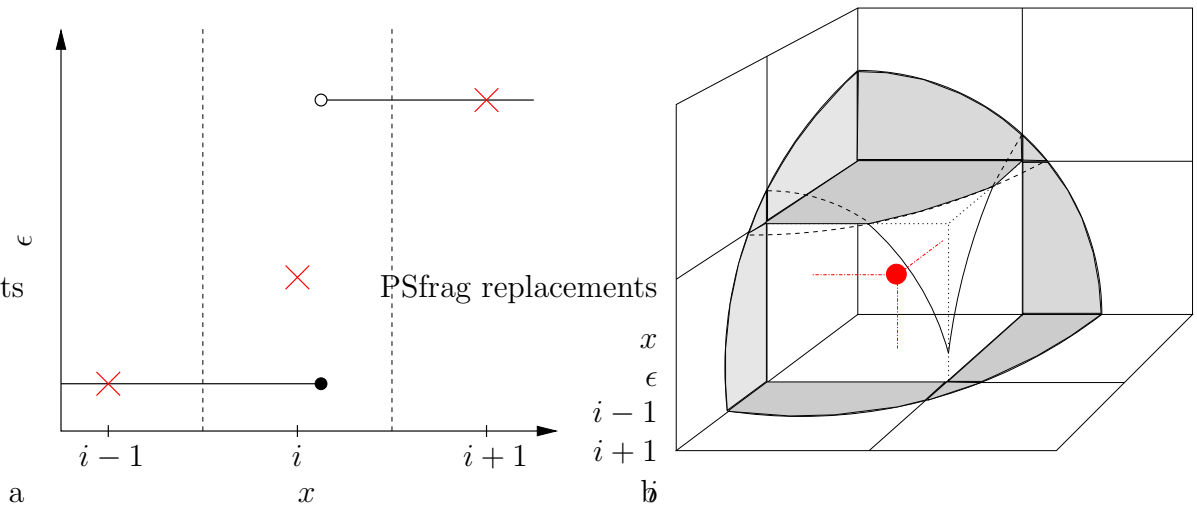


Figure 3.2.: Part (a) shows the principle of aliasing in one dimension. The dielectric constant at the grid position i (marked as red x) is calculated by the normalised integral of the function ϵ over the whole cell i . Part (b) shows the principle of fractioning the cell by the distribution of the material in three dimensions for the part of a dielectric sphere.

3.3. Boundary Conditions

The differential equations used to investigate electrodynamic problems, like the Maxwell curl equations, have to be closed at some point as mentioned above. Closing these discrete equations (3.14) and (3.15) is done by one of the following boundary conditions.

There are boundary conditions representing all kinds of real world systems. Metallic or closed boundary conditions are simple to implement, as the field value is just assumed to be vanishing on the surface of the simulation space. Electromagnetic waves are then totally reflected.

Periodic boundaries represent a certain kind of Bloch condition.

And for many applications, so called open boundaries have to be used which are simulating open, infinite space. Therefore open boundaries should absorb energy which is impinging on them. They should not distort the shape of the phase fronts of incoming waves. And last but not least, they should also carry forward evanescent waves.

Many attempts have been made to achieve the requirements for open boundary conditions for Maxwell equations. At least two are still being used. These are the Mur boundary condition of first or second order (introduced by Mur in 1981 [32]) and the so called perfectly matching layers (PML) boundary condition which was introduced by Bérenger in 1994 [33].

3.3.1. Metallic Boundary Condition

Metallic boundary conditions are a kind of Dirichlet boundary condition, where the values on the border of the simulation space is known. A metal surface with assumed

perfect conductivity requires the transverse components of the electric field to be 0. This kind of boundary condition totally reflects electromagnetic waves, implying a phase shift of π on them.

Only the electric field components along the border have to be set to 0 in the algorithm calculating the boundary values, and luckily these are the only ones which are accessed on the border by the core algorithm. The magnetic field positions outside do not have to be calculated as only the transverse electric field components on the border would rely on them but they are forced to be 0 anyway.

3.3.2. Using Symmetries to Create Boundary Conditions

Boundary conditions which can be derived from symmetry features of the dielectric system, e.g. a mirror symmetry at an axis, restrict the number of solutions to just the ones obeying the symmetries. This can sometimes be useful to minimise numerical errors or to minimise memory requirements, if only certain types of solutions are of interest. A boundary condition for symmetric (+) or antisymmetric (-) solutions, for example is

$$f(-x) = \pm f(+x). \quad (3.17)$$

3.3.3. Periodic Boundaries

In systems which show a translational symmetry in their material constants (the dielectric ϵ and diamagnetic μ)

$$\epsilon(\mathbf{r} + \mathbf{\Lambda}) = \epsilon(\mathbf{r}), \text{ and } \mu(\mathbf{r} + \mathbf{\Lambda}) = \mu(\mathbf{r}), \quad (3.18)$$

the Bloch theorem states that the associated electromagnetic fields must obey

$$\mathbf{E}(\mathbf{r} + \mathbf{\Lambda}) = \mathbf{E}(\mathbf{r}) e^{i\mathbf{k}\cdot\mathbf{r}}, \quad \mathbf{H}(\mathbf{r} + \mathbf{\Lambda}) = \mathbf{H}(\mathbf{r}) e^{i\mathbf{k}\cdot\mathbf{r}}, \quad (3.19)$$

where $\mathbf{\Lambda}$ can be any lattice vector. This requirement can be directly used as a conditional equation (3.20), relating field values on opposing surfaces of the computational domain (see fig. 3.3).

$$f(0) = f(\mathbf{\Lambda}) \cdot e^{i\mathbf{k}\cdot\mathbf{\Lambda}} \quad (3.20)$$

As can be immediately seen, the condition generally requires not only the amplitude of the function, but the phase information as well. For general values of \mathbf{k} , the field values have to be complex. The real and imaginary part can be computed separately with the same algorithm (eqs. 3.14 and 3.15) as in the purely real calculation. They then couple through the Bloch condition at the boundary. Figure 3.3 shows the required exchange of next-to-boundary values to the opposing boundary with an additional change in phase ($\mathbf{k}\cdot\mathbf{\Lambda}$). Chan *et al.* reported [4] on using this method in 1995 to calculate band structures of 2 and 3 dimensional periodic systems which were compared to analytical results.

3. Finite Difference in Time Domain Method

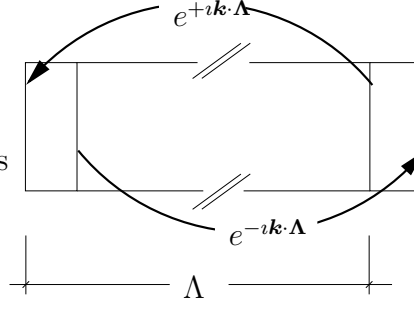


Figure 3.3.: The process of switching opposing boundary field values to ensure the Bloch boundary condition.

Another possibility, to cope with periodic systems, would be to assume the Bloch form of the field functions (i.e. $f(\mathbf{r}) = \tilde{f}_k(\mathbf{r}) e^{i\mathbf{k} \cdot \mathbf{r}}$, \tilde{f} is periodic) and to use the Maxwell curl equations (eqs. 3.4) to derive equations for the reduced fields ($\tilde{\mathbf{E}}$ and $\tilde{\mathbf{H}}$)

$$\begin{aligned} i\mathbf{k} \times \tilde{\mathbf{E}} + \mathbf{curl} \tilde{\mathbf{E}} &= -\frac{\partial \tilde{\mathbf{H}}}{\partial t} \\ i\mathbf{k} \times \tilde{\mathbf{H}} + \mathbf{curl} \tilde{\mathbf{H}} &= \epsilon(\mathbf{r}) \frac{\partial \tilde{\mathbf{E}}}{\partial t}. \end{aligned} \quad (3.21)$$

The solution of the above equations involves more operations than the explicit calculation of the Maxwell equations with the periodic boundary condition. The direct calculation is therefore more efficient and will be used in this work.

3.3.4. Mur Open Boundary Condition

The article by Gerrit Mur suggesting these boundary conditions for open space simulations of electromagnetic scattering problems [32] is based on the idea of carrying forward a plane wave across the boundary. For that reason, it can not cope with evanescent waves. The Mur scheme is an application of the Engquist-Majda boundaries [34] to the Maxwell equations. To make this approach, a Taylor series expansion is needed. The number of terms used in the expansion is the order of the Mur boundary condition by which it is classified.

For simplicity, we investigate the surface at $x = 0$. Plane waves $\Psi(\mathbf{r}, t)$ travelling to the left with a normalised wave vector \mathbf{n} hit the surface.

$$\Psi(\mathbf{r}, t) = \Psi_0 \cdot f\left(t - \frac{k}{\omega} \mathbf{n} \cdot \mathbf{r}\right) \quad (3.22)$$

The behaviour of waves in free space is governed by the wave equation (3.23). If the boundary condition would carry the wave forward so that this equation wave equation would be satisfied, the wave would be perfectly absorbed.

$$(\Delta - c^{-2} \partial_t^2) \Psi = 0 \quad (3.23)$$

An equation which is compatible to the wave equation (3.23) for a plane wave across the surface at $x = 0$ is the transport differential equation

$$\left(\partial_x \mp \frac{k}{\omega} n_x \partial_t \right) \Psi|_{x=x_{\text{Rand}}} = 0. \quad (3.24)$$

If the wave is coming from the right, the sign should be a “−”, if it is coming from the left, the sign should be a “+”.

To realise the boundary condition, the inverse phase velocity $\frac{k}{\omega} n_x$ has to be expressed by n_y and n_z

$$\frac{k}{\omega} n_x = \frac{k}{\omega} \sqrt{1 - (n_y^2 + n_z^2)}. \quad (3.25)$$

A Taylor series expansion for $n_y, n_z \ll n_x$ gives the following approximation to first order

$$\frac{k}{\omega} n_x \approx \frac{k}{\omega} \left(1 - \frac{1}{2} (n_y^2 + n_z^2) \right). \quad (3.26)$$

Murs boundary condition of m -th order follows from the transport differential equation (3.24) with regard to the approximated inverse phase velocity $\frac{k}{\omega} n_x$ to m -th order. In zeroth order, it reads

$$(\partial_x \mp c^{-1} \partial_t) \Psi|_{x=x_{\text{Rand}}} = 0. \quad (3.27)$$

For one dimensional systems, the Mur boundary condition of 0th order (3.27) is already accomplishing all the necessities for plane waves. It has a reflection error of about 1 parts in a thousand in one dimensional systems. It would require a “−” on the left border and a “+” on the right border. In more than one dimension it lacks the preservation of the shape of the phase fronts. Waves which are not normal to the border plane are not correctly absorbed. As the angle between the wave vector and the normal vector increases, the absorption gets worse and the phase fronts are distorted.

For bevel impinging waves, the approximation of first order (3.28) shows a significant improvement in absorption.

$$\left[c^{-1} \partial_x \partial_t - c^{-2} \partial_t^2 + \frac{1}{2} (\partial_y^2 + \partial_z^2) \right] \Psi|_{x=x_{\text{Rand}}} = 0 \quad (3.28)$$

Equation (3.28) can be deduced from equation (3.24) by inserting the approximation of equation (3.26) and then by temporal differentiation with an additional substitution of $\frac{k^2}{\omega^2} n_{\{y,z\}}^2 \partial_t^2$ with $\partial_{\{y,z\}}^2$. Higher order Mur boundaries are especially tedious to implement in more than two dimensions.

3.3.5. PML and UPML

Perfectly matching or matched layers (PML) are trying to resolve the problems of the other open boundary techniques. They consist of one or more additional layers of grid

3. Finite Difference in Time Domain Method

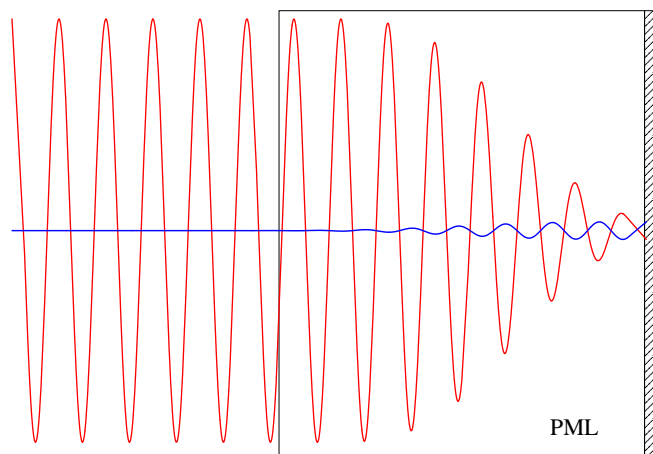


Figure 3.4.: A wave (red) coming from the left enters the PML region and is dampened. It is reflected on the right by a perfectly conducting wall and passes the PML region again (blue) being still further absorbed before reaching the simulation core again.

points surrounding the core simulation region. Their material properties are matched to the core region layers in their vicinity with the intention to totally absorb them. Sacks *et al.* [35] were the first to present a derivation of the Uniaxial Perfectly Matching Layers (UPML) formalism, which is just another manifestation of the PMLs which were introduced by Berenger [33]. A thorough investigation of the reflection error and the absorption behaviour of the UPMLs was published by Gedney [36]. Early investigations by Mittra and Pikel [37] mention instabilities with layered dielectric regions due to evanescent waves.

The PML formulation of Berenger is also often called a split field variant of the PML method while the U in UPML can also mean U for unsplit. This is due to the fact, that Berenger introduced new fields to model the material properties on which a PML approach is based. The UPML formulation on the other hand uses special kinds of material tensors (the dielectric constant and the permeability) to get the same behaviour, as we will see. PMLs are no boundary condition in the usual sense. They form a sheath between the core region and an outer boundary, which could be a perfectly conducting condition for example. Figure 3.4 shows this setup and the effect it has on a wave which is coming from the left. The wave is not reflected at the PML surface. It is being absorbed by travelling through the PML before being totally reflected by the metallic boundary condition. On the way back to the core simulation region it is furthermore being absorbed. Ideally it should be absorbed as much as possible without any reflections occurring on the PML surfaces. These properties can be achieved by setting up a special kind of material tensor which will be derived in the following. Berenger's approach is not used as it would need additional field values. The UPML algorithm can make use of the electric displacement and the magnetic induction fields. In the simulation of non-linear materials the electric displacement field is already stored in memory, and therefore only

the additional magnetic induction field has to be allocated.

The wave equations for the electric and magnetic fields in materials with anisotropic dielectric and permeability tensors are (compare with eqs. 3.4)

$$\begin{aligned}\mathbf{curl} (\boldsymbol{\mu}^{-1} \cdot \mathbf{curl} \mathbf{E}) &= -\boldsymbol{\epsilon} \cdot \frac{\partial^2 \mathbf{E}}{\partial t^2} \\ \mathbf{curl} (\boldsymbol{\epsilon}^{-1} \cdot \mathbf{curl} \mathbf{H}) &= -\boldsymbol{\mu} \cdot \frac{\partial^2 \mathbf{H}}{\partial t^2}.\end{aligned}\quad (3.29)$$

In figure 3.4, the PML sheath should begin at some position $z = 0$ along the z axis, which is the horizontal axis. The medium on the left ($z < 0$) should be isotropic, the speed of light in that medium u should therefore be defined by $u^{-2} = \epsilon_r \mu_r$. The PML medium on the right is assumed to be of uniaxial, anisotropic form $\boldsymbol{\mu} = \mu_r \boldsymbol{\Lambda}_\mu$ and $\boldsymbol{\epsilon} = \epsilon_r \boldsymbol{\Lambda}_\epsilon$. As rotational symmetry should apply for x and y coordinates, we can assume $\Lambda_{\epsilon,xx} = \Lambda_{\epsilon,yy}$ and $\Lambda_{\mu,xx} = \Lambda_{\mu,yy}$. The most general form for the two material tensors is

$$\boldsymbol{\Lambda}_\epsilon := \begin{bmatrix} a & 0 & 0 \\ 0 & a & 0 \\ 0 & 0 & b \end{bmatrix}; \quad \boldsymbol{\Lambda}_\mu := \begin{bmatrix} c & 0 & 0 \\ 0 & c & 0 \\ 0 & 0 & d \end{bmatrix}.\quad (3.30)$$

With uniaxial tensors, the Maxwell equations (3.29) in the PMLs still have solutions of the form $e^{i(\mathbf{k} \cdot \mathbf{r} - \omega t)}$, which represent impinging plane waves. The wave equation (3.29) for the magnetic field with that ansatz will transform to

$$\begin{aligned}0 &= \mathbf{k} \times [\boldsymbol{\epsilon}^{-1} \cdot (\mathbf{k} \times \mathbf{H})] + \omega^2 \boldsymbol{\mu} \cdot \mathbf{H} \\ 0 &= \begin{bmatrix} c \frac{\omega^2}{u^2} - \frac{k_y^2}{b} - \frac{k_z^2}{a} & \frac{k_x k_y}{b} & \frac{k_x k_z}{a} \\ \frac{k_x k_y}{b} & c \frac{\omega^2}{u^2} - \frac{k_x^2}{b} - \frac{k_z^2}{a} & \frac{k_y k_z}{a} \\ \frac{k_x k_z}{a} & \frac{k_y k_z}{a} & d \frac{\omega^2}{u^2} - \frac{k_x^2}{a} - \frac{k_y^2}{a} \end{bmatrix} \cdot \mathbf{H},\end{aligned}\quad (3.31)$$

in the PML sheath. Without loss of generality, we can assume that $k_y = 0$ as we claimed rotational symmetry around the z axis. Two nontrivial dispersion relationships can be derived from the determinant of the matrix operator, and they can be labelled transverse magnetic (TM) and transverse electric (TE) according to the form of the eigensolutions of \mathbf{E} and \mathbf{H} .

$$\begin{aligned}c \frac{\omega^2}{u^2} &= \frac{k_x^2}{b} + \frac{k_z^2}{a}, & \text{TM}_y \\ a \frac{\omega^2}{u^2} &= \frac{k_x^2}{d} + \frac{k_z^2}{c}, & \text{TE}_y.\end{aligned}\quad (3.32)$$

The wave equation for the electric field \mathbf{E} leads to the same equations.

Similar to the derivation of reflection and transmission coefficients on dielectric boundaries (see [25]), the derivation of the UPML material tensors starts with the assumption of an impinging $k_z > 0$ wave in the region $z < 0$, a reflected wave ($k_z < 0$) in the same region, and a transmitted wave ($k_z > 0$) in the PML region ($z \geq 0$).

3. Finite Difference in Time Domain Method

In the case of a TM wave, the magnetic and electric fields in the isotropic medium on the left can be expressed by a combination of an incoming and a reflected plane wave

$$\begin{aligned} \mathbf{E}(x, y, z, t)_{TM,1} &= \hat{H}_1 \left[\frac{k_{z,1}}{\omega\epsilon_r} (1 - \Gamma e^{-2ik_{z,1}z}) \mathbf{e}_x - \right. \\ &\quad \left. \frac{k_{x,1}}{\omega\epsilon_r} (1 + \Gamma e^{-2ik_{z,1}z}) \mathbf{e}_z \right] e^{i(k_{x,1}x + k_{z,1}z - \omega t)} \\ \mathbf{H}(x, y, z, t)_{TM,1} &= \hat{H}_1 (1 + \Gamma e^{-2ik_{z,1}z}) \mathbf{e}_y e^{i(k_{x,1}x + k_{z,1}z - \omega t)}. \end{aligned} \quad (3.33)$$

In the PML region, the plane wave will also be TM like and the fields only consist of one transmitted, therefore outgoing wave

$$\begin{aligned} \mathbf{E}(x, y, z, t)_{TM,2} &= \hat{H}_2 \left[\frac{k_{z,2}}{a} \mathbf{e}_x - \frac{k_{x,2}}{b} \mathbf{e}_z \right] (\omega\epsilon_r)^{-1} e^{i(k_{x,2}x + k_{z,2}z - \omega t)} \\ \mathbf{H}(x, y, z, t)_{TM,2} &= \hat{H}_2 \mathbf{e}_y e^{i(k_{x,2}x + k_{z,2}z - \omega t)}. \end{aligned} \quad (3.34)$$

The dynamic properties are contained in the boundary conditions (see Jackson [25]). Tangential components to the surface normal \mathbf{e}_z of \mathbf{E} and \mathbf{H} have to be continuous at $z = 0$ for all x, y and t . A first result is that $\omega -$ we already used this in equations (3.33) and (3.34) – and k_x have to be equal ($k_{x,1} = k_{x,2}$).

In equation (3.33) we used the factor Γ to act as a measure of the reflection at the PML surface. By using the boundary condition for the transverse part of the electric and magnetic fields, we obtain an equation for this reflection coefficient.

$$\Gamma = \frac{k_{z,1} - a^{-1}k_{z,2}}{k_{z,1} + a^{-1}k_{z,2}} \quad (3.35)$$

PMLs should act as non-reflecting media and by requiring $\Gamma = 0$ we end up with the relation

$$a = \frac{k_{z,2}}{k_{z,1}}. \quad (3.36)$$

Using this result in the PML dispersion relation (3.32) for the TM waves and comparing the result with the dispersion relation in free space

$$k_{z,1}^2 + k_{x,1}^2 = \frac{a}{c} k_{z,1}^2 + (cb)^{-1} k_{x,1}^2, \quad (3.37)$$

we can deduce that $a = c$ and $a = b^{-1}$.

The resulting fields for a TE like mode setup are

$$\begin{aligned} \mathbf{E}(x, y, z, t)_{TE,1} &= \hat{E}_1 (1 + \Gamma e^{-2ik_{z,1}z}) \mathbf{e}_y e^{i(k_{x,1}x + k_{z,1}z - \omega t)} \\ \mathbf{H}(x, y, z, t)_{TE,1} &= -\hat{E}_1 \left[\frac{k_{z,1}}{\omega\mu_r} (1 - \Gamma e^{-2ik_{z,1}z}) \mathbf{e}_x - \right. \\ &\quad \left. \frac{k_{x,1}}{\omega\mu_r} (1 + \Gamma e^{-2ik_{z,1}z}) \mathbf{e}_z \right] e^{i(k_{x,1}x + k_{z,1}z - \omega t)}, \end{aligned} \quad (3.38)$$

in free space and in the PML medium

$$\begin{aligned}\mathbf{E}(x, y, z, t)_{TE,2} &= \hat{E}_2 \mathbf{e}_y e^{i(k_x,2x+k_z,2z-\omega t)} \\ \mathbf{H}(x, y, z, t)_{TE,2} &= \hat{E}_2 \left[-\frac{k_{z,2}}{c} \mathbf{e}_x + \frac{k_{x,2}}{d} \mathbf{e}_z \right] (\omega\mu_r)^{-1} e^{i(k_x,2x+k_z,2z-\omega t)}.\end{aligned}\quad (3.39)$$

Applying the same boundary conditions as in the TM case, we end up with the conditions $a = c = d^{-1} = b^{-1}$. With the definitions (3.30) of Λ_μ and Λ_ϵ this is equivalent to an impedance matching condition,

$$\frac{\epsilon}{\epsilon_r} = \frac{\mu}{\mu_r}, \quad (3.40)$$

and the two tensors have to be equal ($\Lambda = \Lambda_\mu = \Lambda_\epsilon$).

Consequently, the dispersion relations (3.32) in the PML region for TE and TM polarised waves, collapse to one general dispersion relation.

A plane wave hitting the medium with the above derived properties, is not being reflected. This is independent of frequency, wave vector or polarisation. Our task now is to find an expression for a so that a wave will be attenuated along the z axis. The most general form of a wave travelling in the PML along the z direction, with a wave vector \mathbf{k} in free space, is

$$\begin{aligned}\mathbf{E}(x, y, z, t) &= \begin{pmatrix} \hat{E}_x \\ \hat{E}_y \\ \hat{E}_z \end{pmatrix} f(x, y, z, t) \\ \mathbf{H}(x, y, z, t) &= (\omega\mu_r) \begin{pmatrix} a^{-1}k_y\hat{E}_z - k_z\hat{E}_y \\ k_z\hat{E}_x - a^{-1}k_x\hat{E}_z \\ ak_x\hat{E}_y - ak_y\hat{E}_x \end{pmatrix} f(x, y, z, t),\end{aligned}\quad (3.41)$$

with the function

$$f(x, y, z, t) = e^{i(k_x x + k_y y + a k_z z - \omega t)}. \quad (3.42)$$

Attenuation along z will be expressed by an exponential decay with a factor $-\alpha$. We can deduce that a should be of the form $a = \kappa + i\alpha$ so that (3.42) becomes

$$f(x, y, z, t) = e^{i(k_x x + k_y y + \kappa k_z z - \omega t)} e^{-\alpha k_z z}. \quad (3.43)$$

In a three dimensional simulation of a region in open space, the simulation core has to be surrounded by 6 sides, 8 corners and 12 edges as shown in figure 3.5. Each part has got to have a different combination of directions along which the waves are attenuated. The sides only should be absorbing normal to the surface, the edges should be absorbing along the two short dimensions, and the corners should be absorbing in all 3 dimensions. When taking all this into account, we end up with a general form of the tensor Λ being defined as

$$\Lambda := \begin{bmatrix} \frac{\Lambda_y \Lambda_z}{\Lambda_x} & & 0 \\ & \frac{\Lambda_x \Lambda_z}{\Lambda_y} & \\ 0 & & \frac{\Lambda_x \Lambda_y}{\Lambda_z} \end{bmatrix}; \quad \Lambda_i = \kappa_i - \frac{\sigma_i}{i\omega}, \quad (3.44)$$

3. Finite Difference in Time Domain Method

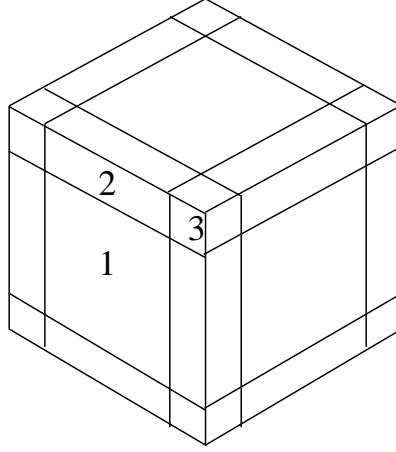


Figure 3.5.: The faces (1), edges (2) and corners (3) a PML has to be separated into.

with i being one of the coordinate indices x , y or z . The real part κ is attenuating evanescent waves and leads to a change in wavelength along i , whereas the imaginary part σ attenuates waves along i .

In frequency space, the Maxwell curl equations (3.4) with the special, tensorial material constants which were derived above then read

$$\begin{aligned} \mathbf{curl} \mathbf{H} &= -\imath\omega \epsilon_r \boldsymbol{\Lambda} \cdot \mathbf{E} \\ \mathbf{curl} \mathbf{E} &= \imath\omega \mu_r \boldsymbol{\Lambda} \cdot \mathbf{H} . \end{aligned} \quad (3.45)$$

The conversion of the differential equation (3.45) from frequency domain to time domain requires the introduction of two new fields \mathbf{D} and \mathbf{B} as shown in equation (3.46) to avoid the calculation of a convolution integral.

$$\mathbf{D} = \epsilon_r \begin{bmatrix} \frac{\Lambda_z}{\Lambda_x} & & 0 \\ & \frac{\Lambda_x}{\Lambda_y} & \\ 0 & & \frac{\Lambda_y}{\Lambda_z} \end{bmatrix} \cdot \mathbf{E}; \quad \mathbf{B} = \mu_r \begin{bmatrix} \frac{\Lambda_z}{\Lambda_x} & & 0 \\ & \frac{\Lambda_x}{\Lambda_y} & \\ 0 & & \frac{\Lambda_y}{\Lambda_z} \end{bmatrix} \cdot \mathbf{H} \quad (3.46)$$

With this substitution, it is possible to separate the real and imaginary parts occurring on the right side of equation (3.45). The transformation to time-domain is then simply the substitution of $-\imath\omega$ by the time derivative.

$$\begin{aligned} \nabla \times \mathbf{H} &= \begin{bmatrix} \kappa_y & & 0 \\ & \kappa_z & \\ 0 & & \kappa_x \end{bmatrix} \cdot \frac{\partial \mathbf{D}}{\partial t} + \begin{bmatrix} \sigma_y & & 0 \\ & \sigma_z & \\ 0 & & \sigma_x \end{bmatrix} \cdot \mathbf{D} \\ \nabla \times \mathbf{E} &= - \begin{bmatrix} \kappa_y & & 0 \\ & \kappa_z & \\ 0 & & \kappa_x \end{bmatrix} \cdot \frac{\partial \mathbf{B}}{\partial t} - \begin{bmatrix} \sigma_y & & 0 \\ & \sigma_z & \\ 0 & & \sigma_x \end{bmatrix} \cdot \mathbf{B} \end{aligned} \quad (3.47)$$

$$\begin{aligned}
 & \begin{bmatrix} \kappa_x & & 0 \\ & \kappa_y & \\ 0 & & \kappa_z \end{bmatrix} \cdot \frac{\partial \mathbf{D}}{\partial t} + \begin{bmatrix} \sigma_x & & 0 \\ & \sigma_y & \\ 0 & & \sigma_z \end{bmatrix} \cdot \mathbf{D} = \\
 & \quad \epsilon_r \left\{ \begin{bmatrix} \kappa_z & & 0 \\ & \kappa_x & \\ 0 & & \kappa_y \end{bmatrix} \cdot \frac{\partial \mathbf{E}}{\partial t} + \begin{bmatrix} \sigma_z & & 0 \\ & \sigma_x & \\ 0 & & \sigma_y \end{bmatrix} \cdot \mathbf{E} \right\} \\
 & \begin{bmatrix} \kappa_x & & 0 \\ & \kappa_y & \\ 0 & & \kappa_z \end{bmatrix} \cdot \frac{\partial \mathbf{B}}{\partial t} + \begin{bmatrix} \sigma_x & & 0 \\ & \sigma_y & \\ 0 & & \sigma_z \end{bmatrix} \cdot \mathbf{B} = \\
 & \quad \mu_r \left\{ \begin{bmatrix} \kappa_z & & 0 \\ & \kappa_x & \\ 0 & & \kappa_y \end{bmatrix} \cdot \frac{\partial \mathbf{H}}{\partial t} + \begin{bmatrix} \sigma_z & & 0 \\ & \sigma_x & \\ 0 & & \sigma_y \end{bmatrix} \cdot \mathbf{H} \right\}
 \end{aligned} \tag{3.48}$$

Discretisation of the equations (3.47) and (3.48) is straightforward with regard to the discretisation rule, equation (3.8). The resulting discretized equations are given in appendix B. These equations rely on the coefficients a_p , b_p , c_p and d_p which are introduced with $p \in \{x, y, z\}$. The coefficient functions of i are given in equation (3.49). The parameter i is referring to the position along the axis described by the index p .

$$\begin{aligned}
 a_p|_i &= \kappa_p(i) + \frac{1}{2} \sigma_p(i) \delta t \\
 b_p|_i &= \left(\kappa_p(i) + \frac{1}{2} \sigma_p(i) \delta t \right)^{-1} \\
 c_p|_i &= \kappa_p(i) - \frac{1}{2} \sigma_p(i) \delta t \\
 d_p|_i &= \frac{\kappa_p(i) - \frac{1}{2} \sigma_p(i) \delta t}{\kappa_p(i) + \frac{1}{2} \sigma_p(i) \delta t}
 \end{aligned} \tag{3.49}$$

The implementation of just one highly absorbing sheath with a high absorption coefficient σ , results in a large numerical error at the interface to the inner region. This error expresses itself in an artificial reflection. Berenger ([33]) relates this to the field vector components not being defined at the same point in space. A border of the PML sheath is therefore not well defined which leads to an artificial reflection error. It turns out that the use of several layers of such a medium with increasing absorption coefficient, so that there is a smooth increase in absorption from inside out, resolves the problem. The same goes for the coefficient κ . A potential rising has proven to be a good approach and is shown in equation (3.50).

$$\sigma(x) = \sigma_{\max} \left(\frac{x}{d} \right)^p \quad \kappa(x) = 1 + (\kappa_{\max} - 1) \left(\frac{x}{d} \right)^p \tag{3.50}$$

The parameter d is the thickness in layers of the boundary. The exponent p and the values for σ_{\max} and κ_{\max} can be freely chosen. Taflov shows in his excellent book on FDTD methods [24] that a choice for p between 3 and 4 gives reasonable results.

3. Finite Difference in Time Domain Method

He also shows that the reflection coefficient R , which is dependent on the angle φ of the incoming wave, can be approximated by equation (3.51).

$$R(\varphi) = \exp \left[-2\eta_{\text{fs}} \epsilon_{\text{r}} \cos \varphi \int_0^d \sigma(x) dx \right] \quad (3.51)$$

The impedance in free space is $\eta_{\text{fs}} \approx 733 \Omega$. The reflectivity R has to be minimised, by adjusting the parameters of the PMLs in such a way that the wave is damped as much as possible while keeping the numerical reflection error low. This is resulting in an optimal value for σ_{max} .

3.4. Simulation Setups

In the following chapters, different types of simulations are performed with the basic algorithms which were described before. Each simulation has a certain core algorithm – with either real or complex field components – and a matching boundary condition that is chosen in accordance with the problem type. In chapter 5, systems with translational symmetry are investigated which requires periodic or Bloch boundary conditions and complex fields. Whereas in chapter 6 open boundaries and real fields are employed. In addition to solving the Maxwell equations, special initial conditions are implemented and different physical entities are extracted from the simulation runs. The setup process and the post-processing of these simulations is outlined in this section.

3.4.1. Ho's Method and Band Structure calculations

If the dielectric material setup is translational symmetric, or in other words is periodic in one or more dimensions, the so called method of Ho (Chin *et al.* [4]) can be applied to compute the eigenfrequencies and eigenfunctions. The method is a combination of the core algorithm (eqs. 3.14 and 3.15) with complex fields and at least one periodic boundary condition (eq. 3.19). The other remaining boundaries can be truncated with whatever method is suitable. An initial field setup which has to be compatible with the material setup and the Maxwell equations, should probe the system for modes of interest. In particular the magnetic and the electric field must be divergence free. It therefore has to have a non-zero projection on these modes.

Following Ho's method we use a complexified \mathbf{H} field which is a superposition of special, periodic plane waves. The wave vector \mathbf{k} has to be the same as the periodic boundary wave vector. Each of the superposed plane waves is defined by an arbitrary phase ϕ , an arbitrary vector \mathbf{v} and the reciprocal grid vector \mathbf{G}

$$\mathbf{H}(\mathbf{r}) = \sum_{\mathbf{G}} [\mathbf{v} \times (\mathbf{k} + \mathbf{G})] \cdot \exp [i(\mathbf{k} + \mathbf{G}) \cdot \mathbf{r} + i\phi]. \quad (3.52)$$

A superposition of a certain number of reciprocal grid vectors \mathbf{G} contains enough degrees of freedom to excite as many field modes in the dielectric material, as desired. The

components of the vector \mathbf{G} must be an integer multiple of the associated component of the reciprocal grid vector. It is readily proven that the resulting magnetic field is divergence free. The phase factor ϕ can be chosen to shift the offset of the sine and cosine functions throughout the computational domain. By choosing a proper direction for the vector \mathbf{v} , the type of mode – the direction of the electric or magnetic field components – can be selected.

The simulation is started with this setup and is run for a certain total simulation time span T . Electromagnetic field components are recorded at several positions on the computational grid at every time step. These time series are Fourier transformed and the spectra are searched for peaks. The peaks that are still present in later times of the simulation belong to the eigenfrequencies of the periodic, dielectric system. The necessity to predefine a certain wave vector to compute the periodic boundary condition in equation (3.19) requires several simulation runs to cover enough points in reciprocal space for a band structure analysis. In order to get the eigenfunctions, the so called mode structures, a spatially resolved, discrete Fourier transform at the eigenfrequency of the mode is performed in a second simulation run.

Simulations with open boundary conditions always feature transient behaviour to a steady state. The time series of these simulations is generally not periodic. Gibbs oscillations accompany the peaks in spectra which are computed. Filter functions can be applied to the time series to suppress such cut-off phenomena.

A function which should be transformed into frequency space is $f(t)$, and which is defined during the simulation time $0 \leq t \leq T$. The filter function is then multiplied with the time series before the Fourier transformation is applied.

A filter function which is used in the following chapters is

$$g(t) = f(t) \cdot \frac{1}{2} \left(1 - \cos \left(2\pi \frac{t}{T} \right) \right). \quad (3.53)$$

Different filter functions and their resulting spectra can be compared in figure 3.6.

The accuracy of the algorithm is limited by two factors, the length of the time-step δt and the total simulation time T . Increasing the simulation time decreases the smallest detectable frequency as $\omega_{\min} \sim 2\pi/T$ and similarly defining the frequency resolution. The time-step Δt is linked to the highest measurable frequency $\omega_{\max} \sim 2\pi/\Delta t$.

In chapter 5 band structure and mode structure calculations will be presented for systems which are open in one dimension, and periodic in the other two dimensions. The open dimension (x) is modelled by an UPML boundary sheath which is terminated by a metallic boundary condition, while the other two dimensions are closed by a periodic boundary condition for a given wave-vector \mathbf{k} . If the third dimension (z) is designated to have a translational invariance, it is set to be just 3 grid cells thick making the simulation quasi 2 dimensional. The open dimension has got the most grid points so it is chosen to form the fastest index on the computational grid for non-strided memory access.

The probing of this system is done by using an initial magnetic field setup similar to equation (3.52). The range of the integer multiples of the reciprocal grid vector \mathbf{G} which are usually used is between -5 and 5 for the components in the periodic dimensions. Higher orders are normally not necessary when only the low frequency bands of the

3. Finite Difference in Time Domain Method

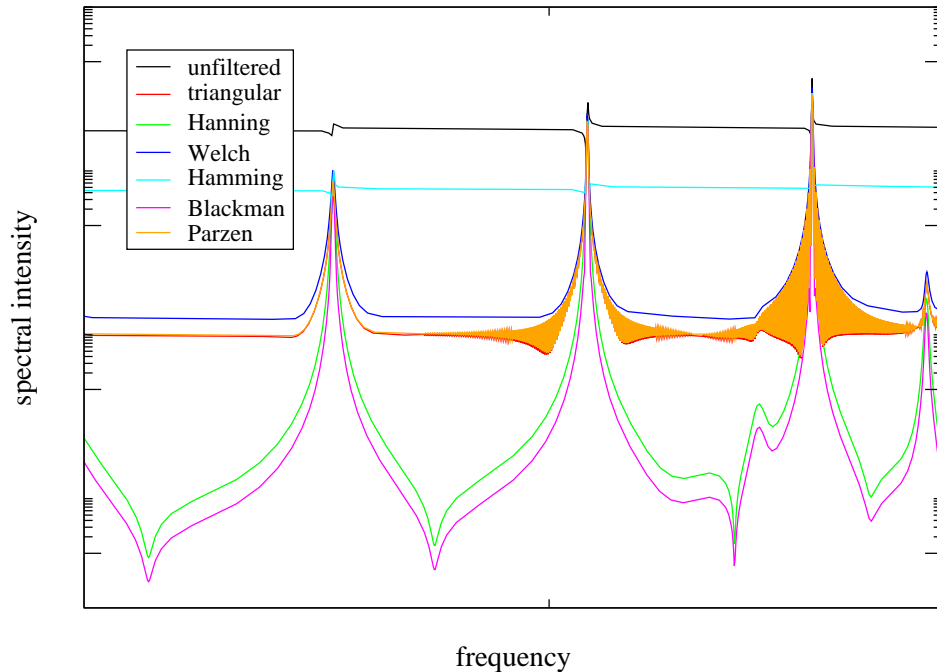


Figure 3.6.: Effects of different filter functions on the spectrum of cylindrical cavity.

dispersion diagram are of interest. The polarisation of the modes is selected by the vector \mathbf{v} . In the open dimension, a Gaussian envelope with its peak in the centre of the dielectric structure forces the fields to vanish before entering the PML layers. Following the work of Chan *et al.* [4], the magnetic field at four to eight, randomly chosen positions in the simulation space are recorded during the simulation time. An FFT with appropriate filtering of the time series to avoid Gibbs oscillations is used to calculate the spectrum at each point. These spectra are then added to avoid losing modes due to positions at modal nodes. The peak positions in the spectrum can be detected manually or by a simple maximum search algorithm. Mode structures are calculated by doing a spatially resolved on-the-fly filtered, Fourier transformation at the modes eigenfrequency. Tests with up to 64 grid points did not improve the accuracy of the simulation.

The simulations did reveal late time instabilities which can be attributed to the combination of periodic and PML boundary conditions. The precise cause of these instabilities could not be determined yet. Their time of appearance is linked to the Bloch vector, defining the boundary conditions. In the simulations of chapter 5 the instabilities occurred after about 200.000 time-steps for small Bloch vectors. Bloch vectors at the boundary of the first Brillouin zone could induce instabilities which already arose after 50.000 time-steps. It seems also to be related to the PML boundary conditions and their placement relative to the scattering objects in the simulation region. An increasing distance from the dielectric structures to the absorbing boundary conditions delayed the instabilities. The vanishing of group velocities at band gaps might also be responsible for the exponential increases of the energy which are symptomatic for the instabilities.

3.4.2. One Dimensional Plane-Wave Simulations

In chapter 4, one dimensional simulations will be made to verify the implementation of additional partial differential equations to the FDTD algorithm. These one dimensional simulations all include the core algorithm for a plane wave with the electric field polarised along the z direction as in equations (3.10). The wave should be propagating along the x axis with Mur open boundary conditions (eq. 3.24) closing the simulation region on both sides. Initially the simulations are started with no electric or magnetic field ($\mathbf{E}(t=0) = \mathbf{H}(t=0) = 0$). To excite or probe the system, a Gaussian pulse is inserted (generally on the left) by the total field, scattered field method. Total field/scattered field stands for the superposition of the initial field \mathbf{E}_{in} and the field response \mathbf{E}_{sc} – the scattered field – of the dielectric that is investigated. The superposition of both fields is called the total field $\mathbf{E}_{\text{tot}} = \mathbf{E}_{\text{sc}} + \mathbf{E}_{\text{in}}$. In order to separate both fields, the simulation region is divided into a region where the superposition is calculated and a region which only contains the scattered part of the electromagnetic field.

In order to get insight into the method, the dielectric constant of free space will be assumed across the whole simulation domain. A plane wave should be inserted on the left side at position i_b and travel to the right. If we calculate the field values with the now known Yee-scheme, the discretised equations for the inner region, containing both the inserted field and the scattered field, are as follows:

$$\begin{aligned} H_{y,\text{tot}}|_{i+\frac{1}{2}}^m &= H_{y,\text{tot}}|_{i+\frac{1}{2}}^{m-1} + c \frac{\delta t}{\delta x} \left(E_{z,\text{tot}}|_{i+1}^{m-\frac{1}{2}} - E_{z,\text{tot}}|_i^{m-\frac{1}{2}} \right) \\ E_{z,\text{tot}}|_i^{m+\frac{1}{2}} &= E_{z,\text{tot}}|_i^{m-\frac{1}{2}} + c \frac{\delta t}{\delta x} \left(H_{y,\text{tot}}|_{i+\frac{1}{2}}^m - H_{y,\text{tot}}|_{i-\frac{1}{2}}^m \right). \end{aligned} \quad (3.54)$$

In the outer region, only the scattered field is present, we therefore calculate the following:

$$\begin{aligned} H_{y,\text{sc}}|_{i+\frac{1}{2}}^m &= H_{y,\text{sc}}|_{i+\frac{1}{2}}^{m-1} + c \frac{\delta t}{\delta x} \left(E_{z,\text{sc}}|_{i+1}^{m-\frac{1}{2}} - E_{z,\text{sc}}|_i^{m-\frac{1}{2}} \right) \\ E_{z,\text{sc}}|_i^{m+\frac{1}{2}} &= E_{z,\text{sc}}|_i^{m-\frac{1}{2}} + c \frac{\delta t}{\delta x} \left(H_{y,\text{sc}}|_{i+\frac{1}{2}}^m - H_{y,\text{sc}}|_{i-\frac{1}{2}}^m \right). \end{aligned} \quad (3.55)$$

A combination of the total and the scattered field in one equation is only to be calculated at the position $i_b - \frac{1}{2}$ in the magnetic field update equation, and at the position i_b within the electric field update equation

$$\begin{aligned} H_{y,\text{sc}}|_{i_b-\frac{1}{2}}^m &= H_{y,\text{sc}}|_{i_b-\frac{1}{2}}^{m-1} + c \frac{\delta t}{\delta x} \left(E_{z,\text{tot}}|_{i_b}^{m-\frac{1}{2}} - E_{z,\text{sc}}|_{i_b-1}^{m-\frac{1}{2}} \right) \\ E_{z,\text{tot}}|_{i_b}^{m+\frac{1}{2}} &= E_{z,\text{tot}}|_{i_b}^{m-\frac{1}{2}} + c \frac{\delta t}{\delta x} \left(H_{y,\text{tot}}|_{i_b+\frac{1}{2}}^m - H_{y,\text{sc}}|_{i_b-\frac{1}{2}}^m \right). \end{aligned} \quad (3.56)$$

In the simulation, the calculation of both fields on all the grid points is done with the same algorithm. With the exception of the electric field at position i_b and the magnetic field at position $i_b - \frac{1}{2}$, the fields at every grid point are therefore correctly calculated. The magnetic Field \mathbf{H} , at grid point $i_b - \frac{1}{2}$ should be calculated by only taking into

3. Finite Difference in Time Domain Method

account the scattered field. We therefore have to subtract the inserted electric field value at position i_b after having used the total electric field before

$$H_{y,\text{sc}}|_{i_b-\frac{1}{2}}^m = H_{y,\text{sc}}|_{i_b-\frac{1}{2}}^{m-1} + c \frac{\delta t}{\delta x} \left(E_{z,\text{tot}}|_{i_b}^{m-\frac{1}{2}} - E_{z,\text{sc}}|_{i_b-1}^{m-\frac{1}{2}} - E_{z,\text{in}}|_{i_b}^{m-\frac{1}{2}} \right). \quad (3.57)$$

The electric field \mathbf{E} at position i_b is in the inner region containing the superposition of incident and scattered fields. The calculation at this point did refer to the magnetic field \mathbf{H} from the outer region, which is only consisting of the scattered field. A correction has to be applied that subtracts the inserted magnetic field value

$$E_{z,\text{tot}}|_{i_b}^{m+\frac{1}{2}} = E_{z,\text{tot}}|_{i_b}^{m-\frac{1}{2}} + c \frac{\delta t}{\delta x} \left(H_{y,\text{tot}}|_{i_b+\frac{1}{2}}^m - H_{y,\text{sc}}|_{i_b-\frac{1}{2}}^m - H_{y,\text{in}}|_{i_b-\frac{1}{2}}^m \right). \quad (3.58)$$

The values of the incident fields $E_{z,\text{in}}$ at position i_b and $H_{y,\text{in}}$ at position $i_b - \frac{1}{2}$ have to be given.

The inserted fields are interacting with the material in the core region of the simulation. Transmission or reflection spectra of the system which is investigated are obtained by probing the material system with a Gaussian pulse which is spectrally broad enough to excite all the frequencies of interest. Electric or magnetic field values are recorded in front of or behind the region of interest. One simulation is done without the material to normalise the transmission and reflection spectra to the spectrum of the pulse itself. A second run with the material then gives the reflected and transmitted pulse time series which is transformed to frequency space with an FFT and then normalised with the FFT spectrum of the normalisation run. The intensity spectrum is readily taken as the magnitude of the sine and cosine parts of the FFT. In order to compute the phase spectrum, the real and imaginary part of the Fourier transformed time series have to be normalised by the amplitude of the intensity spectrum. The normalised complex Fourier transform f_ω then gives the 2π periodic phase ϕ_ω

$$\phi_\omega = \arctan \left(\frac{\Im(f_\omega)}{\Re(f_\omega)} \right). \quad (3.59)$$

A simple algorithm which checks for 2π discontinuities can then stitch the parts together.

3.4.3. Three Dimensional Micro-Cavity Simulations

The micro-cavity simulations in chapter 6 and chapter 7 feature open boundaries in all three dimensions in contrast to the above mentioned simulations. Due to the evanescent waves occurring near the surfaces of the cavities, the distance to the PML layers should be at least one wavelength. The initial excitation of the electromagnetic field is achieved by a localised point source current. In order to excite a certain mode in the dielectric cavity, the position of this source should be in an antinode position. The temporal envelope of the current is a Gaussian which starts with a value which is only 10^{-3} times the peak amplitude. A sine which is oscillating at the centre frequency of the Gaussian in frequency space is underlying the envelope function.

The resonance spectrum of the dielectric cavity is computed in a way which is related to the Ho method. Electric or magnetic field components are recorded at randomly distributed positions in the simulation domain. Their time series are then Fourier transformed to the resonance spectrum where filter functions can be applied if necessary. Of more interest than in the simulation of periodic systems are lossy modes. The width of the peaks in the spectrum are a measure of the cavity mode loss and can be taken as an estimate for the decay time of the modal energy as will be shown in chapter 6. The mode structure is computed as before, by taking the spatially resolved, discrete Fourier transform at the eigenfrequency of the mode.

3.4.4. Discrete Poynting Theorem

To conclude this chapter, the Poynting theorem (3.60) (see also [25]) will be translated to the discrete formalism of the Yee scheme. The theorem states that the electromagnetic work that matter is setting free in a volume V is equal to the loss over the surface C of that volume plus the energy stored in the fields inside of this volume. A measure for the loss on the surface is the so called Poynting vector \mathbf{S} .

$$\int_V \mathbf{J} \cdot \mathbf{E} \, dr^3 = \int_V -\nabla \cdot \underbrace{(\mathbf{E} \times \mathbf{H})}_{\mathbf{S}} + \frac{1}{2} (\mathbf{E} \cdot \mathbf{D} + \mathbf{H} \cdot \mathbf{B}) \, dr^3 \quad (3.60)$$

The direct analogy of this theorem in differential form to the discretised form in the FDTD scheme does not work well as the vector components of the fields are not positioned at the same point in space and time. Not only are the electric field vector components at different positions as the magnetic field components, but also the components of one vectorial entity is scattered inside a cell of the discretisation grid as shown in the figure 3.1. Following a paper of De Moerloose und De Zutter [38], which deduces the correct form of the discrete Poyntings theorem we present the result which is used in calculating the field energy and the Poynting vector.

If the rules for translating the differential operator to the discrete differencing operator (rule (3.8)) are obeyed, some physical entities are not defined on the required positions in space and time. It is therefore necessary to apply the averaging operator (rule (3.9)) to interpolate the physical entities from surrounding points. This leads to the Poynting theorem in discrete form (3.61) which is compatible to the FDTD algorithm on a Yee grid.

$$\sum_V W_{EJ} = \sum_V \left\{ -\hat{\nabla} \cdot \bar{\mathbf{S}} + \frac{1}{2} \hat{d}_t (W_{\text{Feld},H} + W_{\text{Feld},E}) \right\} \quad (3.61)$$

The entities defined on a discrete grid in space and time, the work W_{EJ} of a current J on the electromagnetic field, the nabla operator $\hat{\nabla}$, the Poynting vector $\bar{\mathbf{S}}$ translate to

3. Finite Difference in Time Domain Method

the following form in the Yee scheme

$$\begin{aligned}
W_{EJ} &= \hat{m}|_x (E_x \hat{m}|_t J_x) \\
\hat{\nabla} &= \hat{d}|_x \mathbf{e}_x + \hat{d}|_y \mathbf{e}_y + \hat{d}|_z \mathbf{e}_z \\
\bar{\mathbf{S}} &= \begin{pmatrix} \hat{m}|_y [\hat{m}|_x [E_y] \hat{m}|_t [H_z]] - \hat{m}|_z [\hat{m}|_t [H_y] \hat{m}|_x [E_z]] \\ \hat{m}|_z [\hat{m}|_y [E_z] \hat{m}|_t [H_x]] - \hat{m}|_x [\hat{m}|_t [H_z] \hat{m}|_y [E_x]] \\ \hat{m}|_x [\hat{m}|_z [E_x] \hat{m}|_t [H_y]] - \hat{m}|_y [\hat{m}|_t [H_x] \hat{m}|_z [E_y]] \end{pmatrix}.
\end{aligned} \tag{3.62}$$

And the important energies which are stored in the electric and magnetic fields $W_{\text{Feld},E}$ and $W_{\text{Feld},H}$, are in the simulations calculated according to

$$\begin{aligned}
W_{\text{Feld},E} &= \hat{m}|_x \left[\epsilon |E_x|^{m-\frac{1}{2}} |E_x|^{m+\frac{1}{2}} \right] + \hat{m}|_y \left[\epsilon |E_y|^{m-\frac{1}{2}} |E_y|^{m+\frac{1}{2}} \right] + \\
&\quad \hat{m}|_z \left[\epsilon |E_z|^{m-\frac{1}{2}} |E_z|^{m+\frac{1}{2}} \right] \\
W_{\text{Feld},H} &= \hat{m}|_y \hat{m}|_z [\mu H_x^2] + \hat{m}|_x \hat{m}|_z [\mu H_y^2] + \hat{m}|_x \hat{m}|_y [\mu H_z^2].
\end{aligned} \tag{3.63}$$

4. Nonlinear, Active Materials

Although the description of light matter interaction in the semi-classical framework can be dated back to at least 1963, the computational complexity of a full description of the electromagnetic vector fields and the complex density matrix of the atomic system still poses quite a challenge to the implementation and calculation even on modern computer systems. The earliest publications on the semi-classical description of the coupled two-level atomic systems and light field are from Haken and Sauermann [39] in 1963 and Lamb [40] in 1964. The semi-classical approach combines the classical world of the Maxwell equations with the atomic systems, described by the Bloch equations which are derived in the framework of quantum mechanics. Especially the complexity of the partial differential Maxwell equations which describe the electromagnetic field prevented a complete and approximation free calculation of real device geometries. With the possibility of large scale FDTD simulations in the 1980s and 90s renewed interest in tackling the realisation of this description without approximations showed up in several papers (e.g. [41], [42], [43] and [44]). But these papers still constrict the model to a reduced spatial dimensionality. In essence, two different methods have been used to extend the Maxwell-Bloch equations to an FDTD form.

One possible approach which was first published by Ziolkowski *et al.* [43] is based on a predictor corrector scheme to solve the first order differential density matrix equations. As Feynman, Vernon and Hellwarth [45] showed with their precession model describing a MASER system, the complex Bloch equations can be transformed to real value equations. It is then possible to keep the real valued FDTD implementation and simply extend it with three, real valued difference equations of first order, to model a dipolar coupling of a two level atomic system with the electric field.

Another approach which was first presented by Nagra and York in 1998 [44] is based on the laser equations which are derived in the book of Siegman [46]. In this derivation, the rate equation which describes the evolution of the occupation probability of the atomic levels is introduced into an oscillator model describing the macroscopic polarisation density as part of the Maxwell material equations. It will be shown later that the transformation from first order Bloch differential equations to the second order Lorentz differential equation and the first order rate equation can be done rigidly.

This chapter will give a quantum mechanically founded derivation of these additional, full-vectorial, difference equations with the inclusion of phenomenological decay and pumping terms. To verify the implementation, exemplary runs and comparisons to approximative calculations will be presented. This chapter will conclude with a one dimensional simulation of the Rabi splitting or normal mode coupling effect in a Bragg

mirror cavity and the relaxation oscillation behaviour in one dimensional VCSEL type system.

4.1. Full Vectorial Maxwell-Bloch Equations

The coupling of material properties to the equations which describe the behaviour of the electromagnetic fields (eqs. 3.4) in the framework discussed here is established by the functional dependence of the electric displacement to the electric field and the macroscopic polarisation. This work is restricted to an atomic, two level system that is interacting with the electromagnetic field by the dipolar Hamiltonian. But extensions to semiconductor Bloch equations have recently been made. The quantum mechanical behaviour of such an atomic system is described by complex pseudo-spin equations. The real valued Maxwell equations have to be coupled to these.

In the previous chapter concerning the FDTD algorithm a linear functional dependence of the electric field \mathbf{E} and the dielectric displacement field \mathbf{D} was assumed. This is no longer valid when active materials are to be modelled. The nonlinear part of the dependence is carried by the macroscopic polarisation density function \mathbf{p} . The dependence of the fields \mathbf{B} and \mathbf{H} should still be linear. Matter is isotropic in space, leading to scalar valued material tensors ϵ and μ . For the sake of simplicity, it is assumed that there is no magnetic moment $\boldsymbol{\mu}$, so the material equations read

$$\begin{aligned} \mathbf{D} &= \epsilon \cdot \mathbf{E} + \mathbf{p} \\ \mathbf{B} &= \mathbf{H}. \end{aligned} \tag{4.1}$$

The atomic dipole moment \mathbf{m} is related to the macroscopic dipole polarisation density \mathbf{p} by the atomic dipole density n_a

$$\mathbf{p} = n_a \mathbf{m}. \tag{4.2}$$

The dielectric displacement field \mathbf{D} and the electric field \mathbf{E} are both defined at the same time step $m + \frac{1}{2}$ in equation (3.14) and equation (3.15). In the simulation, the computation of the electric field vector components from the dielectric displacement field vector components and the macroscopic polarisation vector components is straight forward and can be readily employed in the “leap-frog” scheme of the FDTD algorithm

$$E_x|_i^{m+\frac{1}{2}} = \frac{1}{\epsilon} \cdot \left(D_x|_i^{m+\frac{1}{2}} - p_x|_i^{m+\frac{1}{2}} \right). \tag{4.3}$$

4.1.1. Quantum Mechanics, Semi-Classical Approach

This approach is based on work published by Haken and Sauermann [39], Davis [47] or Lamb [40] around 1963 to tackle the theoretical modelling of optical and microwave amplification by stimulated emission of radiation. The earliest reported time domain implementation of a one dimensional problem with real, full vector fields was done by Ziolkowski *et al.* [43] in 1995.

The idea is to treat the atom quantum mechanically and link the resulting Bloch equations through the macroscopic polarisation \mathbf{p} to the well known Maxwell equations which describe the electric and magnetic fields. To get an idea we look at a system of two non-degenerate atomic eigenstates which should be labelled a and b. The Schrödinger equation (4.4) for the unperturbed atomic Hamiltonian \hat{H}_{at}

$$\hat{H} |\Psi\rangle = i\hbar \partial_t |\Psi\rangle, \quad (4.4)$$

would then have the two linear independent solutions (eigenfunctions) $|\Psi_a\rangle$ and $|\Psi_b\rangle$ with the eigenvalues E_a and E_b representing the energies of the levels. E_a and E_b should be related to each other by the transition frequency Ω obeying

$$\hbar\Omega = E_b - E_a. \quad (4.5)$$

The eigenfunctions should have the form

$$\Psi_i(\mathbf{r}, t) = \phi_i(\mathbf{r}) \cdot e^{-i\frac{E_i}{\hbar}t}, \quad (4.6)$$

so that the eigenproblem reduces to

$$\hat{H}_{\text{at}} |\phi_i\rangle = E_i |\phi_i\rangle, \quad (4.7)$$

with ortho-normalised eigenfunctions $\langle \phi_i | \phi_j \rangle = \delta_{i,j}$.

If the atomic dipole moment interacts with the electromagnetic field, the Hamiltonian changes to an interaction Hamiltonian of the form

$$\hat{H} = \hat{H}_{\text{at}}(\mathbf{r}) + \hat{V}(\mathbf{r}, t). \quad (4.8)$$

The additional dipole Hamiltonian \hat{V} of the system should be represented by the potential energy of a dipole of charge q . The spatial variation of the electric field is expected to be much smaller than the atomic radius and the electric field is hence taken at the atoms centre of mass,

$$\hat{V}(\mathbf{r}, t) = -q \hat{\mathbf{r}} \cdot \mathbf{E}(t). \quad (4.9)$$

The wave function then becomes a quantum mechanical superposition of the atomic eigenstates

$$|\Psi(\mathbf{r}, t)\rangle = c_a(t) \cdot |\Psi_a\rangle + c_b(t) \cdot |\Psi_b\rangle. \quad (4.10)$$

The projection of the Schrödinger equation (4.4) onto the two unperturbed states ($\langle \Psi_a |$ and $\langle \Psi_b |$) leads to the following equations which describe the evolution of the time dependent, complex parameters c_a and c_b

$$\begin{aligned} i\hbar\partial_t c_a(t) &= \langle \phi_a | \hat{V} | \phi_a \rangle \cdot c_a(t) + e^{-i\Omega t} \langle \phi_a | \hat{V} | \phi_b \rangle \cdot c_b(t) \\ i\hbar\partial_t c_b(t) &= e^{+i\Omega t} \langle \phi_b | \hat{V} | \phi_a \rangle \cdot c_a(t) + \langle \phi_b | \hat{V} | \phi_b \rangle \cdot c_b(t). \end{aligned} \quad (4.11)$$

4. Nonlinear, Active Materials

At this point, the transition dipole moment \mathbf{d}_{ab} between the atomic levels a and b should be defined to shorten the following equations

$$\begin{aligned}\mathbf{d}_{ab} &:= q \cdot \langle \phi_a | \hat{\mathbf{r}} | \phi_b \rangle \\ &= q \cdot \int \phi_a^*(\mathbf{r}) \cdot \mathbf{r} \cdot \phi_b(\mathbf{r}) \, dV.\end{aligned}\tag{4.12}$$

This quantity is a real value for bound atomic levels with real wave functions $\phi(\mathbf{r})$.

We now introduce the density matrix ρ for a two level system. The components ρ_{ij} of this matrix are defined as follows

$$\begin{aligned}\rho_{ij} &= \rho_{ji}^* \\ &= c_i \cdot c_j^*\end{aligned}\tag{4.13}$$

and their time derivatives are therefore easily determined by

$$\dot{\rho}_{ij} = \dot{c}_i \cdot c_j^* + c_i \cdot \dot{c}_j^*.\tag{4.14}$$

So the temporal evolution of the density matrix is entirely described by the differential equations of the four density matrix elements

$$\begin{aligned}\dot{\rho}_{aa} &= -\frac{i}{\hbar} \mathbf{d}_{ab} \cdot \mathbf{E}(t) \{ e^{i\Omega t} \rho_{ab} - e^{-i\Omega t} \rho_{ba} \} \\ \dot{\rho}_{bb} &= -\dot{\rho}_{aa} \\ \dot{\rho}_{ab} &= -\frac{i}{\hbar} \mathbf{d}_{ab} \cdot \mathbf{E}(t) \cdot e^{-i\Omega t} \cdot \{ \rho_{aa} - \rho_{bb} \} \\ \dot{\rho}_{ba} &= \dot{\rho}_{ab}^*.\end{aligned}\tag{4.15}$$

With the transformation to the rotating solution of $\tilde{\rho}_{ab} := e^{i\Omega t} \rho_{ab}$, $\tilde{\rho}_{ba} := \tilde{\rho}_{ab}^* = e^{-i\Omega t} \rho_{ba}$ and $N := \rho_{aa} - \rho_{bb}$ this leads to three independent equations, similar to the optical Bloch equations.

$$\begin{aligned}\dot{\tilde{\rho}}_{ba} &= -i\Omega \tilde{\rho}_{ba} + \frac{i}{\hbar} \mathbf{d}_{ab} \cdot \mathbf{E}(t) \cdot N \\ \dot{N} &= -2\frac{i}{\hbar} \mathbf{d}_{ab} \cdot \mathbf{E}(t) \cdot \underbrace{(\tilde{\rho}_{ba}^* - \tilde{\rho}_{ba})}_{=-2i\Im[\tilde{\rho}_{ba}]} = -\frac{4}{\hbar} \mathbf{d}_{ab} \cdot \mathbf{E}(t) \cdot \Im[\tilde{\rho}_{ba}]\end{aligned}\tag{4.16}$$

The relation between the expectation value for the upper (ρ_{bb}) and lower (ρ_{aa}) levels and the entity N is established with the normed trace of the density matrix

$$\text{Tr}[\rho] = \rho_{aa} + \rho_{bb} = 1.\tag{4.17}$$

The value range of the population difference probability N is between -1 (system is totally excited) and 1 (perfectly unexcited), and it can be expressed by the occupation probabilities

$$N = 2\rho_{aa} - 1 = 1 - 2\rho_{bb},\tag{4.18}$$

and is related to the inversion of the atomic system.

Once the density matrix element $\tilde{\rho}_{ba}(t)$ is known, the dipole moment \mathbf{m} of the two level system is given by the expectation value of the position operator $\hat{\mathbf{r}}$ times the systems charge q

$$\begin{aligned}\mathbf{m} &= \langle \Psi | q \cdot \hat{\mathbf{r}} | \Psi \rangle \\ &= 2 \Re [c_a^*(t) c_b(t) \cdot e^{-i\Omega t} \cdot \mathbf{d}_{ab}] \\ &= 2 \Re [\tilde{\rho}_{ba}(t)] \mathbf{d}_{ab}.\end{aligned}\tag{4.19}$$

4.1.2. Relation between Maxwell-Bloch and Oscillator Differential Equation

It will be verified in this section that a calculation of the Lorentz equation, which describes the material polarisation, coupled to a rate equation which is expressing the inversion of the atomic system is equivalent to calculating the Maxwell-Bloch equations. A transformation of the driven Lorentz differential equation of second order

$$\frac{d^2 P(t)}{dt^2} + 2\gamma \frac{dP(t)}{dt} + \omega_0^2 P(t) = F(t),\tag{4.20}$$

to the quantum mechanically derived optical Bloch differential equations of first order (4.16) will be shown. All constants (the damping factor γ and the eigenfrequency ω_0) and the functions (the polarisation P and the driving force F) should be of real value as they are measurable entities ($\gamma, \omega_0, P, F \in \mathbb{R}$). The driving force F of the polarisation is proportional to the electric field \mathbf{E} and the population probability difference N .

A differential equation of order o and constant coefficients is equivalent to a system of coupled differential equations of dimension o . To establish the equivalence in this case, we introduce a new value $Q = \dot{P}$ transferring equation (4.20) into two coupled differential equations

$$\begin{aligned}\dot{P} &= Q \\ \dot{Q} &= -\omega_0^2 P - 2\gamma Q + F.\end{aligned}\tag{4.21}$$

For simplicity the further notation will be put into vectorial form

$$\dot{\mathbf{x}} = \mathbf{A} \cdot \mathbf{x} + \mathbf{b},\tag{4.22}$$

with P and Q forming a time dependent vector in a 2 dimensional real space ($\mathbf{x} \in \mathbb{R}^2$). \mathbf{A} is a 2x2 constant matrix with real coefficients.

$$\mathbf{x} = \begin{bmatrix} P \\ Q \end{bmatrix}; \quad \mathbf{A} = \begin{bmatrix} 0 & 1 \\ -\omega_0^2 & -2\gamma \end{bmatrix}; \quad \mathbf{b} = \begin{bmatrix} 0 \\ F \end{bmatrix}\tag{4.23}$$

A principal axis transformation of this linear equation system will transform the matrix \mathbf{A} to a diagonal form and thereby decouple the two differential equations. They still are

4. Nonlinear, Active Materials

of first order as the Bloch equations to which they should be related. The Eigenvalues and Eigenvectors of the matrix \mathbf{A} are

$$\lambda_{1,2} = -\gamma \mp \sqrt{\gamma^2 - \omega_0^2} \quad \mathbf{v}_{1,2} = \begin{bmatrix} \frac{-\gamma \pm \sqrt{\gamma^2 - \omega_0^2}}{\omega_0^2} \\ 1 \end{bmatrix}. \quad (4.24)$$

Suppose that $\omega_0 > \gamma$, which is the case in most physical systems, the eigenvalues become complex values and we therefore define a real quantity $\Omega^2 := \omega_0^2 - \gamma^2$.

To bring \mathbf{A} to principal axis form (diagonal form) we have to apply the following transformation

$$\mathbf{U}^{-1} \cdot \dot{\mathbf{x}} = \mathbf{U}^{-1} \cdot \mathbf{A} \cdot \mathbf{U} \cdot \underbrace{\mathbf{U}^{-1} \cdot \mathbf{x}}_{=: \mathbf{y}} + \underbrace{\mathbf{U}^{-1} \cdot \mathbf{b}}_{=: \mathbf{e}}, \quad (4.25)$$

leading to the transformed and decoupled differential set of equations

$$\dot{\mathbf{y}} = \mathbf{D} \cdot \mathbf{y} + \mathbf{e}. \quad (4.26)$$

In the general case of a time dependent matrix \mathbf{U} , the derivative of \mathbf{y} is given by

$$\dot{\mathbf{y}} = \mathbf{U}^{-1} \cdot \dot{\mathbf{x}} + \dot{\mathbf{U}}^{-1} \cdot \mathbf{x}, \quad (4.27)$$

and the matrix \mathbf{D} will be defined by

$$\mathbf{D} := \mathbf{U}^{-1} \cdot \mathbf{A} \cdot \mathbf{U} + \dot{\mathbf{U}}^{-1} \cdot \mathbf{U}. \quad (4.28)$$

The transformation matrix \mathbf{U} is composed of the Eigenvectors of the matrix \mathbf{A}

$$\mathbf{U} = \eta \begin{bmatrix} \frac{-\gamma + i\Omega}{\omega_0^2} & \frac{-\gamma - i\Omega}{\omega_0^2} \\ 1 & 1 \end{bmatrix}. \quad (4.29)$$

A choice of an arbitrary norm η of the Eigenvectors will become useful when establishing the relation to the Bloch equations. The inverse of \mathbf{U} is

$$\mathbf{U}^{-1} = \frac{1}{2\Omega\eta} \begin{bmatrix} -i\omega_0^2 & -i\gamma + \Omega \\ i\omega_0^2 & i\gamma + \Omega \end{bmatrix}. \quad (4.30)$$

In this case of time independent transformation matrices, the diagonal matrix \mathbf{D} and the vectors \mathbf{y} and \mathbf{e} become

$$\begin{aligned} \mathbf{y} &= -\frac{i}{2\eta\Omega} \left\{ \begin{bmatrix} \omega_0^2 \\ -\omega_0^2 \end{bmatrix} P + \begin{bmatrix} \gamma + i\Omega \\ -\gamma + i\Omega \end{bmatrix} Q \right\} \\ \mathbf{D} &= \begin{bmatrix} -\gamma - i\Omega & 0 \\ 0 & -\gamma + i\Omega \end{bmatrix} \\ \mathbf{e} &= \frac{1}{2\eta} \begin{bmatrix} 1 - \frac{i\gamma}{\Omega} \\ 1 + \frac{i\gamma}{\Omega} \end{bmatrix} F. \end{aligned} \quad (4.31)$$

The two decoupled differential equations of first order are complex conjugated to each other.

The first condition which is to be imposed on the norm η is, that the form of the complex differential equation should be that of the Bloch equation (4.32) from quantum mechanical considerations (eqs. 4.16), with an additional, phenomenological damping or dephasing factor γ ,

$$\dot{\tilde{\rho}}_{ba} = -(\gamma + \imath\Omega) \tilde{\rho}_{ba} + \imath \underbrace{\frac{1}{\hbar} \mathbf{d}_{ab} \cdot \mathbf{E} \cdot N}_{=: \tilde{F}}. \quad (4.32)$$

It is required that the driving force F in the Lorentz equation (4.20) is proportional to \tilde{F} in the optical Bloch equation with a proportionality factor f . The parts (4.31) of the general solution inserted in equation (4.26) give

$$-\frac{\imath}{2\eta\Omega} \left\{ \omega_0^2 \dot{P} + (\gamma + \imath\Omega) \ddot{P} \right\} = \frac{\imath}{2\eta\Omega} (\gamma + \imath\Omega) \left\{ \omega_0^2 P + (\gamma + \imath\Omega) \dot{P} \right\} + \frac{f\tilde{F}}{2\eta} \left(1 - \imath\frac{\gamma}{\Omega} \right). \quad (4.33)$$

The driving term on the right hand side of the above equation should be the same as the driving term in equation (4.32). With this requirement the norm η becomes

$$\eta = -\frac{f}{2} \left(\imath + \frac{\gamma}{\Omega} \right). \quad (4.34)$$

The linear term in equation (4.33) should be equal to $-(\gamma + \imath\Omega) \tilde{\rho}_{ba}$. As the polarisation is to be coupled to the Maxwell equations, the real part of the first component of the solution vector \mathbf{y} should have the meaning of the polarisation and should therefore be equal to P .

$$P \stackrel{!}{=} \Re \left\{ \frac{\imath}{f(\imath\Omega + \gamma)} [\omega^2 P + (\gamma + \imath\Omega) Q] \right\} \quad (4.35)$$

This requires that $f = \omega_0^2/\Omega$ and as a result the norm becomes

$$\eta = -\frac{\omega_0^2}{2\Omega} \left(\imath + \frac{\gamma}{\Omega} \right). \quad (4.36)$$

The driving force F in equation (4.20) is

$$F = \frac{\omega_0^2}{\hbar \sqrt{\omega_0^2 - \gamma^2}} N \mathbf{d}_{ab} \cdot \mathbf{E} \quad (4.37)$$

The diagonalisation of the differential equation system and normalisation lead to a equation which is similar to the optical Bloch equation

$$\dot{y}_1 = -(\gamma + \imath\Omega) \cdot y_1 + \frac{\imath}{\hbar} N \mathbf{d}_{ab} \cdot \mathbf{E}. \quad (4.38)$$

4. Nonlinear, Active Materials

The relation between $\tilde{\rho}_{ba}$ and P is

$$\tilde{\rho}_{ba} = \left(1 + \frac{\gamma^2}{\Omega^2}\right)^{-1} P + \imath \left\{ \left(\frac{\Omega}{\gamma} + \frac{\gamma}{\Omega}\right)^{-1} P + \frac{\Omega}{\omega_0^2} \dot{P} \right\}. \quad (4.39)$$

We stated earlier, that in most systems, $\gamma \ll \omega_0$. The additional term in the real part of $\tilde{\rho}_{ba}$ is negligible, and the small additional term proportional to P in the imaginary part leads to a tiny phase shift which is also unimportant. In the limit of a vanishing damping parameter γ , the polarisation is then equal to the real part of the off diagonal elements in the quantum mechanical density matrix of the atomic system.

Starting with the quantum mechanical derived complex differential equation of first order for the polarisation term (eq. 4.16), we end up with the following real differential equation of second order for a real quantity P .

$$\ddot{P} + 2\gamma\dot{P} + \omega_0^2 P = \frac{\omega_0^2}{\hbar\sqrt{\omega_0^2 - \gamma^2}} \mathbf{d}_{ab} \cdot \mathbf{E} \cdot N \quad (4.40)$$

The complex part of $\tilde{\rho}_{ba}$ is given by equation (4.39) with the norm factor η of equation (4.36) which is needed in the calculation of the evolution of the occupation probabilities.

$$\Im[\tilde{\rho}_{ba}] = \frac{\sqrt{\omega_0^2 - \gamma^2}}{\omega_0^2} \dot{P} \quad (4.41)$$

The rate equation equivalent to equation (4.16) becomes

$$\dot{N} = -4 \frac{\sqrt{\omega_0^2 - \gamma^2}}{\hbar\omega_0^2} \dot{P} \mathbf{d}_{ab} \cdot \mathbf{E}. \quad (4.42)$$

If we again neglect the small damping term γ , the right side of the above equation is the work which is done by the field on the dipoles (compare the Poynting theorem) and vice versa, divided by the energy quantum. A direct connection to the well known rate equations is established.

The coupling to the Maxwell equations is achieved by converting the microscopic, two level polarisation quantity $\tilde{\rho}_{ba}$ with the density of two level systems n_a regarding equation (4.19) which gives

$$\mathbf{p} = 2n_a \mathbf{d}_{ab} P. \quad (4.43)$$

The dielectric material relation of the Maxwell equations becomes

$$\mathbf{D} = \epsilon_0 \epsilon_r \mathbf{E} + 2n_a \mathbf{d}_{ab} P(t). \quad (4.44)$$

The combined translated Bloch equations in real value form (Lorentz-Bloch) with the material coupling equation of the Maxwell set of equations does then read

$$\begin{aligned} \ddot{P} + 2\gamma\dot{P} + \omega_0^2 P &= \frac{\omega_0^2}{\hbar\sqrt{\omega_0^2 - \gamma^2}} \mathbf{d}_{ab} \cdot \mathbf{E} \cdot N \\ \dot{N} &= -4 \frac{\sqrt{\omega_0^2 - \gamma^2}}{\hbar\omega_0^2} \mathbf{d}_{ab} \cdot \mathbf{E} \cdot \dot{P} \\ \mathbf{D} &= \epsilon_0 \epsilon_r \mathbf{E} + 2n_a \mathbf{d}_{ab} P(t). \end{aligned} \quad (4.45)$$

In order to get to a vectorial description of the polarisation P , we transform the two equations by replacing P with the polarisation density vector $\mathbf{p} = 2n_a \mathbf{d}_{ab} P$ and the population difference N with the population difference density $n = n_a N$.

$$\begin{aligned} \ddot{\mathbf{p}} + 2\gamma \dot{\mathbf{p}} + \omega_0^2 \mathbf{p} &= \frac{2\omega_0^2}{\hbar\sqrt{\omega_0^2 - \gamma^2}} \mathbf{d} \cdot \mathbf{E} n \\ \dot{n} &= -2 \frac{\sqrt{\omega_0^2 - \gamma^2}}{\hbar\omega_0^2} \mathbf{E} \cdot \dot{\mathbf{p}} \end{aligned} \quad (4.46)$$

The driving force for the polarisation density incorporates a matrix constant \mathbf{d} which replaces the construct $\mathbf{d} \cdot \mathbf{E} = (\mathbf{d}_{ab} \cdot \mathbf{E}) \mathbf{d}_{ab}$ and is given by

$$\mathbf{d} = \begin{bmatrix} d_1^2 & d_1 d_2 & d_1 d_3 \\ d_1 d_2 & d_2^2 & d_2 d_3 \\ d_1 d_3 & d_2 d_3 & d_3^2 \end{bmatrix} \quad (4.47)$$

4.1.3. Phenomenological Terms

The aim of this section is to introduce phenomenological terms, that cover non-radiative pumping and relaxation of the atomic system, into the derived real, full vectorial, optical Maxwell-Bloch equations (4.45).

If the atomic system is coupled non-radiatively to a bath of a certain temperature, the excited states relax to a thermal equilibrium distribution. The relaxation rate should be γ_{nr} and the occupation probability of the level with higher energy ρ_{bb} should approach ρ_0 for infinitely large times.

$$\left. \partial_t \rho_{bb} \right|_{nr} = -\gamma_{nr} \cdot (\rho_{bb} - \rho_0) \quad (4.48)$$

The thermal equilibrium occupation ρ_0 is set to 0 in all the simulations.

With equation (4.18) it can be easily deduced, that the evolution of the value $N = \rho_{aa} - \rho_{bb}$ is

$$\left. \partial_t N \right|_{nr} = -\gamma_{nr} \cdot (N - (1 - 2\rho_0)) = -\gamma_{nr} \cdot (N - N_0) . \quad (4.49)$$

In the following sections and chapters we will simulate pumped, lasing material systems. The pumping of the high energy state will increase the occupation probability in a non radiative way with a rate Λ . Equation (4.18) leads to

$$\left. \partial_t N \right|_{\text{pump}} = -2\Lambda . \quad (4.50)$$

Combining those two additional terms and inserting them in the equation (4.42) results in the following evolution equation for the population difference N .

$$\dot{N} = -4 \frac{\sqrt{\omega_0^2 - \gamma^2}}{\hbar\omega_0^2} \mathbf{d}_{ab} \cdot \mathbf{E} \cdot \dot{\mathbf{P}} - 2\Lambda - \gamma_{nr} \cdot (N - N_0) \quad (4.51)$$

In 2000 Bidégaray *et al.* published a paper [48] on the accuracy and stability of additional phenomenological terms in the Bloch equations in the predictor corrector algorithm which Ziolkowski used.

4.1.4. Discrete Full-Vectorial Maxwell-Bloch Equations

The full vectorial discrete Maxwell-Bloch equations which are related to the differential Maxwell-Bloch equations in the last section have been used before to describe the behaviour of active, non-linear materials and laser systems (see Siegman [46]). It has not yet been applied to simulations with more than one dimensional spatial grids. An extension of this scheme to semiconductor Bloch equations is currently being developed. But many non-linear effects of light and matter interaction can already be described on this fundamental level.

To recapitulate the properties of the described semi-classical two level approach, we point out that the polarisation is governed by a damped harmonic oscillator which is driven by the electric field. This is related to a quantum mechanical two level system with a frequency separation of $\hbar\Omega = \Delta E$, whose occupation probability evolution is determined by equation (4.51). This frequency Ω is equal to the resonance frequency $\sqrt{\omega_0^2 - \gamma^2}$ of a damped harmonic oscillator with an eigenfrequency ω_0 and the damping factor γ . The system is non-radiatively coupled to a bath (relaxation constant γ_{nr}), and it is pumped (pumping rate Λ) by inducing a occupation difference in a non-radiative way. A special material equation which relates the electric displacement and the electric field to each other completes the Maxwell equations. It couples the quantum mechanic polarisation P , which is described by the Bloch equations, to the macroscopic polarisation

$$\begin{aligned} \mathbf{D} &= \epsilon_0 \epsilon_r \mathbf{E} + 2n_a \mathbf{d}_{ab} P \\ \ddot{P} + 2\gamma \dot{P} + \omega_0^2 P &= \frac{\omega_0^2}{\Omega} \frac{1}{\hbar} \mathbf{d}_{ab} \cdot \mathbf{E} N \\ \dot{N} &= -2\Lambda - \gamma_{nr} (N - N_0) - 4 \frac{\Omega}{\hbar \omega_0^2} \mathbf{d}_{ab} \cdot \mathbf{E} \dot{P}. \end{aligned} \quad (4.52)$$

\mathbf{D} and \mathbf{E} are vectorial fields, but P and N are scalar and unit-less entities. The connection to the vectorial electric field with units of V m^{-1} is established through the density n_a and the vectorial dipole transition moment \mathbf{d}_{ab} between the excited (b) and the ground state (a) of the quantum mechanical system.

The oscillator equation for the polarisation is being discretised by applying the differencing (3.8) and averaging rules (3.9) and centring the time steps around $m - \frac{1}{2}$.

$$\begin{aligned} P|_{i,j,k}^{m+\frac{1}{2}} &= \frac{2 - \omega_0^2 \delta t^2}{1 + \gamma \delta t} \cdot P|_{i,j,k}^{m-\frac{1}{2}} \\ &\quad - \frac{1 - \gamma \delta t}{1 + \gamma \delta t} \cdot P|_{i,j,k}^{m-\frac{3}{2}} \\ &\quad + \frac{\omega_0^2 \delta t^2}{\hbar \Omega} (1 + \gamma \delta t)^{-1} (\mathbf{d}_{ab} \cdot \mathbf{E})|_{i,j,k}^{m-\frac{1}{2}} N|_{i,j,k}^{m-\frac{1}{2}} \end{aligned} \quad (4.53)$$

Only the old electric field vector and the old population difference value N are required. Discretising the population difference probability differential equation is done by centring

the difference operator to time step m .

$$\begin{aligned}
 N|_{i,j,k}^{m+\frac{1}{2}} &= \frac{2 - \gamma_{\text{nr}}\delta t}{2 + \gamma_{\text{nr}}\delta t} N|_{i,j,k}^{m-\frac{1}{2}} \\
 &+ \frac{2\delta t}{2 + \gamma_{\text{nr}}\delta t} \cdot (-2\Lambda + \gamma_{\text{nr}} N_0) \\
 &- \frac{4\Omega}{\hbar\omega_0^2} (2 + \gamma_{\text{nr}}\delta t)^{-1} \left(\mathbf{d}_{\text{ab}} \cdot \left(\mathbf{E}|_{i,j,k}^{m+\frac{1}{2}} + \mathbf{E}|_{i,j,k}^{m-\frac{1}{2}} \right) \right) \Big|_{i,j,k}^m \\
 &\quad \left(P|_{i,j,k}^{m+\frac{1}{2}} - P|_{i,j,k}^{m-\frac{1}{2}} \right)
 \end{aligned} \tag{4.54}$$

For N at the new time step, we require the value of both, the electric field and the polarisation at the new time step. When the polarisation has been calculated at the new time step, the new electric field can be calculated from it and the new dielectric displacement \mathbf{D} .

$$\begin{aligned}
 E_x|_{i+\frac{1}{2},j,k}^{m+\frac{1}{2}} &= \epsilon_r^{-1}|_{i+\frac{1}{2},j,k} \left(D_x|_{i+\frac{1}{2},j,k}^{m+\frac{1}{2}} - 2n_a d_{\text{ab},x}|_{i+\frac{1}{2},j,k} P|_{i+\frac{1}{2},j,k}^{m+\frac{1}{2}} \right) \\
 E_y|_{i,j+\frac{1}{2},k}^{m+\frac{1}{2}} &= \epsilon_r^{-1}|_{i,j+\frac{1}{2},k} \left(D_y|_{i,j+\frac{1}{2},k}^{m+\frac{1}{2}} - 2n_a d_{\text{ab},y}|_{i,j+\frac{1}{2},k} P|_{i,j+\frac{1}{2},k}^{m+\frac{1}{2}} \right) \\
 E_z|_{i,j,k+\frac{1}{2}}^{m+\frac{1}{2}} &= \epsilon_r^{-1}|_{i,j,k+\frac{1}{2}} \left(D_z|_{i,j,k+\frac{1}{2}}^{m+\frac{1}{2}} - 2n_a d_{\text{ab},z}|_{i,j,k+\frac{1}{2}} P|_{i,j,k+\frac{1}{2}}^{m+\frac{1}{2}} \right)
 \end{aligned} \tag{4.55}$$

Therefore the sequence of values to be calculated is started with the original FDTD algorithm, calculating the magnetic field followed by the dielectric displacement field a half time step later. The additional equations are then evaluated by first computing the new polarisation, then the new electric field and finally the population difference probability N . Additional storage space for the old polarisation value is required as it is a differential equation of second order in time.

4.2. Absorption and Phase Shift in a Linear Material

Multiple simulations of electromagnetic pulses propagating through material which is modelled by the above two level system, will be presented in this section. The parameters defining these two level systems and the one dimensional setups were chosen in order to compare the results to the theoretical investigation in Siegman [46] and the related numerical work of Nagra and York [44]. The electric field of the electromagnetic pulse is polarised along the z direction. The pulse has a spectrum with a Gaussian envelope which is centred at the resonance frequency of the material. Siegman's theoretical small signal analysis is based on the linear susceptibility theory. As the occupation probability density N is assumed to be constant, the general functional $\mathbf{D}[\mathbf{E}]$ is reduced to a linear dependence. The results will be compared to this linear theory.

4.2.1. Theoretical Description

The functional dependence is generally expressed as a power series of the electric field

$$\begin{aligned} \mathbf{D}(\omega) = \epsilon_0 \{ & \epsilon_r \mathbf{E}(\omega) + \boldsymbol{\chi}_1(\omega) \cdot \mathbf{E}(\omega) + \\ & \boldsymbol{\chi}_2(\omega) \cdot \mathbf{E}^2(\omega) + \boldsymbol{\chi}_3(\omega) \cdot \mathbf{E}^3(\omega) + \dots \}. \end{aligned} \quad (4.56)$$

If all terms higher than the first order are vanishing, the system is said to behave in a linear way

$$\begin{aligned} \mathbf{D}(\omega) &= \epsilon_0 \{ \epsilon_r \mathbf{E}(\omega) + \boldsymbol{\chi}_1(\omega) \cdot \mathbf{E}(\omega) \} \\ &= \epsilon_0 \epsilon_r \mathbf{E}(\omega) + \mathbf{p}(\omega). \end{aligned} \quad (4.57)$$

The dielectric displacement field \mathbf{D} is expressed by the electric field \mathbf{E} and the macroscopic polarisation density \mathbf{p} with the proportionality constants ϵ_0 and $\boldsymbol{\chi}_1(\omega)$. The linear susceptibility tensor $\boldsymbol{\chi}_1$ will be reduced to a scalar entity in the oncoming discussion of a one dimensional model.

The form and behaviour of the Fourier components of the macroscopic polarisation is determined by the material equation (4.44) and the Lorentz equation (4.40). Equation (4.44) relates the unit-less atomic polarisation $P(t)$ to the macroscopic polarisation density $\mathbf{p}(t)$. The spectral relation is

$$\mathbf{p}(\omega) = 2n_a \mathbf{d}_{ab} P(\omega). \quad (4.58)$$

The Lorentz equation (4.40) is defining the temporal evolution of the polarisation. A Fourier transformation of this equation and the following comparison with equation (4.57) leads to the resonance characteristic which is expressed in the linear susceptibility

$$\chi(\omega) = \frac{2n_a \omega_0^2}{\epsilon_0 \hbar \Omega} d_{ab}^2 N [\omega_0^2 - \omega^2 - 2i\omega\gamma]^{-1}. \quad (4.59)$$

A separation into the real and imaginary part leads to

$$\begin{aligned} \chi(\omega) &= \chi'(\omega) + i\chi''(\omega), \quad \forall \chi', \chi'' \in \mathbb{R} \\ \chi'(\omega) &= \frac{2n_a \omega_0^2}{\epsilon_0 \hbar \Omega} d_{ab} \frac{N(\omega)}{\omega^2} \frac{\omega_0^2 - \omega^2}{(\omega_0^2 \omega^{-1} - \omega)^2 + 4\gamma^2} \\ \chi''(\omega) &= \frac{2n_a \omega_0^2}{\epsilon_0 \hbar \Omega} d_{ab} \frac{N(\omega)}{\omega^2} \frac{2\gamma\omega}{(\omega_0^2 \omega^{-1} - \omega)^2 + 4\gamma^2} \end{aligned} \quad (4.60)$$

The population difference which is calculated by equation (4.51) is a function of \mathbf{E} and P . If this functional dependence is weak, meaning that a change in the electric field does only slightly affect the value of N , the system is still reacting linearly. This is no longer the case if the electric field amplitude is large and the coupling, which is mainly determined by the atomic dipole transition moment \mathbf{d}_{ab} and the atomic density n_a is strong.

In every single mode cw-laser system a resonator resonance frequency should be close to the material resonance frequency Ω . For damping constants γ which are much smaller than the frequency ω_0 , a simple approximation to the equations can be applied

$$\omega_0^2 - \omega^2 = (\omega_0 - \omega) \underbrace{(\omega_0 + \omega)}_{\approx 2\omega} \approx 2\omega (\omega_0 - \omega). \quad (4.61)$$

This approximation leads to the well known Lorentzian form of the linear susceptibility

$$\begin{aligned} \chi'(\omega) &\stackrel{\omega \rightarrow \omega_0}{=} \frac{2n_a \omega_0^2}{\epsilon_0 \hbar \Omega} d_{ab} \frac{N(\omega)}{2\omega} \frac{\omega_0 - \omega}{(\omega_0 - \omega)^2 + \gamma^2} \\ \chi''(\omega) &\stackrel{\omega \rightarrow \omega_0}{=} \frac{2n_a \omega_0^2}{\epsilon_0 \hbar \Omega} d_{ab} \frac{N(\omega)}{2\omega} \frac{\gamma}{(\omega_0 - \omega)^2 + \gamma^2}. \end{aligned} \quad (4.62)$$

A solution for a plane wave which is travelling through the linear susceptibility medium must obey the Helmholtz or wave equation

$$0 = \Delta \mathbf{E}(t) - \mu_0 \frac{\partial^2 \mathbf{D}}{\partial t^2} \quad (4.63)$$

which is transformed to frequency space with the assumption of a linear susceptibility as given by equation (4.57)

$$0 = \left[\Delta + \frac{\omega^2}{c^2} (\epsilon_r + \chi(\omega)) \right] \mathbf{E}(\omega). \quad (4.64)$$

The assumption of an E_z polarised plane wave, travelling along the x axis, reduces this equation to

$$0 = \frac{\partial^2 E_z(x, \omega)}{\partial x^2} + \frac{\omega^2}{c^2} (\epsilon_r + \chi(\omega)) E_z(x, \omega) \quad (4.65)$$

The ansatz $E_z(x, \omega) = E_z(\omega) \exp(\imath kx)$ is made to reduce this problem to a plane wave which is travelling in positive x direction with a wave vector k . The wave equation relates the wave vector to the material properties and the frequency, establishing the dispersion relation $k^2 = \omega^2 c^{-2} (\epsilon_r + \chi(\omega))$ which we will approximate through $k \approx \sqrt{\epsilon_r} \omega c^{-1} (1 + 0.5 \epsilon_r^{-1} \chi(\omega))$. The Fourier components of the electric field can therefore be represented by the approximate equation

$$E_z(\omega) \approx \hat{E}_z \exp\left(-\frac{1}{2} \frac{\omega}{c} \chi''(\omega) x\right) \exp\left(\imath \frac{\omega}{c} \sqrt{\epsilon_r} \left(1 \pm \frac{1}{2} \frac{1}{\epsilon_r} \chi'(\omega)\right) x\right). \quad (4.66)$$

4.2.2. Simulation

The first test to verify the correctness and accuracy of the numerical approach was a one dimensional simulation of an electromagnetic pulse passing through a two level medium, similar to the work of Nagra and York [44].

4. Nonlinear, Active Materials

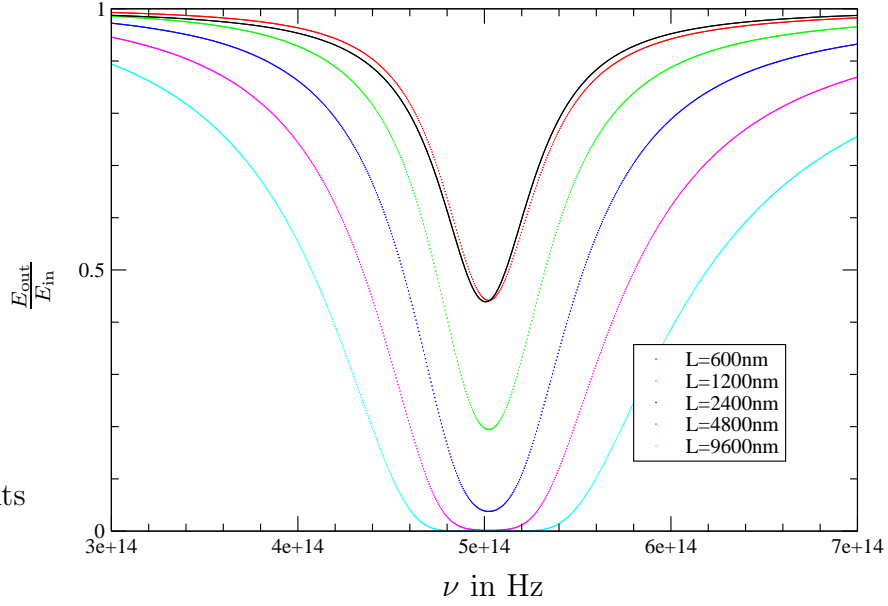


Figure 4.1.: Absorption spectrum of a pulse with $\hat{E} = 2.5 \cdot 10^8 \text{ V/m}$ travelling through absorbing media of different thicknesses L .

The simulation region is consisting of 2048 grid points with a grid spacing of 6 nm in physical space. It is closed by Mur boundary conditions of first order which result in less than 0.1% reflection error. The background refractive index ϵ_r is set to 1. The region of the two level system material begins at grid point 100. Five different material region lengths, ranging from 600 nm to 9600 nm were simulated. The resonance frequency is $\Omega = 5 \times 10^{14} \text{ Hz}$ and the full width at half maximum Γ of the Lorentz absorption line shape is $\Gamma = 2\gamma = \pi \times 10^{14} \text{ s}^{-1}$. The dipole moment is oriented along the z axis and has a strength of $d_{\text{ab},z} = -1.957 \times 10^{-29} \text{ A s m}$. At the beginning of the simulation, at time $t = 0$, the system is in the ground state. It is not pumped and the non-radiative relaxation rate to the lower level is $\gamma_{\text{nr}} = 5 \times 10^7 \text{ s}^{-1}$. The steady state occupation probability of the upper level is $\rho_{\text{bb, therm}} = 0$. The insertion of the pulse is done by the total field, scattered field method at grid point 50. The E_z polarised electromagnetic pulse with a Gaussian envelope is spectrally broad enough to cover the whole spectral range of interest. Its centre frequency is the same as the resonance frequency of the two level system. The amplitude of the electric field at the centre frequency is $2.5 \times 10^8 \text{ V/m}$ which is still in the range of the small signal analysis. This was also verified in the output of the simulation.

Equation (4.66) contains two exponential functions. The first exponential function has a real exponent which is attenuating the amplitude of the electric field. The second exponential function has an imaginary exponent, thereby shifting the phase of spectral components. The relative amplitude spectrum is shown in figure 4.1 and the phase shift is shown in figure 4.2.

A theoretical estimate of the amplitude attenuation and the phase shift can be obtained

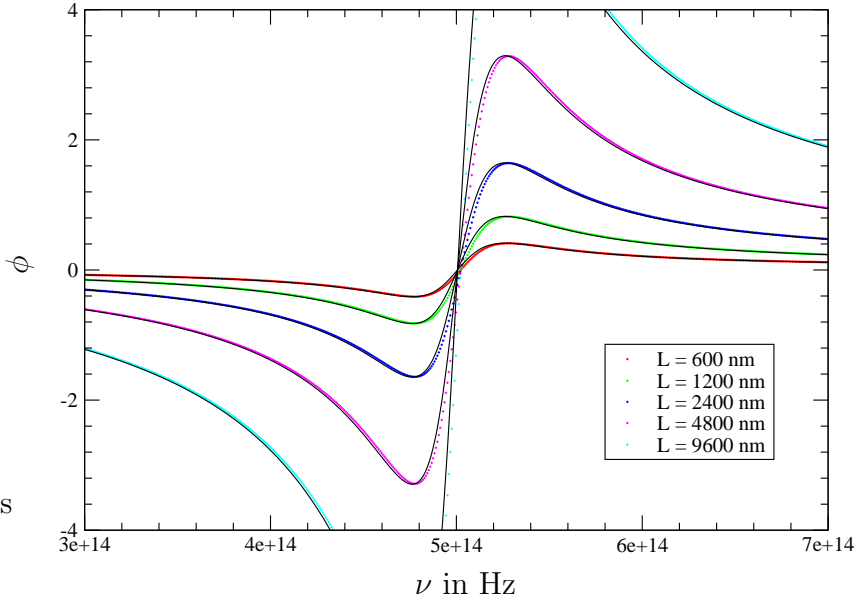


Figure 4.2.: Phase spectrum of a pulse with $\hat{E} = 2.5 \cdot 10^9 V/m$ travelling through absorbing media of different thicknesses L . There is no phase shift at the resonance frequency.

from equation (4.66). If a pulse is passing through the medium, the Fourier components of the electric field E_{in} and E_{out} , which are separated by the distance L are attenuated according to

$$\frac{E_{out}(\omega)}{E_{in}(\omega)} = \exp\left(-\frac{1}{2} \frac{\omega}{c} \chi''(\omega) L\right). \quad (4.67)$$

Equally interesting is the phase shift ϕ which is occurring during the passage through the medium. It is given by

$$\phi(\omega) = -\frac{1}{2} \frac{\omega}{c} \sqrt{\epsilon_r} \chi'(\omega) L. \quad (4.68)$$

In the simulation, the transmitted wave was probed at grid position 2000. Figure 4.1 shows the effect of the increasing thickness L of the absorbing linear susceptible medium on the absorption spectrum of the travelling pulse. With increasing material region length L , the dip of the absorption curve gets deeper and the phase shift larger (see fig. 4.2). Eventually the resonance frequency is totally absorbed. The absorption coefficient is limited to this total absorption and longer distances in the material lead to flat absorption spectra around the resonance frequency.

The phase shift on the other hand is not limited to a maximum. An increase in the material length L leads to ever increasing phase shift spectra.

The absorption spectrum of the data set belonging to the length $L = 0.6 \mu m$ is compared

to the analytic version and shows only a very small deviation. Analytic and calculated solutions are shifted in frequency by about 3 parts in a thousand. The same shift to higher frequencies is also present in compared theoretical and numerical predicted phase shifts of the spectral parts of the pulse.

4.3. Ultra-Fast Pulse Interaction

Time-domain simulations are the first choice for interactions of ultra-short pulses with materials due to the restrictions on the time-step imposed by the Courant criterion. In the late 1980s and then with increasing computational power in the 1990s several auxiliary differential equation (ADE)-FDTD approaches were made to simulate pulse propagation in non-linear materials. Joseph *et al.* [49] and Radic and George [50] investigated a pulse train in a periodic setup in 1991, followed by Goorjian and Taflove [51] in 1992 who simulated femto-second pulse propagation in dispersive media. All these approaches are based on an ADE-FDTD method in which the functional dependence between the dielectric displacement and the electric field is modelled without the quantum mechanical simulation of the atoms. Körner and Fichtner [52] published a closer investigation on the accuracy and efficiency of the ADE-FDTD methods in 1997. Other direct simulations of the light matter interactions related to the pulse area theorem which was proposed in 1968 by McCall and Hahn [53] was already simulated with a time-domain approach by Davis and Lin in 1973 [54]. The investigated a ultra-fast pulse travelling in a two level system.

To further test the full implementation of the optical Maxwell-Bloch difference equations, we analyse the ultra-fast interaction of plane waves and light pulses with the quantum mechanical system describing the atoms. Rabi oscillations (see for example Loudon, “The quantum theory of Light” [55]) are an ultra-fast phenomenon which has analytic expressions to which we can compare our simulations. Quantum mechanical systems with discrete energy levels which are interacting with a sinusoidal excitation undergo oscillations in their occupation probabilities. This optical effect is similar to solutions that describe spin systems subjected to an oscillatory magnetic field as in nuclear or electronic magnetic resonance experiments.

These oscillations, which are due to an interaction of the atomic system with an electromagnetic field, can be theoretically understood in terms of the equations (4.40) and (4.51) coupled to a sinusoidal electric field which is oscillating with the frequency ω . Non-radiative pumping processes are not considered here. These two equations describe the temporal evolution of the quantum mechanical density matrix

$$\begin{aligned} \ddot{P} + 2\gamma \dot{P} + \omega_0^2 P &= \frac{\omega_0^2}{\Omega} \frac{1}{\hbar} d_{ab,z} \cdot E_z N \\ \dot{N} &= -\gamma_{nr} (N - N_0) - 4 \frac{\Omega}{\hbar \omega_0^2} d_{ab,z} \cdot E_z \dot{P}. \end{aligned} \tag{4.69}$$

The electric field should be a sinusoidal wave with the amplitude \hat{E} . Its frequency should

be near the resonance frequency of the atomic system $\omega = \Omega + \Delta\omega$, $\Delta\omega \ll \Omega$.

$$E_z(t) = \hat{E} \sin(\omega t) = -i \frac{1}{2} \hat{E} (e^{i\omega t} - e^{-i\omega t}) \quad (4.70)$$

The polarisation which is in near resonance with the driving electric field is phase shifted by $-\pi/2$. It is assumed that the function which describes the behaviour in time of the polarisation is a product of a fast oscillating part with frequency ω and a slowly varying envelope function $\tilde{P}(t)$

$$P(t) = -\tilde{P}(t) \cos(\omega t) = -\frac{1}{2} \tilde{P}(t) (e^{i\omega t} + e^{-i\omega t}) . \quad (4.71)$$

This ansatz is called the slowly varying envelope approximation (SVEA) and can be used in the above differential equations if the parameters comply with the requirements. The differential equations are decoupled in this process. The resulting differential equation, of second order which describes the population difference N reads

$$\frac{\partial^2 \tilde{N}(t)}{\partial t^2} + (\gamma + \gamma_{\text{nr}}) \frac{\partial \tilde{N}(t)}{\partial t} + \left(\gamma\gamma_{\text{nr}} + \frac{d_{\text{ab}}^2}{\hbar^2} \hat{E}^2 \right) \tilde{N}(t) = \gamma\gamma_{\text{nr}} N_0 . \quad (4.72)$$

Now the so called Rabi frequency ω_{R} is defined

$$\omega_{\text{R}}^2 := \frac{d_{\text{ab}}^2}{\hbar^2} \hat{E}^2 . \quad (4.73)$$

The second order differential equation which describes the slowly changing polarisation $\tilde{P}(t)$ is similarly derived and both independent equations are

$$\begin{aligned} \ddot{\tilde{P}} + (\gamma + \gamma_{\text{nr}}) \dot{\tilde{P}} + (\omega_{\text{R}}^2 + \gamma\gamma_{\text{nr}}) \tilde{P} &= \frac{\omega_0 |d_{\text{ab}}|^2}{\hbar\Omega} \gamma_{\text{nr}} \hat{E} N_0 \\ \ddot{\tilde{N}} + (\gamma + \gamma_{\text{nr}}) \dot{\tilde{N}} + (\omega_{\text{R}}^2 + \gamma\gamma_{\text{nr}}) \tilde{N} &= \gamma\gamma_{\text{nr}} N_0 . \end{aligned} \quad (4.74)$$

4.3.1. Rabi Flopping

The simulation which should model the system that is investigated in Loudon [55] is started with all two level systems being in their lower, unexcited state ($N = 1$). The thermal equilibrium occupation of the upper level is $\rho_{\text{bb,therm}} = 0$. A plane electromagnetic wave with the same frequency as the material resonance $\Omega = 3.1416 \times 10^{15} \text{s}^{-1}$ is travelling through the material region. The density of the dipoles is set to be $n_{\text{a}} = 10^{26} \text{m}^{-3}$ as before. The dipole moment is $d_{\text{ab}} = -1.957 \times 10^{-29} \text{A s m}$. The half width at half maximum of the Lorentzian absorption line shape is $\gamma = 1.571 \times 10^{14} \text{s}^{-1}$ and the non radiative decay rate is $\gamma_{\text{nr}} = 5 \times 10^7 \text{s}^{-1}$. Five different amplitudes of the impinging wave, in the range of $1 \times 10^8 \text{V/m}$ to $5 \times 10^9 \text{V/m}$ reveal two different reaction schemes of the two levels. Figure 4.3 shows the resulting behaviour of the population difference N .

The comparison of these numerical results to the analytical solution for a dipolar two level system which is driven by an electromagnetic field as mentioned above is achieved by

4. Nonlinear, Active Materials

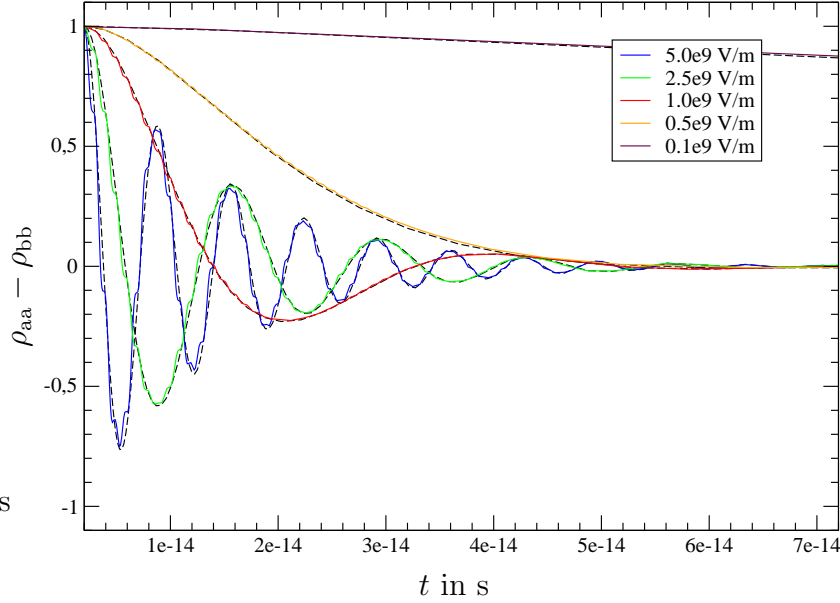


Figure 4.3.: Rabi flopping behaviour of a two level system which is coupled to an electromagnetic field by a dipole Hamiltonian. The system is in resonance with the probing field. The occupation probability difference for various amplitudes over time is compared to analytic expressions as described in the text.

solving equation (4.74) for the amplitude of the occupation difference $\tilde{N}(t)$. To shorten the analytical expressions of the solutions, the characteristic time $T_1 := 2(\gamma + \gamma_{nr})^{-1}$ which measures the decay of the inversion is introduced and for a damped Rabi oscillation the frequency $\Omega_R^2 := \omega_R^2 - \frac{1}{4}(\gamma - \gamma_{nr})^2$ is defined. The initial conditions ($N(t=0) = 1$ and no field at $t=0$) of the simulation setup leads to two different analytical solutions of equations (4.74) which are classified by the amplitude of the electric field. They represent an over-damped oscillator for a low electric field and an oscillating solution for a large driving electric field

$$\begin{aligned} \tilde{N}(t) &= e^{-\frac{t}{T_1}} \left[\cosh \sqrt{-\Omega_R^2} t + \frac{T_1^{-1}}{\sqrt{-\Omega_R^2}} \sinh \sqrt{-\Omega_R^2} t \right] & \forall \frac{1}{2} (\gamma - \gamma_{nr}) \geq \Omega_R \\ \tilde{N}(t) &= e^{-\frac{t}{T_1}} \left[\cos \Omega_R t + \frac{T_1^{-1}}{\Omega_R} \sin \Omega_R t \right] & \forall \frac{1}{2} (\gamma - \gamma_{nr}) < \Omega_R. \end{aligned} \quad (4.75)$$

All results decay towards a certain inversion for large times which is given by the saturated inversion

$$\tilde{N}_{\text{sat}} := \tilde{N}(t \rightarrow \infty) \rightarrow N_0 \cdot \left(\frac{\Omega_R^2}{\gamma\gamma_{nr}} + 1 \right)^{-1}. \quad (4.76)$$

The five amplitudes which were used in the simulations of figure 4.3 were chosen to cover the entire range of different dynamical behaviour. With large amplitudes of

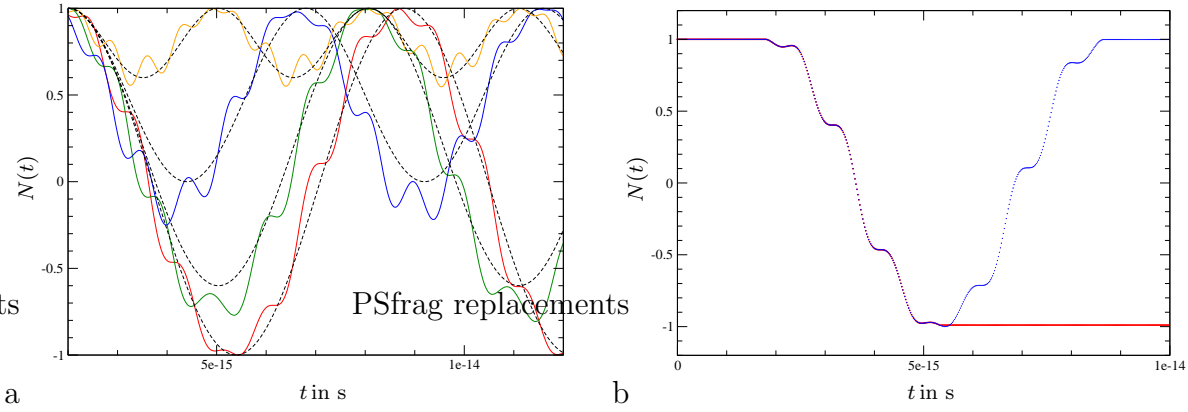


Figure 4.4.: Part (a) shows five simulation results presenting Rabi flopping behaviour with different degrees of frequency detuning. Part (b) demonstrates the effect of so called π and 2π pulses (pulses of certain lengths) on the occupation difference N of an initially unexcited system.

the incoming electric field the dipole transition undergoes damped Rabi oscillations to a steady state population difference of equation (4.76), also called Rabi flopping. For weaker electromagnetic fields the behaviour is more like an over-damped harmonic oscillator, approaching the saturated inversion density. The numerical calculation as seen in figure 4.3, shows very good compliance compared to the theoretical estimates of the inversion behaviour described by equation (4.75). In addition to the slow change in inversion density the simulation also shows fast oscillation about the analytic SVEA result.

4.3.2. Rabi Flopping with Detuned Excitation

As another test we check the effect of detuning the frequency of the probing wave away from the resonance frequency of the two level system. This is done in analogy to figure 2.5 from [56]. The simulation parameters are unchanged if not otherwise noted. In the simulations, we artificially reduce the line width of the dipole transition and the non radiative recombination rate γ_{nr} to zero. Thus the decay rate of the Rabi oscillation Γ_R vanishes. The amplitude of the probing wave is set to $\hat{E} = 5 \times 10^9$ V/m. Five different ratios of detuned probing field frequencies $|\Omega - \omega|/\Omega_R$, (0, 0.5, 1, 2) were compared to the theoretically derived behaviour in equation (4.74). The simulation results are shown in figure 4.4a for the relative detuning $|\omega_0 - \omega|/\Omega_R \in \{0, 0.5, 1, 2\}$. Similar to the previous example, the results match very well the analytically predicted behaviour (dashed lines).

4.3.3. Pi-Pulse Propagation

The usual theoretical model which describes the optical pulse interaction with the atomic system is based on the SVEA as shown above. Effects which are due to the fast oscillation of the electromagnetic field are not included in the resulting equations. Figure 4.4 clearly

4. Nonlinear, Active Materials

shows this different behaviour of the population difference N between the full-vectorial time-domain model which produces the small, fast, underlying oscillations and the SVEA approach.

In 1998 Hughes [57] employed a fourth order Runge-Kutta method to solve the Bloch equations in addition to a standard FDTD approach. He showed that a pulse travelling through a material consisting of two level systems, with pulse areas larger than 2π , higher spectral components on the propagating pulse are produced which are not predicted by the slowly varying-envelope approximation (SVEA). Hughes shows that this is due to “electric field time derivative effects” which leads to “carrier wave Rabi flopping”.

Optical pulses of certain lengths which are propagating through a medium consisting of two level systems, do either leave the medium unchanged or completely invert the occupation of the quantum mechanical system.

In the following description and simulation, it is assumed that the quantum mechanical system is completely decoupled from any bath and the decay constants γ and γ_{nr} have therefore vanished. The system is not non-radiatively pumped. The other simulation parameters and the setup is as before. The pulses which are interacting with the two level system have a certain duration T_{pulse} (a rectangular envelope) and frequency which is equivalent to the transition frequency ω_0 that is defined by the energy difference of the atomic levels. Pulse lengths equal to half the duration of one Rabi oscillation – so called π pulses, $T_{\text{pulse}} = \pi/\omega_R$ – inverts the occupation between state a and b. Likewise, the application of pulses with the length of an entire Rabi oscillation period – so called 2π pulses – leave the occupation probabilities unchanged, as can be seen in figure 4.4a for the simulation without detuning.

4.4. Normal Mode Coupling

The Systems investigated so far only include the material part of a laser active device. Now we will introduce a dielectric Bragg mirror cavity into the simulation setup providing feedback. The consideration of a steady pumping process to sustain laser operation will not be employed until the next section. The simulation of a normal mode coupling is related to the first publication by Weisbuch *et al.* [58] of such an effect in a semiconductor micro-cavity in 1992. The setup of the Bragg mirror cavity is taken from this paper and figure 4.5a shows the dielectric constant at each grid point in the simulation core with a magnification of the defect cavity region. The dielectric system in the reflection experiment was grown on a GaAs wafer ($n \approx 3.675$). Thirty-three Bragg layers made of a quarter-wavelength $\text{Al}_{0.4}\text{Ga}_{0.6}\text{As}$ layer ($n \approx 3.4$) followed by a quarter-wavelength AlAs layer ($n \approx 2.95$) form the right Bragg mirror in figure 4.5a. The wavelength long defect is grown of $\text{Al}_{0.2}\text{Ga}_{0.8}\text{As}$ ($n \approx 3.52$) with a 76 Å thick GaAs quantum well in the middle. The left Bragg mirror consists of 24 repetitions of the quarter-wavelength double layer structure, which is started with an AlAs layer.

Figure 4.5b shows the transmission and reflection spectra of the empty cavity. In the middle of the stop band a pronounced defect mode is visible. The position in frequency space is defined by the length of the defect in the cavity.

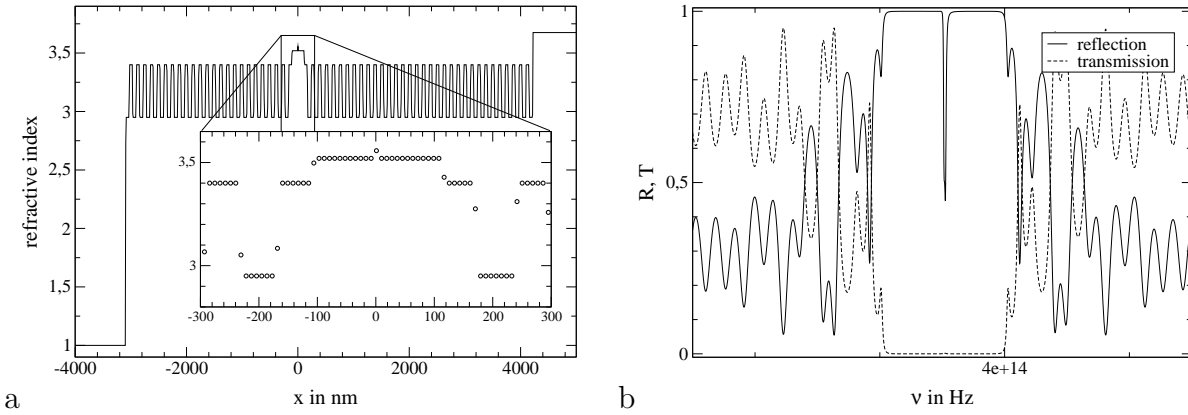


Figure 4.5.: Part (b) shows the transmission and reflection spectra of the dielectric Bragg mirror defect cavity which is presented in part (a). The Bragg mirror is made of twenty-four quarter-wavelength stacks on the left side of a λ defect in the centre and thirty-three stacks on its right.

The excitonic states of the quantum well material are modelled by a two level system with a density constant $n_a = 1 \times 10^{27} \text{ m}^{-3}$, a dipole moment $d_{ab} = -4.806 \times 10^{-29} \text{ A s m}$, no non-radiative recombination processes and a damping factor $\gamma = 1.52 \times 10^{12} \text{ s}^{-1}$. The system is initially entirely in its ground state. The transition frequency of the two level system is tuned to different values around 1.577 eV instead of changing the dielectric resonators dimensions, as it was done in the mentioned publication.

This coupled system is probed by a short Gaussian pulse with central frequency of about $3.815 \times 10^{14} \text{ Hz}$ and a half width of $8 \times 10^{13} \text{ s}^{-1}$. The initially used amplitude of the electric field is $5 \times 10^8 \text{ V m}^{-1}$. The reflection spectrum reveals two dips in the stop band of the Bragg mirror. If the detuning of the transition frequency to the cavity defect mode is large, one of the dips can be clearly associated with the two level system and the other with the cavity mode. But if the detuning is getting smaller, figure 4.6 shows the anti-crossing behaviour at the positions of the two dips. An anti-crossing gap of 0.004 eV is found when the two frequencies match, which is in good agreement to the measurement of Weisbuch *et al.* This effect is called Rabi splitting or normal mode coupling. Two good review articles which describe this effect in semiconductor laser systems are Khitrova *et al.* [59] in 1999, or Skolnick *et al.* [60] in 1998.

On a fundamental level, the anti-crossing is modelled in terms of a coupling between the optical and excitonic oscillatory systems. The coupling strength identifies two different regimes of coupling. A splitting only occurs under certain conditions which are then called the strong coupling regime. In the weak coupling regime, no splitting effect can be observed in the experiments and the two dips in the reflection spectrum seem to pass unaffected over each other with changing detuning.

Theoretical descriptions that also take into account the more complex cavity properties of the experiments, like the Bragg mirror cavity of the initial experiments by Weisbuch, are based on a transfer-matrix description. Jorda [61] presented such a theoretical model in 1994, and the numerical calculation related to the original measurement by Weisbuch

4. Nonlinear, Active Materials

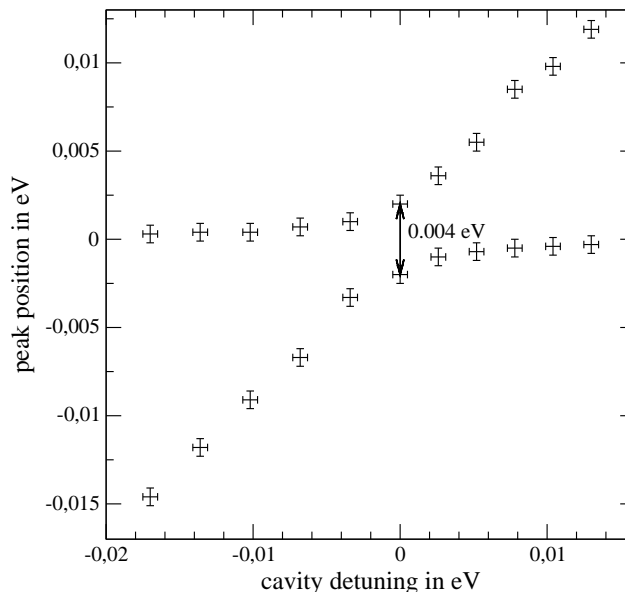


Figure 4.6.: The frequency of the calculated peak positions in eV over the detuning of the cavity resonance to the transition frequency of the two level system.

et al. Recently Lagoudakis *et al.* [62] reported coexistence of weak and strong coupling in a VCSEL micro-cavity.

For very small line widths of the QW absorption line shape, the refractive index has a pronounced refractive index change. The cavity mode position is determined by the length of the defect in the Bragg mirror and its refractive index. If the refractive index change induced by the QW coincides with the position of the QW absorption characteristic, more than one frequency of the electromagnetic field might interfere constructively. This results in more than one dip in the reflection spectrum for strong coupling. It should be obvious that the splitting is strongly dependent on the QW oscillator strength, its absorption characteristic including the line width, and the loss of the cavity which are directly linked to the shape of the reflection dip of the cavity mode. The oscillator strength is proportional to the density n_a and the dipole moment d_{ab} .

Figure 4.7 shows results from the simulations in the situation of no frequency detuning between the empty cavity mode and the absorption resonance. The amplitude of the probe pulse is changed over a very broad range (part a). Weak electromagnetic fields do not perturb the two level occupation probabilities noticeably and the occupation difference N is approximately constant. For electric field strengths smaller than $5 \times 10^8 \text{ V m}^{-1}$ no change in the gap size is visible. Stronger electric fields lead to smaller gap sizes. This transition field strength is well in accordance with earlier section results (see fig. 4.3), marking the boundary between over-damped Rabi flopping and Rabi oscillations.

Figure 4.7b shows the dip positions for different polarisation damping rates γ . Large line-widths lead to smaller dip separations. In addition, large values of γ or γ_{cav} (the cavity loss) can lead to an indistinguishable superposition of both dipo.

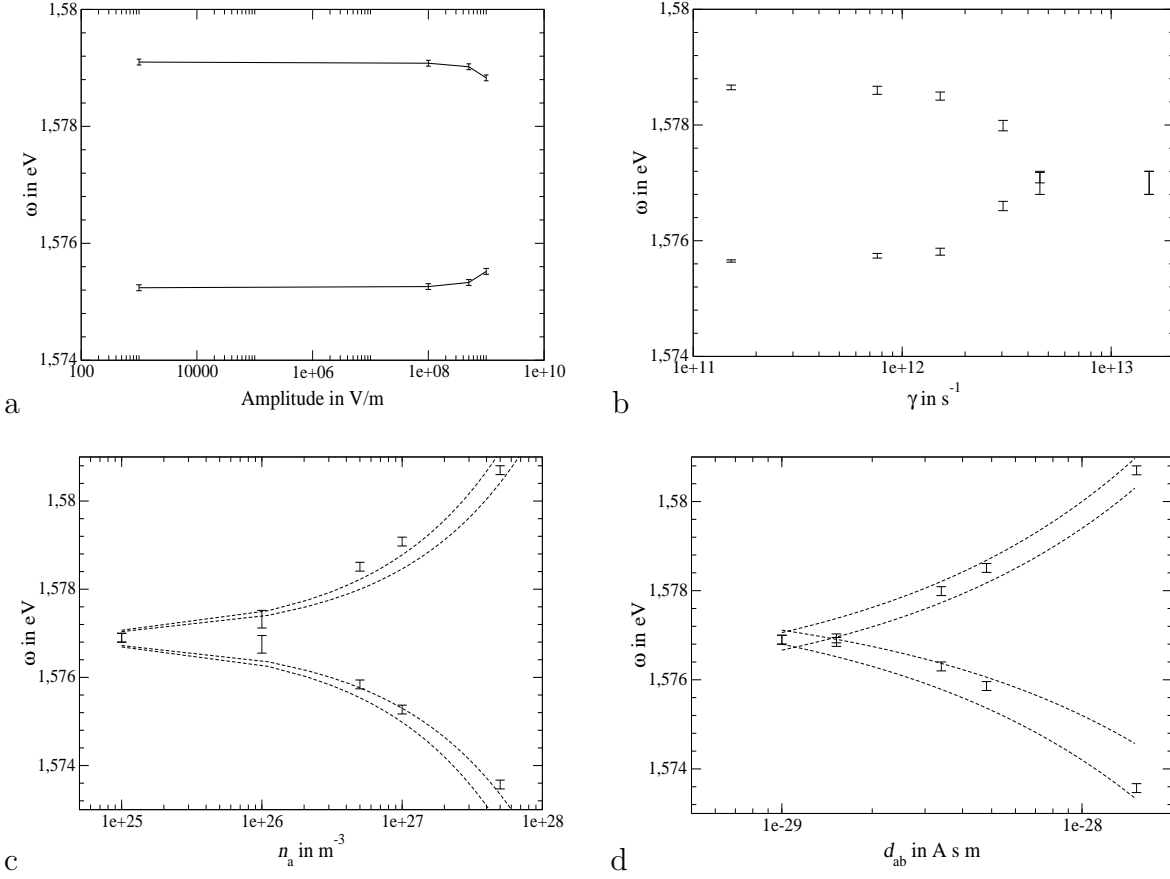


Figure 4.7.: The dependence of anti-crossing gap size on parameters. Probe pulse amplitude (a), polarisation damping factor (b), increasing density (c) and increasing dipole moment strength (d).

The dependence of the gap size on the oscillator strength, a combination of the dipole density n_a and the dipole moment d_{ab} is presented in figure 4.7, parts (c) and (d). Skolnick *et al.* [60] give a square root dependence of the gap size to the oscillator strength. The oscillator strength is proportional to the density of the dipoles n_a and the dipole moment d_{ab} . A fit of the simulation results in figure 4.7c and d to this square root behaviour is shown.

4.5. Stimulated Systems

Finally we will close this chapter with the simulation of a VCSEL type system that is non-radiatively pumped from the time $t = 0$ and shows transitional relaxation oscillation behaviour as expected. Following the book “Lasers” of Siegman [46] we introduce the laser cavity equations which will be compared to the simulation results. A stability analysis will then give an approximative estimate of the relaxation oscillation frequency and decay times.

The last section of this chapter presents the relaxation oscillation simulation in time and a reduced phase space diagram.

4.5.1. Laser Cavity Equations

In general, a laser can be described with a reduced set of variables. The two physical entities that will represent the evolution of the system in this section, are the envelope amplitude A of the electric field and the inversion n at the same position in the cavity. The differential equations in time which describe these two entities will be derived from the following basic assumptions.

Although we want to compare the laser cavity equations with the simulation of a VCSEL system with a complex dielectric structure in the Bragg mirrors and the QW cavity a first assumption will be a homogeneous refractive index ϵ_r inside the cavity. It should be an extremely good cavity with very small loss. The electromagnetic field outside the cavity is assumed to be negligible. We therefore can restrict the electromagnetic field calculations to the cavity volume V_{cav} . It will be shown that the comparison still gives a reasonable agreement.

An important assumption is that the pseudo modes in the non-linear cavity should be similar to the modes in the cold cavity. The electric field should always be a superposition of the linear cold cavity solutions

$$\mathbf{E}(\mathbf{r}, t) = \sum_i \hat{E}_i(t) \mathbf{u}_i(\mathbf{r}), \quad (4.77)$$

which satisfy the Helmholtz equation. The mode structure $\mathbf{u}_i(\mathbf{r})$ then has to obey

$$\left\{ \Delta + \frac{\epsilon_r}{c^2} \omega_i^2 \right\} \mathbf{u}_i(\mathbf{r}) = 0 \quad (4.78)$$

with the appropriate boundary conditions. The cold cavity modes have to be orthogonal to each other, and to simplify matters there should be no degeneracy

$$\iiint_{\text{cav}} \mathbf{u}_i(\mathbf{r}) \cdot \mathbf{u}_j(\mathbf{r}) d^3\mathbf{r} = \begin{cases} 0 & \forall i \neq j \\ V_i & \forall i = j \end{cases}. \quad (4.79)$$

The mode structure \mathbf{u}_i^2 should be normalised by definition so that its maximal value is equal to 1.

$$\mathbf{u}_i^2 = \max [|\mathbf{E}|^2(\mathbf{r})]^{-1} |\mathbf{E}|^2(\mathbf{r}) \quad (4.80)$$

The norm volume V_i in the case of a rectangular cavity with perfectly conducting, metallic boundary conditions would be half the cavity volume.

To simplify matters further, we restrict the model to a one dimensional problem along the x direction with a TE_z polarised plane standing wave in the cavity of length L . Maxwell equations including the macroscopic induced polarisation density $p_z(x, t)$ lead to a wave equation for the electric field component $E_z(x, t)$

$$-\frac{\partial^2 E_z(x, t)}{\partial x^2} + \frac{\epsilon_r}{c^2} \frac{\partial^2 E_z(x, t)}{\partial t^2} = -\mu_0 \frac{\partial^2 p_z(x, t)}{\partial t^2}. \quad (4.81)$$

The decomposition of the electric field given by equation (4.77) replaces the electric field, and the use of the eigenvalue equation (4.78) leads to

$$\sum_i \left\{ \omega_i^2 \hat{E}_i(t) + \frac{\partial^2 \hat{E}_i(t)}{\partial t^2} \right\} u_{z,i}(x) = -(\epsilon_0 \epsilon_r)^{-1} \frac{\partial^2 p_z(x, t)}{\partial t^2}. \quad (4.82)$$

A multiplication of both sides with $u_{z,j}(x)$ and the integration over the cavity volume, using the orthogonality relation (4.79) produces

$$\omega_j^2 \hat{E}_j(t) + \frac{\partial^2 \hat{E}_j(t)}{\partial t^2} = -(\epsilon_0 \epsilon_r)^{-1} V_j^{-1} \frac{\partial^2}{\partial t^2} \iiint_{\text{cav}} p_z(x, t) u_{z,j}(x) d^3 \mathbf{r}. \quad (4.83)$$

If the system behaves in a linear way and the active material is homogeneously distributed, the polarisation density $p_z(x, t)$ can be expanded into linear superpositions of the electric fields eigenmodes $u_{z,i}(x)$

$$p_z(x, t) = \sum_i \hat{p}_i(t) u_{z,i}(x). \quad (4.84)$$

It is claimed that only one longitudinal mode j is present in the cavity. The polarisation density p_z will then have the same spatial pattern as the electric field mode, namely $u_{z,j}(x)$.

So far, only a lossless cavity is described. Loss in the cavity and on the cavity surfaces will be taken care of by a phenomenologically introduced loss rate γ_{cav} .

$$\frac{\partial^2 \hat{E}_j(t)}{\partial t^2} + 2\gamma_{\text{cav}} \frac{\partial \hat{E}_j(t)}{\partial t} + \omega_j^2 \hat{E}_j(t) = -(\epsilon_0 \epsilon_r)^{-1} V_j^{-1} \iiint_{\text{act}} u_{z,j}^2 d^3 \mathbf{r} \frac{\partial^2 \hat{p}(t)}{\partial t^2}. \quad (4.85)$$

A so called filling factor η_{cav} (sometimes also called the confinement factor) should be introduced

$$\eta_{\text{cav}} := \left\{ \iiint_{\text{act}} u_{z,j}^2 d^3 \mathbf{r} \right\} \left\{ \iiint_{\text{cav}} u_{z,j}^2 d^3 \mathbf{r} \right\}^{-1}. \quad (4.86)$$

This factor is always smaller than 1. It is not only the fraction of the active to the cavity volume, but also a measure of the relative strength of the electric field at the position of the active laser medium. For example no coupling between the electromagnetic field

4. Nonlinear, Active Materials

and the active medium will occur, if the material is positioned at a node of the electric field.

Applying a SVEA and expressing the macroscopic polarisation density p_z by the polarisation P (eq. 4.43) gives us the relation between the slowly varying envelope of the electric field \tilde{E} of the laser mode j , and the slowly varying polarisation \tilde{P}

$$\frac{\partial \tilde{E}(t)}{\partial t} + [\gamma_{\text{cav}} + \imath(\omega_{\text{cav}} - \omega)] \tilde{E}(t) = \imath\omega \eta_{\text{cav}} \frac{n_a d_{\text{ab}}}{\epsilon_0 \epsilon_r} \tilde{P}(t). \quad (4.87)$$

The polarisation P is adiabatically eliminated by use of the Lorentzian line shape (eq. 4.59) and equation 4.57.

$$\frac{\partial \tilde{E}(t)}{\partial t} = -\gamma_{\text{cav}} \tilde{E}(t) + \eta_{\text{cav}} \frac{\omega_0^2 d_{\text{ab}}^2 n_a}{2\Omega \hbar \epsilon_0 \epsilon_r} [\gamma + \imath(\omega_0 - \omega)]^{-1} \tilde{N}(t) \tilde{E}(t) \quad (4.88)$$

For the oncoming relation to the semiconductor laser rate equations, we introduce a new inversion rate n .

$$n := 2\rho_{\text{bb}} = 1 - N \quad (4.89)$$

To make things shorter two new constants are introduced. The constant $\kappa\gamma$ should represent the strength of the active material, and the constant α is called the line width enhancement factor:

$$\begin{aligned} \kappa &:= \eta_{\text{cav}} \frac{\omega_0^2 d_{\text{ab}}^2 n_a}{2\Omega \hbar \epsilon_0 \epsilon_r} [\gamma^2 + (\omega_0 - \omega)^2]^{-1} \\ \alpha &:= \frac{1}{\gamma} (\omega_0 - \omega). \end{aligned} \quad (4.90)$$

All this leads to the first rate equation governing the evolution of the slowly varying electric field

$$\frac{\partial \tilde{E}(t)}{\partial t} = \{-\gamma_{\text{cav}} - \imath(\omega_{\text{cav}} - \omega - \kappa\gamma\alpha) + \kappa\gamma [(n(t) - 1) - \imath\alpha n(t)]\} \tilde{E}(t). \quad (4.91)$$

The imaginary part which is independent of the inversion can be removed by substitution of a new electric field $\tilde{e}(t) = \tilde{E}(t) \exp(\imath\beta t)$ where β should represent $\omega_{\text{cav}} - \omega - \kappa\gamma\alpha$.

The above equation also depends on the slowly varying inversion rate \tilde{n} . So far we have derived an equation which describes the fast oscillating occupation probability difference N (eq. 4.51). In the case of a one dimensional TE_z polarised wave, this equation reads

$$\frac{\partial N(x, t)}{\partial t} = -2\Lambda - \gamma_{\text{nr}} (N(x, t) - N_0) - 4 \frac{\Omega}{\hbar\omega_0^2} d_{\text{ab}} E_z(x, t) \frac{\partial P(x, t)}{\partial t}. \quad (4.92)$$

If only one mode i is to be excited in the resonator, we can substitute the mode expansion for the electric field and the polarisation

$$\frac{\partial N(x, t)}{\partial t} = -2\Lambda - \gamma_{\text{nr}} (N(x, t) - N_0) - 4 \frac{\Omega}{\hbar\omega_0^2} d_{\text{ab}} |u_{z,i}(x)|^2 \hat{E}_i(t) \frac{\partial \hat{P}(x)}{\partial t}. \quad (4.93)$$

Applying the SVEA to this equation leads to a slowly varying inversion $\tilde{N}(x, t)$ and reduces the term $\hat{E}_z(t) \partial_t \hat{P}(t)$ to $i\omega/4 [\tilde{E}(t) \tilde{P}^*(t) - \tilde{E}^*(t) \tilde{P}(t)]$. Again, the polarisation P is given by the functional relation to the electric field E , which is essentially the susceptibility function. With the use of the introduction of the inversion rate (eq. 4.89) and the above, we end up with the second laser rate equation

$$\frac{\partial \tilde{n}(x, t)}{\partial t} = 2\Lambda - \gamma_{\text{nr}} \tilde{n}(x, t) - \frac{|u_{z,i}(x)|^2 d_{\text{ab}}^2}{\hbar^2} \frac{\gamma}{\gamma^2 + (\omega_0 - \omega)^2} (\tilde{n}(t) - 1) |\tilde{E}(t)|^2. \quad (4.94)$$

Two abbreviating constants should be introduced. The inversion pump rate J and the coupling constant c

$$\begin{aligned} J &:= 2\Lambda \\ c &:= \frac{|u_{z,i}(x)|^2 d_{\text{ab}}^2}{\hbar^2} \frac{\gamma}{\gamma^2 + (\omega_0 - \omega)^2}. \end{aligned} \quad (4.95)$$

Substituting c and J for the constant expressions above leads to a simple form which is similar to the so called semiconductor laser rate equations

$$\begin{aligned} \frac{\partial e}{\partial t} &= -\gamma_{\text{cav}} e + \kappa\gamma [(n - 1) - i\alpha n] e \\ \frac{\partial n}{\partial t} &= J - \gamma_{\text{nr}} n - c(n - 1) |e|^2. \end{aligned} \quad (4.96)$$

We can furthermore decompose the electric field e into its amplitude $A(t)$ and its phase $\Phi(t)$ by using the Euler depiction $e(t) = A(t) \exp(i\Phi(t))$. This decomposition proves useful in the numerical investigation of such systems with real values.

$$\begin{aligned} \frac{\partial A}{\partial t} &= -\gamma_{\text{cav}} A + \kappa\gamma (n - 1) A \\ \frac{\partial \Phi}{\partial t} &= -\kappa\gamma\alpha n \\ \frac{\partial n}{\partial t} &= J - \gamma_{\text{nr}} n - c(n - 1) A^2 \end{aligned} \quad (4.97)$$

One of the fundamental characteristics of the equations describing the electric field e , A and Φ is that the rate of change is directly proportional to the electric field already present. If there is initially no electric field, no pumping current can ever produce one. This unphysical situation can only be resolved by including the process of spontaneous emission. The first term $-\gamma_{\text{cav}} e$ is a loss term also proportional to the electric field. The second term $\kappa\gamma(n - 1)e$ can be a gain term if $n > 1$ that means inversion is present. If $n < 1$ then the second term also reduces the electric field. If the gain term exceeds the first cavity induced loss term than the electric field will be increased.

The imaginary third term will only shift the phase and will not change the amplitude. Characteristics of the rate equation for the inversion n are that if $n > 1$ then the field will reduce the inversion. If $n < 1$ the field will increase the inversion. This term in the

4. Nonlinear, Active Materials

equation acts just the other way as the related term in the electric field rate equation does.

J is the pumping strength which increases the inversion and is counteracting the relaxation term $-\gamma_{\text{nr}}n$.

The steady state condition $\dot{A} = 0$ and $\dot{n} = 0$ leads to a stationary inversion and amplitude.

$$\begin{aligned} n_{\text{st}} &= 1 + \frac{\gamma_{\text{cav}}}{\kappa\gamma} \\ A_{\text{st}}^2 &= \frac{\kappa\gamma J}{c\gamma_{\text{cav}}} - \frac{\gamma_{\text{nr}}}{c\gamma_{\text{cav}}} (\kappa\gamma + \gamma_{\text{cav}}) \end{aligned} \quad (4.98)$$

The stationary inversion is independent of the pump power. No matter how strong the system is pumped, the stationary inversion always is pinned at the so called threshold inversion density $n_{\text{thr}} = n_{\text{st}}$. The threshold inversion is always larger than one, that is the transparency inversion.

The stationary field amplitude can be entirely imaginary if the pump power is below the threshold

$$J_{\text{thr}} = \frac{\gamma_{\text{nr}}}{\kappa\gamma} (\kappa\gamma + \gamma_{\text{cav}}). \quad (4.99)$$

A linear stability analysis of equations (4.97) reveals a specific frequency of the oscillatory behaviour. This frequency Ω_{relax} is called the relaxation oscillation frequency

$$\Omega_{\text{relax}} = \frac{\gamma_{\text{nr}}}{2} \sqrt{-\frac{\kappa^2 \gamma^2}{\gamma_{\text{cav}}^2} \left(\frac{J}{\gamma_{\text{nr}}} - 1\right)^2 + \frac{8 \kappa \gamma}{\gamma_{\text{nr}}} \left(\frac{J}{\gamma_{\text{nr}}} - \frac{\gamma_{\text{cav}}}{\kappa \gamma} - 1\right)}. \quad (4.100)$$

Associated with this frequency is also a relaxation decay constant

$$\Gamma_{\text{relax}} = \frac{\gamma_{\text{nr}} \kappa \gamma}{2 \gamma_{\text{cav}}} \left(\frac{J}{\gamma_{\text{nr}}} - 1\right). \quad (4.101)$$

When the lasing process kicks off, the relaxation peaks of the electric field amplitude are extremely pronounced and large compared to the later oscillatory behaviour. The time interval between two neighbouring peaks is bigger than the period of the relaxation oscillation given in equation (4.100).

4.5.2. Spiking and Relaxation Oscillations

All parts of a laser system are present in this section in form of a one dimensional model of a VCSEL. The simulation consists of the inverted, active material, the resonator cavity which is responsible for the optical feedback and the energy source in form of the non-linear pumping term. The VCSEL system has got Bragg mirrors consisting of twenty layers on each side with a λ wide defect in between. The dielectric constant of the defect cavity material is $\epsilon_r = 3.5^2$. The Bragg layers adjacent to the cavity are a combination

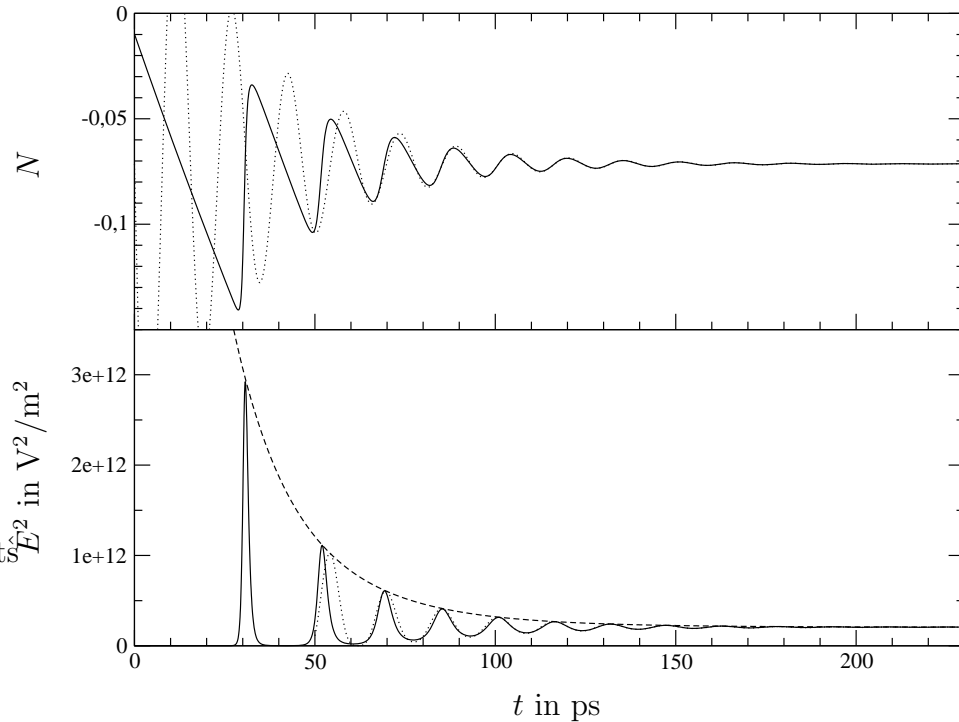


Figure 4.8.: Plots of $\hat{E}(t)$ and $N(t)$ showing a relaxation oscillation in a symmetric VCSEL structure. The parameters of the simulation are given in the text. In addition to the simulation result, the theoretical decay and oscillation frequency of the relaxation process are shown in the graph.

of two $\lambda/4$ pieces of dielectric constant $\epsilon_r = 3.2^2$ and $\epsilon_r = 3.5^2$, in that order. In the centre of the cavity is a thin active element, 5 nm wide, representing a two level system with parameters which are given in this paragraph. The thermal equilibrium occupation of the upper level is zero. The density of the dipoles is $n_a = 10^{26} \text{ m}^{-3}$ with a dipole strength of $d_{ab} = -4.806 \times 10^{-29} \text{ Asm}$. Light with a frequency of $\Omega = 3.1416 \times 10^{15} \text{ s}^{-1}$ should be in resonance with the dipoles. The polarisation decay is represented by $\gamma = 1.5708 \times 10^{13} \text{ s}^{-1}$. Inversion should relax to the thermal equilibrium occupation with the relaxation rate $\gamma_{nr} = 5 \times 10^9 \text{ s}^{-1}$ while being pumped with $\Lambda = 2\gamma_{nr}/2$. At the start of the simulation, the occupation probability of the two levels is equal. An initial optical pulse of low intensity is initially exciting the electromagnetic fields so that the electric field E is different from 0 and the coupling to the polarisation and inversion can begin. The filling factor of this cavity is $\eta \approx 0.0088$.

The occupation probability difference N and the field energy E^2 in the active region during the first 230 ps of the simulation are presented in figure 4.8. A typical relaxation oscillation behaviour of these entities to the steady state lasing operation can be seen. During one of the relaxation peaks, the occupation of the higher energy level is increased by the non-radiative pumping term until the inversion in the system is large enough to use the cavity feedback for stimulated emission. The electric field amplitude is rising exponentially as the population probability of the upper level is turned into field energy.

4. Nonlinear, Active Materials

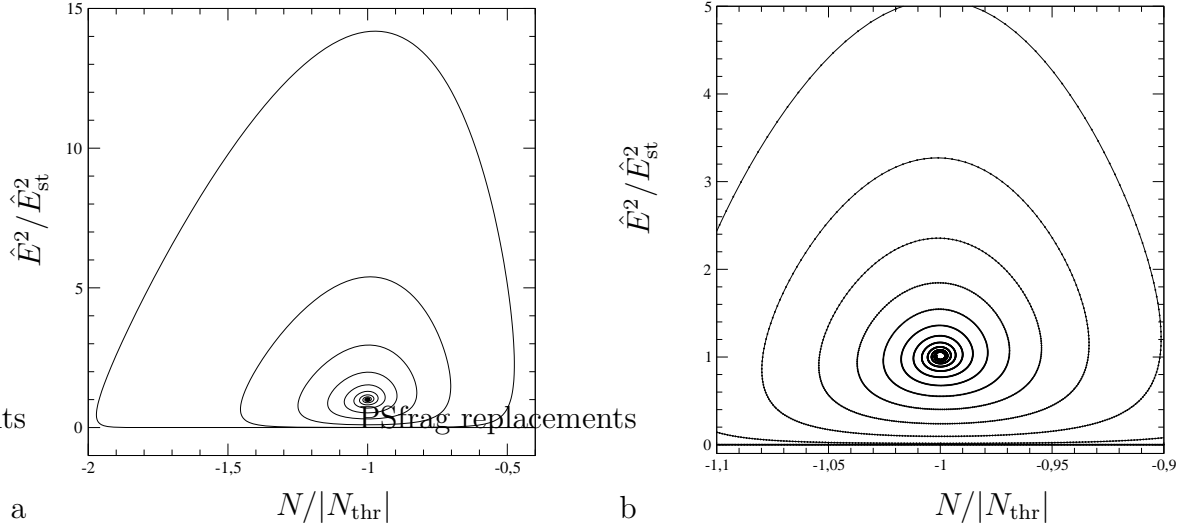


Figure 4.9.: Reduced phase space diagram of a relaxation oscillation in a VCSEL structure with an active 2 level material. The threshold inversion was $N_{thr} \approx -0.0714$ and the amplitude of the electric field $\hat{E}_{st} \approx 4.54 \times 10^5 \text{V/m}$. Part (b) shows a magnified section of part (a).

This process is continuing as long as the inversion is above threshold. As the inversion is consumed by the light field and forced below the threshold inversion, the lasing process can no longer be adhered. The field dies away and the occupation difference N reaches its maximum. The linear pumping characteristic takes over and the whole process is started again.

A fit of the threshold inversion to the simulation results in a cavity decay constant $\gamma_{cav} \approx 1.273 \times 10^{12} \text{s}^{-1}$. The relaxation oscillation frequency and decay constant which are calculated with equations (4.100) and (4.101) are used to plot the dotted and dashed curves in figure 4.8. They perfectly match the simulation result.

Figure 4.9 shows the relaxation oscillation of figure 4.8 in a reduced phase space plot of the energy over the occupation probability difference. The trajectory is spiralling towards the point given by the steady state values of the electric field E_{st} and the occupation difference N_{thr} . This laser system can be uniquely described by two free physical variables as there is no crossing of the trajectory.

5. Plane DFB Structures

Various resonator types like micro-cavities, micro-droplets, micro-rings and different planar waveguide structures have been used to build cavities for lasers with organic active materials. At the turn of the century distributed feedback (DFB) structures have attracted much interest in organic laser systems [63, 5]. Lateral DFB geometries are particularly interesting since low-cost methods can be employed to create such resonators. They also present most promising approaches towards an organic large area lasing device of virtually any shape.

To optimise those resonators for application in organic laser diodes, the characterisation of one- and two- dimensional DFB systems through computational methods is highly desirable.

Through varying the geometrical properties of the corrugation, first or second order Bragg scattering can be achieved, resulting in edge or surface emitting lasers. Because of the type of feedback mechanism, very narrow oscillation line widths are possible. By changing the thickness of the active layer, the wavelength of the laser radiation can be tuned over the broad gain spectrum of organic laser active media.

In this chapter an introduction to slab waveguides will be given, followed by the extension to one dimensionally corrugated waveguides, which form simple DFB structures. Electromagnetic radiation in these cavities will then be investigated with the FDTD method for partially periodic systems. This method has been described in chapter 3. Exemplary dispersion diagrams and mode structures of DFB plastic laser cavities which were studied in related experiments are presented to give insight into fundamental aspects of the lasing operation. Furthermore the tunability of the lasing wavelength with the layer thickness is numerically evaluated and compared to experimental results. At the end of this chapter, an exemplary dispersion relation of a two dimensionally corrugated waveguide will be presented and discussed.

5.1. Guided Modes in Thin Dielectric Slabs

Before we extend the investigation to corrugated waveguides, a short wrap-up on the physics of guided modes in a thin sheet of dielectric material will be given. The coordinate system and geometrical setup for the discussion is shown in figure 5.1a. Layer 3 is sometimes called the substrate, layer 2 the film and layer 1 the cover. As our sole intention for now is the investigation of guided, non radiating modes in the film, the electromagnetic fields should be decaying in regions 1 and 3 in the x direction, away

5. Plane DFB Structures

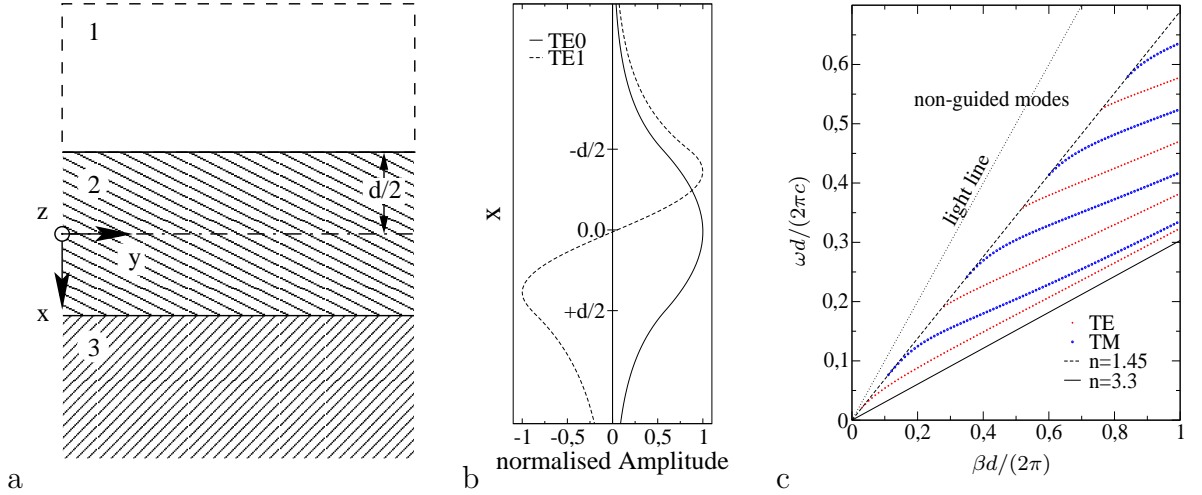


Figure 5.1.: (a) Geometrical setup of a waveguide in y -direction, with thickness d . (b) Mode profiles for the 1st and 2nd TE mode. (c) TE and TM mode dispersion diagram of a waveguide with refractive index 3.3 on a substrate with refractive index 1.45 in air.

from layer 2. We will see that the refractive index of layer 2 must be higher than the refractive index of both, the cover and the substrate.

Without free charges or currents, and without paramagnetic materials, the Maxwell equations can be reduced to the wave equation for each field component Ψ (for a Cartesian coordinate system)

$$\left\{ \underbrace{[\partial_x^2 + \partial_y^2 + \partial_z^2]}_{\Delta_{\text{Cartesian}}} + \frac{\omega^2}{c^2} \epsilon_r \right\} \Psi = 0. \quad (5.1)$$

The time dependence $\exp(-i\omega t)$ has already been separated.

In this simple example, the dielectric constant is a function of only the x -coordinate. The use of the separation ansatz $\Psi(x, y, z) = f(x)g(y)h(z)$ is therefore mandatory. A first result is the form of the solutions $g(y)$ and $h(z)$ which must be oscillatory as we want to observe guided waves.

$$\begin{aligned} g(y) &= \exp(\pm i\beta_y y) \\ h(z) &= \exp(\pm i\beta_z z) \end{aligned} \quad (5.2)$$

Without loss of generality, we can restrict the investigation to just one out of those four solutions with eigenvalue β , fixing the direction of the in-plane wave-vector along the positive y direction. This wave-vector β can be expressed by the free-space wave-vector $k_0 = \omega/c$ with the introduction of an effective refractive index n_{eff}

$$\beta = n_{\text{eff}} k_0. \quad (5.3)$$

Both, the electric as well as the magnetic field have to obey the wave equation (5.1). It can be shown that the electric and magnetic fields for homogeneous, isotropic dielectric constants have to be perpendicular to the wave-vector of a plane wave. With these restrictions, we can distinguish between transverse electric (TE) and transverse magnetic (TM) modes. The TE modes have only the z component which is non zero, the TM modes only have the z component of the magnetic field which is non zero.

With the assumption of a TE wave, the solutions of the wave equation for $E_z(x, y)$ have the form

$$E_z(x, y) = \hat{E} \exp(i\beta y) \begin{cases} \exp(\pm \gamma(x)x) & \forall \beta^2 \geq k_0^2 \epsilon_r(x) \\ \exp(\pm i\kappa(x)x) & \forall k_0^2 \epsilon_r > \beta^2(x) \end{cases} \quad (5.4)$$

The real coefficients γ and κ were introduced to shorten the equations. In the geometry shown in figure 5.1a they are

$$\begin{aligned} \kappa^2 &= k_0^2 \epsilon_2 - \beta^2 \\ \gamma_i^2 &= \beta^2 - k_0^2 \epsilon_i, \quad i \in \{1, 3\}. \end{aligned} \quad (5.5)$$

Normal components of \mathbf{D} and \mathbf{B} at the surfaces of layer 2, as well as the tangential components of \mathbf{E} and \mathbf{H} have to be continuous (see Jackson [25]). This implies that the wave-vector β as well as the frequency ω have got to be independent of time or position, for all three regions. As energy should be confined to the waveguide, another boundary condition is the decay of the fields along the x coordinate away from the origin. The solution $f(x)$ then separates into three partial solutions for each material region leading to

$$E_z(x) = \hat{f} \begin{cases} \kappa \frac{\exp(\gamma_1(x + \frac{d}{2}))}{\gamma_1 \sin(\frac{1}{2}\kappa d) + \kappa \cos(\frac{1}{2}\kappa d)} & \forall x \leq -\frac{d}{2} \\ \cos(\kappa x) + \frac{\gamma_1 \cos(\frac{1}{2}\kappa d) - \kappa \sin(\frac{1}{2}\kappa d)}{\gamma_1 \sin(\frac{1}{2}\kappa d) + \kappa \cos(\frac{1}{2}\kappa d)} \sin(\kappa x) & \forall |x| < \frac{d}{2} \\ \kappa \frac{\exp(\gamma_3(\frac{d}{2} - x))}{\gamma_3 \sin(\frac{1}{2}\kappa d) + \kappa \cos(\frac{1}{2}\kappa d)} & \forall x \geq \frac{d}{2}. \end{cases} \quad (5.6)$$

In addition we also have a hyperbolic conditional relation between κ , γ_1 and γ_2 .

The same derivation can be applied to TM modes (only H_z has a nonzero value), then leading to

$$H_z(x) = \hat{f} \begin{cases} \epsilon_1 \kappa \frac{\exp(\gamma_1(x + \frac{d}{2}))}{\epsilon_2 \gamma_1 \sin(\frac{1}{2}\kappa d) + \epsilon_1 \kappa \cos(\frac{1}{2}\kappa d)} & \forall x \leq -\frac{d}{2} \\ \cos(\kappa x) + \frac{\epsilon_2 \gamma_1 \cos(\frac{1}{2}\kappa d) - \epsilon_1 \kappa \sin(\frac{1}{2}\kappa d)}{\epsilon_2 \gamma_1 \sin(\frac{1}{2}\kappa d) + \epsilon_1 \kappa \cos(\frac{1}{2}\kappa d)} \sin(\kappa x) & \forall |x| < \frac{d}{2} \\ \epsilon_3 \kappa \frac{\exp(\gamma_3(\frac{d}{2} - x))}{\epsilon_2 \gamma_3 \sin(\frac{1}{2}\kappa d) + \epsilon_3 \kappa \cos(\frac{1}{2}\kappa d)} & \forall x \geq \frac{d}{2}. \end{cases} \quad (5.7)$$

The resulting conditions relating κ , γ_1 and γ_2 are shown in equation (5.8) for TE and TM modes. Each of the three quantities is again a function of β and ω . The shape of this hyper plane in two dimensions is given by the parameters $\epsilon_i, i \in \{1, 2, 3\}$ and d .

5. Plane DFB Structures

To solve the root finding problem, the bisection algorithm was found to achieve the highest stability in finding the most roots in contrast to Newton-Raphson for example. The Newton-Raphson root searching algorithm has problems with the poles of the tan function. It becomes unstable due to divergent or oscillatory behaviour.

$$\begin{aligned}\tan(\kappa d) &= \frac{\kappa(\gamma_1 + \gamma_3)}{\kappa^2 - \gamma_1\gamma_3} & \text{TE} \\ \tan(\kappa d) &= \frac{\kappa(\epsilon_2\epsilon_3\gamma_1 + \epsilon_1\epsilon_2\gamma_3)}{\epsilon_1\epsilon_3\kappa^2 - \epsilon_2^2\gamma_1\gamma_3} & \text{TM}\end{aligned}\tag{5.8}$$

If these equations have no real valued solution for a certain frequency, then no guided mode (either TE or TM, or both) can exist in the waveguide. In figure 5.1c the dispersion diagram for a waveguide with index $n_2 = 3.3$ on a substrate with index $n_3 = 1.45$ is shown. Transverse electric and transverse magnetic modes are occurring in alternating order for a fixed frequency or a fixed wave-vector β in the waveguide. Below the line $\omega(\beta) = \beta/n_2$, no solution would be physically relevant as the wave-vector in the guiding direction would be larger than the associated plane wave vector in the material. Above the line $\omega(\beta) = \beta/n_3$, solutions can exist but have complex eigenvalues representing leaking or radiating modes. These non-guided modes also exist outside the waveguide and will become important in the corrugated waveguide structures in DFB lasers. If n_1 is larger than n_3 , those two refractive indices are swapped due to the symmetric properties of the geometric setup. The light line represents the dispersion relation of free space ($n = 1$).

It is possible that more than one solution of equation (5.8) exists for a certain frequency. Electromagnetic radiation can then be guided in different ways inside the dielectric structure. Roots with increasing effective index belong to transverse mode structures with increasing number of node planes in the high dielectric constant region. The structure of the first two TE modes at $\beta = d/\pi$ in the exemplary dispersion diagram of figure 5.1c are shown in figure 5.1b.

A different approach to this problem is proposed in Ebeling [64] (in chapter 3.1.2). Basically it is a plane wave approach for the light rays travelling inside the dielectric slab and being reflected at the two surfaces. Guided solutions to this problem can only exist in case of constructive interference, if the phase after one cycle of reflection, propagation, reflection and back propagation is an integer multiple m of 2π . This characteristic equation for the wave vector k and the angle between the normal to the surfaces and this vector θ is

$$2\frac{\omega}{c}n_2\cos(\theta)d - 2\Phi_1 - 2\Phi_3 = 2\pi m, \quad m \in \mathcal{N}.\tag{5.9}$$

The phase shifts for total internal reflection are given by (see Ebeling [64])

$$\begin{aligned}\tan(\Phi_{\text{TE}}) &= \frac{\sqrt{n_2^2\sin^2(\theta) - n_i^2}}{n_2\cos(\theta)} \\ \tan(\Phi_{\text{TM}}) &= \frac{n_2^2}{n_i^2} \frac{\sqrt{n_2^2\sin^2(\theta) - n_i^2}}{n_2\cos(\theta)},\end{aligned}\tag{5.10}$$

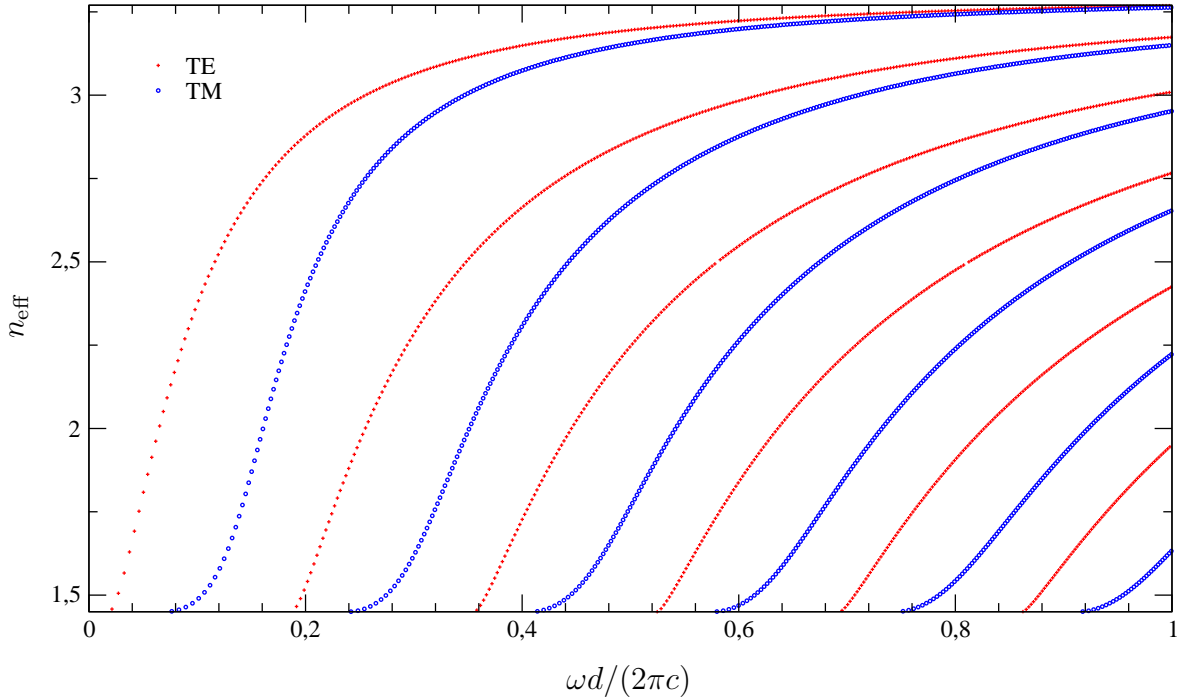


Figure 5.2.: Effective index over frequency for different orders of TE and TM modes in a waveguide with refractive index 3.3 on a substrate with refractive index 1.45 surrounded by air.

for waves travelling in the guiding medium 2 to the boundary with medium i . Equation (5.9) with the adequate phase shifts is equivalent to either one of equations (5.8) (depending on the polarisation).

With equation (5.3) we can also plot a diagram which relates the mode attributes (TM, TE, node numbers) and frequency to the effective index which would allow us to treat the guided mode like a plane wave in a material with this refractive index. Such a diagram is shown in figure 5.2 for the exemplary values used before. When the modes appear for small frequencies, the effective refractive index is the higher index surrounding the guiding layer. For increasing frequencies, the effective index approaches asymptotically the refractive index of the slab.

5.2. One Dimensional Patterned Organic DFB Lasers

The initial work by Stefan Riechel [65] on thin plate plastic lasers used an organic semiconductor film on prestructured plastic substrates. Of particular interest for organic solid-state lasers are substrates which still offer the advantages of organic materials like mechanical flexibility, softness or large area, cheap fabrication techniques.

A material which represents these vantages is poly(ethylen terephtalate) (PET) which was used in the above work. PET has a refractive index of $n \in \{1.45..1.64\}$ in the inves-

5. Plane DFB Structures

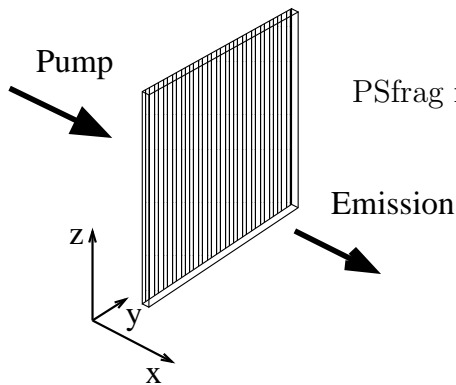


Figure 5.3.: The geometry used in the experiments on lasing in thin film DFB structures on plastic substrates. Emission can occur in different directions, along the x direction as well inside the y - z plane.

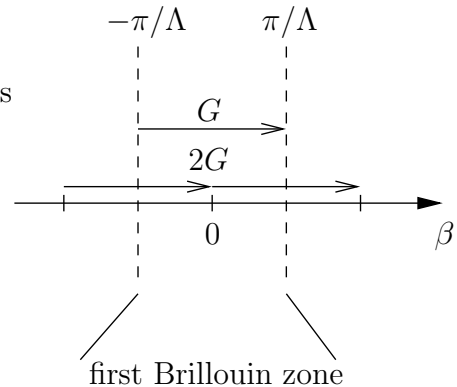


Figure 5.4.: Reciprocal space for a one dimensional periodic DFB system showing the first Brillouin zone.

tigated wavelength range. Surface patterning was achieved by embossing the sinusoidal corrugation with a Nickel shim onto the PET foil. Due to the holographic technique used to create the Nickel shim, the periodicity and the period length Λ have a very small uncertainty. Large areas of up to 400 cm^2 were uniformly patterned with this technique. The assumption of infinite extension of the substrate plane is therefore adequate.

First experiments used one dimensionally corrugated substrates which were pumped from behind as shown in figure 5.3. The introduction of two dimensional corrugation significantly improved the emission characteristics of the organic semiconductor material. Two different techniques were employed to deposit the organic, laser active material on top of the corrugated surface. Each technique lead to a typical air to film surface. The evaporation onto the substrate resulted in an imitation of the substrate surface by the film to air boundary. Both surfaces show the same corrugation. Spin casting the organic onto the substrate resulted in flat substrate to air surface (see fig. 5.5a).

In the course of the dissertation of Stefan Riechel, two so called disordered organic semiconductors were used in the experiments. Samples using the guest-host system $\text{Alq}_3\text{:DCM}$ which is a combination of the chelate metal complex tris-(8-hydroxyquinoline)-aluminium doped with the laser dye 4-dicyanmethylen-2-methyl-6-(p-dimethylaminostyryl)-4H-pyran showed corrugations on both surfaces. Stefan Riechel reports a refractive index between 1.70 and 1.74 in the spectral range of DCM emission ($\lambda = \{550..730\} \text{ nm}$) for the $\text{Alq}_3\text{:DCM}$ film. This guest-host system was co-evaporated onto the PET substrate and therefore shows a corrugation at the air surface. The methyl substituted ladder-type poly(*para*-phenylene) (MeLPPP) conjugated polymer based samples were created by spin casting the MeLPPP material onto the substrate.

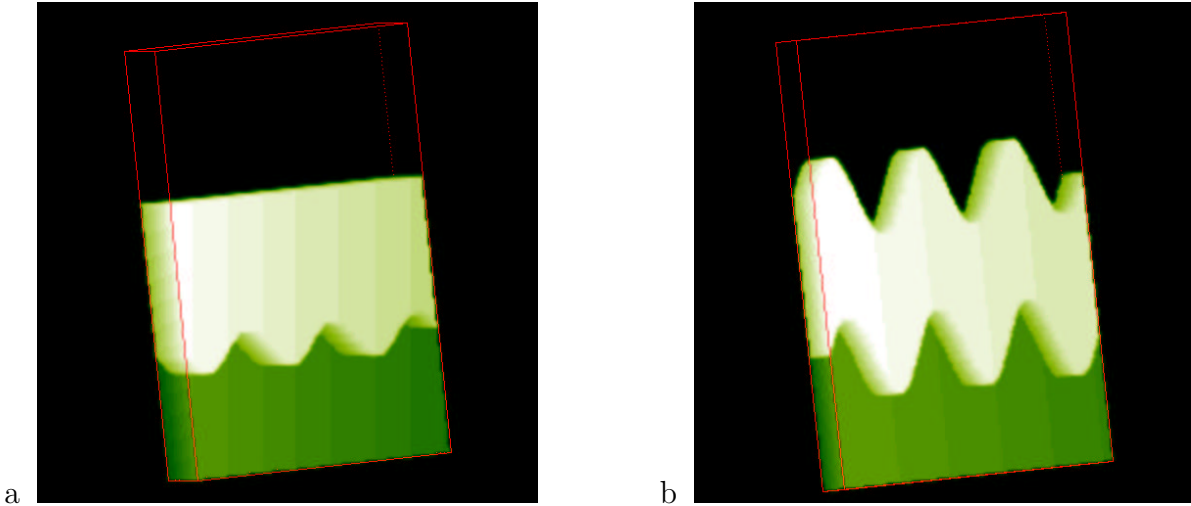


Figure 5.5.: The geometrical setup of the one dimensionally corrugated MeLPPP (a) and the Alq₃:DCM (b) samples. In the simulations, MeLPPP was assumed to have a refractive index of $n_2 = 1.70$ and the substrate was modelled with $n_3 = 1.45$. Alq₃:DCM has a refractive index of $n_2 = 1.75$ and the substrate index is assumed to be $n_3 = 1.505$. The corrugation length for the MeLPPP system was set to $\Lambda_a = 300$ nm and $\Lambda_b = 400$ nm for the Alq₃:DCM material system. The film thickness in (a) is 300 nm with a corrugation amplitude of 45 nm and in (b) the film is 275 nm thick and the corrugation amplitude is 90 nm.

The samples showed a nearly flat film to air surface.

The refractive index of the MeLPPP varies between 1.45 to 1.95 (Sturm *et al.* [66]) in the wavelength region of $\lambda = \{350..550\}$ nm. A measurement of the refractive index at a wavelength of 490 nm (the wavelength of lasing in the 2nd order DFB laser) gives $n \approx 1.70$.

Figures 5.5a and b show the geometrical setup for the MeLPPP and Alq₃:DCM samples respectively. Figure 5.6 shows the emission spectra of the two sample types ([65]).

5.2.1. The Distributed Feedback Mechanism

In 1971 Kogelnik and Shank [67] introduced the idea of feedback due to a periodic structure in the gain region of a laser. Optical feedback in DFB lasers is not achieved by reflection at local reflectors but by Bragg scattering due to periodically distributed optical inhomogeneities. Theoretical investigations on DFB resonators (summarised by Kneubühl and Gnepf for example [68]) are based on three different approaches.

A theory of coupled modes (see [69]) travelling back and forth can only cope with weak modulation of either the refractive index or the gain.

Transfer matrix methods require piecewise constant dielectric constants or gain regions to be accurate.

The third method which is described by Gnepf and Kneubühl is the application of

5. Plane DFB Structures

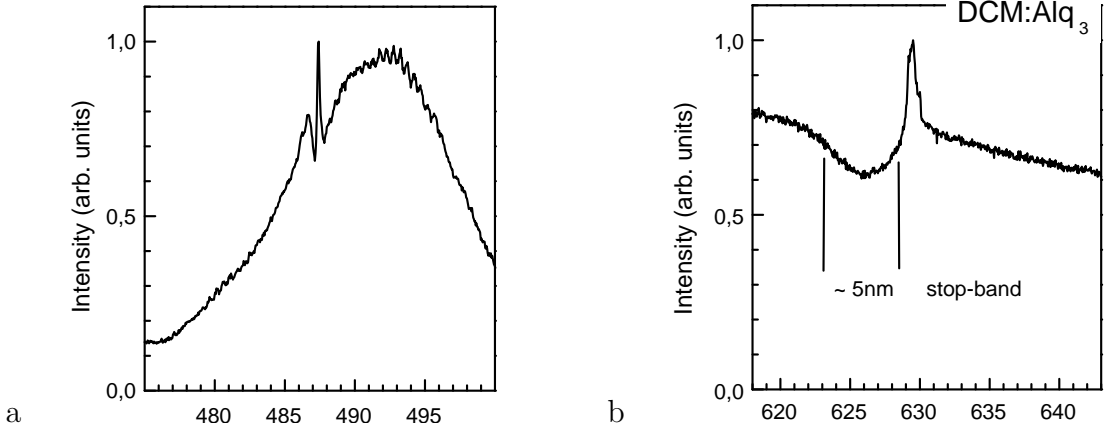


Figure 5.6.: Luminescence spectra of the two different kinds of samples. Part (a) shows the spectrum for the MeLPPP system and (b) the associated spectrum of $\text{Alq}_3\text{:DCM}$ (S. Riechel [65]).

Floquet solutions to Hill differential equations.

In general, the periodic structure can be a variation of either the refractive index ($n_{\text{eff}}(y) = n_{\text{eff}}(y + \Lambda)$) or the gain or loss ($g(y) = g(y + \Lambda)$) in the cavity. This periodic modulation introduces scattering to the guided waves in a slab waveguide with corrugated surfaces. Back scattered waves can couple to guided modes which travel in opposing directions. Constructive interference between guided modes and back scattered guided modes is achieved if the Bragg condition (eq. 5.11) for the wave vector β is satisfied (see [64] chapter 3.3.2).

$$2\beta\Lambda = 2\pi m, \quad m \in \mathcal{N} \quad (5.11)$$

If the order m of the Bragg condition is higher than one, light will be scattered out of the waveguide as a rule. For $m = 2$ light will be emitted perpendicular to the surface of the waveguide.

With this Bragg condition we can fix the propagation constant β inside the guiding layer for a certain m . In a dispersion diagram for periodic structures this will either be the point $\beta = 0$ or the edge of the first Brillouin zone $\beta = \pi/\Lambda$. The first constructive interference will occur for $m = 1$ at $\beta = \pi/\Lambda$. The second constructive interference is at the opposite side of the Brillouin zone, at $\beta = 0$ for $m = 2$. This alternating change of Brillouin zone boundaries for increasing frequencies is shown in figure 5.7. Equation (5.8) will give us a rough indication of the frequencies for a certain thickness at which a mode will be constructively enhanced by the DFB grating.

In reciprocal space (k-space, see fig. 5.4) which can be described in one dimension for a one dimensional corrugation, the periodic modulation of the waveguide is represented by a lattice of points separated by the lattice vector $\mathbf{G} = 2\pi/\Lambda\mathbf{e}_y$. Following the previous theoretical investigation this periodicity should be introduced along the y direction (see fig. 5.1a). The direction perpendicular to the corrugation and the normal vector to the waveguide plane (z in figure 5.3) can be included in figure 5.4 having a translational

symmetry.

The Bragg condition 5.11 then becomes the Laue condition in analogy to scattering of X-rays in crystal lattices.

$$2\mathbf{k} \cdot \mathbf{G} = |\mathbf{G}|^2 \quad (5.12)$$

A generalised wave vector is $\mathbf{k} = \beta \mathbf{e}_y + k_z \mathbf{e}_z$, including β from the one dimensional investigation plus an additional part k_z perpendicular to the direction of β and in the plane of the film. The part k_z is along a translational symmetric direction and does therefore not require any Bragg condition for constructive interference of back scattered waves.

Until further precautions are taken, the 1D DFB laser will operate on many lateral modes. If the modes propagate exactly parallel to the one dimensional grating, then no coupling between TE and TM modes can occur. However, if the wave vector \mathbf{k} is oblique incident on the one dimensional grating, it is possible that TE and TM modes couple to each other. The vectorial nature of the Maxwell equations introduces subtle but very important effects due to the depolarisation of the x component of the electric or magnetic field (see [70]).

The coupled wave theory (see [69]) shows that only Bragg scattering at the edges of the Brillouin zone is to be taken into account. According to Bloch's theorem, every state of the infinitely extended reciprocal space can be represented by a vector within the first Brillouin zone by translation with a reciprocal lattice vector. States originally located outside the first Brillouin zone are then attributed to a higher band of the corresponding state inside the first Brillouin zone (reduced zone scheme, see fig. 5.7). We therefore only have to investigate the edges of the first Brillouin zone at $\beta = 0$ and $\beta = \pi/\Lambda$.

By means of symmetry, the first Brillouin zone can be further diminished to the irreducible Brillouin zone. This reduction of the DFB waveguide dispersion diagram to the first Brillouin zone is shown in figure 5.7.

In the vicinity of β_{Bragg} (the solutions of the Bragg condition (5.11) for different orders m) the solution of the Helmholtz equation (5.1) is approximated by a superposition of a right and left running plane wave (see [69]). For Bragg orders of one, the coupled wave theory leads to the dispersion relation

$$\begin{aligned} \beta^2 &= \left[\frac{n_{\text{eff}}}{c} (\omega - \omega_{\text{Bragg}}) + i\gamma \right]^2 - \kappa^2 \\ \kappa &= \frac{|\mathbf{G}_0|}{4n_{\text{eff}}} \Delta n + \frac{1}{2} i\Delta\gamma, \end{aligned} \quad (5.13)$$

with the Bragg frequency ω_{Bragg} , the field gain coefficient γ and the amplitudes of the weak sinusoidal gain and/or index modulations Δn and $\Delta\gamma$ ([65]).

This relation accounts for two types of DFB coupling. Namely index and gain coupling.

For $m = 1$, the FDTD simulation in this chapter can only cope with index coupling ($\Delta n \neq 0$, $\Delta\gamma = 0$). In this case the propagation constant β is purely real. The dispersion relation (eq. 5.13) at the edge of the first Brillouin zone leads to an anti-crossing around the Bragg frequency. This stop band should have the width $\Delta\omega_{\text{sb}} = 2\kappa c$. As the splitting

5. Plane DFB Structures

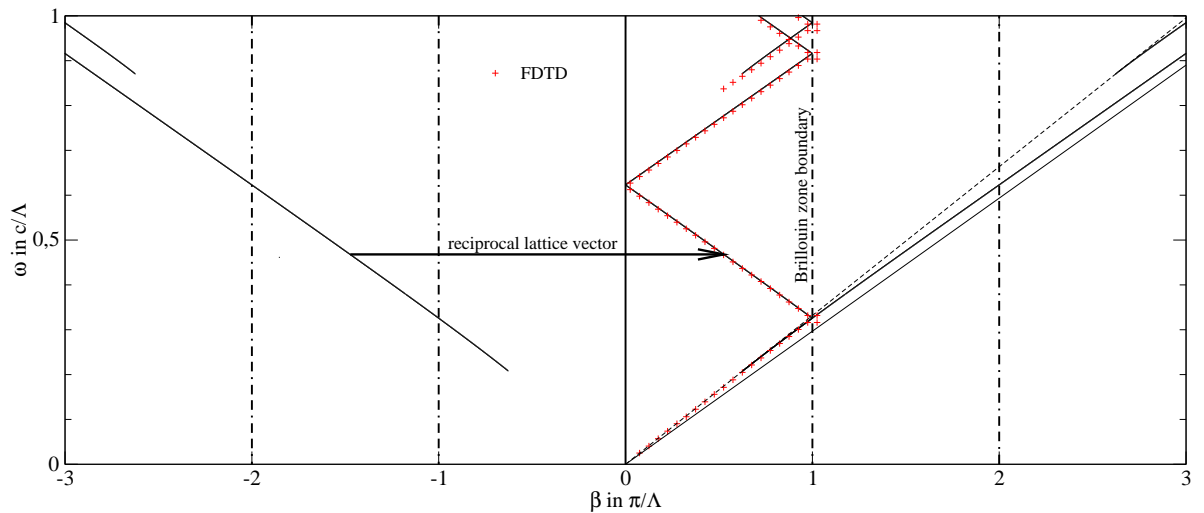


Figure 5.7.: The folding of the dispersion diagram of a slab waveguide with $n_2 = 1.685$, $n_3 = 1.507$ and $d = 300$ nm on air. FDTD simulation results are shown in the first Brillouin zone with the folded dispersion relation.

of the first band and the second band introduces an increase of the mode density at the edges of the stop band, lasing should occur on both sides.

For $m = 2$ and above, loss occur due to the scattering of light out of the waveguide. DFB lasers using these higher orders of Bragg scattering for the feedback mechanism always show a mixture of index and gain coupling.

A detailed transmission measurement of the band structure of wavelength scale periodic textured waveguides was done in 2000 and 2001 by Salt, Barnes and others ([71], [72] and [73]).

5.2.2. FDTD Simulations

The periodicity of DFB resonators implies the use of methods applied to photonic crystals. In this area the band structures are either calculated by using Ho's method (based on the FDTD method described in chapter 3), or a plane wave method in frequency domain and the reciprocal space. This three dimensional system is not periodic in the open direction normal to the films surfaces. The corrugation of either one or two of the waveguide surfaces that is essential for the feedback mechanism results in emission of light. This prevents the (artificial) treatment of a full periodic system by simply applying a periodic condition in the normal direction of the waveguide. Whereas the translational invariant direction can be simulated by introducing an artificial periodicity. A full description in the reciprocal space is not possible and the plane wave method can therefore not be used.

Due to the open direction, Ho's method does not directly apply, but can be extended to open boundary conditions. The method described here is based on the FDTD al-

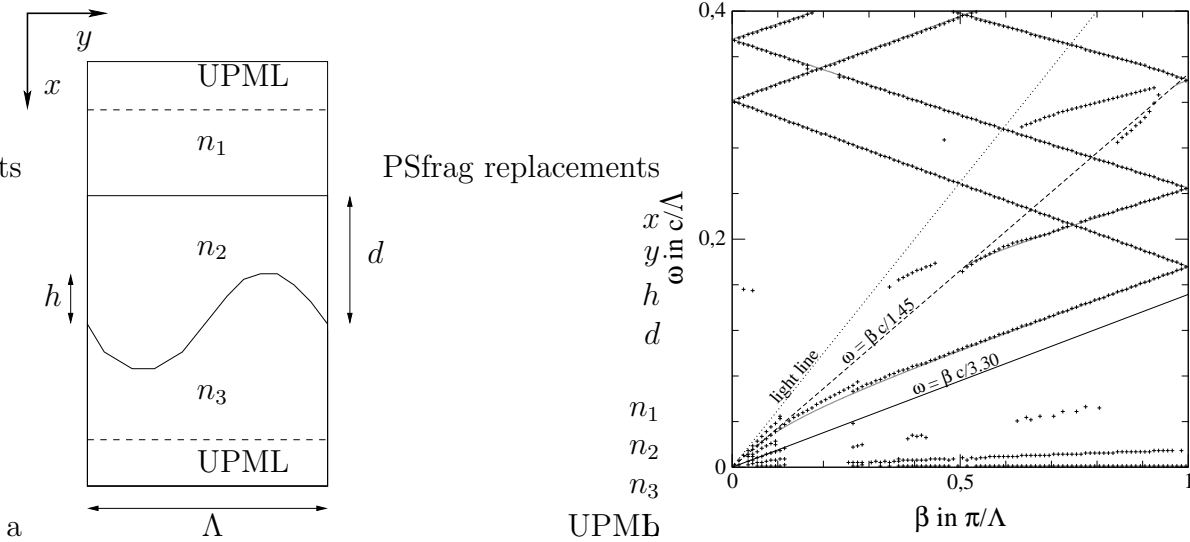


Figure 5.8.: Geometrical setup of the simulation (a) and the resulting mode diagram of the folded dispersion relation (b) of a slab waveguide of thickness $d = 320$ nm with $n_2 = 3.30$ and $n_3 = 1.45$ in air. The 'assumed' periodicity for further calculations with corrugation was $\Lambda = 300$ nm which was resolved with a grid cell size of $(10 \text{ nm})^3$. Grey FDTD calculation results (+) show all found peaks in the spectra, and the black results represent the processed values.

gorithm as described in chapter 3. In summary we need complex field values for the Bloch boundaries, a straight-forward extension of the UPMLs to complex fields and an extension to Ho's initial condition to excite the modes we want to investigate. A transfer of Ho's initial condition to mixed boundary conditions can be achieved by assuming a Gaussian profile in the open direction. The maximum of the Gaussian profile is set in the high index region. Modes which are weakly confined to the waveguide are absorbed very fast by the UPML and only guided modes stay in the simulation region.

The Bloch boundary condition requires a certain wave vector. In order to calculate a band structure, one simulation for each point in k -space has to be made. Luckily Blochs theorem lets us restrict the calculations to the first Brillouin zone (see fig. 5.8b). The FFT spectrum of the time series for a certain k value results in a slice of the band structure.

The simple algorithm, detecting peaks as local maxima in the spectrum, is not capable of distinguishing between maxima in the spectrum associated with guided modes, non-guided modes or numerical artifacts related to the FFT like Gibbs oscillations or remains of the initial field setup. Additional peaks are appearing in the diagram. A Fourier transform of a simulated time-series of field values will also reveal the strongly confined modes as peaks with small FWHM in the spectrum. Fitting Lorentzian curves to the found maxima leads to a comparable FWHM value for each peak. The maximum is to be shown in the dispersion diagram, if the FWHM for a certain peak is below a threshold value. Peaks which are appearing below the line $\omega = c/n_{\max} \beta$, with n_{\max}

5. Plane DFB Structures

being the highest refractive index which is present in the simulation domain, are ruled to be artifacts.

If the time series for the Fourier transformation is not taken from the start of the simulation but with a certain offset, then non-guided modes will already have been attenuated by the PMLs. Their peaks in the spectrum are getting smaller, with increasing time offsets and can therefore be distinguished from guided modes.

An FDTD simulation result for initial TE mode excitation in a slab waveguide is shown in figure 5.8b. The resulting dispersion diagram is compared to theoretical results calculated with equation (5.8). All peaks which are found in the spectra of the time-series from time step 20000 to 100000 are compared to the processed number of peaks which have only FWHMs of less than 10^{13} s^{-1} . To avoid calculation of the FFT spectra at a node position, 8 time-series which were recorded at randomly distributed positions were combined. Only TE modes were excited and the E_z component was used for the FFT. A Part of the Gibbs oscillation artifacts is vanishing as well as several peaks which can be related to radiating modes. Still a large number of peaks below the dispersion line in a medium of the highest refractive index remain and a few of the peaks representing guided modes disappeared too. Especially interesting is the presence of peaks related to bands of higher order guided TE modes, which are appearing in the FDTD calculation before the solution of equation (5.8) becomes real.

5.2.3. Band Structure

The basic principles of the band structures of corrugated systems can be understood simply by folding the plane waveguide dispersion relation into the irreducible Brillouin zone as shown in figure 5.7. The FDTD calculation of the uncorrugated waveguide which is also shown in figure 5.8b is simply matching the theoretical prediction of equation (5.8). When corrugation is introduced, the regions where bands are overlapping are possible candidates for anti-crossing behaviour of the then coupled modes. To make the effects of corrugation more visible, the shown dispersion diagrams were calculated with a film refractive index of 3.3 instead of the 1.7 which is the assumed index of the organic dye in the experiments. The effects which are shown are nevertheless qualitatively the same.

Starting with the initial band structure of an unpatterned waveguide (fig. 5.8), a corrugation with a small amplitude $h = 50 \text{ nm}$ is introduced on both surfaces of the waveguide, as in the $\text{Alq}_3\text{:DCM}$ system geometry, then being increased to $h = 100 \text{ nm}$. The resulting band diagrams (a) and (b) are shown in figure 5.9. 100000 time steps are used in an FFT leading to spectra which are then searched for every local maximum. These maxima are plotted in the diagrams. The first intriguing fact is that there is nearly no deviation of the dispersion relation for the first band between $\beta = 0$ to $\beta = \pi/\Lambda$ to the plane waveguide dispersion behaviour. Only a slight shift to higher frequencies can be read from the calculations. This slight shift could be compensated in the plane waveguide calculation (eq. 5.8) by a slightly decreasing film thickness.

The second notable feature is a drastic anti-crossing of the second band TE_0 and the first band of the TE_1 mode. This gap is increasing with larger corrugation amplitude. Further features of interest are the band gaps at $\beta = 0$, which are increasing with the

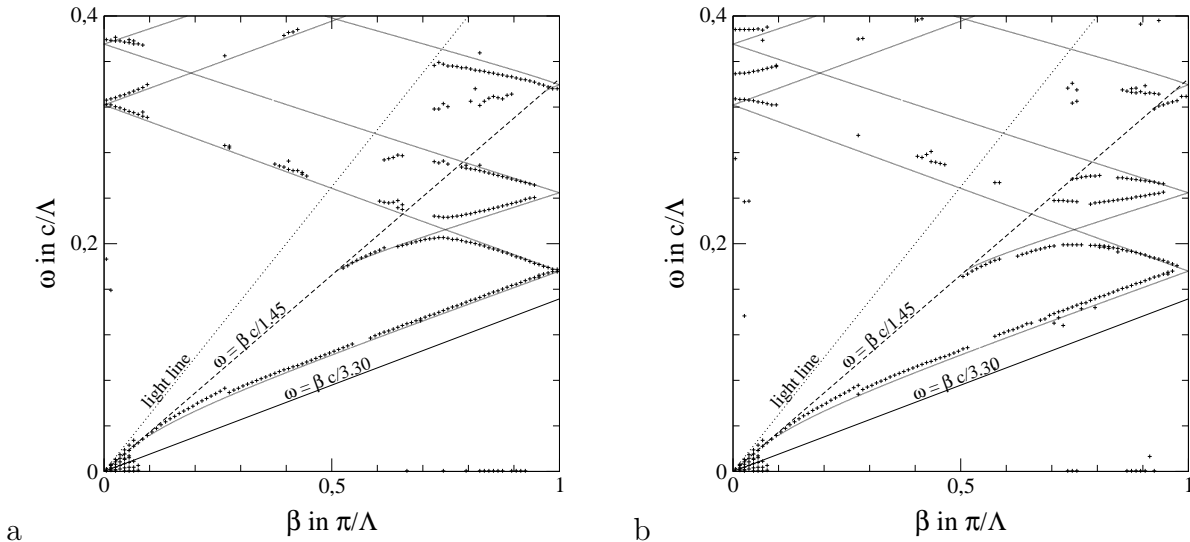


Figure 5.9.: The dispersion relation of the high index contrast 1D-DFB Alq₃:DCM structure. The corrugation amplitude h is 50 nm in (a) and $h = 100$ nm in (b) on both surfaces of the high index film. All the other parameters are as in fig. 5.8.

increasing corrugation amplitude, and the very small, nearly non visible band gaps at $\beta = \pi/\Lambda$. Peaks along the second bands in the centre of the Brillouin zone, which were found in the plane waveguide calculation (shown in figure 5.8b) can no longer be detected. It can be assumed that these modes are highly lossy and quickly scattered into the PMLs where they are absorbed.

The conclusion from these simulations for the DFB structure of the Alq₃:DCM system is that the best suitable point for DFB operation in these band diagrams is at $\beta = 0$ around the band gap between the second and third bands of the TE₀ modes. Accompanied with the band gap is a vanishing group velocity $d\omega/dk$ around the band edges [74]. The local density of states at these band edges increases and also the spontaneous emission rate (Fermis golden rule). This also enhances the gain [75]. Unlike in defect-mode photonic band-gap lasers, which rely on a complete, well pronounced, large photonic band-gap, the DFB mechanism uses the gain enhancement at the band edges. Large photonic band-gaps require large refractive index contrasts and therefore high index materials. This is not possible with organics, as their refractive index is too low.

The spin coated MeLPPP DFB system has a waveguide geometry with only one corrugated surface. The same type of calculations with the Alq₃:DCM type geometry are made with the MeLPPP system geometry to compare them. A corrugation amplitude of $h = 50$ nm and $h = 100$ nm was used to calculate the band structures shown in figure 5.10. Again, especially the lower bands stick to the uncorrugated waveguide dispersion relation with some avoided crossings between TE modes of different orders. Only a small shift to higher frequencies is present.

5. Plane DFB Structures

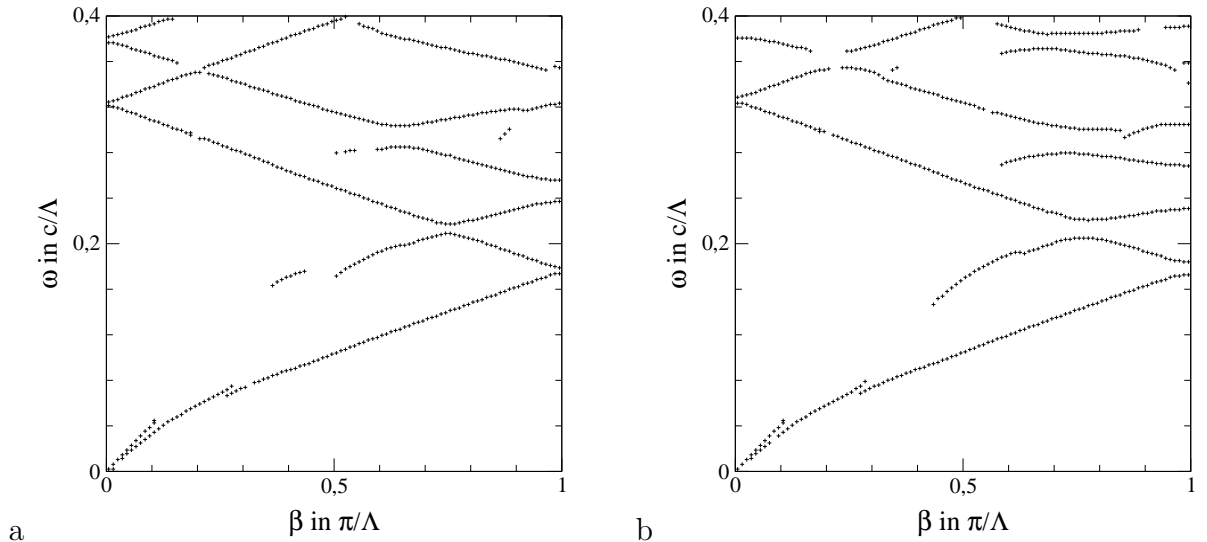


Figure 5.10.: The dispersion relation of the high index contrast 1D-DFB structure. The corrugation amplitude h is 50 nm in (a) and $h = 100$ nm in (b). Only 50000 time-steps were used in the FFT. All other parameters are as in fig. 5.8.

It can be seen easily, that there is a band gap at $\beta = \pi/\Lambda$ between the first and the second band of TE_0 mode. The avoided crossing effect is smaller than in the Alq_3 :DCM geometry whereas the band gaps are larger for the MeLPPP geometry.

The following calculations of dielectric structures with realistic refractive indices of the organic materials are using parameters which are mentioned in the associated work [65]. But as it will turn out, a fit of the simulations to the measurements of the laser emission frequencies requires slightly different dielectric indices. The MeLPPP system has a reported refractive index of $n_2 = 1.70$ on a substrate with $n_3 = 1.45$ in air, whilst the Alq_3 :DCM system has a recommended refractive index of $n_2 = 1.685$ and a substrate with $n_3 = 1.507$.

5.2.4. Mode Structure

The FDTD method not only calculates the band structure, but also the precise spatial mode structure of the modes occurring in the dielectric setup. The accuracy of the mode structures is mainly limited by the spatial resolution of the computational grid. After determining the frequencies of the modes at a special wave-vector β , a spatial resolved discrete Fourier transformation will lead to the distribution of the mode in the space region of the simulation. This is shown exemplarily for two distinct positions in the band diagrams of the above investigated systems. These Fourier transforms use 40000 time steps starting with the beginning of the simulation.

Figures 5.11a and b show the structure of the TE modes at the top of the first and the bottom of the second band in the MeLPPP system at $\beta = \pi/\Lambda$. Only one anti-node is either near the thicker or thinner part of the guiding layer. The mode with the lower frequency (top of the first band, fig. 5.11a) has its maximum shifted to the thicker part

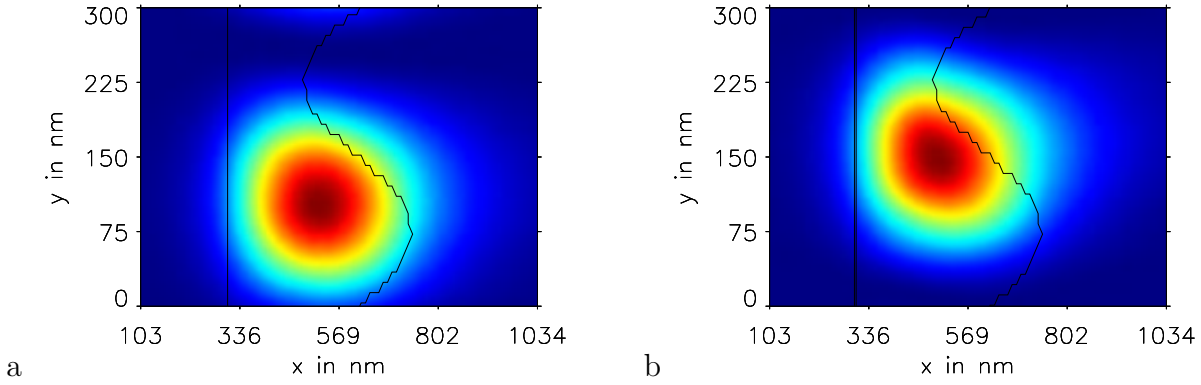


Figure 5.11.: The mode structure at the top of the first band and the bottom of the second band at $\beta = \pi/\Lambda$ in the MeLPPP system with a guiding layer thickness of 250 nm, a periodicity of 300 nm and a corrugation amplitude of 130 nm. The colour represents the amplitude of the field energy ranging from dark blue to dark red.

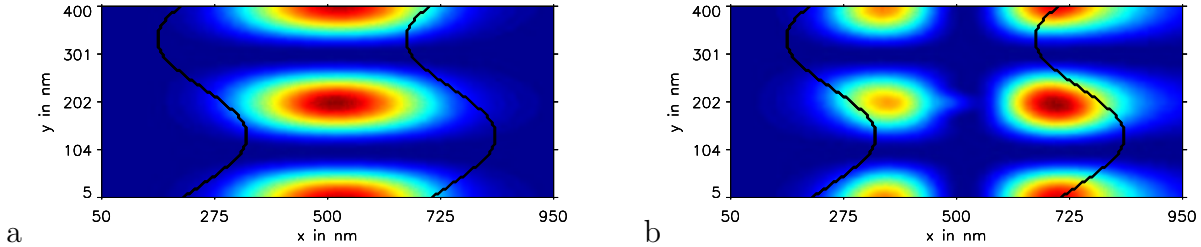


Figure 5.12.: The mode structure at the top of the second band at $\beta = 0/\Lambda$ in the Alq₃:DCM system with a guiding layer thickness of 500 nm, a periodicity $\Lambda = 400$ nm and a corrugation amplitude of 90 nm. The colour represents the amplitude of the z component of the electric field ranging from dark blue to dark red.

of the layer, whilst the mode with the higher frequency (bottom of the second band, fig. 5.11b) has its maximum shifted to the thinner part.

As the material with the higher index of refraction represents the active laser material, the modes in the lower band near the Brillouin zone boundary have a stronger spatial overlap with the gain medium. In agreement with experiment (see fig. 5.6), lasing occurs on the higher wavelength side of the band gap, corresponding to lower frequency and therefore the lower band, in index coupled DFB resonators.

Figure 5.12a and b show the mode structures of the second band TE₀ and TE₁ modes near $\beta = 0/\Lambda$ for a thickness of $d = 500$ nm of the Alq₃:DCM system. Without a periodic symmetry, this point in k-space would represent $\beta = 2\pi/\Lambda$ and therefore the “wavelength” of the structure is equal to Λ as can be clearly seen in the figure showing two anti-nodes in the y direction. Part a of this figure shows no node in the x direction representing the TE₀ mode, whilst part b of the figure shows one node in the middle of

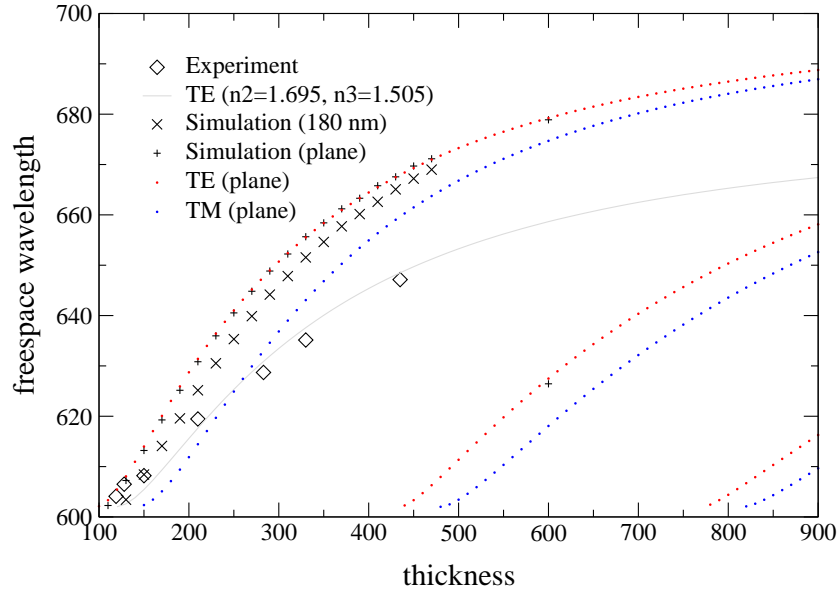


Figure 5.13.: The theoretical predicted behaviour for TE and TM waves (according to eq. (5.8)) is compared to FDTD simulation results (+) ($n_1 = 1.0$, $n_2 = 1.75$ and $n_3 = 1.505$). The periodicity of the system was $\Lambda = 400\text{nm}$. Plane waveguide properties are shown by the red and blue dots for the TE and TM modes. FDTD results (x) for a corrugation amplitude of 90 nm show only a slight shift to higher frequencies. Experimental data (diamonds), taken from [65] with a fit to a plane slab waveguide.

the layer and therefore represents the TE_1 mode.

The TE_1 field anti- node positions are near the surfaces of the laser active film in contrast to the TE_0 anti- node position, which is in the middle of the film. The overlap with the gain material is therefore higher for the TE_0 mode. Lasing should be easier to achieve for the zeroth order of the TE modes.

5.2.5. Tunability

Three parameters can be chosen when designing the plastic laser DFB cavities for a certain organic dye. Corrugation period and film thickness are both determining the frequency of lasing operation which has to match the gain spectrum of the dye. They are also both relevant parameters which determine the band structure of the photonic system. The corrugation amplitude only introduces small changes in the overall band structure as the previous FDTD simulations have shown. They are responsible for the size of the band gaps. The MeLPPP geometry with only one corrugated film surface is a better candidate for larger band-gaps.

To show the accuracy of the FDTD method, we compare the simulation results to the numerically evaluated equation 5.8. The simulation uses a TE field setup and

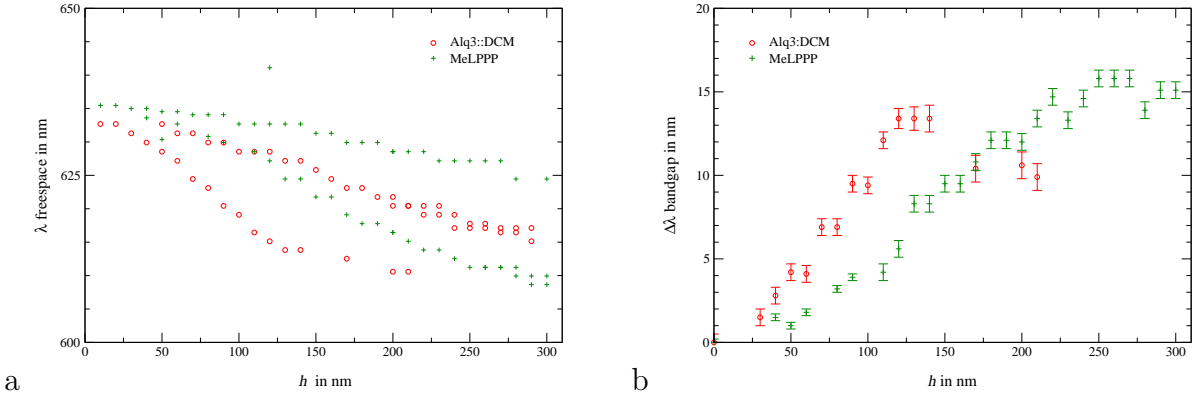


Figure 5.14.: The position of the second band-gap with increasing corrugation amplitude h in the MeLPPP and the Alq₃:DCM system with thickness $d = 330$ nm and corrugation period $\Lambda = 400$ nm. Part (a) shows the position of the second and third band with increasing amplitude. Part (b) shows the band gap width $\Delta\lambda$ over amplitude.

therefore only reproduces the TE mode behaviour. Figure 5.13 shows the excellent match between the theory and the FDTD simulation. The number of time-steps which are used in the Fourier transform were chosen between 20000 to 200000. The uncertainty of the frequency is only given by the resolution of the Fourier transformation, which is proportional to the inverse of the number of time steps. For 0 nm corrugation amplitude the FDTD calculation matches exactly the values computed from equation (5.8).

The film thickness and the corrugation amplitude were varied in the experiments to show the possibility of generating lasers with different emission wavelengths and the optimal working parameters. Figure 5.13 shows the calculated behaviour of the lasing wavelength for TE and TM mode, second order DFB operation with varying film thickness. No mode which is to be supported by the Bragg grating is lossless below a thickness of $d = 100$ nm. At a thickness of $d \approx 450$ nm the second order of TE modes appears, having one node in the middle of the high refractive index layer (as in fig. 5.12b). In the simulation of a layer with $d = 600$ nm and no grating two peaks are found which result to the first and second TE mode in accordance with equation (5.8).

In order to show the slight effect of a corrugation on the waveguide relation, the figure also shows the FDTD result of a strongly corrugated waveguide. The Alq₃:DCM geometry (both surfaces of the film show the same corrugation) was used to allow comparison to experimental data. Increasing amplitudes shift the curve to the right. A shift of about 25 nm to higher film thicknesses is found. This can be explained by the decrease of the effective refractive index of the film due to the corrugation. A higher thickness would therefore be required to achieve the same effective index as for the slab waveguide.

Experimental data (taken from [76]) with the reported refractive indices is not matched by the simulation. A fit of the experimental data to equation (5.8) would require $n_2 \approx 1.685$ and $n_3 \approx 1.507$ to fit the TE₀ mode in a slab waveguide, assuming sec-

ond order DFB operation. The literature value ([77] $n_2 \approx 1.75$ which was initially used is too high for the used samples in Riechels experiments [65].

Furthermore, calculations with a realistic set of parameters produced the first band gap position and sizes which are shown in figure 5.14. Riechel states [65] that the lasing process is occurring at the second order DFB Bragg reflection which is situated at a wave-vector $\beta = 0$. The thickness of the film layer d and the corrugation period Λ are kept constant at $d = 330$ nm and $\Lambda = 400$ nm. The scan was done for single and double sided corrugations and for amplitudes h ranging from 10 nm to 300 nm. In figure 5.14a the positions of the second and third band are plotted. Part (b) of the figure shows the gap size over increasing corrugation amplitude in both geometries. A comparison to experimental measurements (fig. 5.6b) reveals a corrugation height of approximately 100 nm which is matching the 90 nm, which are reported in [63], very well. Also the wavelength of 630 nm of the second band position are in perfect accordance with the measurement.

5.3. Two Dimensional Corrugation

One of the major disadvantages of 1D-DFB resonators in DFB lasers is the presence of a large divergent emission. In order to improve the emission characteristic, the broad range of lateral degrees of freedom of the modes has to be reduced. The conventional way is the creation of a lateral waveguide with the width of several wavelengths, as in semiconductor DFB laser structures. A two dimensional corrugation of the guiding layer surface is to be preferred in the small refractive index contrast materials of organic materials. The holographic fabrication technology guarantees a nearly perfect homogeneous grating profile over a large area.

To use a two dimensional modulation of the refractive index to create a DFB resonator structure was already proposed and experimentally verified in 1973 by Wang and Sheem [78]. Only the recent interest in photonic crystal and photonic band gap systems brought new attention to this idea with several new publications (for a wrap up see [65]).

The concepts discussed before can be extended to a two-dimensional periodic corrugation, then creating a 2D-DFB resonator cavity. In 2000, Paddon and Young expanded the coupled mode theory for one dimensional DFB structures to two dimensional patterned, planar waveguides [70]. In contrast to the 1D-DFB resonators, the coupling possibilities are much richer. The distinction of TE and TM modes is no longer possible due to the general non separability of the dielectric coefficient function ϵ of x , y and z . A calculation involving the full vectorial nature of the electromagnetic fields is therefore compulsory. With the FDTD method a straight forward calculation in three dimensions with high accuracy is possible. The accuracy of the results is only limited by the grid resolution and the number of time steps which is used in the Fourier transform, as before.

We concentrate the further description to square lattice corrugations because it is the simplest non-trivial symmetry that illustrates most of the effects. The refractive index distribution in the computational core region, of size $30 \times 30 \times 100$, is shown in

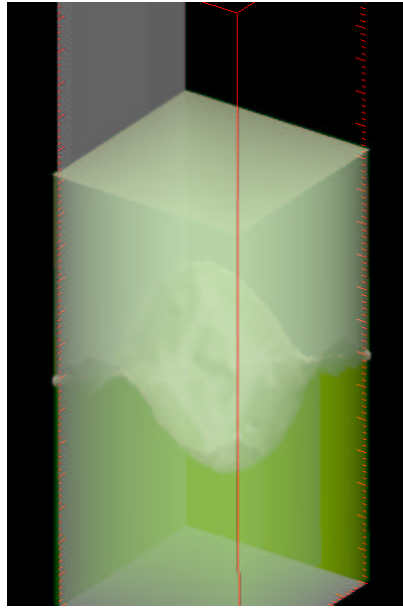


Figure 5.15.: The computational cell with the distribution of the dielectric constant. 1.7 to 1.45 and air. 31x31x100 grid points with $\Delta = 10\text{nm}$.

figure 5.15. The cell size is $(10\text{ nm})^3$ big. The dielectric structure is made up of a thin sheet of high index material which is joined by a lower index substrate material. The interface between those two materials is corrugated in two dimensions to form a egg carton type structure.

In figure 5.16 a sample band structure diagram of the irreducible Brillouin zone is shown. The 100000 time step calculation was performed for LPPP (1.7, 1.45 with thickness 330 nm and amplitude 10 nm). The Plane waveguide TE and TM solutions (eq. 5.8) are plotted for comparison. Initial field configuration $G_y -5..5$, $G_z -5..5$ Ez (TE along y). TE and TM modes can be identified in the diagram although the initial field setup only excited the “TE modes”. The TM modes are strongly excited for higher frequencies. Especially the interaction of TE and TM modes at the M point are of interest. This region at the M point is closely investigated in the above mentioned paper of Paddon and Young [70]. The band gaps which opened up at the X and M point are also shown in a magnified part of the graph. The FDTD calculated result matches the result of the coupled mode theory. Some avoided crossings between band three of the TE and TM modes of the lowest order and the associated modes of order one can be seen.

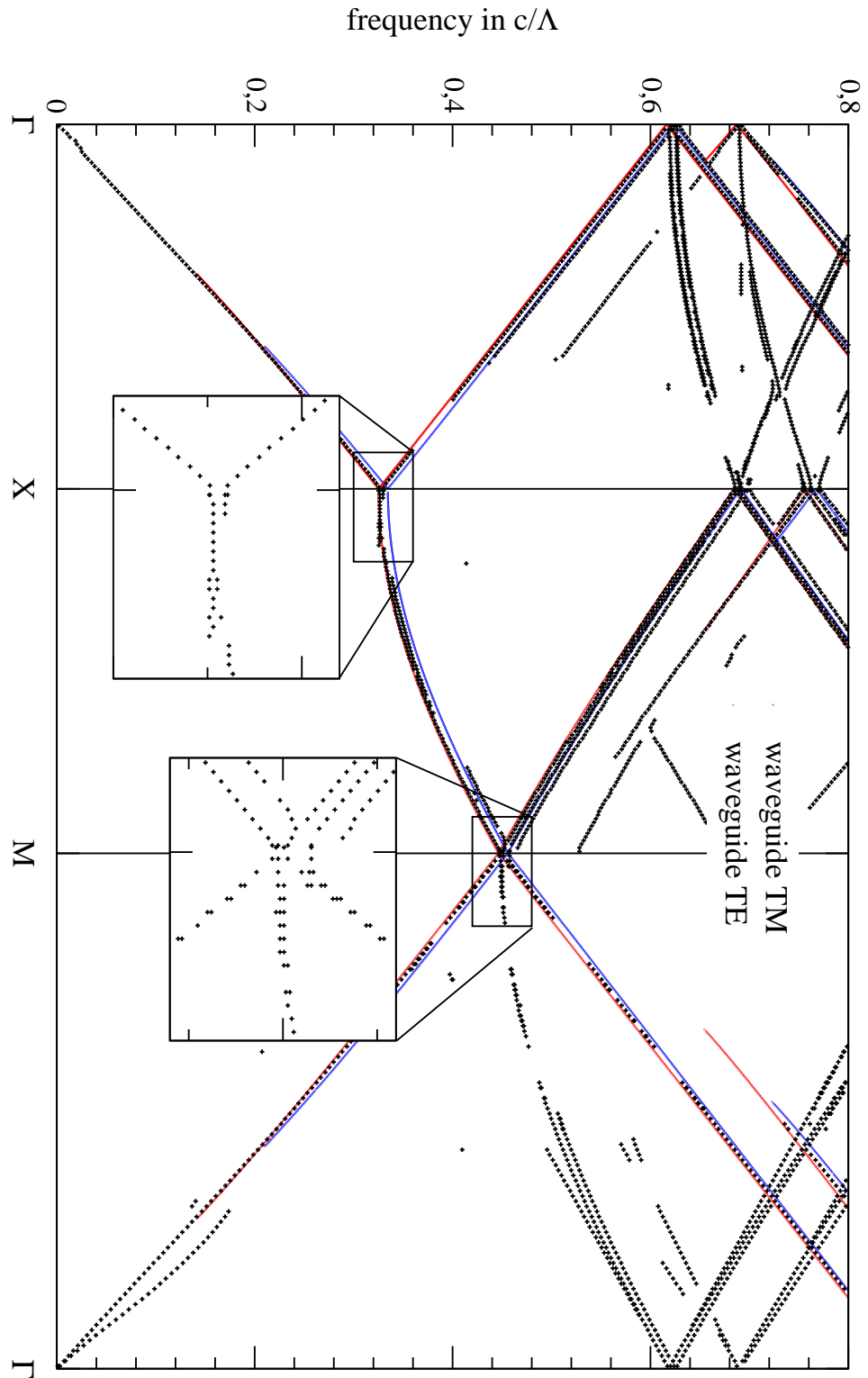


Figure 5.16.: Band-structure of the 2D corrugated DFB laser cavity assuming a sinusoidal patterning of the surfaces.

6. Microdisk

In 1992 McCall, Levi, Slusher, Pearton and Logan from the AT&T Bell Laboratories in New Jersey published a paper [16] called “Whispering-gallery mode microdisk lasers”. This was the first paper to show experimental evidence of lasing in a semiconductor microdisk. Their impelling motivation was the creation of electronic integrated circuit (IC) like chips for optoelectronics. The on-chip conversion of electric to optical signals in such devices is highly favoured over the tedious attempt to couple light into the wavelength sized structures. Stated aims for these radiation generating elements are low power consumption and micro scale size. Both are requirements which have to be fulfilled if methods from semiconductor integrated circuit fabrication should be applied in the manufacturing process of optoelectronic chips. McCall *et al.* chose the cylindrical geometry of a microdisk for this purpose.

The disk shape is the most simple micro-cavity geometry to fabricate with common techniques while still having very small optical loss. This is due to a special type of electromagnetic modes inside the cavity. In an analogy to the acoustics of the Whispering Gallery in St. Paul’s Cathedral in London, and due to the scientific paper from 1912 entitled ‘The Problem of the Whispering Gallery’ of Lord Rayleigh these modes are usually called Whispering Gallery Modes (WGMs). A whisper at one position near the wall can be easily heard on the opposite site, halfway around the gallery. The acoustic phenomenon on which the Whispering Gallery effect relies on, is the total reflection of shallow impinging sound waves at the circular gallery wall. It seems that the sound is travelling along the bent wall. The parallel effect in optics which leads to the WGMs in dielectric, cylindric cavities, is called total internal reflection at dielectric surfaces.

Plane waves originating from the material with high refractive index and which are incident on an interface to a material with lower refractive index, experience transmission and reflection which depend on the angle of incidence. If the angle is larger or equal to the specific total internal reflection angle, which is depending on the refractive indices of the materials and the polarisation of the wave, no energy flow normal to the boundary in the lower refractive index material will occur. In the lower index material, the electromagnetic field is decaying exponentially as it was shown for a dielectric slab waveguide in chapter 5. This field behaviour at material boundaries is called an evanescent field (e.g. Jackson [25]). In the limit of a very small curvature of the dielectric cylinder, in relation to the wavelength of the electromagnetic radiation, the approximation of a local plane surface gives an accurate model of the reflection at the dielectric interface. The association of a plane wave which is being totally reflected when impinging the surface at a steep angle is in analogy with the acoustic phenomenon in whispering galleries.

6. Microdisk

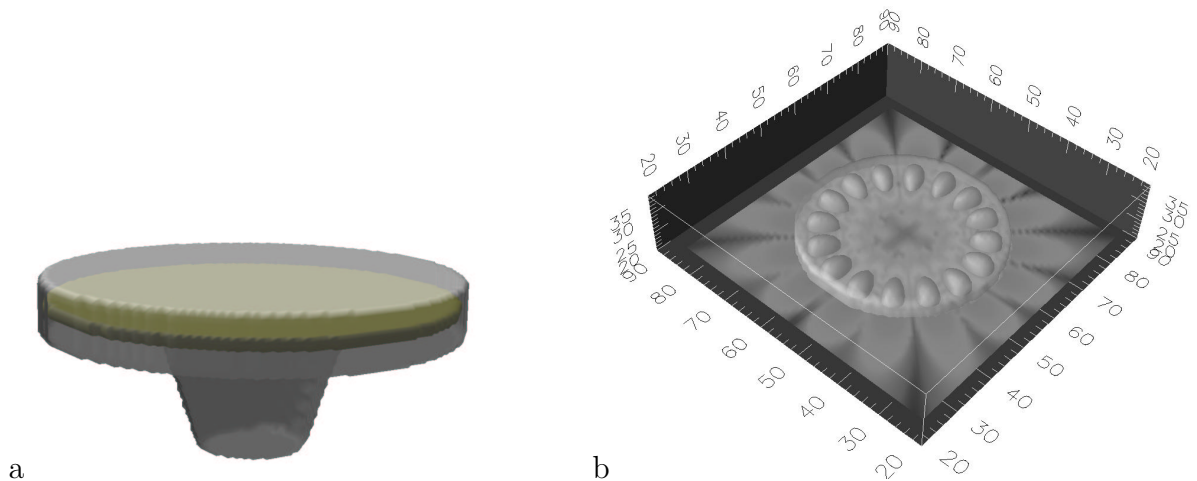


Figure 6.1.: Part (a) shows the dielectric microdisk structure with an embedded laser active material region (yellow) as it is used in experiments. The disk is resting on a pedestal which is linked to the substrate (not shown in the figure). Part (b) presents the HEM_{810} mode on the FDTD grid which is represented by the axial component of the magnetic field. The antinodes are visualised by iso-surfaces, and a coloured slice shows a logarithmic scale colour plot of the field strength.

With the disk radius shrinking to the order of the electromagnetic radiation's free space wavelength, this plane wave association no longer holds. For correct results a solution of the wave equation for this specific geometry is compulsive. A direct, analytic solution of the Maxwell equations (3.1) have, to our knowledge not been reported so far. But a wide variety of approximative approaches to solve this eigenvalue problem have been reported (e.g. Kajfez and Guillon [79]). The most common simplification which is applied to create approximative analytical solutions is the assumption of an effective refractive index in accordance to the dielectric slab waveguide as discussed in chapter 5. This allows for a reduction of the three dimensional problem by eliminating the axial coordinate. The remaining problem of the radial and azimuthal coordinates can then be solved analytically.

A numerical evaluation of the eigenvalue problem is generally based on the FDTD method. The first publication of an FDTD based calculation of whispering gallery modes in microdisks was reported by Li and Liu in 1996 [80]. In 1997, Hagness *et al.* [81] calculated modes in ring and disk resonators, followed by Sakai and Baba in 1999 [82] who simulated photonic devices and circuits of microdisk based resonators. In 2000, Xu *et al.* [83] used the FDTD method to calculate mode structures and quality factors of WGMs in microdisks.

In this chapter we will first present the common analytical approximative solution of the spatial structure and the resonance frequencies of electromagnetic modes in dielectric disks. The basic features of WGMs will be introduced.

FDTD simulations of microdisks without active material (so called cold cavity sim-

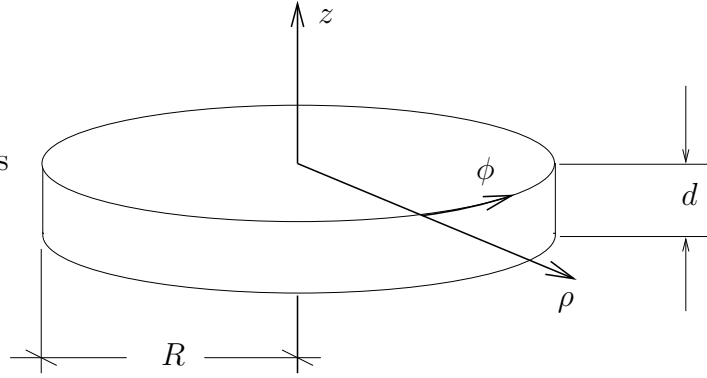


Figure 6.2.: Geometry of a disk with radius R and thickness d in a cylindrical coordinate system.

ulations) will give the eigenfrequencies, mode structures and quality factors of WGMs. These results will give an indication on how the 'modes' in hot cavity simulations will look like and which resonance frequencies of the hot cavity can be expected. The basic dynamical features of the lasing process of a pumped, active medium inside the dielectric microdisk resonator will be presented in the last part of this chapter. The coupled set of Maxwell-Bloch equations as it was introduced in chapter 4 models the material properties of the active material.

6.1. Whispering Gallery Modes

The calculation of resonant frequencies and the spatial structure of the modes in dielectric microdisk cavities is an eigenvalue problem. Due to the symmetry, this eigenvalue problem is best investigated in a cylindrical coordinate system. Figure 6.2 introduces the labels of the radial ρ , azimuthal ϕ and axial z coordinates which will be used in the oncoming discussion. The cylindrical structure with dielectric constant ϵ_r should be defined by the radius R and the thickness d . The Maxwell equations for cold cavity investigations are scale invariant. The resonance frequencies of a disk shaped resonator are only depending on the material constants ϵ_r and μ_r and on the aspect ratio R/d . The cold cavity should be homogeneously filled with a gain- or lossless material which has a real dielectric constant ϵ_r and a permeability of $\mu_r = 1$. The whole structure should be placed in vacuum and the pedestal is not considered until the next chapter.

The homogeneous Helmholtz eigenvalue equation in cylindrical coordinates that determines the function $\Psi(\rho, \phi, z, \omega)$ which is derived from the Maxwell equations (3.1) with the ansatz of a time variation $\exp(-i\omega t)$ reads

$$\underbrace{\left[\frac{1}{\rho} \partial_\rho (\rho \partial_\rho) + \frac{1}{\rho^2} \partial_\phi^2 + \partial_z^2 \right]}_{\Delta_{\text{cylinder}}} \Psi(\rho, \phi, z, \omega) = -\frac{\omega^2}{c^2} \epsilon_r(\rho, z) \Psi(\rho, \phi, z, \omega). \quad (6.1)$$

6. Microdisk

The function Ψ is a wild card for any component of the magnetic field. The parameter c is the speed of light in free space and the spatially dependent parameter $\epsilon_r(\rho, z)$ describes the disk with the surrounding material properties.

A closed mathematical description of the eigenmodes in cylindrical dielectric resonators can be obtained by applying a perfectly conducting material boundary condition at the surface of the disk with a homogeneous dielectric constant. The resulting eigenvalue problem has two independent solutions. One solution features only transverse electric field components in the disk plane (TE polarised) and the other solution has a zero axial magnetic field component (TM polarised). The function Ψ which then represents both, the electric as well as the magnetic field components, separates into a product of three functions of one associated coordinate each. Along the azimuthal coordinate the solution is a sine with an arbitrary phase. The arbitrary phase represents a continuous, infinite degeneracy of the eigensolutions.

A Bessel type differential equation describes the radial problem. The Bessel differential equation has two different types of solutions, the Bessel functions of first and second kind. Bessel functions of the second kind can be ignored as they are singular at the centre of the cylinder along the axis and this would be an unphysical result. Resonances for this idealised setup can be strictly derived (e.g. Jackson [25]) and they appear at frequencies which are given by

$$\begin{aligned}\omega_{lmn,TE}^2 &= \frac{1}{\mu\epsilon} \left(\frac{y_{lm}^2}{R^2} + \frac{n^2\pi^2}{d^2} \right) \\ \omega_{lmn,TM}^2 &= \frac{1}{\mu\epsilon} \left(\frac{x_{lm}^2}{R^2} + \frac{n^2\pi^2}{d^2} \right),\end{aligned}\tag{6.2}$$

where x_{lm} is the m th root of the Bessel function $J_l(x)$ and y_{lm} is the m th root of the first derivative of the Bessel function $J'_l(x)$. The eigenvalues l , m and n are positive integers, where l and n can also be 0.

This approach requires the tangential electric field components to vanish at the disk surface. This is clearly not the case for microdisk resonators of finite dielectric constant, as can be seen in figure 6.1b. None the less this result is valid for very high refractive index contrasts or disk sizes which are much larger than the wavelength of the electromagnetic radiation.

Resonant frequencies of disks with large aspect ratios can be approximated by applying a perfect conducting boundary condition only to the circumference of the cylinder, at the disk radius. Again, the eigensolution Ψ separates into three functions of just one coordinate.

A rigorous analytic treatment of the Helmholtz equation is no longer possible without the assumption of conducting boundary conditions at the surface of the microdisk. Better approximative results for the eigenfrequencies are obtained by a separation of the different spatial regions with a homogeneous constant dielectric. The Helmholtz equation is then solved in each region and the solutions are combined by boundary conditions which are connecting them at the surfaces of the microdisk. In the following section this method will be introduced, as it sufficiently reveals the general properties of the modes

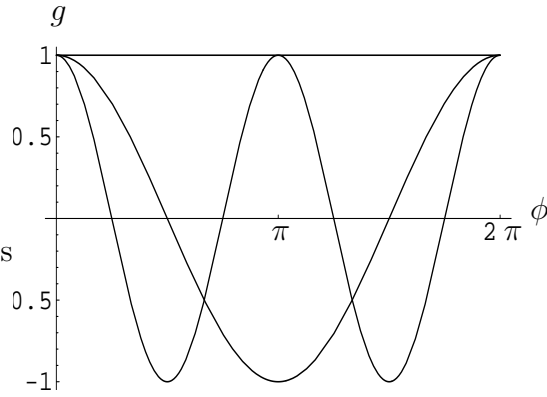


Figure 6.3.: The solution in azimuthal direction (ϕ) for three different orders of ν .

which are present in disk shaped dielectric cavities. This approach was presented by Wang and Dumitrescu [84] or in the book on dielectric resonators by Kajfez and Guillon [79]. But it must be mentioned that with shrinking disk radius and aspect ratios, which are eventually reaching the wavelength scale of the electromagnetic field under investigation, the assumptions made for this ansatz to produce reasonable results are being more and more violated.

6.1.1. Product Ansatz

It is assumed that a decomposition of the solution Ψ of the wave equation (6.1) into a product of three different functions, of only one coordinate respectively, is possible

$$\Psi(\rho, \phi, z) = f(\rho) \times g(\phi) \times h(z). \quad (6.3)$$

This product ansatz requires a dielectric constant function ϵ_r that only consists of a sum of functions of only one coordinate each. This is not the case in a dielectric disk system, where

$$\epsilon_r(\rho, z) \neq \epsilon_{r,\rho}(\rho) + \epsilon_{r,z}(z). \quad (6.4)$$

The product ansatz is valid only in systems with certain boundary conditions, like a perfectly conducting surface around the circumference of the disk or an entire perfectly conducting disk surface. The three different functions (f , g and h) of just one respective parameter transform the wave equation into

$$\frac{1}{\rho} \frac{f'(\rho)}{f(\rho)} + \frac{f''(\rho)}{f(\rho)} + \frac{1}{\rho^2} \frac{g''(\phi)}{g(\phi)} + \frac{h''(z)}{h(z)} = - \underbrace{\frac{\omega^2}{c^2} \epsilon_r(\rho, z)}_{k^2(\rho, z)}. \quad (6.5)$$

In a cylindrical cavity, the material constant ϵ_r is only a function of the radial and the azimuthal coordinates.

6. Microdisk

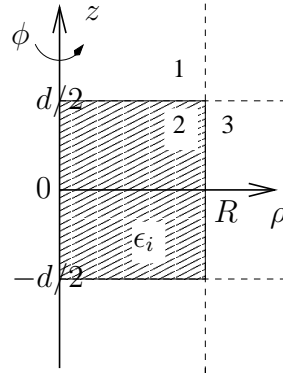


Figure 6.4.: The three different regions of space. The solutions in these domains are linked by the boundary conditions at the interfaces.

A second order, linear differential equation in ϕ can be rigorously derived, because only the third term in equation (6.5) is depending on ϕ . The solution of the linear differential equation for $g(\phi)$ is always correct in problems with cylindric symmetry along the azimuthal direction.

$$g(\phi) = A \cos(\nu\phi + \chi) \quad \nu \in \mathbb{Z} \quad (6.6)$$

One boundary condition to the solution is, that it must be 2π periodic to match the field values when the angle ϕ is changed by 360 degrees. The eigenvalue ν must therefore be an integer number. Figure 6.3 presents the first three normalised solutions for $\nu \in 0, 1, 2$. The eigenvalue ν gives half the number of nodes that the eigensolution has along the azimuthal direction.

There is an infinite and continuous degeneracy, represented by the angle χ , as the disk can be turned around its axis, without any possibility to tell the new position apart from the old one.

The remaining two dimensional problem is separated into two different domains. Figure 6.4 shows the regions and their boundaries which form the problem domains. Domain one is along the axial direction, and domain two is along the radial direction. The problem in domain one is of the slab waveguide type, as it was discussed in chapter 5 but with a different orientation of the coordinate system. It consists of the area above and below the disk and the disk itself (regions one and two). The material constant ϵ_r is only a function of the axial coordinate z in this domain. This problem has a solution which can be used to define an effective refractive index. This effective refractive index can then be used in the radial problem domain. The radial domain consists of the area inside the disk (region one) and region three, which extends from the disk surface to infinity. The material constant ϵ_r is only a function of the radial coordinate ρ in this domain. Both domains are thought of being separate from each other.

The separated equation (6.5) gives two differential equations of second order. An axial, linear differential equation and a Bessel type differential equation for the radial function f .

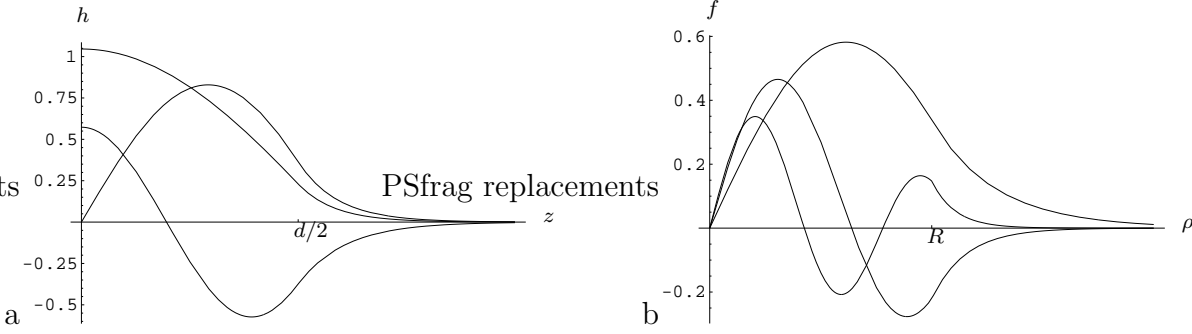


Figure 6.5.: Part (a) shows three fitted partial solutions of lowest order in axial direction $h(z)$. Part (b) shows the three fitted partial solutions in radial direction ρ for different eigenvalues.

The solution for the function h of the axial coordinate z is of the same type as it was for a slab waveguide

$$h(z) = \begin{cases} B \exp\left(-\gamma\left(z - \frac{d}{2}\right)\right) & \forall z > \frac{d}{2} \\ C \exp(\imath\kappa z) + D \exp(-\imath\kappa z) & \forall \frac{d}{2} \geq z \geq -\frac{d}{2} \\ B \exp\left(\gamma\left(z + \frac{d}{2}\right)\right) & \forall z < -\frac{d}{2} \end{cases} . \quad (6.7)$$

The parameter γ can in principle be complex. This would represent solutions which are not confined to the interior of the disk, between $z \in \{-d/2, d/2\}$, but are also oscillatory outside the disk. But as we are only interested in confined modes, this parameter must be real. Then, the field is decaying exponentially away from the disk surface to satisfy the boundary condition at $|z| \rightarrow \infty$, where it must vanish. The form of the function h is shown in figure 6.5a. As will be shown later, there is also an eigenvalue defining the mode structure in this direction. This eigenvalue is related to the number of nodes (points where the function is equal to zero). The figure shows therefore the modes of axial order 0, 1 and 2. The parameters B, C and D are related to each other by the different boundary conditions at the disk surface. The unknown parameters in this solution will be determined by the interplay of all three solutions in the Maxwell equations.

The solution f to the radial differential equation is given by Bessel and Hankel functions.

$$f(\rho) = \begin{cases} E J_\nu(\beta \rho) & \beta = \sqrt{k^2(\rho, z) - \kappa^2} & \forall \rho \leq R \\ F K_\nu(\alpha \rho) & \alpha = \sqrt{\kappa^2 - k^2(\rho, z)} & \forall \rho > R \end{cases} \quad (6.8)$$

Bessel functions are the solutions inside the disk ($\rho \leq R$) and the Hankel functions are the solutions outside the disk. In principle there are also solutions which have oscillating parts outside the disk, but these should not be considered here as they represent lossy modes. Figure 6.5b shows the essential properties of three different solutions to the problem in the radial domain. These solutions are also classified by the number of nodes inside the disk along the radial coordinate. The figure shows the modes of order one to three. They are all decaying exponentially outside the disk.

6. Microdisk

The solutions in the different regions in figure 6.4 have to be brought together by certain boundary conditions to the electric and magnetic field components. The first region is defined by $\rho \leq R$ and $z > d/2$. This is the region above the disk. The region below the disk is similar to this and leads to the same conditional equations which define the unknown parameters. The material parameter ϵ_r is one in this area.

The second region is defined by $\rho \leq R$ and $-d/2 \leq z \leq d/2$. It represents the interior of the disk. The dielectric constant ϵ_r is larger than one.

The third region of space is defined by $\rho > R$ and $-d/2 \leq z \leq d/2$. This is the area of free space outside the perimeter of the disk where the refractive index is also one.

The other regions which are not mentioned here result either in similar boundary conditions, with the same solutions, or they lead to conflicting conditions which can not be fulfilled at the same time. This is due to the impossibility to separate the dielectric constant into a product of functions of only one coordinate parameter.

The general solution of the wave equation (6.1) is given by the product of equation (6.6), equation (6.7) and equation (6.8) according to the modes principal features in their respective spatial regions. The mode in region one and three should for example be non-radiating. The index i indicates the region of space where they are defined. We will assume E_z and H_z to be given by the following functions

$$\begin{aligned} E_z(\rho, \phi, z) &= \hat{E}_i \begin{cases} J_\nu(\beta\rho) & \begin{cases} \exp(-\gamma(z - \frac{d}{2})) \\ c_1 \cos(\kappa z) + c_2 \sin(\kappa z) \end{cases} \\ K_\nu(\alpha\rho) & \end{cases} \cos(\nu\phi) \\ H_z(\rho, \phi, z) &= \hat{H}_i \begin{cases} J_\nu(\beta\rho) & \begin{cases} \exp(-\gamma(z - \frac{d}{2})) \\ c_3 \cos(\kappa z) + c_4 \sin(\kappa z) \end{cases} \\ K_\nu(\alpha\rho) & \end{cases} \cos(\nu\phi + \chi). \end{aligned} \quad (6.9)$$

In order to fit all solutions together, whilst obeying the boundary conditions at the interfaces, an eigenvalue equation has to be derived. Starting with the ansatz for E_z and H_z , which is made to satisfy the wave equation (6.1), the curl part of the Maxwell equations in frequency space leads to the solution for the remaining components E_ρ , E_ϕ , H_ρ and H_ϕ .

$$\begin{aligned} [k_0^2 \epsilon_r + \partial_z^2] E_\rho &= \imath \omega \frac{1}{\rho} \partial_\phi H_z + \partial_z \partial_\rho E_z \\ [k_0^2 \epsilon_r + \partial_z^2] E_\phi &= \frac{1}{\rho} \partial_z \partial_\phi E_z - \imath \omega \partial_\rho H_z \\ [k_0^2 \epsilon_r + \partial_z^2] H_\rho &= -\imath \omega \frac{\epsilon_r}{\rho} \partial_\phi E_z + \partial_z \partial_\rho H_z \\ [k_0^2 \epsilon_r + \partial_z^2] H_\phi &= \frac{1}{\rho} \partial_z \partial_\phi H_z + \imath \omega \epsilon_r \partial_\rho E_z \end{aligned} \quad (6.10)$$

The interface condition at the boundary between region one and two leads to the same eigenvalue equation as for a dielectric slab waveguide (see chapter 5). At this boundary ($z = d/2$) the radial and azimuthal components of the electric (\mathbf{E}) and the magnetic (\mathbf{H}) field, which are tangential to the interface normal have to be continuous.

This leads to four equations defining the four unknown amplitudes $\hat{E}_{\{1,2\}}$ and $\hat{H}_{\{1,2\}}$.

$$\mathbf{A} \cdot \begin{pmatrix} \hat{E}_1 \\ \hat{H}_1 \\ \hat{E}_2 \\ \hat{H}_2 \end{pmatrix} = 0 \quad (6.11)$$

The components of matrix \mathbf{A} are given in appendix A. A solution requires the determinant of the matrix \mathbf{A} to vanish

$$\begin{aligned} \text{Det}(\mathbf{A}) &= \frac{\omega^2}{(\gamma^2 + k_0^2)^2 (\kappa^2 - \epsilon_r k_0^2)^2 \rho^4} \cdot \\ &\quad \left\{ (c_3\gamma + c_4\kappa) \cos(\kappa \frac{d}{2}) + (-c_3\kappa + c_4\gamma) \sin(\kappa \frac{d}{2}) \right\} \cdot \\ &\quad \left\{ (-c_1\kappa + c_2\epsilon_r\gamma) \cos(\kappa \frac{d}{2}) - (c_2\kappa + c_1\epsilon_r\gamma) \sin(\kappa \frac{d}{2}) \right\} \cdot \\ &\quad \left(\beta^2 \rho^2 J_\nu'^2(\beta\rho) \cos(\nu\phi) \cos(\nu\phi + \chi) + \nu^2 J_\nu^2(\beta\rho) \sin(\nu\phi) \sin(\nu\phi + \chi) \right)^2 \\ &= 0. \end{aligned} \quad (6.12)$$

This leads to two independent conditional equations

$$\begin{aligned} \tan(\kappa \frac{d}{2}) &= \frac{c_3\gamma + c_4\kappa}{-c_4\gamma + c_3\kappa} \\ \tan(\kappa \frac{d}{2}) &= \frac{\epsilon_r c_2\gamma - c_1\kappa}{\epsilon_r c_1\gamma + c_2\kappa}. \end{aligned} \quad (6.13)$$

The compliance of either equation leads to a solution of the wave equation for this problem domain. The solutions are related to the transverse electric (TE) or the transverse magnetic (TM) solutions in a dielectric slab as mentioned before. For the above equations to be solvable only either c_1 or c_2 , and either c_3 or c_4 can not be 0. Every combination is either representing a symmetric or an anti-symmetric solutions for either the TE or TM case. All four relations between γ and κ are shown in equation (6.14).

$$\begin{aligned} \tan(\kappa \frac{d}{2}) &= \frac{\gamma}{\kappa} && \text{TE-s} \\ \tan(\kappa \frac{d}{2}) &= -\frac{\kappa}{\gamma} && \text{TE-a} \\ \tan(\kappa \frac{d}{2}) &= \frac{\epsilon_r \gamma}{\kappa} && \text{TM-s} \\ \tan(\kappa \frac{d}{2}) &= -\frac{\kappa}{\epsilon_r \gamma} && \text{TM-a} \end{aligned} \quad (6.14)$$

These four equations are compatible with the equations (5.8) which were derived in chapter 5.

6. Microdisk

The missing relation for the eigenvalue β is established at the interface between region two and region three. This surface at $\rho = R$ requires a continuous transition of the tangential vector components of \mathbf{E} and \mathbf{H} . Tangential means perpendicular to the normal vector of the surface. Affected are E_ϕ , E_z , H_ϕ and H_z . This again leads to four equations for the four unknown constant amplitudes $\hat{E}_{\{2,3\}}$ and $\hat{H}_{\{2,3\}}$

$$\mathbf{R} \cdot \begin{pmatrix} \hat{E}_2 \\ \hat{H}_2 \\ \hat{E}_3 \\ \hat{H}_3 \end{pmatrix} = 0. \quad (6.15)$$

The components of the matrix \mathbf{R} are also presented in appendix A. As before a solution requires the determinant of the matrix \mathbf{R} to be equal to zero

$$\begin{aligned} \text{Det}(\mathbf{R}) &= \frac{\cos(\nu\phi) \cos(\nu\phi + \chi)}{(k_0^2 - \kappa^2)^2 (k_0^2 \epsilon_r - \kappa^2)^2} \cdot \\ &\quad \left\{ [c_1 \cos(\kappa z) + c_2 \sin(\kappa z)] [c_3 \cos(\kappa z) + c_4 \sin(\kappa z)] \right\} \\ &\quad \epsilon_r \omega^2 \beta^2 (k_0^2 - \kappa^2)^2 K_\nu^2(y) J_\nu'^2(x) \cos(\nu\phi) \cos(\nu\phi + \chi) \cdot \\ &\quad [c_1 \cos(\kappa z) + c_2 \sin(\kappa z)] [c_3 \cos(\kappa z) + c_4 \sin(\kappa z)] \\ &\quad - (\epsilon_r + 1) \omega^2 \alpha \beta (k_0^2 - \kappa^2) (k_0^2 \epsilon_r - \kappa^2) J_\nu(x) K_\nu(y) J_\nu'(x) K_\nu'(y) \cdot \\ &\quad \cos(\nu\phi) \cos(\nu\phi + \chi) \cdot \\ &\quad [c_1 \cos(\kappa z) + c_2 \sin(\kappa z)] [c_3 \cos(\kappa z) + c_4 \sin(\kappa z)] \\ &\quad + \omega^2 \alpha^2 (k_0^2 \epsilon_r - \kappa^2)^2 J_\nu^2(x) K_\nu'^2(y) \cos(\nu\phi) \cos(\nu\phi + \chi) \cdot \\ &\quad [c_1 \cos(\kappa z) + c_2 \sin(\kappa z)] [c_3 \cos(\kappa z) + c_4 \sin(\kappa z)] \\ &\quad - \frac{(\epsilon_r - 1)^2}{R^2} k_0^4 \kappa^2 \nu^2 J_\nu^2(x) K_\nu^2(y) \sin(\nu\phi) \sin(\nu\phi + \chi) \cdot \\ &\quad \left\{ [c_2 \cos(\kappa z) - c_1 \sin(\kappa z)] [c_4 \cos(\kappa z) - c_3 \sin(\kappa z)] \right\} \\ &= 0 \end{aligned} \quad (6.16)$$

The following substitutions were used to shorten the representation

$$\begin{aligned} x &:= \beta R \\ y &:= \alpha R. \end{aligned} \quad (6.17)$$

It is necessary that $\cos(\nu\phi + \chi) = \sin(\nu\phi)$ must be satisfied and either c_1 and c_4 , or c_2 and c_3 are zero, for the determinant to vanish at all positions given by z and ϕ . If the electric field ansatz in equation (6.9) is symmetric, the magnetic field ansatz has to be anti-symmetric and vice versa.

This leads to the following conditional equation

$$\begin{aligned}
& \epsilon_r x^2 (\kappa^2 - k_0^2)^2 \frac{J_\nu'^2(x)}{J_\nu^2(x)} + y^2 (k_0^2 \epsilon_r - \kappa^2)^2 \frac{K_\nu'^2(y)}{K_\nu^2(y)} \\
& + (\epsilon_r + 1) (\kappa^2 - k_0^2) (k_0^2 \epsilon_r - \kappa^2) xy \frac{J_\nu'(x) K_\nu'(y)}{J_\nu(x) K_\nu(y)} \\
& = \frac{(\epsilon_r - 1)^2}{\omega^2} k_0^4 \kappa^2 \nu^2.
\end{aligned} \tag{6.18}$$

The solution of the radial part introduced α and β as

$$\begin{aligned}
\alpha^2 &= \kappa^2 - k_0^2 \\
\beta^2 &= k_0^2 \epsilon_r - \kappa^2
\end{aligned} \tag{6.19}$$

which is now used to eliminate α and β . A transformation which is used in the book by Kajfez and Guillon on microwave resonators [79] leads to an eigenvalue equation for k_0

$$\frac{\kappa^2 \nu^2}{k_0^2 \epsilon_r} \left(\frac{1}{x^2} + \frac{1}{y^2} \right)^2 = \left(\frac{J_\nu'(x)}{x J_\nu(x)} + \frac{K_\nu'(y)}{y K_\nu(y)} \right) \left(\frac{J_\nu'(x)}{x J_\nu(x)} + \frac{K_\nu'(y)}{\epsilon_r y K_\nu(y)} \right). \tag{6.20}$$

To get an overall solution both eigenvalue equations (6.14) and (6.20) must be satisfied at once.

The solutions of equation (6.14) have been discussed in detail in chapter 5. They are characterised by the number of nodes m along the axial direction and their polarisation (TE or TM like). A second characteristic number is ν which gives the number of nodal planes along the azimuthal direction. If ν is fixed the radial eigenvalue equation (6.20) can have more than one solution, because the Bessel functions are oscillatory and can have more than one root. The index of the radial eigenvalue is given by the node number of the Bessel function and relates to the number of node planes inside the disk along the radial direction. WGMs start with a radial mode number 1 which is the node at the centre of the disk. No nodal plane would require the energy of the mode being placed at the centre of the disk and not at its circumference. These modes could therefore not be labelled as WGMs.

For a given frequency and given the disk parameters, the thickness d , radius R , dielectric constant ϵ_r , the equation (6.14) can be solved numerically and thus determining the solutions of κ . This solution of the wave number κ and the other parameters in addition to the frequency and the eigenvalue ν can be used to find the solution to the radial eigenvalue equation (6.20). This set of parameters is only related to a WGM if both equations are satisfied for the same value of κ . Figure 6.6 shows an example of a graphical solution method to the WGM problem. The abscissa is a scale invariant value $k_0 R$, therefore the graph is valid not only for one radius but for a certain type of disk with a aspect ratio of 4.583 and a refractive index of 3.6. Two lines are restraining the region of possible solutions (see also chapter 5). The light line $\kappa = k_0 = \omega/c$ and $\kappa = k_0 \sqrt{\epsilon_r - 1}$.

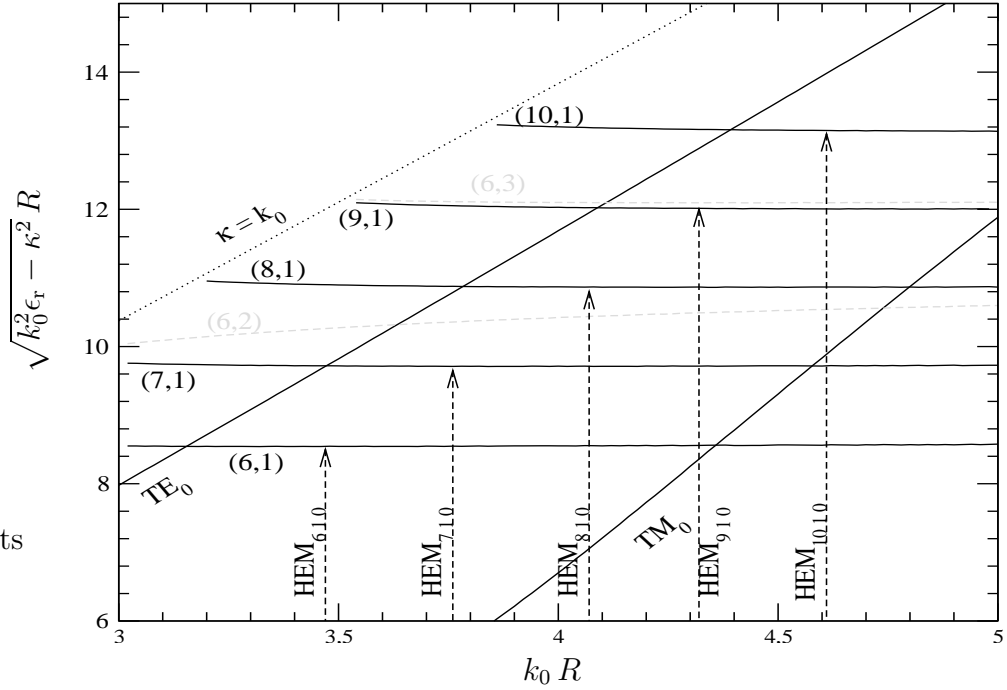


Figure 6.6.: Graphical solution of the approximate solution of the mode spectrum of a microdisk with aspect ratio $110/24$ and a refractive index of 3.6 . Comparison of the intersection points with FDTD simulation results.

These approximative solutions would still be either TE or TM polarised. But the FDTD calculations show that this is not correct. We will call the modes hybrid electromagnetic modes (HEM). Never the less they still are either like TE or TM modes, that means they have only negligible axial electric or magnetic field components respectively. These modes are therefore said to be either TE or TM like. The nomenclature of the modes inside dielectric disk resonators stems from the classification of the WGM modes as derived above. The three eigenvalues, the azimuthal, the radial and the axial are used to describe their features.

Despite the fact that the resonances inside a microdisk are lossy and as such are not static, they are still generally called modes. The FDTD simulations will show that the features of the resonances can be linked to the features of the WGMs inside the resonator.

6.1.2. Different Analytical Methods

It was stated in the last section that a separation ansatz to the wave equation is only possible if the material constants can be described by a sum of functions which are only depending on one coordinate each (see also [79]). In the case of a spatial separation into partial problem domains of homogeneous, constant dielectric they can then be solved analytically. This method works well for high index contrasts between the dielectric resonator and the surrounding material. The WGMs are largely confined to the inside of the resonator. Other types of cylindric resonators in which this approximation works

well have either very large or very small aspect ratios.

All analytic methods which are reported in the literature depend on the separation of the axial problem from the radial and azimuthal part. The most common technique to achieve this is the effective refractive index method, which was already mentioned before. In chapter 5 the method to calculate the effective index of a slab waveguide is outlined. The remaining two dimensional problem in the disk plane has been investigated for two different types of solutions. The first type of ansatz assumes that the mode is totally confined to the disk and exponentially decaying outside the radius as it was assumed in the last section. This ansatz was used for example by Chin *et al.* [85]. The other type of solutions are also oscillating outside the disk. Their eigenvalues are complex and give information about the loss of the mode. Frateschi and Levi [86] used this assumption. The ansatz of lossy eigenmodes improves the accuracy of the approximative calculation of the last section. Both works used the conformal mapping method to calculate the resonant frequencies. The conformal mapping method was used by Heiblum and Harris [87] to calculate loss in curved optical waveguides.

6.2. Cold Cavity FDTD Simulations

The method of choice to compute the cold cavity resonance spectra of wavelength scale microdisks and the associated loss of the eigenmodes which is used most often in literature is the FDTD scheme. Several approximations have been applied, and different coordinate systems have been used in the algorithms. The majority of the simulations is performed on a uniform Cartesian grid in two or three dimensions.

Many publications report the use of the effective refractive index method or approximation to reduce the dimensionality of the problem. This method reduces the problem to the two dimensional radial and azimuthal disk plane. The variation of the dielectric constant of the disk along the axial coordinate is replaced by an effective constant. This effective constant is estimated in an analogy to the slab waveguide approximation, where the effective index represents the slab of dielectric material as a homogeneous medium. A plane wave of certain frequency in a medium with this effective index would have the same wavelength as a guided wave of the same frequency in a slab waveguide along the propagation direction. The calculation of this frequency dependent refractive index is outlined in chapter 5.

In 1997 Hagness *et al.*[81] published results on two dimensional FDTD calculations of disk resonators which are used as add-drop filters. A comparison to experimental results showed good quantitative agreement.

Also in 1997, Li and Liu [88] investigated the frequency dependence and loss of two surface roughness types on the surface of the disk resonator. The roughness types were a sinusoidal variation of its circumference and the other a Gaussian distributed random change of radius along the azimuthal angle. The method which they applied is similar to the work done by Hagness *et al.*, namely an FDTD algorithm on a regular, two dimensional Cartesian grid with an effective refractive index which replaces the inhomogeneity of the dielectric constant along the axial direction.

6. Microdisk

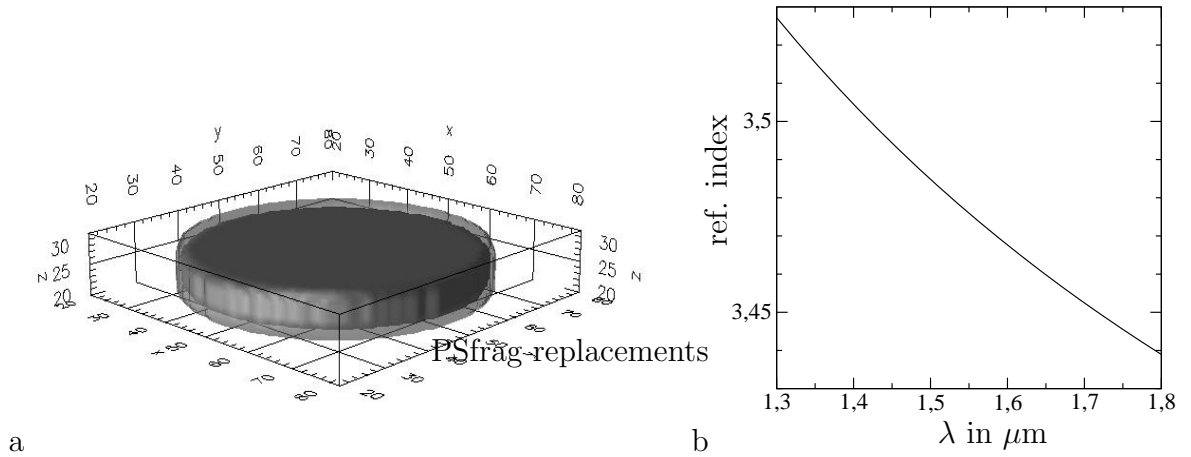


Figure 6.7.: Part (a) shows the dielectric setup of the simulation. Shown are the disk (hollow cylinder) and the embedded active region (solid core) on the computational grid with a resolution of 30 nm. Part (b) gives the wavelength dependent refractive index of the disk material (from [86]).

Simulations of cavities with rotational symmetry could also use the separation of the azimuthal direction. Li and Liu [80] were the first to report such a two dimensional FDTD simulation which uses a cylindrical coordinate system, consisting of the axial and radial dimensions. Stability problems which arise from the decreasing grid cell size towards small radii were resolved by the introduction of a special boundary condition at a certain distance from the axis of the cylinder. The use of such special adapted grid systems leads to faster convergence of the FDTD algorithm over the Cartesian grid. This method on the other hand calculates the Maxwell equations with the assumption of a special solution type along the angular direction. On this account, it has to be used for each of those special solution types to get the complete frequency spectrum of the resonator.

A first three dimensional FDTD calculation has been reported in 1999 by Vuckovic *et al.* [89]. This work reported on the loss and spontaneous emission factors of the modes in a microdisk cavity. In 2000, the same group (Xu *et al.* [83]) published calculated spontaneous emission factors of the whispering gallery modes in a microdisk with aspect ratio 4.44. The theoretical background of the calculations was presented in a preceding paper by Xu *et al.* [15]. The relative change of the spontaneous emission factor compared to the free space value is given by the fraction of the radiation loss of the embedded to the radiation loss of the dipole in free space.

Several of the above mentioned papers calculate the eigenfrequencies and quality factors of the microdisk which was experimentally studied by Levi *et al.* [90]. In order to compare the accuracy of the three dimensional FDTD method on a Cartesian grid with UPML boundaries as described in chapter 3, the properties of this experimentally as well as theoretically thoroughly studied dielectric resonator was chosen to posture as the archetype in the upcoming simulations. The resonance frequencies and losses of the cold

Table 6.1.: Comparison of eigenfrequencies and quality factors calculated with different methods as described in the text. Different literature values are compared to this work, all based on the geometry used in [86] and [90] (PL – photoluminescence spectra, EIM – effective index method, CM-EI – conformal mapping with effective index, Cyl – cylindrical coordinate system, EI – effective index).

	HEM ₄₁₀		HEM ₅₁₀		HEM ₆₁₀	
	$\lambda(\mu\text{m})$	Q	$\lambda(\mu\text{m})$	Q	$\lambda(\mu\text{m})$	Q
PL [90]	1690	-	1542	-	-	-
EIM [90]	1634	-	1480	-	-	-
CM-EI [86]	1680	21	1520	70	1340	410
2D-Cyl FDTD [80]	1706	164	1535	899	1401	5252
2D-EI FDTD [88]	-	-	1572	156	-	-
3D-FDTD [89]	-	-	1550	740	-	-
3D-FDTD, this work	1707	160 ± 5	1539	770 ± 40	1410	3000 ± 300

cavity modes which appear in the literature references are compared to the results of this work in table 6.1. In addition to the literature values which are produced with FDTD methods, the reported resonances of photoluminescence measurements and theoretical calculated values are also used in the comparison. The deviations and differences are discussed at the end of this section. In addition to the eigenfrequencies and losses which were published before, we also compute the mode structure and the mode volume of the three WGMs.

The archetypical microdisk which is investigated in the works of table 6.1 is based on the properties which were reported by Frateschi and Levi [86]. Figure 6.7a shows the geometrical setup which was used in the simulations. This experimentally studied microdisk has an aspect ratio of $R/d \approx 4.44$, with a radius $R = 0.8 \mu\text{m}$ and a height $d = 0.18 \mu\text{m}$. The experimental results were obtained in the free space wavelength range of $\lambda \in \{1.3 \mu\text{m} .. 1.8 \mu\text{m}\}$. In this infrared range, the refractive index of the dielectric material inside the disk changes strongly with the wavelength. Levi *et al.* [90] present an approximative behaviour which is visualised in figure 6.7b.

6.2.1. Resonance Frequencies and Mode Structure

A photoluminescence spectrum from Frateschi and Levi [86] is included in figure 6.8. The dotted line shows one very strong peak around a wavelength of 1542 nm and a smaller peak at $\lambda \approx 1690$ nm. The above mentioned paper attributes these peaks to an HEM₅₁₀ and an HEM₄₁₀ WGM. The conformal mapping analysis predicts a lossless third mode which should have a free space wavelength of 1340 nm. Its mode structure is supposed to be a WGM of type HEM₆₁₀. This mode does not appear in the photoluminescence

6. Microdisk

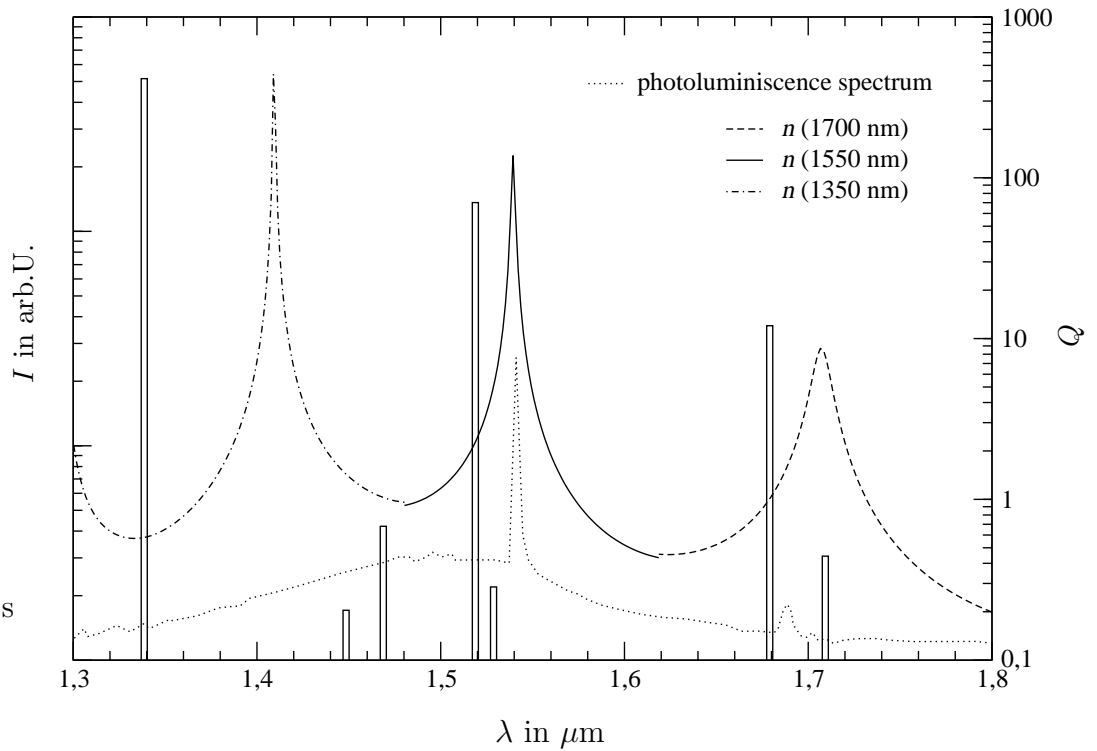


Figure 6.8.: Three response spectra of the investigated microdisk as described in the text. The refractive index is calculated from the behaviour which is given by Frateschi and Levi for the different peaks. Included is their photoluminescence spectrum and their calculated positions and Q-factors, displayed as bars.

spectrum because the gain of the active semiconductor material at this frequency is negative. Three different simulations are performed with an estimate of the respective refractive indices since the variation of the refractive index of the disk semiconductor material with frequency or wavelength is not negligible (see fig. 6.7). The three refractive indices for increasing wavelength are $n(1340 \text{ nm}) \approx 3.51$, $n(1542 \text{ nm}) \approx 3.48$ and $n(1690 \text{ nm}) \approx 3.45$.

Following a method of Chan *et al.* [4] which was used to calculate the band structures in periodic, photonic crystal systems, the frequencies and losses of the modes are determined. This method was outlined in chapter 3. A localised, short pulse current generates a broad spectral electromagnetic pulse which probes the dielectric structure for resonant frequencies in the time domain. The response of the electric or magnetic field to this pulse is recorded during the simulation at one or more spatial points.

The three dimensional FDTD simulation on a Cartesian grid is performed with a grid cell size of $(30 \text{ nm})^3$ and $(15 \text{ nm})^3$. The resonance wavelengths change by less than 0.1 percent

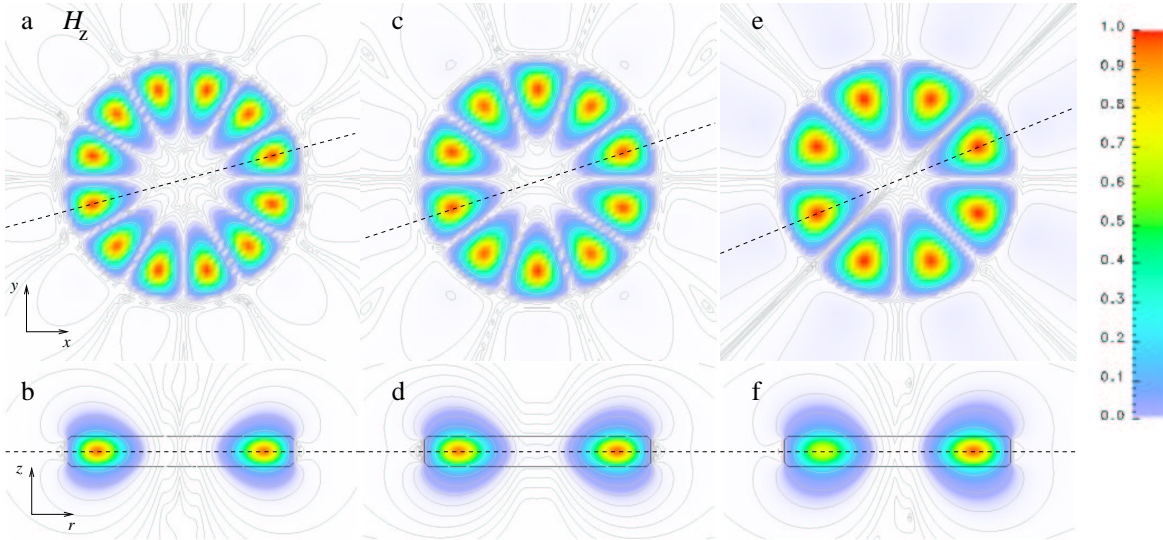


Figure 6.9.: Discrete, spatially resolved Fourier transforms of the axial magnetic field component. The colour represents the normalised strength of the magnetic field. The contour lines show the logarithmic decay of the field. Parts a, c and e show the HEM_{610} , HEM_{510} and HEM_{410} modes respectively on a plane cutting the disk in half. Parts c, d and f show the fields of the above modes on a r - z plane. The black rectangle indicates the location of the dielectric disk structure.

between the two simulations of different grid cell sizes, thus it is assumed that the algorithm has already converged. The results in figure 6.8 are based on calculations of 200,000 time steps on the finer grid of size $200 \times 200 \times 100$ with eight PMLs.

The FDTD simulation response spectra of the Cartesian in-plane components of the electric field show three distinct peaks in the wavelength range. The axial electric field component does not show significant maxima at these positions, which is an indication for the TE like polarisation of these modes. Figure 6.8 presents the three obtained line shapes at the appertaining refractive indices with the photoluminescence spectrum and the peak positions and quality factors from the conformal mapping, effective index calculations by Frateschi and Levi. The quantitative results can be looked up in table 6.1 where they are compared to various other reported calculations or measurements.

The classification of the modes succeeds the calculation of their eigenfrequencies. To classify the modes we have already determined the type of polarisation the WGMs have. TE like modes can be best identified by the axial component of the magnetic field. A second simulation run with a discrete, spatially resolved Fourier transform (see chapter 3) of the H_z field at the eigenfrequencies, filters out the structure of the associated cavity mode. It can be consecutively classified by the three eigenvalues (the azimuthal, radial and axial number of node planes). Figure 6.9 presents the obtained mode structures of the three lossless eigenmodes given in table 6.1. This investigation then reveals that the three peaks in figure 6.8 belong to the HEM_{610} , HEM_{510} and HEM_{410} modes. They all

6. Microdisk

share one nodal point in the centre of the disk, no nodal point along the axial direction and 6, 5 or 4 nodal planes respectively around the disk.

In the simulation the discretised version of the Maxwell curl equations in Cartesian form is simulated which does not fit to the cylindrical geometry of the microdisk. The in plane components E_x and E_y have mirror symmetries about the x- and y-axis, but no rotational symmetry around the axis of the cylindrical resonator. The Cartesian components of the electric field \mathbf{E} , which belongs to the HEM₅₁₀ WGM of figure 6.9b, are presented in figure 6.10. It shows the spatial dependence of the Cartesian electric field components on the x-y- and the x-z-plane which is cutting the disk in half. The strength of the electric field is given by the same linear colour depiction that is also used in figure 6.9. It is normalised to the maximum field strength of the electric field component. The contour lines give the logarithmic decay of the field strength. Field components which are perpendicular to the surface of the dielectric resonator show a non-continuous gradient at the disk surface.

6.2.2. Mode Volume

The mode volume is defined as the overlap integral of the electric field energy with the cavity volume (see Coccioli *et al.* 1998 [91]), or more precisely the quantisation space

$$V = \frac{\iiint_{\text{cavity}} \epsilon(\mathbf{r}) |E(\mathbf{r})|^2 d^3\mathbf{r}}{\max[\epsilon(\mathbf{r}) |E(\mathbf{r})|^2]}. \quad (6.21)$$

The integral is evaluated numerically from the cold cavity spectra which is obtained by the FDTD simulation as described above. The microdisk has a computed volume of $V \approx 0.36577 \mu\text{m}^3$. The mode volume of the HEM₄₁₀ mode is $0.091 V$. The HEM₅₁₀ features a smaller mode volume of $0.080 V$ and the HEM₆₁₀ produced 0.075 times the disk volume. This result is related to figure 6.9 which shows the spatial mode structure of the three modes. The position of the field maximum is shifting towards the perimeter of the disk for increasing azimuthal mode order. This leads to a decrease in the overlap integral of the field energy, which defines the mode volume.

6.2.3. Quality Factor

The post processing of the FDTD simulation data in the cited literature, is done in different ways to calculate the eigenfrequencies and decay constants of the lossy WGMs. Xu *et al.* [83] calculate the quality factor, which is related to the mode loss, by using the energy inside the disk and the flow of energy through the disk surface at one time step in the simulation run. The flow of energy is evaluated by summing up the Poynting vectors over the surface of the disk. According to the Poynting theorem (3.60), this represents the energy loss at the time of the quadrature. This method requires only one mode to be present in the disk. For this purpose, Xu *et al.* first calculate the precise mode structure and successively start another simulation with this mode as an initial condition. Li and Liu [88] use an algorithm, which is called the Prony method, that originates from

the signal processing of exponentially decaying time series. This method essentially consists of finding the roots of the characteristic polynomial, to which the generating differential equation of the signal is related. It was quite popular to use this method following FDTD calculations around the year 1990 due to the slow speed of computers back then. At best, the method of Prony needs only a few time steps to get a good estimate on the decay constants and frequencies. The problem is that a very good preconditioning (decimation, aliasing and low pass filtering) of the signal is required before the Prony method will be stable and give accurate results. The results can be quite misleading if this is not taken care of.

Another method which is applied here, is based on the fitting of Lorentzian line shapes to the peaks in a Fourier spectrum analysis of the simulation results (see chapter 3). Today's computers can handle the calculation of time series that are long enough to result in a discrete spectrum with high resolution. The resolution must be sufficient to differentiate the maxima and give information on the line shape of the resonances. It can be verified, that this is the case in the FDTD simulations of this work, by comparing the different calculated Q factors in table 6.1.

The Helmholtz equation which is describing the electromagnetic field inside a resonator can be extended by a damping term to an Abraham-Lorentz type. This phenomenologically introduced damping factor γ is related to the full width at half of the maximum (FWHM) of the spectral resonance lines in the Fourier transformed time series of the electric or magnetic field (e.g. Jackson [25]). We assume that the damping or decay factor γ is much smaller than the resonance frequency. With this assumption, the Abraham-Lorentz differential equation

$$\partial_t^2 x(t) + 2\gamma \partial_t x(t) + \omega_0^2 x(t) = \hat{E} e^{-i\omega t} \quad (6.22)$$

has the following characteristic solutions

$$x_{1,2}(t) = \hat{x}_{1,2} e^{-\gamma t} e^{\pm i\sqrt{\omega_0^2 - \gamma^2} t}. \quad (6.23)$$

These solutions vanish with the decay constant γ . The particular solution which is driven by the right hand side of this differential equation is

$$x_{\text{part}}(t) = \hat{E} \left[(\omega^2 - \omega_0^2)^2 + 4\omega^2\gamma^2 \right]^{-\frac{1}{2}} e^{-i\omega t + i\Phi} \quad (6.24)$$

with Φ being a constant phase shift

$$\tan \Phi = \frac{-2\gamma\omega}{\omega^2 - \omega_0^2}. \quad (6.25)$$

The particular solution is oscillating with the same frequency as the driving term on the right side of the differential equation (6.22) but shifted by a constant phase Φ and with an amplitude which is given by the frequency dependent function

$$L(\omega) = \left[(\omega^2 - \omega_0^2)^2 + 4\omega^2\gamma^2 \right]^{-\frac{1}{2}}. \quad (6.26)$$

6. Microdisk

This resonance behaviour has the maximum at the frequency $\omega_{\text{res}}^2 = \omega_0^2 - 2\gamma^2$, where the oscillator x and the driving term are in resonance. With the approximation of $\omega_{\text{res}} \gg \gamma$, the resonance equation (6.26) can be further approximated by

$$L(\omega) \approx \frac{1}{2\omega_{\text{res}}} [(\omega - \omega_{\text{res}})^2 + \gamma^2]^{-\frac{1}{2}}. \quad (6.27)$$

This line shape has a FWHM of 2γ .

Another quantity which classifies the loss of a cavity mode is the quality factor Q . It is defined ([25]) as 2π times the ratio of the time-averaged energy stored in the cavity to the energy loss per oscillation cycle relative to the assumed lossless eigenfrequency ω_0

$$Q = \omega_0 \frac{\text{stored energy}}{\text{power loss}}. \quad (6.28)$$

If an exponential decay with the decay constant γ of the stored energy inside the loaded cavity in free space is assumed, the quality factor will be given by

$$Q = \frac{\omega_0}{2\gamma}. \quad (6.29)$$

The Fourier transform of the electric field over time leads to a spectrum with a Lorentzian line shape. A Lorentzian is defined by two properties, by a FWHM Γ and a resonance frequency ω_{res} . An investigation of the spectrum leads to the resonance frequency and the line width. This is related to the quality factor Q by equation (6.29)

$$Q = \sqrt{\frac{\omega_{\text{res}}^2}{\Gamma^2} - \frac{1}{4}}. \quad (6.30)$$

The results of the fit with a Lorentzian line shape to the spectra in figure 6.8 gives the quality factors which are presented in table 6.1.

6.2.4. Discussion

The overall classification of the three WGMs from Frateschi and Levi [86] is in accordance with the FDTD calculations. All three modes share no axial, one radial and four, five or six azimuthal nodes. In addition to that they are TE like which is in perfect agreement with the measurements on this device type which were reported in Levi *et al.*[90].

The resonance frequencies are within 6 percent deviation. The reported method with the smallest error should be the FDTD calculation on a two dimensional cylindrical grid which was used by Li and Liu [80]. The results of the three dimensional, Cartesian FDTD method with PMLs are less than 0.6 percent apart from this work.

A method called conformal mapping, which also uses the effective index method, targeted at calculating quality factors of the whispering gallery modes in microdisks was applied by Frateschi and Levi in 1996. They also compared their calculated eigenfrequencies with experimental photoluminescence measurements. The central resonance of the WGM which was classified as the TE like HEM_{510} mode has nearly the same frequency as

the resonance in the photoluminescence spectrum. The HEM_{410} eigenmode frequency of the FDTD calculation is smaller than the PL resonance. The refractive index of the microdisk would have to be set to about 3.40 in the FDTD calculation in order to get a close fit of the frequencies. The HEM_{610} mode is not present in the PL spectrum due to the negative gain of the active material [86]. All the resonance frequencies of the conformal mapping method are higher than the predictions of the various reported FDTD simulations.

The very good agreement of the calculated eigenfrequencies can not be transferred to the computed quality factors. The three dimensional FDTD simulations and the two dimensional, cylindrical FDTD simulation are in close range. But they differ quite strongly, by orders of magnitude, from the results of the methods which make use the effective refractive index method. The three dimensional simulations are all featuring a very much larger quality factor, that is similar to lower loss.

We note that other Cartesian FDTD calculations [89] with a different approach to the calculation of Q -factors which are based on relating the energy flow out of disk to the energy stored inside the disk also indicate low loss. Their reported result for the quality factor of the HEM_{510} mode is $Q \approx 740$ which is well inside the error range of the value which was calculated in this work.

6.3. Pumped Non-Linear Dynamics

The non-linearity which is introduced to the Maxwell equations by the macroscopic polarisation renders the above premises inadequate. In 1999 Harayama *et al.* published a paper entitled “Nonlinear Whispering Gallery Modes” [92] which gives solutions to a two dimensional non-linear Schrödinger equation. This wave equation models the non-linearity through a linear Lorentzian gain function and a non-linear gain in the two in-plane dimensions.

The term non-linear WGM can be misleading as the system is no longer linear and eigenfunctions can no longer be strictly derived. But in accordance with literature we will use this term as a description for electromagnetic radiation patterns of a certain frequency which exist a fair period of time. It will be shown that the steady state radiation patterns do not vary noticeably from the cold cavity eigenmodes.

Our study of the cold cavity has shown a quite good quality factor for the HEM_{510} TE like WGM at a wavelength of $\lambda \approx 1539$ nm. Figure 6.10 shows the electric field component properties of this mode on the x-y and the x-z plane through the middle of the disk. The dipole in the following calculations is coupling to the x component of the electric field. While only TE like modes with no significant axial component of the electric field appear in this microdisk in the range of 1300 nm to 1800 nm, we also investigated the transition process to steady state lasing of TM like modes in disks with other aspect ratios. The dipole direction was then set to be parallel to the axis of the disk to radiate into TM like modes. No broken azimuthal symmetry due to the polarisation of the active material was present as it is the case for some polarisation in the disk plane. The principal effects which we will discuss next were qualitatively the same.

6. Microdisk

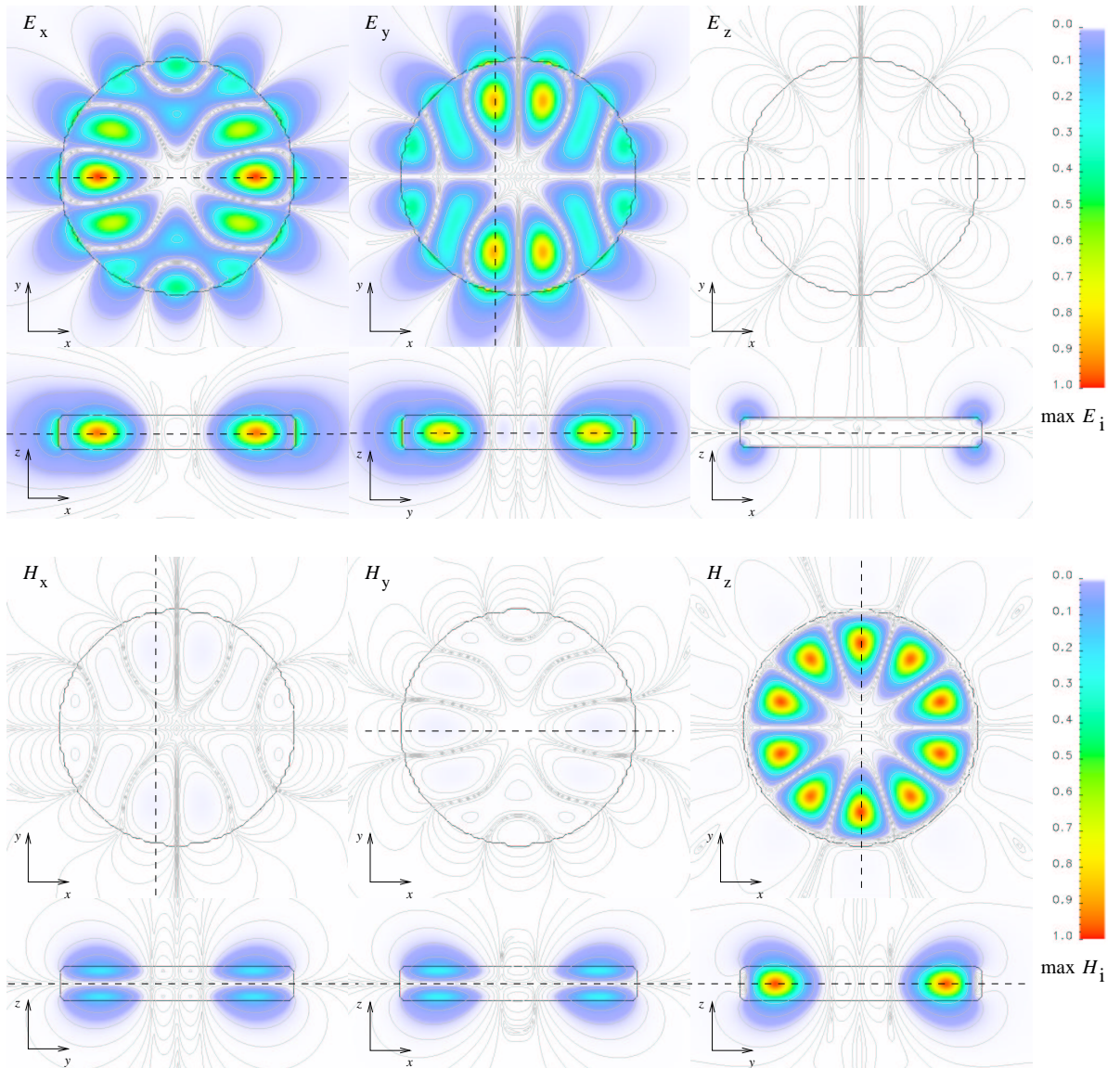


Figure 6.10.: Discrete, spatially resolved Fourier transforms of the Cartesian electric and magnetic field components of the HEM_{510} WGM. The contour lines show the logarithmic decay of the field. The dashed lines show the position of the appertaining slices. The black circle or rectangle shows the position of the microdisk.

Table 6.2.: The setup and parameters of the active microdisk simulation run in figure 6.11.

Entity	Value	Entity	Value
Grid size	$200 \times 200 \times 100$	Geometry	filled microdisk
Cell size	30 nm^3	$\mathbf{d}_{\text{ab}}/ d_{\text{ab}} $	\mathbf{e}_x
$c \frac{dt}{ds}$	0.577	d_{ab}	$-4.806 \times 10^{-29} \text{ A s m}$
$n_{\text{background}}$	1.00	n_{a}	10^{26} m^{-3}
Resonator type	microdisk	γ	10^{12} s^{-1}
$n_{\text{resonator}}$	3.48	ω_0	$1.21526 \times 10^{15} \text{ s}^{-1}$
R	800 nm	γ_{nr}	$1 \times 10^9 \text{ s}^{-1}$
d	180 nm	$\rho_{\text{bb},0}$	0
PML size	8	Λ	$1.25 \left(\frac{1}{2} - \rho_{\text{bb},0}\right) \gamma_{\text{nr}}$
p	3.2	$\rho_{\text{bb}}(t=0)$	0.505
κ_{max}	1.0	Field setup	Gaussian pulse
σ_{max}	1.941		

The material resonance is set to the eigenfrequency of the cold cavity HEM₅₁₀ TE like WGM at 1550 nm in the following simulations. All the simulation parameters are shown in table 6.2. The FWHM of the Lorentzian resonance is small enough not to provide gain to other WGMs with high quality factors. The density of the dipoles is $n_{\text{a}} = 10^{26} \text{ m}^{-3}$ and the dipole strength $\mathbf{d}_{\text{ab}} = -4.806 \times 10^{-29} \text{ A s m} \cdot \mathbf{e}_x$. The thermal equilibrium occupation of the upper level is supposed to be nil and the associated non-radiative decay factor is $\gamma_{\text{nr}} = 10^9 \text{ s}^{-1}$. No pumping profile was used, therefore the non-radiative pumping process is homogeneous and uniform over the whole active material region. To start our FDTD simulations including active materials, the fields are initialised by some noisy electric field of small amplitude, in order to obtain a coupling between the polarisation and the electric field in equations (4.52). The occupation probability of the levels is initially set to 1/2 which is equivalent to an optically transparent material.

The frequency and decay of the initial relaxation oscillations is strongly depending on the pump strength as is predicted by equations (4.100) and (4.101). For large pump factors the decay factor of this process is so large that only one large peak is present in the field energy and the occupation probability. Weak pump factors on the contrary show extensive relaxation oscillation behaviour.

The fast time dynamics of the relaxation oscillation time scale is presented in the next section. When the ultra-fast time scale is investigated in the concluding section of this chapter, an interesting phenomenon can be seen in the evolution of the electromagnetic fields.

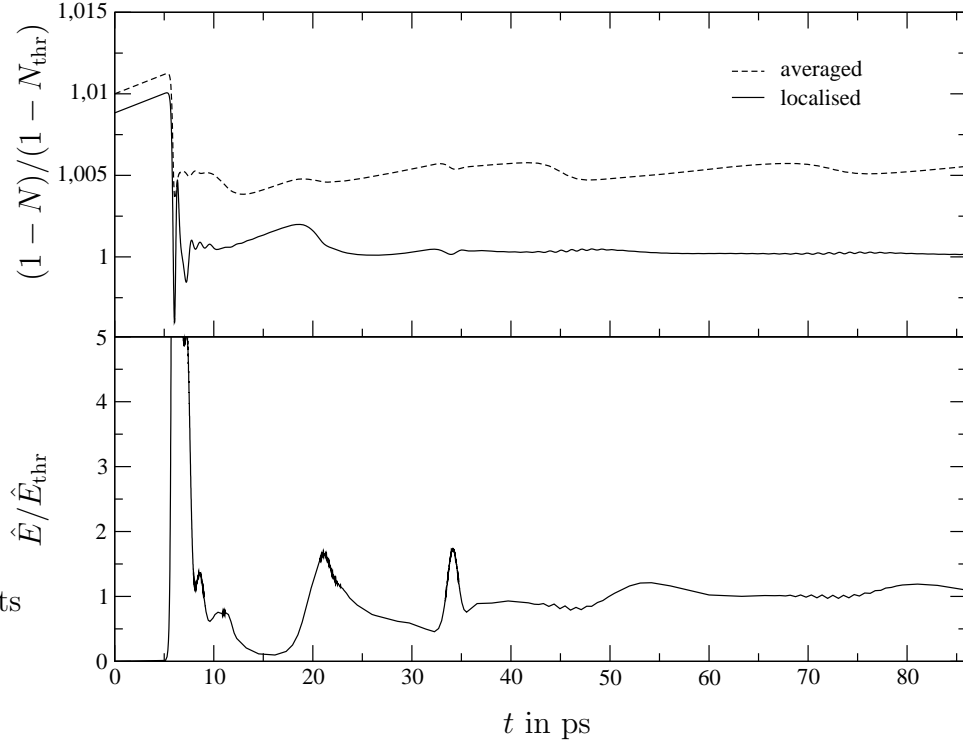


Figure 6.11.: The normalised inversion and the normalised energy inside a microdisk over time. Both are normalised to their threshold values. A localised and the averaged inversion are plotted. The parameters of the 3D simulation are given in the text.

6.3.1. Fast Time Dynamics

In order to discuss the dynamics of the occupation probability difference N and the envelope of the electromagnetic energy in the microdisk, we will in the following focus on the inversion $1 - N$ rather than N as defined above. The inversion has a value range of zero (upper level is unpopulated) to two (upper level is fully populated). Then a value of one would mean that the material is transparent and neither energy is absorbed nor emitted by the active material. Below an inversion of one the material is absorbing and above one it is amplifying. The non-radiative pumping process will increase the inversion instead of decreasing the occupation probability difference N .

In figure 6.12 we plot the inversion during the first 350ps of a simulation, at a point in the region of the disk where the mode is situated and put it into comparison with the average of the inversion over the whole disk. After the first relaxation oscillation, the inversion at the perimeter of the disk is consumed by the TE like HEM_{510} WGM. Subsequently the mode then starts to emit energy through the EM field while continuously being fed by the pump. That is not the case in the middle of the disk where this mode is very weak, with a node in the centre, and so is the coupling to the atomic system. Therefore the inversion near the centre is only weakly affected by the relax-

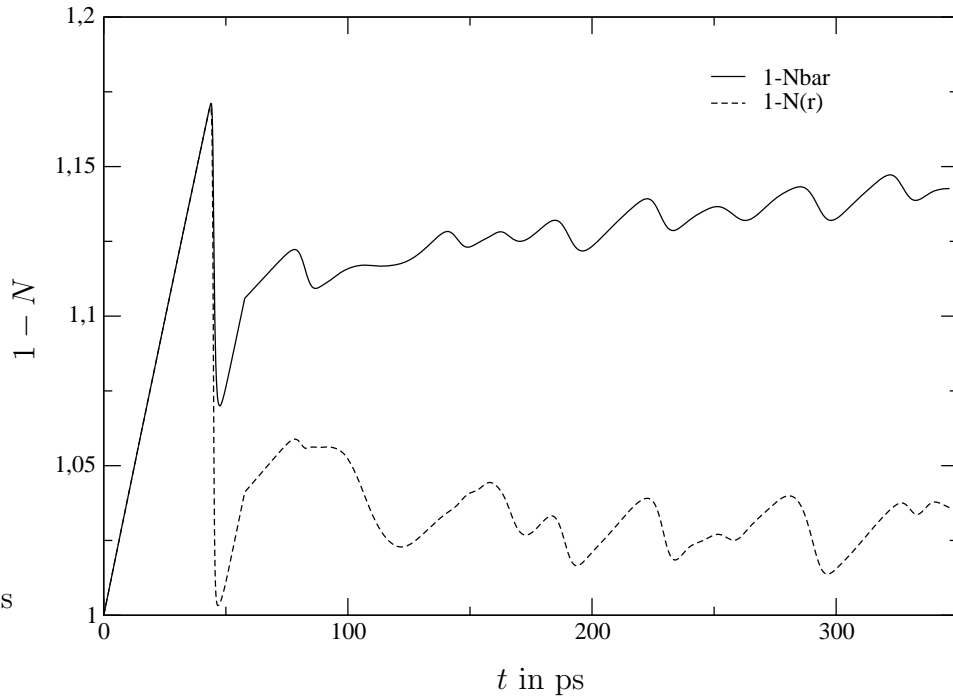


Figure 6.12.: The temporal evolution of the averaged inversion $1 - \bar{N}$ compared to the inversion at a point near the perimeter in the axial middle of the disk. At the beginning of the simulation, the active material was transparent. The active material was filling the whole disk and the pumping rate changed at $t \approx 58$ ps.

ation oscillation. Along the axis, in the centre of the disk, the node in the electric field strength results in a decoupling of the atomic and EM field equations. The pump term in equation (4.51) at this spatial position is only counteracted by the non-radiative loss term. This leads to a steady increase of the upper level occupation probability along the disks axis. Therefore the spatially averaged inversion shows a still increasing slope. As the modes with antinodes in the centre of the microdisk all have very high loss, these modes will eventually show up in a short period of time. This can happen, if the pump strength is above the threshold pump strength associated with these modes. In reality another process will be dominant as it is proposed by Levi *et al.* [93]. Their measurement on microcylinder laser diodes show a strong increase of the incoherent spontaneous emission background with increasing pump current. They claim that this demonstrates the lack of carrier density pinning in the centre of the cavity. This missing pinning effect of the carrier density, or of the occupation probability, is the equivalent to the mounting inversion peak in the centre of the microdisk.

Note that in these present simulations, any possible diffusion of the inversion has been disregarded as it might be caused by diffusion of charge carriers due to carrier transport in real devices.

6. Microdisk

Table 6.3.: The setup and parameters of the active microdisk simulation run in figure 6.13 and figure 6.14.

Entity	Value	Entity	Value
Grid size	$200 \times 200 \times 100$	Geometry	filled microdisk
Cell size	30 nm^3	$\mathbf{d}_{\text{ab}}/ d_{\text{ab}} $	\mathbf{e}_x
$c \frac{dt}{ds}$	0.577	d_{ab}	$-4.806 \times 10^{-29} \text{ A s m}$
$n_{\text{background}}$	1.00	n_{a}	10^{26} m^{-3}
Resonator type	microdisk	γ	10^{12} s^{-1}
$n_{\text{resonator}}$	3.48	ω_0	$1.22395 \times 10^{15} \text{ s}^{-1}$
R	800 nm	γ_{nr}	$1 \times 10^9 \text{ s}^{-1}$
d	180 nm	$\rho_{\text{bb},0}$	0
PML size	8	Λ	$1.100 \left(\frac{1}{2} - \rho_{\text{bb},0}\right) \gamma_{\text{nr}}$
p	3.2	$\rho_{\text{bb}}(t=0)$	0.50034
κ_{max}	1.0	Field setup	Gaussian pulse
σ_{max}	1.941		

Experimental studies of ultra-fast carrier dynamics of quantum-dot microdisk lasers were published in 2001 by Luo *et al.* [94]. The response speeds which were reported in the above mentioned paper (a turn-on time as short as 7.8 ps) match the transient times of the simulations quite well.

6.3.2. Ultra-Fast Time Dynamics

In the above simulations of the transitional behaviour during the switch on time of lasing in this microdisk, a stunning effect of the electric field on an ultra-fast time scale can be observed. This ultra-fast time scale is in the range of several periods of the EM field oscillation. One would expect the field mode to oscillate in-place in a static fashion. But the simulations show a different behaviour during the final 'steady state' lasing. There are to date no measurements of the ultra-fast processes of the EM field in or around a microdisk.

The simulation parameters and the setup of the run that is presented in figure 6.13 are given in table 6.3. This figure 6.13 shows the electromagnetic field in the disk plane represented by the axial component of the magnetic field at consecutive time steps. The azimuthal phase fronts are not straight, they rather show a clockwise spiral form. And there is a shift of the node and antinode positions of the WGM in the counter clockwise direction between consecutive time steps. This rotation of the 'mode' starts during the initial relaxation oscillation peak. If the lasing process breaks down due to a lack of inversion after the initial relaxation peak the rise of the inversion towards a subsequent relaxation peak features a static, in-place oscillation of the mode, as expected. This again turns into a rotation of the mode near the time of the relaxation peak.

Regions with electric field components which couple to the atomic system of high field strengths, that is antinodes of the modes, are pinning the inversion to the threshold

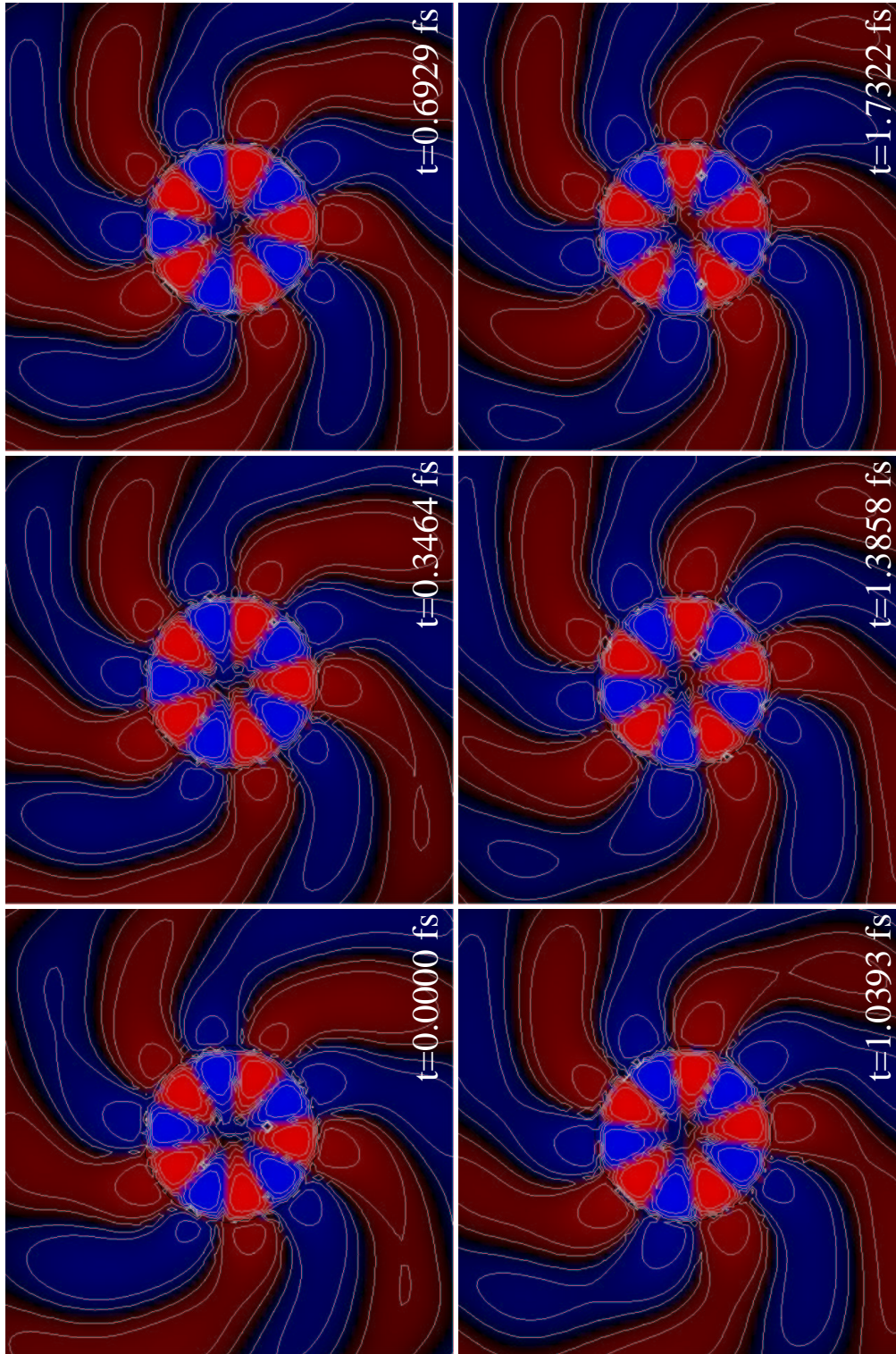


Figure 6.13.: Ultrafast dynamics of the electromagnetic field (represented by the axial component of the magnetic field) produced by a microdisk cavity.

6. Microdisk

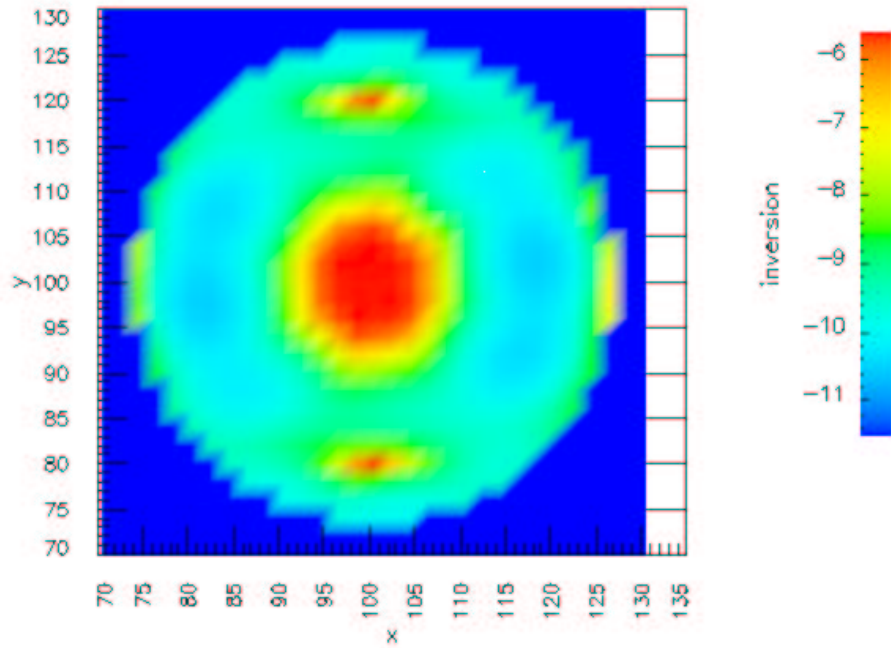


Figure 6.14.: Embossed electromagnetic mode structure in the inversion of a lasing microdisk cavity during steady state operation.

inversion. The steady state inversion then shows a positive gradient towards the nodes of the EM field modes. This spatial hole burning effect of standing waves inside laser resonators is well known. The structure of a static, in-place oscillating EM field mode should be visible as an embossed pattern in the atomic levels occupation probabilities. Such a behaviour will be shown in the final chapter on microgears.

Figure 6.14 presents the structure of the inversion during the steady state operation as it was described above with the peculiar rotating 'mode'. The rotating electric field interacts with the inversion and pins the inversion around the circumference of the microdisk. As the x component of the electric field has a node plane along the y-axis of the cylindrical cavity and especially in the centre of the disk inversion peaks are building up due to the non-radiative pumping process and the missing coupling at these positions.

The WGMs are all continuously degenerate by an arbitrary azimuthal angle. When the first relaxation oscillation peak burns the pattern of one of those degenerate modes into the inversion the azimuthal node planes of the selected mode lead to a higher inversion between the antinodes of this specific mode profile. A symmetry break then leads to the turning of the mode to places with higher inversion in order to maximise its amplification.

Time resolved photoluminescence measurements and micro-PL images which were done by Zwiller *et al.* [95] in 2003 might indicate a rotating electromagnetic field inside the disk.

7. Microgear

The simulation of a microdisk laser in the last chapter revealed some peculiar behaviour of the lasing mode. The mode starts to turn on an ultra-fast time scale in order to feed on all the reachable gain. This is possible due to the continuous degeneracy of the modes in azimuthal direction combined with the non-linearity of the optical Maxwell Bloch equations. The continuous degeneracy can be removed by introducing a grating around the disk. This corrugation along the circumference of a microdisk forms a cavity type which is called 'microgear'.

In order to lower the threshold pump power of microdisk shaped lasers, Fujita and Baba [96] proposed this type of modification of the disk shape in 2001. Such microgear systems were being build and experimentally studied in 2002 by Fujita and Baba [6]. They assumed that in normal disk shaped micro-cavities, the pump power is not only transferred to the lasing but also to other non-lasing modes which all are degenerate, thereby increasing the threshold pump power. By introducing the grating, higher loss of the non-lasing modes and a lower loss for the lasing mode are to be expected. Another article which takes this idea one step further and tries to fuse the microgear idea with photonic crystal micro-cavities, was published in 2003 by Nozaki *et al.* [97].

Figure 7.1 shows the principal setup of a microgear structure as it was used in the experiments of Fujita and Baba. A pedestal of substrate material, with a smaller diameter than the cavity, is topped with a gear of high refractive index material. Embedded in the vertical centre of the gear is a thin layer of quantum well material, which acts as the active region of the laser system. This whole thumbtack like structure is etched out from a substrate wafer.

The first section of this chapter investigates the cold cavity features of the microgears which are used in the work of Fujita and Baba. It will be shown that the pedestal has a negligible effect on the mode structure and eigenfrequency of the WGMs. The change to the noticeable resonance frequencies, in a certain frequency range, for an increasing corrugation amplitude will be given for a typical dielectric device structure. In this context, the removal of the continuous azimuthal degeneracy will be demonstrated in a microgear. Finally the computed change of the mode volumes and quality factors of two particular modes with increasing corrugation amplitude is given.

The second part of this chapter is then related to full vectorial Maxwell Bloch simulations of the initial relaxation oscillation behaviour in a microgear cavity. This part is related to chapter 6 and should show the prevention of the non-linear 'mode' turning effect.



Figure 7.1.: Shape of the simulated microgear cavity with the active layer (yellow) inside the disk.

7.1. Properties of Cold Cavity Microgears

First of all the newly introduced modifications to the simple cylindrical geometry of the microdisk in chapter 6 is discussed. The modifications include a rotational symmetric pedestal structure and a periodic grating along the circumference of the disk.

The pedestal is a remains from the etching process of the dispensable material between the disk and the substrate material of the semiconductor wafer. The assumption that the additional dielectric pedestal has no noticeable effect on the resonance frequencies and the structures of the WGMs is tested first.

The range of gratings which is used in this chapter is defined in the second section, where the basic composition of the dielectric structure is similar to the microdisks and microgears which were discussed in the paper of Nozaki *et al.* [97]. They compare experimental results of microgears with a corrugation order of sixteen or eighteen, to three dimensional FDTD calculations of cold cavity frequency spectra. We define compatible modes, which means that the antinodes of the eigenmode with half the azimuthal order than the corrugation order are at the same angles as the convex antinodes of the corrugation. Every other eigenmode which has its antinodes at different positions, especially at the position of the concave antinodes of the corrugation, is said to be incompatible to the corrugation.

It will be shown that the removed continuous degeneracy leads to a split of the resonance frequency of the appertaining compatible and incompatible modes which were degenerate modes in the cylindrical geometry. Finally, the effects of the corrugation amplitude on the eigenfrequencies and quality factors in a microgear with corrugation order eighteen will be presented.

Figure 7.2 shows the properties and labels of the dielectric microgear as they are used in this chapter.

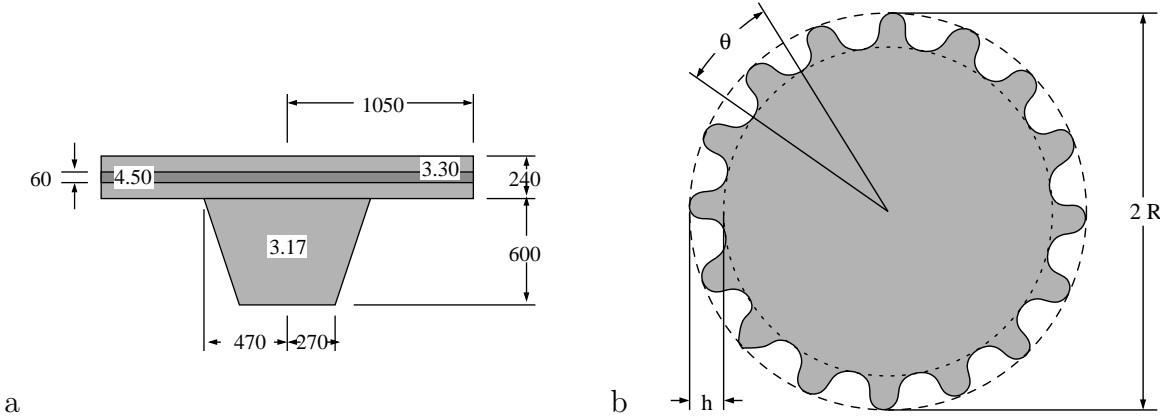


Figure 7.2.: The geometry and refractive indices of the microgear cavity. The length scale is in nm.

7.1.1. Pedestal

The pedestal is a remain of the etching process. It also serves as the supporting structure by which the disk or gear is fixed to the substrate. Fujita [97] presents scanning electron micro-graphs (STM) of their fabricated microgear cavities. The InP pedestal in their work shows a larger radius right beneath the cavity which is getting smaller towards the substrate. Furthermore, their STM images suggest a quadratic cross section of the pedestal shape. Fujita explains this quadratic shape with the crystal structure of InP.

Figure 7.2 shows the geometrical setup that is used in the simulations in this section. The shape of the whole structure is rotational symmetric. The refractive index of the pedestal is $n = 3.17$. It has a height of 600 nm, the radius at the top is 470 nm and at the bottom 270 nm.

The cold cavity spectra of a microdisk and a microgear with and without the pedestal structure are simulated to evaluate the changes in eigenfrequencies. The eigenfrequencies of the WGMs with lowest radial order differ by only ± 0.1 nm. The shift of frequencies of higher radial order modes is around 1 nm to lower frequencies in contrast to the cavity without a supporting structure. As the difference is this small, most of the forthcoming simulations were done without the pedestal beneath the microgear. The spatially resolved mode structures which were extracted from simulations which included a pedestal feature a black circle marking its adjacent end.

Shi *et al.* [98] took a closer look at the dependence of the resonant wavelengths and quality factors of a microdisk with pedestal and substrate. They used a two dimensional, cylindrical coordinate system FDTD code and varied the distance from the substrate surface, to show that the resonant frequencies converge for distances larger than one wavelength in the dielectric material. This can be qualitatively understood in terms of the evanescent modes which decay exponentially away from the surfaces on the scale of one wavelength.

7. Microgear

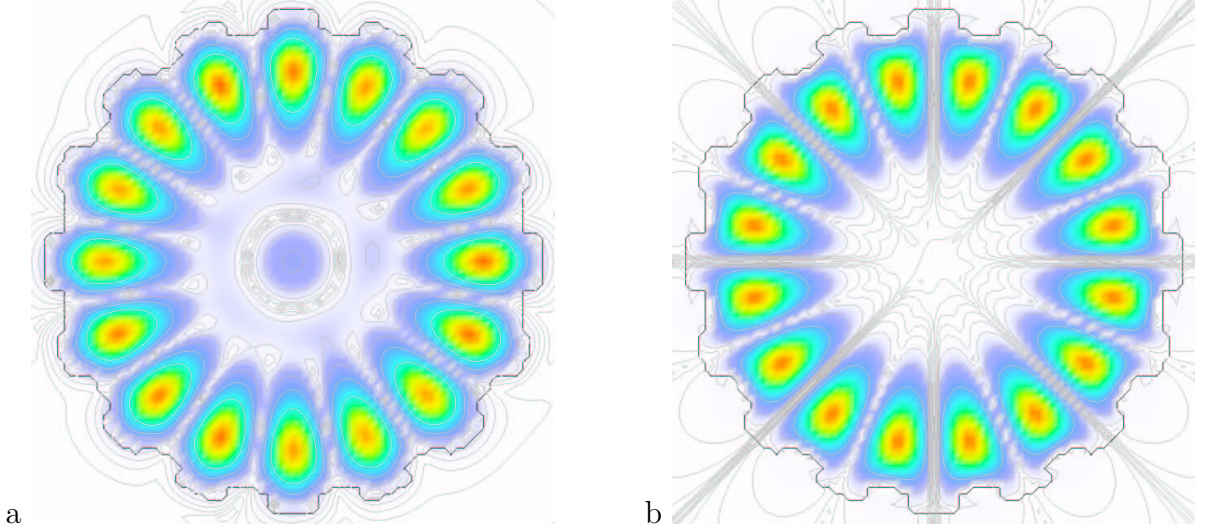


Figure 7.3.: HEM_{810} modes in a microgear cavity without pedestal, with compatible corrugation order 16. The gears teeth are either at the node (a) or antinode (b) position.

7.1.2. Corrugation and Mode Degeneracy

Figure 7.2b shows the geometrical features of the corrugation which is used in the simulations. The disk on top of the pedestal has a sinusoidal variation along the azimuthal direction. The outer radius of the disk is still the defining radius, the corrugation is introduced by a subtracting process. The depth h of the carved corrugation is measured from the circumference. The corrugation period angle θ has to be an integer multiple m^{-1} , $m \in \mathbb{R}$ of 2π . The order m is therefore a defining parameter of the function which describes the corrugation shape

$$f(\varphi) = \begin{cases} R + h [\cos^4(\varphi \frac{m}{2}) - 1] & \forall \cos(\varphi m) < 0 \\ R - h \sin^4(\varphi \frac{m}{2}) & \forall \cos(\varphi m) \geq 0 \end{cases}. \quad (7.1)$$

This corrugation breaks the continuous azimuthal degeneracy. Figure 7.3 shows two shifted mode structures which were degenerate in a disk without the corrugation. Depending on the position of the toothed gear in relation to the mode nodes, the attenuation of the magnetic field outside the disk is either very strong (nodes at the tooth position) or weaker (tooth at the antinode position). What is remarkable in the mode structures of figure 7.3a is the additional weak internal structure of the compatible mode with its nodes at the tooth position. There appears to be an additional maximum in the centre of the disk which is about 10% of the main maximum of this mode.

The separation of the two previously degenerate modes is related to experimental studies of these microgears in Fujita *et al.* [97]. But a simulation with the same parameters as in Fujitas work for a weakly (90 nm) corrugated gear shows a split of 37 nm between the wavelength of the node and the antinode positioned mode at $\lambda_a = 1.747 \mu\text{m}$ and

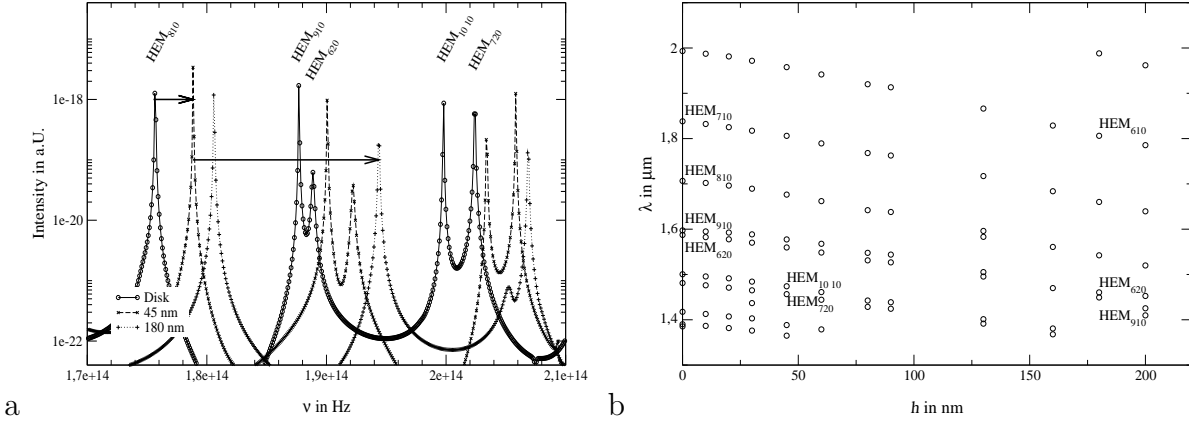


Figure 7.4.: The spectra of a cold microdisk with radius $R = 1.1 \mu\text{m}$, height $d = 240$ nm and refractive index $n = 3.3$, and microgears with the same properties but undulated surface (undulation shape is given by equation (7.1)) of grating depths $h = 45$ nm and $h = 180$ nm in part (a). Part (b) shows the frequency shift of WGMs in the microgears over corrugation depth h .

$\lambda_b = 1.710 \mu\text{m}$. This splitting is an order of magnitude larger than the experimental evidence that the above mentioned paper suggests for a weakly corrugated microdisk.

A thorough investigation of the splitting of eigenfrequencies and Q-factors of previously degenerate eigensolutions, due to periodic variations of the radius is given by Li and Liu, 1997 [88]. Their work also shows that for small perturbation heights, a Gaussian correlated perturbation of the radius leads to a splitting of the resonant frequencies too, but the mean quality factor stays more or less the same.

7.1.3. Resonant Wavelength Shift

The shift of the cold cavity eigenfrequency due to the introduction of the corrugation with order $m = 18$ to higher frequencies with increasing depth h can be explained by the effective index idea. If we decrease the effective index along the circumference of the cylindrical dielectric cavity by cutting away the corrugation the antinode position of the electromagnetic field moves closer to the axis of the cylinder. This leads to an increase in the resonance frequency for this mode (see also chapter 6). The calculated mode structures in figures 7.5, 7.6 and 7.7 demonstrate and verify this effect. Figure 7.4a shows three cold cavity spectra for different corrugation depths which are calculated with the FDTD method. The principal spectrum of the disk with radius $R = 1050$ nm and height 240 nm shifts to higher frequencies with increasing corrugation depth.

Part (b) of figure 7.4 presents the corrugation depth dependent shift of the modes eigenfrequencies in the wavelength range from $\lambda \in \{1.38 \mu\text{m} .. 2.00 \mu\text{m}\}$. One can see that the dependence of resonance wavelength to corrugation depth gets more linear like for modes with lower frequencies. WGMs with small azimuthal mode order and therefore lower frequency, like the HEM_{610} mode feature a nearly linear shift of the free space wavelength with h while the HEM_{1010} mode frequency on the other hand features a

7. Microgear

non-linear dependence. Especially the compatible mode HEM_{910} shifts slower for small corrugation depths.

The dependence of eigenfrequency or wavelength to corrugation depth h of the two modes which are compatible, the HEM_{910} and the HEM_{620} WGM, to the grating period is presented in figure 7.8a. By computing the mode structures at the resonance frequencies of the eigenmodes it will be shown in the next section, that the modes of second order in the radial direction swap their places at a certain corrugation depth with the neighbouring modes of lower radial order. This happens between a corrugation depth of $h = 100 \text{ nm}$ and 160 nm .

7.1.4. Mode Structure

Figures 7.5a-d present the mode structure of the modes in a cold cavity microdisk in the frequency range of $1.6 \times 10^{14} \text{ Hz}$ to $1.9 \times 10^{14} \text{ Hz}$. The microdisk has an aspect ratio 4.375 and a refractive index of 3.3. Four modes can be clearly identified in the spectrum figure 7.4a and their mode structures are in the order of increasing eigenfrequency. The modes are TE like and the electric field along the axial direction E_z is much weaker than the components E_x and E_y in the disk plane. For this reason, the magnetic field component along the axial direction is a good representative of the mode structure (see also chapter 6). The normalised amplitude of this component $H_z(\omega_i)$ is given in the mode structure plots.

None of the modes has a node plane along the axial direction. The mode in figure 7.5d shows a second radial node plane in the disk. The remaining describing number can be derived by counting the number of node planes around the azimuthal direction. It turns out that the double peak in the spectrum (fig. 7.4a) near $1.9 \times 10^{14} \text{ Hz}$ is associated with the HEM_{910} and the HEM_{620} modes in that order. The HEM_{620} WGM features a much smaller quality factor Q than the HEM_{910} mode, as can be seen in figure 7.8b.

Figures 7.6a-f present the modes in the same structure but with 45 nm corrugation which were found in the spectral frequency range of $1.6 \times 10^{14} \text{ Hz}$ to $2.2 \times 10^{14} \text{ Hz}$. The eigenfrequencies of the modes has shifted to higher values as shown in figure 7.4b. The mode volume is decreasing and a slight change in the mode structure at the circumference of the gear can be noticed.

A further increase in the corrugation depth to 180 nm results in the mode structures in figure 7.7a-e. The eigenfrequencies shift further to higher values and the mode structure at the disk edge is strongly altered as a comparison of the contour lines outside the disk and the corrugated gear reveals.

An interesting feature is the frequency order swap that takes place for the HEM_{910} and the HEM_{620} WGMs. The mode with azimuthal mode order nine features the antinodes exactly at the angular position of the convex antinodes of the corrugation with order $m = 18$.

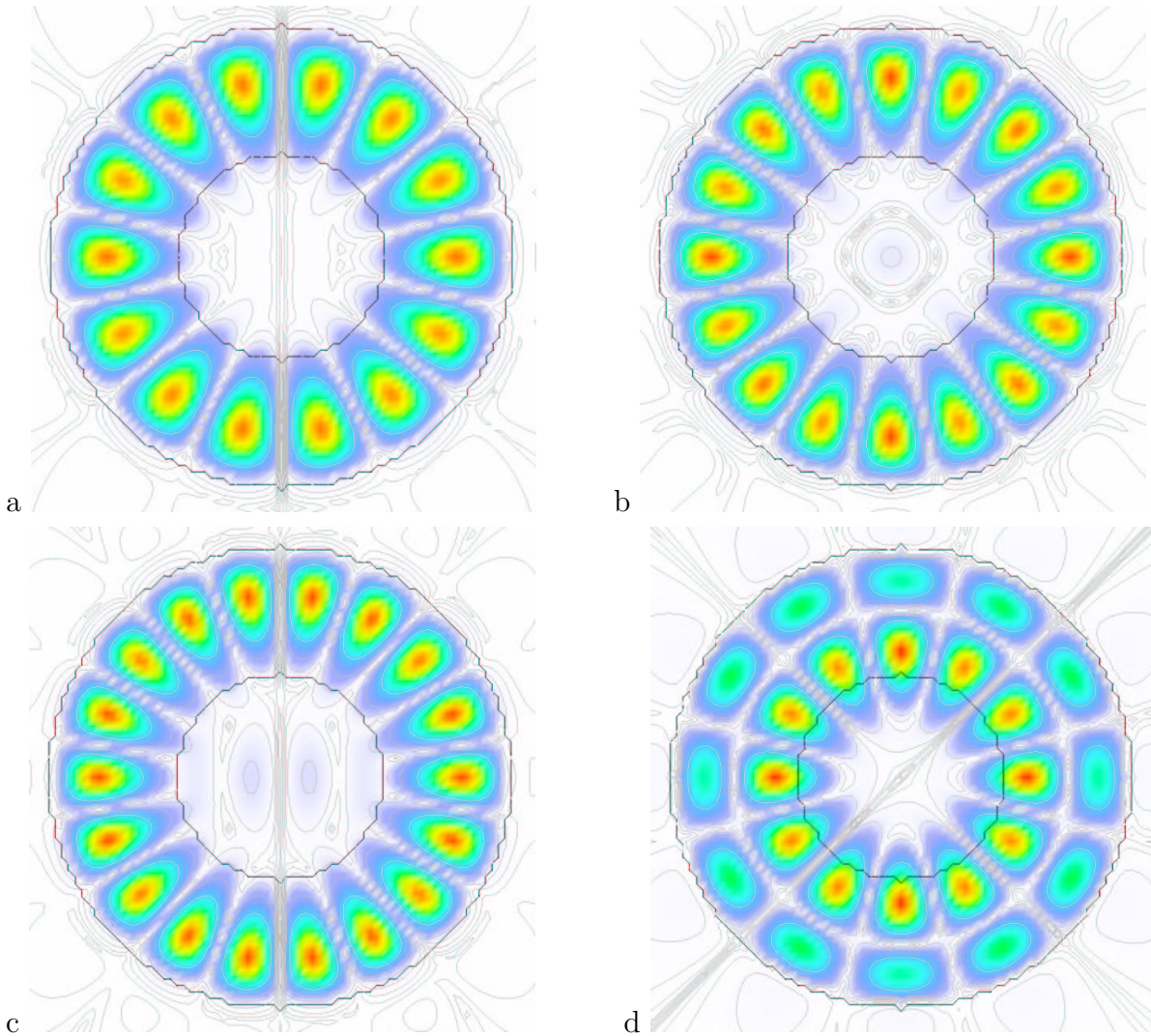


Figure 7.5.: Contour plots of the modal $H_z(\omega)$ field component. The outline of the disk and the top circumference of the pedestal are sketched as black circles. Modes are shown in succession of increasing eigenfrequencies. (a) HEM₇₁₀, (b) HEM₈₁₀, (c) HEM₉₁₀ and (d) HEM₆₂₀.

7. Microgear

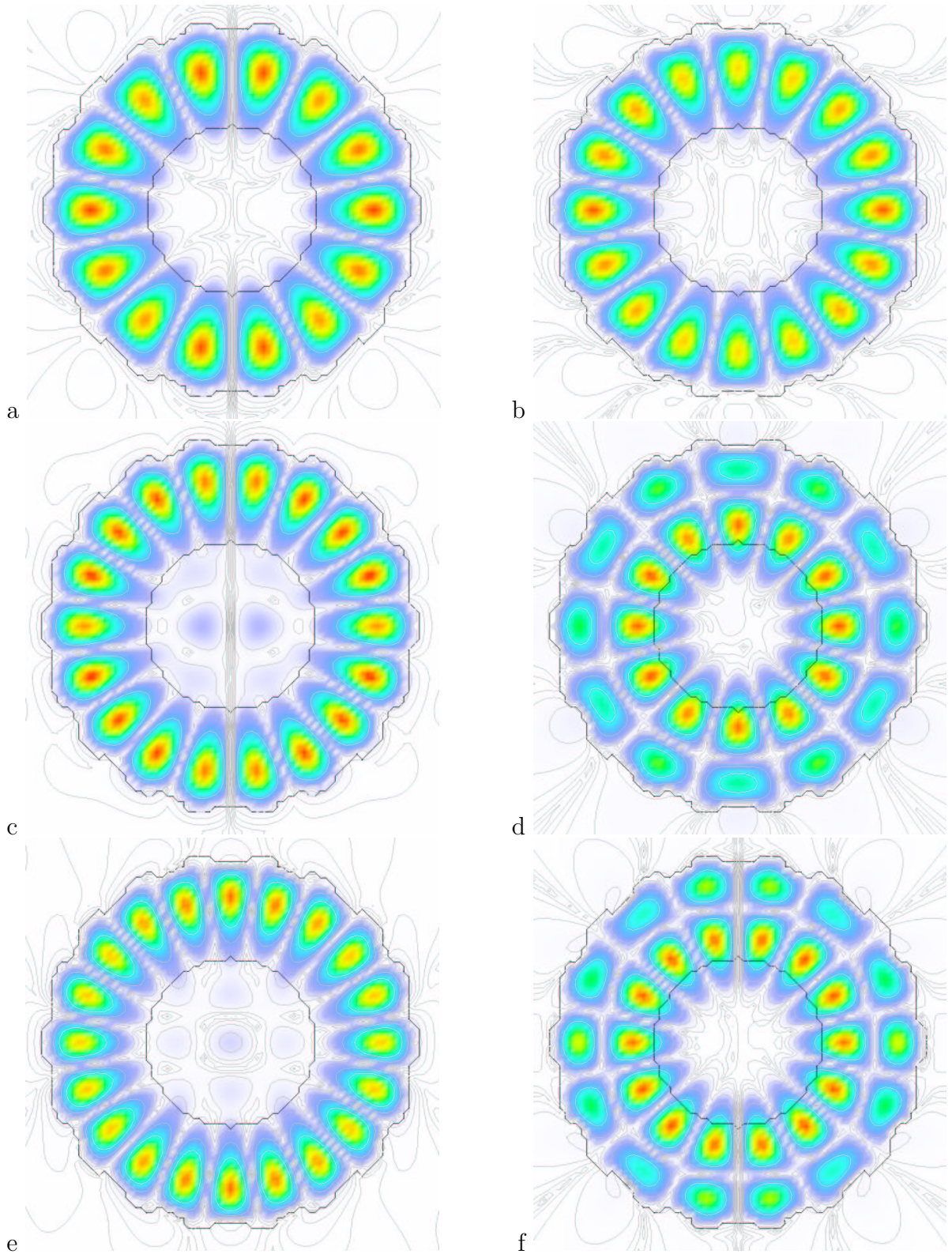


Figure 7.6.: (a) HEM₇₁₀, (b) HEM₈₁₀, (c) HEM₉₁₀, (d) HEM₆₂₀, (e) HEM₁₀₁₀, (f) HEM₇₂₀ modes in a microgear with 45 nm corrugation.

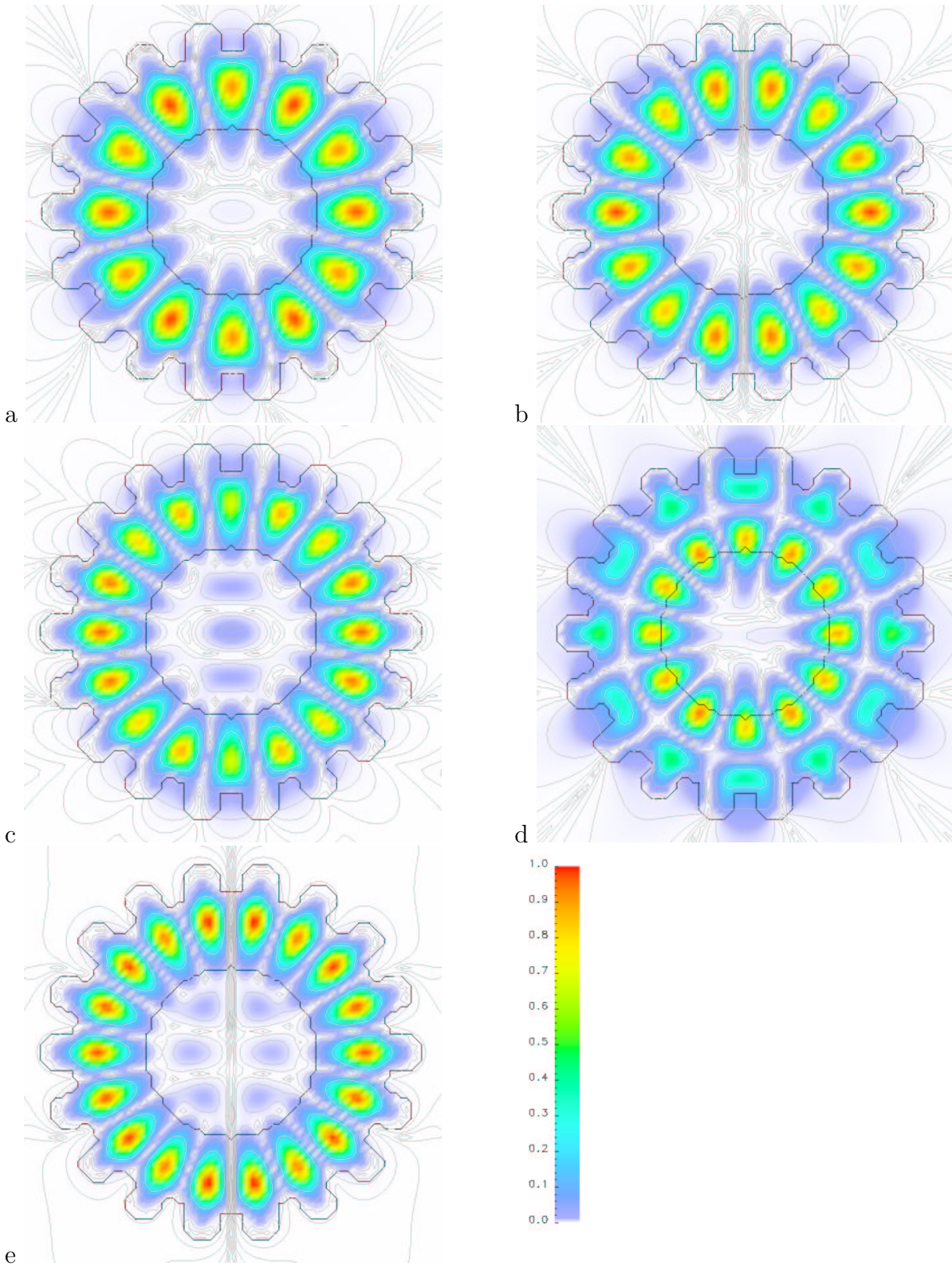


Figure 7.7.: (a) HEM_{610} , (b) HEM_{710} , (c) HEM_{810} , (d) HEM_{620} and (e) HEM_{910} modes in a microgear with 180 nm corrugation.

7. Microgear

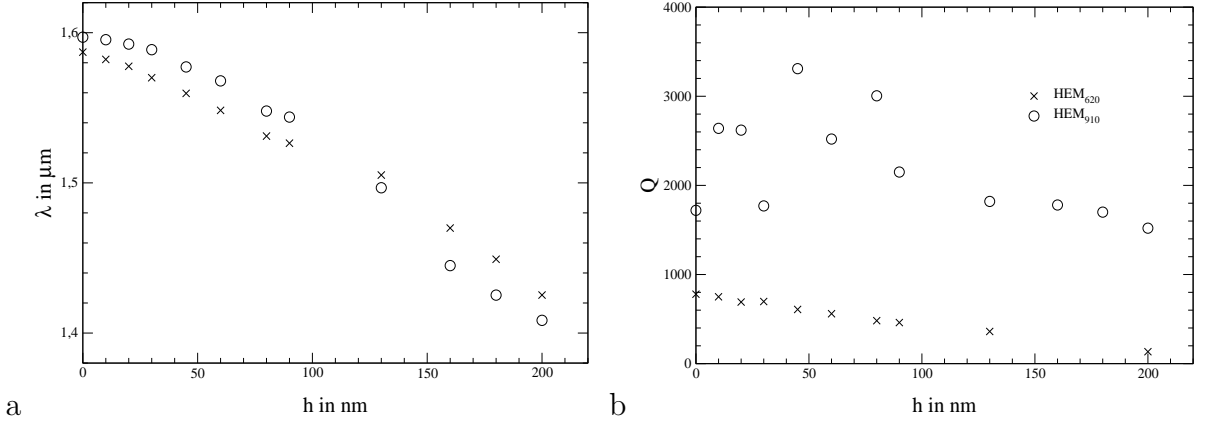


Figure 7.8.: The change of resonance wavelength (a) and quality factor (b) of the WGMs HEM₉₁₀ and HEM₆₂₀, with increasing corrugation depth.

Table 7.1.: The mode volumes of the microgear WGMs which are shown in figure 7.7 plus the HEM₇₂₀ mode.

	HEM ₆₁₀	HEM ₇₁₀	HEM ₈₁₀	HEM ₆₂₀	HEM ₉₁₀	HEM ₇₂₀
V_{rel}	0.0517	0.0460	0.0401	0.0325	0.0411	0.0282

7.1.5. Quality Factors

Figure 7.8b shows the calculated dependence of the quality factor Q on the corrugation depth h of the two modes HEM₉₁₀ and HEM₆₂₀. The HEM₉₁₀ mode is compatible with the corrugation period $m = 18$ which is used in this simulation and the HEM₆₂₀ is not. The six fold azimuthal symmetry of the second order WGM is only matching the positions of the convex corrugation at every second tooth of the microgear.

The quality factor of the HEM₆₂₀ WGM features a constant decrease with increasing corrugation depth. This is in contrast to the quality factor of the HEM₉₁₀ WGM, which is strongly varying up to a corrugation depth of about $h = 100$ nm.

7.1.6. Mode Volume

The microgear cavity without the pedestal, with a corrugation depth of $h = 180$ nm has a volume of $V \approx 0.7009 \mu\text{m}^3$ in the discretised space in the simulation. A disk with the same radius and height would have a volume of $0.9123 \mu\text{m}^3$. The difference is due to the subtracted corrugation. The entire structure, including the pedestal has a computed volume of $1.2057 \mu\text{m}^3$.

In analogy with the last chapter on microdisk modes a calculation of the relative mode volumes, of modes in a microgear with 180 nm corrugation depth, results in the values which are shown in table 7.1. Remarkably, the mode volume decreases with increasing azimuthal mode number with the exception of the mode HEM₉₁₀, which is

Table 7.2.: Active microgear simulation run.

Entity	value	Entity	value
Grid size	$200 \times 200 \times 100$	Geometry	filled microgear
Cell size	30 nm^3	$\mathbf{d}_{ab}/ d_{ab} $	\mathbf{e}_x
$c \frac{dt}{ds}$	0.577	d_{ab}	$-4.806 \times 10^{-29} \text{ A s m}$
$n_{\text{background}}$	1.00	n_a	10^{26} m^{-3}
Resonator type	microgear (no ped.)	γ	10^{12} s^{-1}
$n_{\text{resonator}}$	3.48	ω_0	$1.2368 \times 10^{15} \text{ s}^{-1}$
R	880 nm	γ_{nr}	10^9 s^{-1}
d	180 nm	$\rho_{\text{bb},0}$	0
h	160 nm	Λ	$1.100 \left(\frac{1}{2} - \rho_{\text{bb},0}\right) \gamma_{\text{nr}}$
Tooth count	10	$\rho_{\text{bb}}(t=0)$	0.50034
PML size	8	Field setup	Gaussian pulse
p	3.2		
κ_{max}	1.0		
σ_{max}	1.941		

compatible to the corrugation order $m = 18$. The modes with radial mode number two show a much smaller mode volume than their first order counterparts.

7.2. Pumped Non-Linear Dynamics

In analogy to chapter 6 lasing activity in a microgear laser is simulated in this chapter. The geometry of the microdisk cavity is altered by introduction of a ten-fold corrugation of depth $h = 160 \text{ nm}$ around the disk of refractive index $n = 3.48$. By increasing the radius of the disk by $h/2$, the resonator volume is kept nearly constant.

The cold cavity spectrum reveals a dominant peak at about $\lambda \approx 1523 \text{ nm}$ in contrast to 1539 nm in the plain microdisk which belongs to the compatible HEM_{510} mode that is shown in figure 7.9 and figure 7.11. The quality factor of this mode is $Q \approx 770 \pm 50$. The incompatible mode is associated with a freespace wavelength of 26 nm less (higher frequency) and a poorer quality factor of around 126 ± 12 (see fig. 7.10). In order to match the resonance of the two-level system and thereby retain the coupling factors κ and c (referring to the laser rate eqs. 4.97) of the same magnitude, the frequency ω_0 is shifted in the microgear simulations. The other parameters are kept unchanged, in regard to the microdisk simulations.

7.2.1. Initial Relaxation Oscillation

The first simulation uses the parameter set which is given in table 7.2. The order of the corrugation $m = 10$ is compatible to the azimuthal mode order of the WGM which is in resonance with the active material. The pump strength is 1.1 times the threshold

7. Microgear

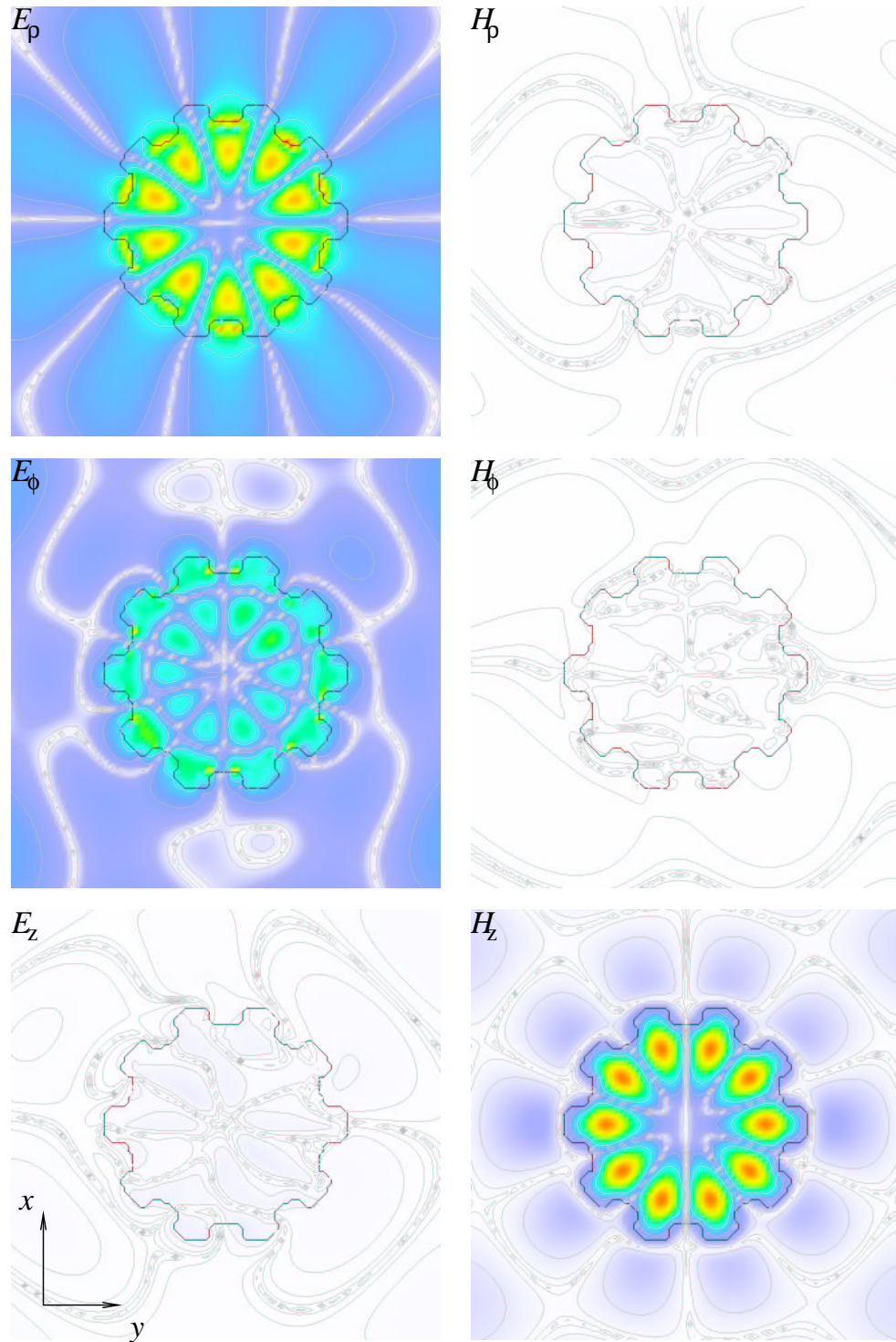


Figure 7.9.: Cold cavity mode pattern of cylindrical electric and magnetic field components of the HEM_{510} WGM in the microgear resonator. The range of the colour representation (see fig. 7.11) is normalised to the maximum field component strength of the electric and magnetic fields respectively.

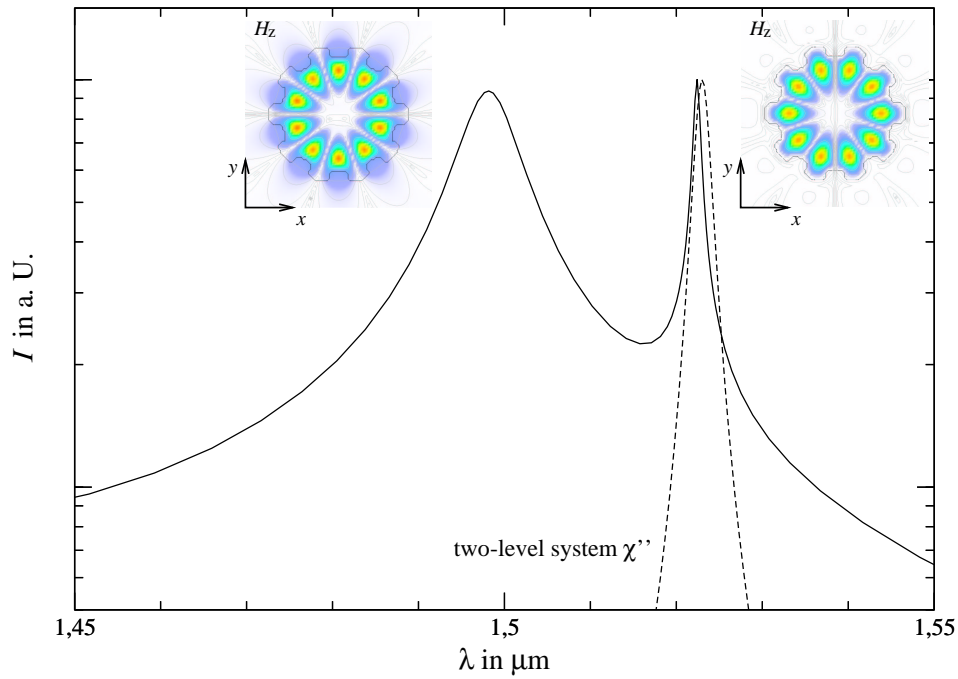


Figure 7.10.: The spectrum of the microgear near the HEM_{510} WGM resonance with the two-level system Lorentzian curve. Both peaks are associated with the spatially resolved cold cavity mode patterns of the axial magnetic field component.

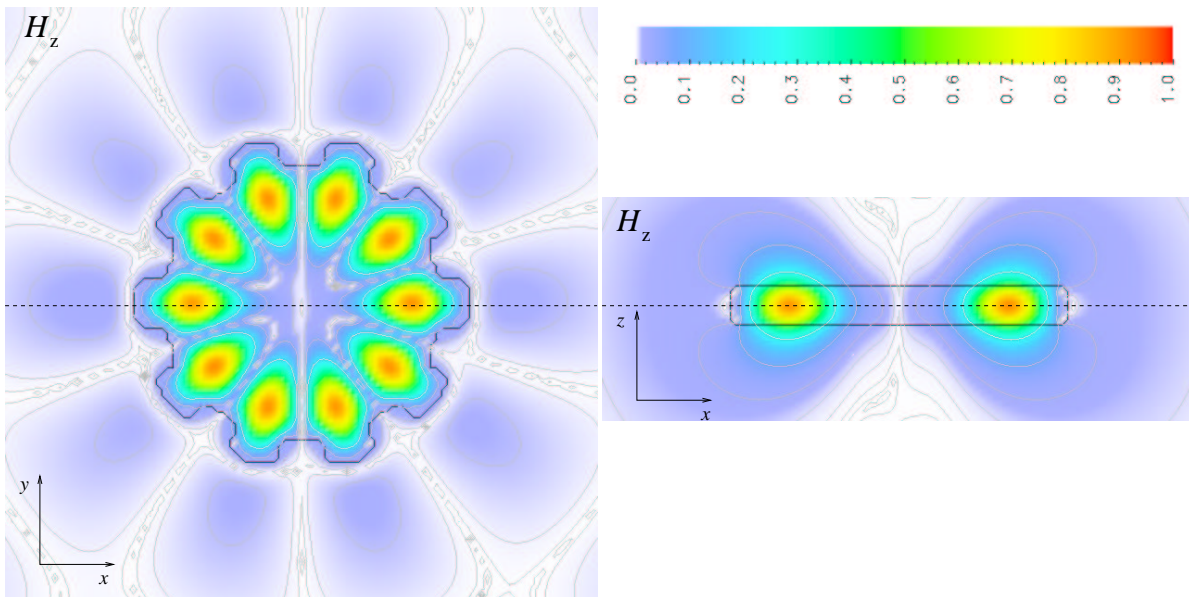


Figure 7.11.: The mode structure of the HEM_{510} WGM in the microgear structure. Shown is the normalised amplitude of the axial component of the magnetic field as a representation of the TE like character of the WGM.

7. Microgear

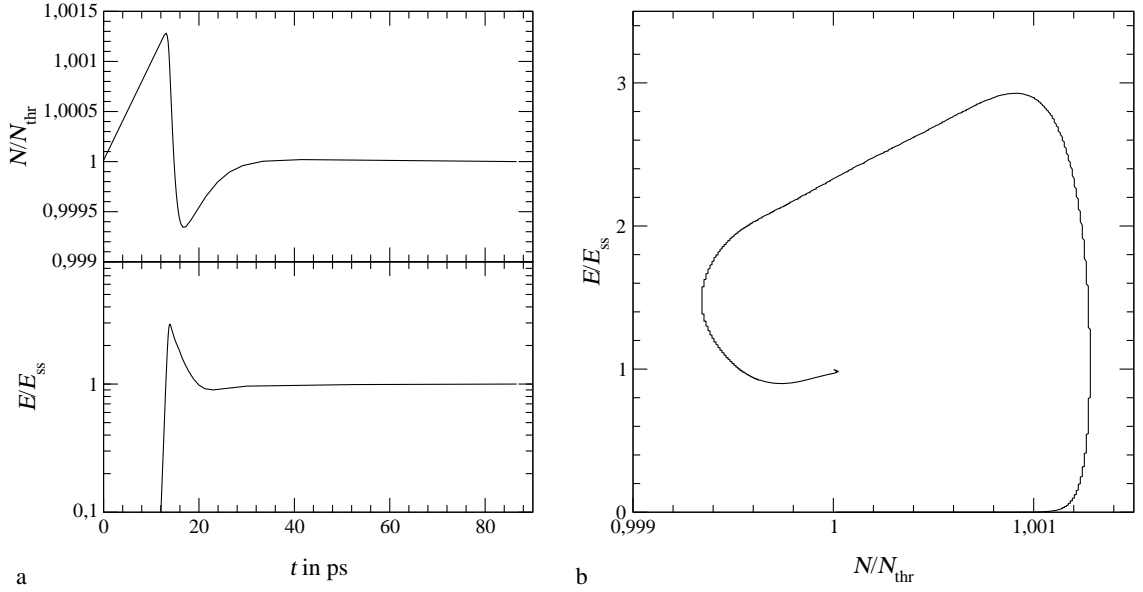


Figure 7.12.: The normalised inversion and energy inside a microgear (a) over time. Reduced phase space diagram (b) of the same relaxation oscillation. Both are normalised to their steady state values ($\rho_{bb,thr} \approx 0.50033$, $E_{ss} \approx 1.21 \times 10^8$ V/m). The parameters of the 3D simulation are given in the text.

pump. The simulation is started with an occupation probability of the two-level system just above the transparency value.

The over-damped relaxation oscillation of this setup is shown in figure 7.12. Part a of the figure shows the normalised envelopes of the electric field and the occupation probability difference during the first 86 ps of the simulation. They are normalised to their steady state values. The upper graph of part a shows the occupation probability difference N of the two-level system at an azimuthal node position of the HEM₅₁₀ WGM. The lower graph presents the electric field envelope at the same position inside the microgear. After a first large relaxation peak the system settles immediately into its steady state. This is moreover depicted in part (b) of this figure, which presents the reduced phase space plot of the same initial relaxation oscillation. The pump strength in this simulation is so high that the relaxation oscillation is over-damped (see also eq. 4.100 and eq. 4.101).

An estimated threshold pump rate is calculated with equation (4.99) from this simulation result. The next simulation is similar, having the same parameters except the pump strength factor was set to 1.001 just above the threshold pump. The initial relaxation oscillation behaviour during the first 600 ps of the run is presented in figure 7.13. The occupation probability of the higher energy level ρ_{bb} at two different positions in the active material is shown, in addition to the averaged occupation probability in the resonator. This graph is related to the averaged field energy \bar{E} in the cavity. A typical initial relaxation oscillation to the steady state field energy is in contrast to the

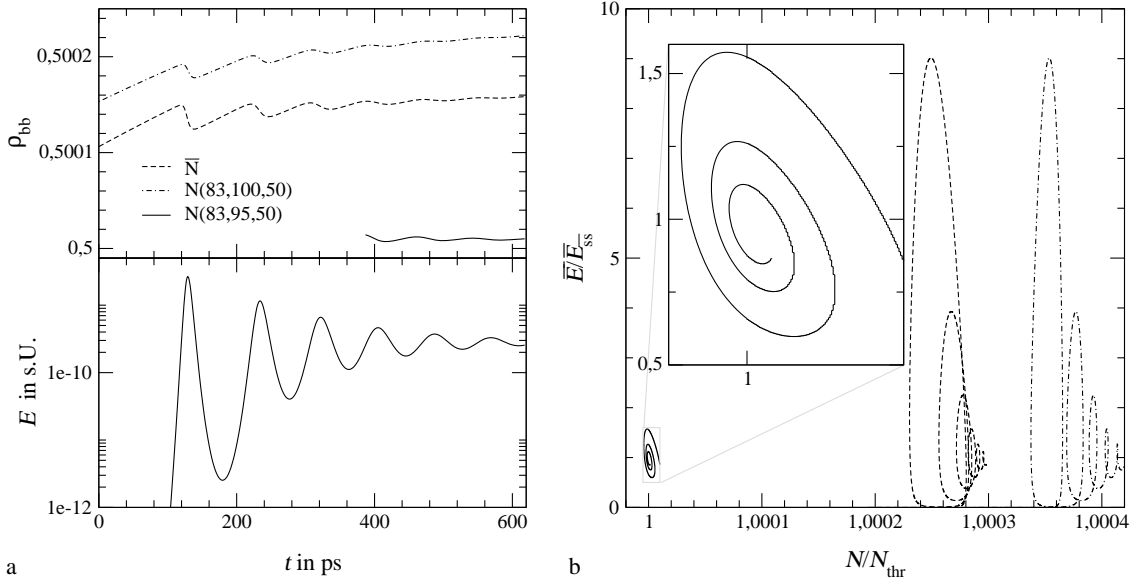


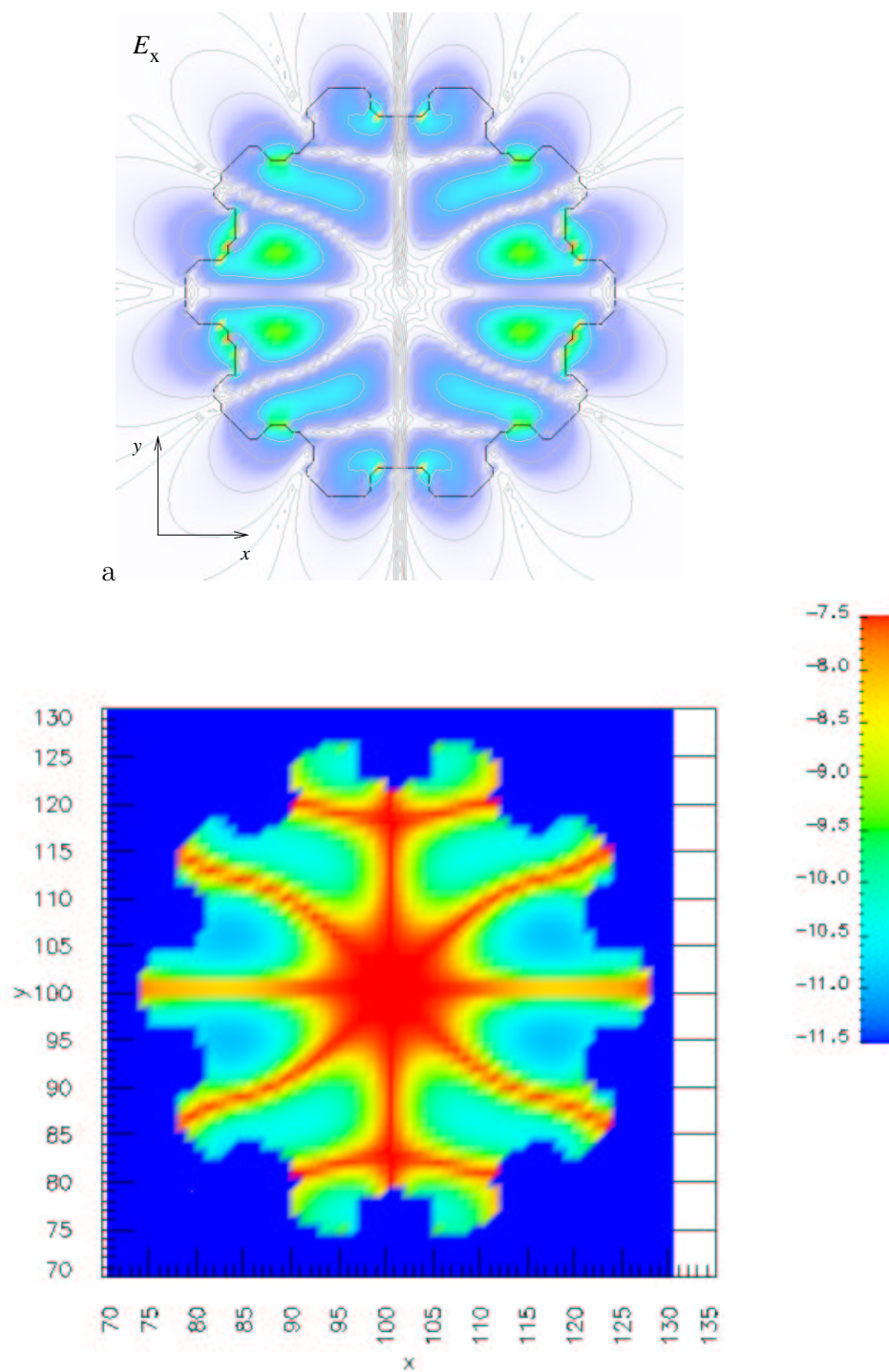
Figure 7.13.: Relaxation oscillation of the occupation probability difference N at two different positions in the microgear and the spatially averaged \bar{N} in a simulation with a low pump strength. The two positions are at a node (83,100,50) and an antinode (83,95,50) of the lasing WGM in the microgear.

oscillations of the different occupation probabilities behaviour. The probability at an antinode position – (83, 95, 50) in simulation grid coordinates – is in qualitative contrast to the averaged value or the value which is recorded at a node position (83, 100, 50). The averaged probability and the probability at the node position increase steadily while the antinode position probability levels at a much lower value. Figure 7.13b combines the two time series to the reduced phase space plot. The two physical entities from part (a) are normalised to steady state values in this plot. Once more, the difference of the inversion oscillation at an antinode position is in contrast to the oscillation of the averaged entity or the inversion at a node position.

7.2.2. Steady State Dynamics of Gear compared to Disk

The results of the last section militate in favour of the assumption, that the combination of a microdisk with a periodic grating removes the degeneracy of the WGMs in azimuthal direction. The existence of nodes in the field which restrict the interaction with the two-level systems in the active material would lead to different evolution of the inversion at node and antinode positions as seen in the last section. This effect has been reported to happen in experiments as early as 1993 by Levi *et al.* [93]. They had to adapt the laser rate equations to their experimental results by including the inversion peak at the centre of a microcylinder. This inversion peak piles up due to the lack of a lasing mode which does not have a node position at the axis of the cylinder.

7. Microgear



b

Figure 7.14.: Embossed mode structure (a) in the inversion (b) in a microgear cavity during steady state operation. The mode is the compatible WGM as shown in fig. 7.9. The spatial dimensions are given in cell numbers and the inversion is in an arbitrary logarithmic scale relative to the threshold occupation probability.

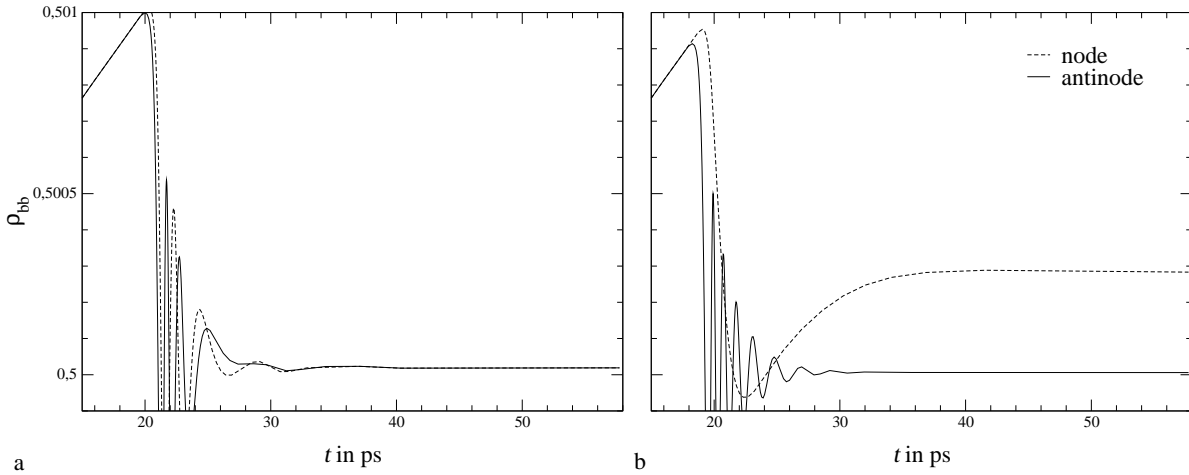


Figure 7.15.: Comparison of the initial relaxation oscillation to steady state in a microdisk (a) and microgear (b) cavity. Shown are the occupation probability of the higher energy level at a azimuthal node and antinode position in the lasing WGM. The disk and the gear have the same overall properties. The microdisk has a lower threshold occupation probability difference of $N_{\text{thr}} \approx -3.8 \times 10^{-5}$ in contrast to the microgear with $N_{\text{thr}} \approx -1.2 \times 10^{-5}$.

In order to investigate the validity of this assumption the spatial inversion structure in the active material is recorded at a time step during the steady state operation in a simulation of an active microgear. Figure 7.14 shows the embossed mode structure of the WGM in the inversion. It visualises the inversion $1 - N$ across the middle plane in axial direction in the microgear with a height profile which is logarithmically scaled to enhance the visibility of the embossed pattern.

The interaction of the active medium and the optical mode is not possible at points where the electric field is not present. At antinode points of the electric field the inversion is transformed with maximal coupling into electromagnetic field energy and vice-versa. This is especially visible at the centre of the disk where all the whispering gallery type modes share a node position. So all the low loss modes can not access this pool of inversion which builds up steadily through the homogeneous pumping term. The position of the nodes and antinodes of the WGM and the peaks in the inversion are static. This is called density pinning.

The appartaining behaviour of the axial component of the magnetic field is shown in figure 7.16. It presents the ultra-fast oscillations as a coloured plot with contour lines in logarithmic scaling at six consecutive time steps. The field is oscillating in a standing wave like fashion. This does not change in the simulated time frame as in the lasing microdisk. The node positions inside the microgear are static and the azimuthal node planes outside the disk are straight. This is in contrast to the steady state behaviour in the microdisk simulations in chapter 6. It can be attributed to the resolved, continuous azimuthal degeneracy, that prevents the mode from changing its position.

Figure 7.15 compares the time dependent behaviour of the occupation probability of

7. *Microgear*

the upper level ρ_{bb} at the node and antinode positions of a WGM in a microdisk and a microgear. Both simulations have the same parameter setup, except energy gap of the two-level system, which is 1523 nm in the microgear and 1539 nm in the microdisk. They are both pumped with a pump factor of 1.1, and the initial occupation probability is $\rho_{bb}(t = 0\text{ s}) = 0.50002$.

The WGM in the microdisk starts to shift to positions with higher gain as soon as the initial inversion peak breaks down. There are therefore no static azimuthal node planes near the perimeter of the disk. Both occupation probabilities in figure 7.15a have the same steady state value. As we have seen before, there are static azimuthal node planes in a microgear. The occupation probability near the node position saturates at a much higher value than near a antinode of the WGM.

The threshold occupation probability difference N_{thr} in the microdisk (antinode position) was almost three times higher than in the microgear. This could be due to a lower quality factor of the WGM in the microdisk.

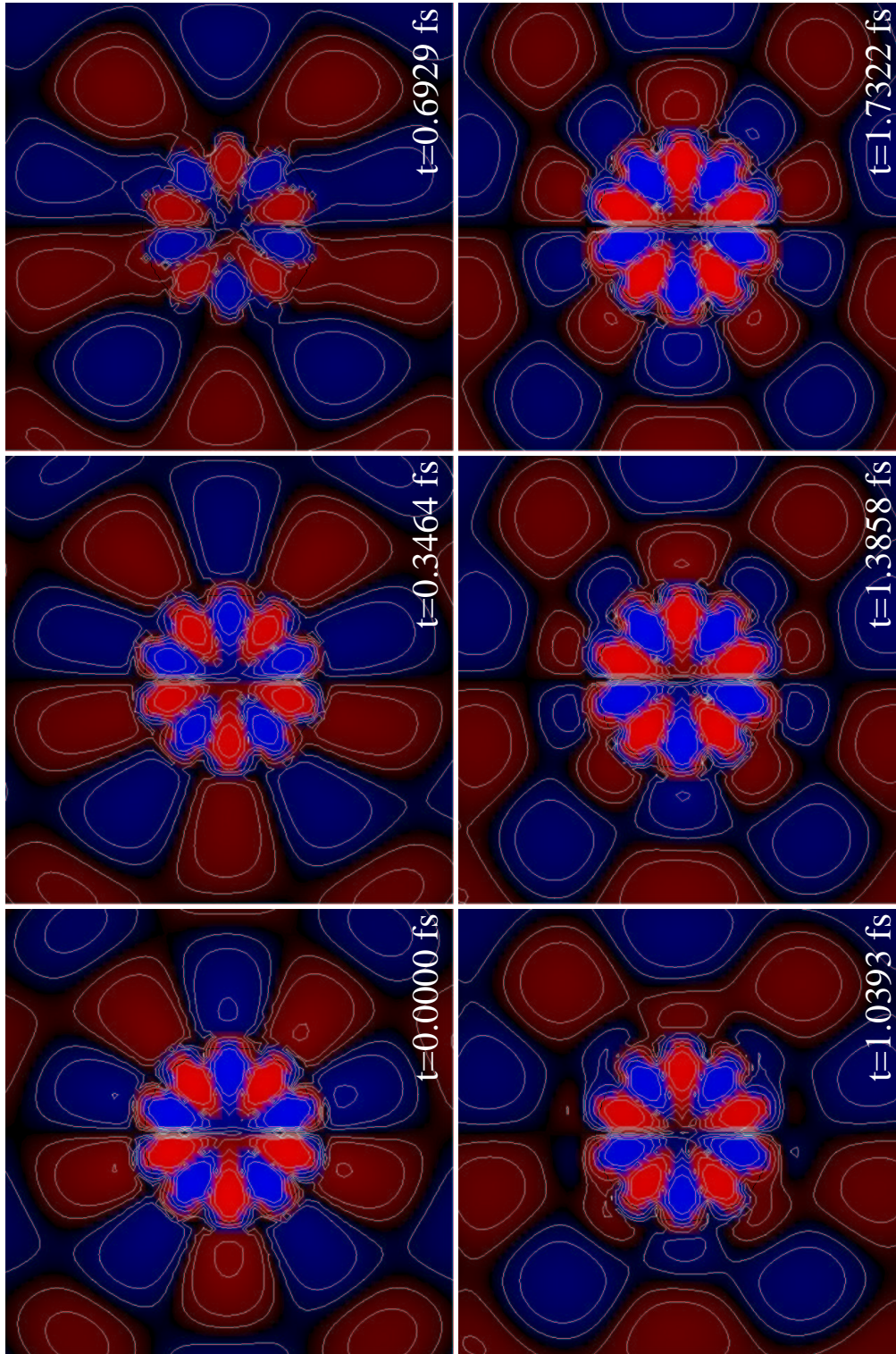


Figure 7.16.: Ultrafast dynamics of the electromagnetic field (represented by the axial component of the magnetic field) produced by a microgear cavity.

7. *Microgear*

A. Matrix

The matrix components which define the amplitude relations along the axial direction domain are:

$$\begin{aligned}
A_{11} &= \frac{\gamma\beta}{k_0^2 + \gamma^2} J'_\nu(\beta\rho) \cos(\nu\phi) \\
A_{12} &= \imath\omega \frac{\nu}{(k_0^2 + \gamma^2)\rho} J_\nu(\beta\rho) \sin(\nu\phi + \chi) \\
A_{13} &= \frac{\kappa\beta}{k_0^2\epsilon_r - \kappa^2} J'_\nu(\beta\rho) \cos(\nu\phi) [c_1 \cos(\kappa d) + c_2 \sin(\kappa d)] \\
A_{14} &= -\imath\omega \frac{\nu}{(k_0^2\epsilon_r - \kappa^2)\rho} J_\nu(\beta\rho) \sin(\nu\phi + \chi) [c_3 \cos(\kappa d) + c_4 \sin(\kappa d)] \\
A_{21} &= \frac{\gamma\nu}{(k_0^2 + \gamma^2)\rho} J_\nu(\beta\rho) \sin(\nu\phi) \\
A_{22} &= -\imath\omega \frac{\beta}{k_0^2 + \gamma^2} J'_\nu(\beta\rho) \cos(\nu\phi + \chi) \\
A_{23} &= \frac{\kappa\nu}{(k_0^2\epsilon_r - \kappa^2)\rho} J_\nu(\beta\rho) \sin(\nu\phi) [c_1 \cos(\kappa d) + c_2 \sin(\kappa d)] \\
A_{24} &= \imath\omega \frac{\beta}{k_0^2\epsilon_r - \kappa^2} J'_\nu(\beta\rho) \cos(\nu\phi + \chi) [c_3 \cos(\kappa d) + c_4 \sin(\kappa d)] \\
A_{31} &= \imath\omega \frac{\nu}{(k_0^2 + \gamma^2)\rho} J_\nu(\beta\rho) \sin(\nu\phi) \\
A_{32} &= -\frac{\gamma\beta}{k_0^2 + \gamma^2} J'_\nu(\beta\rho) \cos(\nu\phi + \chi) \\
A_{33} &= -\imath\omega \frac{\epsilon_r\nu}{(k_0^2\epsilon_r - \kappa^2)\rho} J_\nu(\beta\rho) \sin(\nu\phi) [-c_2 \cos(\kappa d) + c_1 \sin(\kappa d)] \\
A_{34} &= -\frac{\kappa\beta}{k_0^2\epsilon_r - \kappa^2} J'_\nu(\beta\rho) \cos(\nu\phi + \chi) [c_4 \cos(\kappa d) - c_3 \sin(\kappa d)] \\
A_{41} &= \imath\omega \frac{\beta}{k_0^2 + \gamma^2} J'_\nu(\beta\rho) \cos(\nu\phi) \\
A_{42} &= \frac{\gamma\nu}{(k_0^2 + \gamma^2)\rho} J_\nu(\beta\rho) \sin(\nu\phi + \chi) \\
A_{43} &= -\imath\omega \frac{\epsilon_r\beta}{k_0^2\epsilon_r - \kappa^2} J'_\nu(\beta\rho) \cos(\nu\phi) [-c_2 \cos(\kappa d) + c_1 \sin(\kappa d)] \\
A_{44} &= \frac{\kappa\nu}{(k_0^2\epsilon_r - \kappa^2)\rho} J_\nu(\beta\rho) \sin(\nu\phi + \chi) [c_4 \cos(\kappa d) - c_3 \sin(\kappa d)] .
\end{aligned} \tag{A.1}$$

A. Matrix

The matrix components which are relating the amplitudes of the electric and magnetic field along the radial domain are:

$$\begin{aligned}
R_{11} &= J_\nu(\beta R) \cos(\nu\phi) [c_1 \cos(\kappa z) + c_2 \sin(\kappa z)] \\
R_{12} &= 0 \\
R_{13} &= -K_\nu(\alpha R) \cos(\nu\phi) [c_1 \cos(\kappa z) + c_2 \sin(\kappa z)] \\
R_{14} &= 0 \\
R_{21} &= \frac{-1}{k_0^2 \epsilon_r - \kappa^2} \frac{\kappa \nu}{R} J_\nu(\beta R) \sin(\nu\phi) [c_2 \cos(\kappa z) - c_1 \sin(\kappa z)] \\
R_{22} &= \frac{-i\omega}{k_0^2 \epsilon_r - \kappa^2} \beta J'_\nu(\beta R) \cos(\nu\phi + \chi) [c_3 \cos(\kappa z) + c_4 \sin(\kappa z)] \\
R_{23} &= \frac{1}{k_0^2 - \kappa^2} \frac{\kappa \nu}{R} K_\nu(\alpha R) \sin(\nu\phi) [c_2 \cos(\kappa z) - c_1 \sin(\kappa z)] \\
R_{24} &= \frac{i\omega}{k_0^2 - \kappa^2} \alpha K'_\nu(\alpha R) \cos(\nu\phi + \chi) [c_3 \cos(\kappa z) + c_4 \sin(\kappa z)] \\
R_{31} &= 0 \\
R_{32} &= J_\nu(\beta R) \cos(\nu\phi + \chi) [c_3 \cos(\kappa z) + c_4 \sin(\kappa z)] \\
R_{33} &= 0 \\
R_{34} &= -K_\nu(\alpha R) \cos(\nu\phi + \chi) [c_3 \cos(\kappa z) + c_4 \sin(\kappa z)] \\
R_{41} &= \frac{i\omega}{k_0^2 \epsilon_r - \kappa^2} \epsilon_r \beta J'_\nu(\beta R) \cos(\nu\phi) [c_1 \cos(\kappa z) + c_2 \sin(\kappa z)] \\
R_{42} &= \frac{-1}{k_0^2 \epsilon_r - \kappa^2} \frac{\kappa \nu}{R} J_\nu(\beta R) \sin(\nu\phi + \chi) [c_4 \cos(\kappa z) - c_3 \sin(\kappa z)] \\
R_{43} &= \frac{-i\omega}{k_0^2 - \kappa^2} \alpha K'_\nu(\alpha R) \cos(\nu\phi) [c_1 \cos(\kappa z) + c_2 \sin(\kappa z)] \\
R_{44} &= \frac{1}{k_0^2 - \kappa^2} \frac{\kappa \nu}{R} K_\nu(\alpha R) \sin(\nu\phi + \chi) [c_4 \cos(\kappa z) - c_3 \sin(\kappa z)] .
\end{aligned} \tag{A.2}$$

B. Discretised PML Equations

The calculation of the field \mathbf{D} from the electric field is shown in equations (B.1) followed by the equations (B.2) which calculate the electric field from the before computed field \mathbf{D} .

$$\begin{aligned}
 D_x|_{i+\frac{1}{2},j,k}^{m+\frac{1}{2}} &= d_y|_j D_x|_{i+\frac{1}{2},j,k}^{m-\frac{1}{2}} + \\
 &\quad \delta t b_y|_j \delta y^{-1} \left[H_z|_{i+\frac{1}{2},j+\frac{1}{2},k}^m - H_z|_{i+\frac{1}{2},j-\frac{1}{2},k}^m \right] - \\
 &\quad \delta t b_y|_j \delta z^{-1} \left[H_y|_{i+\frac{1}{2},j,k+\frac{1}{2}}^m - H_y|_{i+\frac{1}{2},j,k-\frac{1}{2}}^m \right] \\
 D_y|_{i,j+\frac{1}{2},k}^{m+\frac{1}{2}} &= d_z|_k D_y|_{i,j+\frac{1}{2},k}^{m-\frac{1}{2}} + \\
 &\quad \delta t b_z|_k \delta z^{-1} \left[H_x|_{i,j+\frac{1}{2},k+\frac{1}{2}}^m - H_x|_{i,j+\frac{1}{2},k-\frac{1}{2}}^m \right] - \\
 &\quad \delta t b_z|_k \delta x^{-1} \left[H_z|_{i+\frac{1}{2},j+\frac{1}{2},k}^m - H_z|_{i-\frac{1}{2},j+\frac{1}{2},k}^m \right]
 \end{aligned} \tag{B.1}$$

$$\begin{aligned}
 D_z|_{i,j,k+\frac{1}{2}}^{m+\frac{1}{2}} &= d_x|_i D_z|_{i,j,k+\frac{1}{2}}^{m-\frac{1}{2}} + \\
 &\quad \delta t b_x|_i \delta x^{-1} \left[H_y|_{i+\frac{1}{2},j,k+\frac{1}{2}}^m - H_y|_{i-\frac{1}{2},j,k+\frac{1}{2}}^m \right] - \\
 &\quad \delta t b_x|_i \delta y^{-1} \left[H_x|_{i,j+\frac{1}{2},k+\frac{1}{2}}^m - H_x|_{i,j-\frac{1}{2},k+\frac{1}{2}}^m \right]
 \end{aligned}$$

$$\begin{aligned}
 E_x|_{i+\frac{1}{2},j,k}^{m+\frac{1}{2}} &= d_z|_k E_x|_{i+\frac{1}{2},j,k}^{m-\frac{1}{2}} + \\
 &\quad \frac{b_z|_k}{\epsilon_r|_{i+\frac{1}{2},j,k}} \left\{ a_x|_{i+\frac{1}{2}} D_x|_{i+\frac{1}{2},j,k}^{m+\frac{1}{2}} - c_x|_{i+\frac{1}{2}} D_x|_{i+\frac{1}{2},j,k}^{m-\frac{1}{2}} \right\}
 \end{aligned}$$

$$\begin{aligned}
 E_y|_{i,j+\frac{1}{2},k}^{m+\frac{1}{2}} &= d_x|_i E_y|_{i,j+\frac{1}{2},k}^{m-\frac{1}{2}} + \\
 &\quad \frac{b_x|_i}{\epsilon_r|_{i,j+\frac{1}{2},k}} \left\{ a_y|_{j+\frac{1}{2}} D_y|_{i,j+\frac{1}{2},k}^{m+\frac{1}{2}} - c_y|_{j+\frac{1}{2}} D_y|_{i,j+\frac{1}{2},k}^{m-\frac{1}{2}} \right\}
 \end{aligned} \tag{B.2}$$

$$\begin{aligned}
 E_z|_{i,j,k+\frac{1}{2}}^{m+\frac{1}{2}} &= d_y|_j E_z|_{i,j,k+\frac{1}{2}}^{m-\frac{1}{2}} + \\
 &\quad \frac{b_y|_j}{\epsilon_r|_{i,j,k+\frac{1}{2}}} \left\{ a_z|_{k+\frac{1}{2}} D_z|_{i,j,k+\frac{1}{2}}^{m+\frac{1}{2}} - c_z|_{k+\frac{1}{2}} D_z|_{i,j,k+\frac{1}{2}}^{m-\frac{1}{2}} \right\}
 \end{aligned}$$

B. Discretised PML Equations

Equations (B.3) and (B.4) form the counterpart for the \mathbf{B} field and the magnetic field.

$$\begin{aligned}
B_x|_{i,j+\frac{1}{2},k+\frac{1}{2}}^{m+1} &= d_y|_{j+\frac{1}{2}} B_x|_{i,j+\frac{1}{2},k+\frac{1}{2}}^m + \\
&\quad \frac{\delta t b_y|_{j+\frac{1}{2}}}{\delta y} \left\{ E_z|_{i,j+1,k+\frac{1}{2}}^{m+\frac{1}{2}} - E_z|_{i,j,k+\frac{1}{2}}^{m+\frac{1}{2}} \right\} - \\
&\quad \frac{\delta t b_y|_{j+\frac{1}{2}}}{\delta z} \left\{ E_y|_{i,j+\frac{1}{2},k+1}^{m+\frac{1}{2}} - E_y|_{i,j+\frac{1}{2},k}^{m+\frac{1}{2}} \right\} \\
B_y|_{i+\frac{1}{2},j,k+\frac{1}{2}}^{m+1} &= d_z|_{k+\frac{1}{2}} B_y|_{i+\frac{1}{2},j,k+\frac{1}{2}}^m + \\
&\quad \frac{\delta t b_z|_{k+\frac{1}{2}}}{\delta z} \left\{ E_x|_{i+\frac{1}{2},j,k+1}^{m+\frac{1}{2}} - E_x|_{i+\frac{1}{2},j,k}^{m+\frac{1}{2}} \right\} - \\
&\quad \frac{\delta t b_z|_{k+\frac{1}{2}}}{\delta x} \left\{ E_z|_{i+1,j,k+\frac{1}{2}}^{m+\frac{1}{2}} - E_z|_{i,j,k+\frac{1}{2}}^{m+\frac{1}{2}} \right\}
\end{aligned} \tag{B.3}$$

$$\begin{aligned}
B_z|_{i+\frac{1}{2},j+\frac{1}{2},k}^{m+1} &= d_x|_{i+\frac{1}{2}} B_z|_{i+\frac{1}{2},j+\frac{1}{2},k}^m + \\
&\quad \frac{\delta t b_x|_{i+\frac{1}{2}}}{\delta x} \left\{ E_y|_{i+1,j+\frac{1}{2},k}^{m+\frac{1}{2}} - E_y|_{i,j+\frac{1}{2},k}^{m+\frac{1}{2}} \right\} - \\
&\quad \frac{\delta t b_x|_{i+\frac{1}{2}}}{\delta y} \left\{ E_x|_{i+\frac{1}{2},j+1,k}^{m+\frac{1}{2}} - E_x|_{i+\frac{1}{2},j,k}^{m+\frac{1}{2}} \right\}
\end{aligned}$$

$$\begin{aligned}
H_x|_{i,j+\frac{1}{2},k+\frac{1}{2}}^{m+1} &= d_z|_{k+\frac{1}{2}} H_x|_{i,j+\frac{1}{2},k+\frac{1}{2}}^m + \\
&\quad \frac{b_z|_{k+\frac{1}{2}}}{\mu_r|_{i,j+\frac{1}{2},k+\frac{1}{2}}} \left\{ a_x|_i B_x|_{i,j+\frac{1}{2},k+\frac{1}{2}}^{m+1} - c_x|_i B_x|_{i,j+\frac{1}{2},k+\frac{1}{2}}^m \right\} \\
H_y|_{i+\frac{1}{2},j,k+\frac{1}{2}}^{m+1} &= d_x|_{i+\frac{1}{2}} H_y|_{i+\frac{1}{2},j,k+\frac{1}{2}}^m + \\
&\quad \frac{b_x|_{i+\frac{1}{2}}}{\mu_r|_{i+\frac{1}{2},j,k+\frac{1}{2}}} \left\{ a_y|_j B_y|_{i+\frac{1}{2},j,k+\frac{1}{2}}^{m+1} - c_y|_j B_y|_{i+\frac{1}{2},j,k+\frac{1}{2}}^m \right\} \\
H_z|_{i+\frac{1}{2},j+\frac{1}{2},k}^{m+1} &= d_y|_{j+\frac{1}{2}} H_z|_{i+\frac{1}{2},j+\frac{1}{2},k}^m + \\
&\quad \frac{b_y|_{j+\frac{1}{2}}}{\mu_r|_{i+\frac{1}{2},j+\frac{1}{2},k}} \left\{ a_z|_k B_z|_{i+\frac{1}{2},j+\frac{1}{2},k}^{m+1} - c_z|_k B_z|_{i+\frac{1}{2},j+\frac{1}{2},k}^m \right\}
\end{aligned} \tag{B.4}$$

As in the core algorithm the field vector components are defined at the same positions in space and time as is shown in the Yee cube for the spatial positioning (fig. 3.1). All the equations form a leap frog type evolution of the fields.

C. Software

This work would not have been possible without the use of several software packages. I will only mention the bigger packages of software. It was completed on different hardware platforms with different operating systems. The Linux operating system with all its smaller packages should represent the range of Open Source software which was used. The “Hitachi massively parallel processor operating system” made the SR8000 usable.

XEmacs is still the editor in use to hack in the text and sometimes “good old” vi did a great job too. The typesetting of the thesis was done with L^AT_EX, and the postscript and portable document format post-processing were performed with ghostscript. Bibliographic data was processed with Pybliographer and BibT_EX. Visualisations and illustrations were created with XFig, Grace and OpenDX with additional modules. The additional modules were created as part of this work and include the HDF5 import filter and a vector component translation routine from Cartesian to cylindrical coordinates.

Programming languages which were used include C++ and Fortran 90. Besides the Gnu compiler collection, the platform specific DEC and Intel compiler suite and the Hitachi Fortran 90 compiler converted the source code to executable programs. Two specific libraries should be mentioned here, which were especially useful in the simulations. The input and output of large datasets was achieved platform independently with the HDF5 library. And the self claimed fastest Fourier transforms in the west library was being used for the post-processing Fourier transformations.

Much time was spent with coding from scratch and testing of two large simulation packages. The applications are being used to simulate one and three dimensional electromagnetic phenomena. Christian Hermann and Stefan Scholz are the co-authors of the three dimensional FDTD code, and Klaus Böhringer and Joachim Hamm participated in the creation of the one dimensional code. The three dimensional code is written in Fortran and is specifically optimised for the Hitachi SR8000 hardware platform. The one dimensional program is coded in C++ and is generally optimised for modern pipelined processor architectures.

C. *Software*

Bibliography

- [1] E. M. Purcell. Spontaneous emission probabilities at radio frequencies. *Phys. Rev.*, 69(11-12):681, June 1946.
- [2] M. Fujita, R. Ushigome, and T. Baba. Continuous wave lasing in gainasp microdisk laser with threshold of 40 μa . *Electron. Lett.*, 27:790–791, 2000.
- [3] H. Yokoyama. Physics and Device Applications of Optical Microcavities. *Science*, 256:66–70, 1992.
- [4] C. T. Chan, Q. L. Yu, and K. M. Ho. Order-N spectral method for electromagnetic waves. *Phys. Rev. B*, 51(23):16635–16642, June 1995.
- [5] S. Riechel, C. Kallinger, U. Lemmer, J. Feldmann, A. Gombert, and V. Wittwer. A nearly diffraction limited surface emitting conjugated polymer laser utilizing a two-dimensional photonic band structure. *Appl. Phys. Lett.*, 77(15):2310–2312, September 2000.
- [6] M. Fujita and T. Baba. Microgear Laser. *Appl. Phys. Lett.*, 80(12):2051–2053, March 2002.
- [7] R. K. Chang and A. J. Campilla, editors. *Optical Processes in Microcavities*, volume 3 of *Advanced Series in Applied Physics*. World Scientific, 1996.
- [8] K. J. Vahala. Optical microcavities. *Nature*, 424(8):839–846, August 2003.
- [9] A. Dodabalapur, M. Berggren, R. E. Slusher, Z. Bao, A. Timko, P. Schiortino, E. Laskowski, H. E. Katz, and O. Nalamasu. Resonators and Materials for Organic Lasers Based on Energy Transfer. *IEEE J. Sel. Top. Quant. Electron.*, 4(1):67–74, February 1998.
- [10] S. F. Yu. *Analysis and Design of Vertical Cavity Surface Emitting Lasers*. Series in Lasers and Applications. Wiley-Interscience, 22 August 2003.
- [11] J. M. Gerard, D. Barrier, J. Y. Marzon, R. Kuszelewicz, L. Manin, E. Costard, V. Thierry-Mieg, and T. Rivera. Quantum boxes as active probes for photonic microstructures: The pillar microcavity case. *Appl. Phys. Lett*, 69(4):449–451, April 1996.

Bibliography

- [12] E. Yablonovich. Inhibited spontaneous emission in solid-state physics and electronics. *Phys. Rev. Lett.*, 58(20):2059–2062, May 1987.
- [13] O. Painter, R. K. Lee, A. Scherer, A. Yariv, J. D. O’Brien, P. D. Dapkus, and I. Kim. Two-Dimensional Photonic Band-Gap Defect Mode Laser. *Science*, 284:1819–1821, June 1999.
- [14] P. Michler, A. Kiraz, C. Becher, Lidong Zhang, E. Hu, A. Imamoglu, W. V. Schoenfeld, and P. M. Petroff. Quantum Dot Lasers Using High-Q Microdisk Cavities. *phys. stat. sol. (b)*, 224(3):797–801, March 2001.
- [15] Y. Xu, R. K. Lee, and A. Yariv. Quantum analysis and the classical analysis of spontaneous emission in a microcavity. *Phys. Rev. A*, 61:33807–1–13, 2000.
- [16] S. L. McCall, A. F. J. Levi, R. E. Slusher, S. J. Pearton, and R. A. Logan. Whispering-gallery mode microdisk lasers. *Appl. Phys. Lett.*, 60(3):289–291, November 1991.
- [17] D. K. Armani, T. J. Kippenberg, S. M. Spillane, and K. J. Vahala. Ultra-high Q toroid microcavity on a chip. *Nature*, 421:925–928, February 2003.
- [18] U. Vietze, O. Krauß, F. Laeri, G. Ihlein, F. Schüth, B. Limburg, and M. Abraham. Zeolite-Dye Microlasers. *Phys. Rev. Lett.*, 81(21):4628–4631, November 1998.
- [19] T. Nobis, E. M. Kaidashev, A. Rahm, M. Lorenz, and M. Grundmann. Whispering Gallery Modes in Nanosized Dielectric Resonators with Hexagonal Cross Section. *Phys. Rev. Lett.*, 93(10):103903–1–4, September 2004.
- [20] D. W. Vernooy, V. S. Ilchenko, H. Mabuchi, E. W. Streed, and H. J. Kimble. High-Q measurements of fused-silica microspheres in the near infrared. *Opt. Lett.*, 23(4):247–249, February 1998.
- [21] K. Djordjev, S. J. Choi, and P. D. Dapkus. Microdisk tunable resonant filters and switches. *IEEE Phot. Technol. Lett.*, 14(6):828–830, June 2002.
- [22] K. S. Yee. Numerical solution of initial boundary value problems involving Maxwell’s equations in isotropic media. *IEEE Trans. Antennas Propag.*, 14:302–307, May 1966.
- [23] A. Taflove. *Computational Electrodynamics: The Finite-Difference Time-Domain Method*. Norwood, MA: Artech House, 1995.
- [24] A. Taflove. *Advances in Computational Electrodynamics: The Finite-Difference Time-Domain Method*. Norwood, MA: Artech House, 1998.
- [25] J. D. Jackson. *Classical Electrodynamics*. John Wiley Sons, Inc., 1998.

- [26] A. Taflove and M. E. Brodwin. Numerical Solution of Steady-State Electromagnetic Scattering Problems Using the Time-Dependent Maxwell's Equations. *IEEE Trans. Micro. Theo. Tec.*, MTT-23(8):623–630, August 1975.
- [27] R. Holland. Pitfalls of staircase meshing. *IEEE Trans. Electromag. Compat.*, 35(4):434–439, November 1993.
- [28] A. C. Cangellaris and D. B. Wright. Analysis of the numerical error caused by the stair-stepped approximation of a conducting boundary in FDTD simulations of electromagnetic phenomena. *IEEE Trans. Antennas Propagat.*, 39(10):1518–1525, October 1991.
- [29] J. B. Schneider and K. L. Shlager. FDTD simulations of TEM horns and the implications for staircased representations. *IEEE Trans. Antennas Propagat.*, 45(12):1830–1838, December 1997.
- [30] O. Hess, C. Hermann, and A. Klaedtke. Finite-Difference Time-Domain simulations of photonic crystal defect structures. *Phys. stat. sol. a*, 197(3):605–619, June 2003.
- [31] K.-P. Hwang and A. C. Cangellaris. Effective Permittivities for Second-Order Accurate FDTD Equations at Dielectric Interfaces. *IEEE Micro. Wireless Comp. Lett.*, 11(4):158–160, April 2001.
- [32] G. Mur. Absorbing Boundary Conditions for the Finite-Difference Approximation of the Time-Domain Electromagnetic-Field Equations. *IEEE Trans. Antennas Propagat.*, EMC-23(4):377–382, November 1981.
- [33] J. P. Berenger. A perfectly matched layer for the absorption of electromagnetic waves. *J. Computational Physics*, 114:185–200, 1994.
- [34] B. Engquist and A. Majda. Absorbing boundary conditions for the numerical simulation of waves. *Math. Comput.*, 31(139):629–651, 1977.
- [35] Z. S. Sacks, D. M. Kingsland, R. Lee, and J. F. Lee. A perfectly matched anisotropic absorber for use as an absorbing boundary condition. *IEEE Trans. Anten. Propagat.*, 43(12):1460–1463, December 1995.
- [36] S. D. Gedney. An anisotropic perfectly matched layer-absorbing medium for the truncation of FDTD lattices. *IEEE Trans. Anten. Propagat.*, 44(12):1630–1639, December 1996.
- [37] R. Mittra and Ü. Pekel. A new look at the perfectly matched layer (PML) concept for the reflectionless absorption of electromagnetic waves. *IEEE Microwave and Guided Wave Letters*, 5(3):84–86, March 1995.
- [38] J. De Moerloose and D. De Zutter. Poynting's Theorem for the Finite-Difference-Time-Domain Method. *Mic. Opt. Tec. Letters*, 8(5):257–260, April 1995.

Bibliography

- [39] H. Haken and H. Sauermann. Nonlinear Interactions of Laser Modes. *Z. Physik*, 173:261, 1963.
- [40] Jr. W. E. Lamb. Theory of an Optical Maser. *Physical Review*, 134(6A):A1429, 15 June 1964.
- [41] F. Gardiol. Comments about time domain techniques in electromagnetics. *IEEE Antennas Propagat. Soc. Newsletter*, 31(4):36–37, August 1989.
- [42] E. Sano and T. Shibata. Fullwave Analysis of Picosecond Photoconductive Switches. *IEEE J Quant Elec*, 26(2):372–377, February 1990.
- [43] R. W. Ziolkowski, J. M. Arnold, and D. M. Gogny. Ultrafast pulse interactions with two-level atoms. *Phys. Rev. A*, 52(4):3082–3094, October 1995.
- [44] A. S. Nagra and R. A. York. FDTD Analysis of Wave Propagation in Nonlinear Absorbing and Gain Media. *IEEE Trans. Antennas Propag.*, 46(3):334–340, March 1998.
- [45] R. P. Feynman, F. L. Vernon, and R. W. Hellwarth. Geometrical Representation of the Schrödinger Equation for Solving Maser Problems. *J. Appl. Phys.*, 28(1):49–51, January 1957.
- [46] A. E. Siegman. *Lasers*. Oxford University Press, 1986.
- [47] L. W. Davis. *Proc. Inst. Elec. Engrs.*, 51:76, 1963.
- [48] B. Bidegaray, A. Bourgeade, and D. Reignier. Introducing Physical Relaxation Terms in Bloch Equations. *Journal of Computational Physics*, 170(2):603–613, July 2000.
- [49] R. M. Joseph, S. C. Hagness, and A. Taflove. Direct time integration of Maxwell’s equations in linear dispersive media with absorption for scattering and propagation of femtosecond electromagnetic pulses. *Opt Lett*, 16(18):1412–1414, September 1991.
- [50] S. Radic and N. George. Ultrafast pulse propagation in periodic optical media: a generalized finite-difference time-domain approach. *Opt Lett*, 19(14):1064–1066, July 1994.
- [51] P. M. Goorjian and A. Taflove. Direct time integration of Maxwell’s equations in nonlinear dispersive media for propagation and scattering of femtosecond electromagnetic solitons. *Opt Lett*, 17(3):180–182, February 1992.
- [52] T. O. Körner and W. Fichtner. Auxiliary differential equation: efficient implementation in the finite-difference time-domain method. *Opt Lett*, 22(21):1586–1588, November 1997.
- [53] S. L. McCall and E. L. Hahn. Self-induced transparency. *Phys. Rev.*, 183(2):457–485, July 1969.

- [54] L. W. Davis and Y. S. Lin. Propagation of Optical Pulses in a Saturable Absorber. *IEEE J. Quant. Elec.*, 9(12):1135–1138, December 1973.
- [55] R. Loudon. *The Quantum Theory of Light*. Oxford Science Publications, 1 edition, 1973.
- [56] R. Loudon. *The Quantum Theory of Light*, chapter 2.7, page 71. Oxford University Press, 3rd edition, 2000.
- [57] S. Hughes. Breakdown of the Area Theorem: Carrier-Wave Rabi Flopping of Femtosecond Optical Pulses. *Phys. Rev. Lett.*, 81(16):3363–3366, October 1998.
- [58] C. Weissbuch, M. Nishioka, A. Ishikawa, and Y. Arakawa. Observation of the Coupled Exciton-Photon Mode Splitting in a Semiconductor Quantum Microcavity. *Phys. Rev. Lett.*, 69(23):3314–3317, December 1992.
- [59] G. Khitrova, H. M. Gibbs, F. Jahnke, M. Kira, and S. W. Koch. Nonlinear optics of normal-mode-coupling semiconductor microcavities. *Rev. Mod. Phys.*, 71(5):1591–1639, October 1999.
- [60] M. S. Skolnick, T. A. Fisher, and D. M. Whittaker. Strong coupling phenomena in quantum microcavity structures. *Semicond. Sci. Technol.*, 13:645–669, April 1998.
- [61] S. Jorda. Theory of Rabi splitting in cavity-embedded quantum wells. *Phys. Rev. B*, 50(24):18690–18693, December 1994.
- [62] P. G. Lagoudakis, M. D. Martin, J. J. Baumberg, G. Malpuech, and A. Kavokin. Coexistence of low threshold lasing and strong coupling in microcavities. *J. Appl. Phys.*, 95(5):2487–2489, March 2004.
- [63] S. Riechel, U. Lemmer, J. Feldmann, T. Benstem, W. Kowalsky, U. Scherf, A. Gombert, and V. Wittwer. Laser modes in organic solid-state distributed feedback lasers. *Appl. Phys. B*, 71(6):897–900, December 2000.
- [64] K. J. Ebeling. *Integrated Optoelectronics*. Springer, 1st english edn. edition, 1989.
- [65] S. Riechel. *Organic semiconductor lasers with two-dimensional distributed feedback*. Dissertation, Ludwig-Maximilians-Universität München, 11 February 2002.
- [66] J. Sturm, S. Tasch, A. Niko, E. Toussaere, J. Zyss, T. C. Kowalczyk, K. D. Singer, U. Scherf, and J. Huber. Optical anisotropy in thin films of a blue electroluminescent conjugated polymer. *Thin Solid Films*, 298(1–2):138–142, April 1997.
- [67] H. Kogelnik and C. V. Shank. Stimulated emission in a periodic structure. *Appl. Phys. Lett.*, 18(4):152–154, February 1971.
- [68] F. K. Kneubühl and M. W. Sigrist. *Laser*. Teubner, 5th edition, 1999.

Bibliography

- [69] H. Kogelnik and C. V. Shank. Coupled-wave theory of distributed feedback lasers. *J. Appl. Phys.*, 43(5):2327–2335, May 1972.
- [70] P. Paddon and J. F. Young. Two-dimensional vector-coupled-mode theory for textured planar waveguides. *Phys. Rev. B*, 61(3):2090–2101, January 2000.
- [71] M. G. Salt and W. L. Barnes. Flat photonic bands in guided modes of textured metallic microcavities. *Phys. Rev. B*, 61(16):11125–11135, April 2000.
- [72] M. G. Salt, P. Andrew, and W. L. Barnes. Microcavities, texture symmetry, and photonic bandgaps. *J. Opt. Soc. Am. B*, 18(2):240–243, February 2001.
- [73] G. A. Turnbull, P. Andrew, M. J. Jory, W. L. Barnes, and I. D. W. Samuel. Relationship between photonic band structure and emission characteristic of a polymer distributed feedback laser. *Phys. Rev. B*, 64(12):125122–6, September 2001.
- [74] J. P. Dowling, M. Scalora, M. J. Bloemer, and C. M. Bowden. The photonic band edge laser: A new approach to gain enhancement. *J. Appl. Phys.*, 75(4):1896–1899, February 1993.
- [75] J. P. Dowling and C. M. Bowden. Atomic emission rates in inhomogeneous media with applications to photonic band structures. *Phys. Rev. A*, 46(1):612–622, July 1992.
- [76] S. Riechel, U. Lemmer, J. Feldmann, S. Berleb, A. G. Mueckl, W. Bruetting, A. Gombert, and V. Wittwer. A very compact tunable solid state laser utilizing a thin film organic semiconductor. *Opt. Lett.*, 26(9):593–595, May 2001.
- [77] V. G. Kozlov, V. Bulovic, P. E. Burrows, M. Baldo, V. B. Khalfin, G. Parthasarathy, S. R. Forrest, Y. You, and M. E. Thompson. Study of lasing action based on Forster energy transfer in optically pumped organic semiconductor thin films. *J. Appl. Phys.*, 84(8):4096–4108, October 1998.
- [78] S. Wang and S. Sheem. Two-dimensional distributed-feedback lasers and their applications. *Appl. Phys. Lett.*, 22(9):460–462, May 1973.
- [79] D. Kajfez and P. Guillon. *Dielectric resonators*. Noble Publishing, Atlanta, GA, 2nd edition, 1998.
- [80] B.-J. Li and P. L. Liu. Numerical Analysis of the Whispering Gallery Modes by the Finite-Difference Time-Domain Method. *IEEE J. Quant. Electron.*, 32(9):1583–1587, September 1996.
- [81] S. C. Hagness, D. Rafizadeh, S. T. Ho, and A. Taflove. FDTD Microcavity Simulations: Design and Experimental Realization of Waveguide-Coupled Single-Mode Ring and Whispering-Gallery-Mode Disk Resonators. *J. Lightwave Technol.*, 15(11):2154–2165, November 1997.

- [82] A. Sakai and T. Baba. FDTD Simulation of Photonic Devices and Circuits Based on Circular and Fan-Shaped Microdisks. *J. Lightwave Technol.*, 17(8):1493–1499, August 1999.
- [83] Y. Xu, R. K. Lee, and A. Yariv. Finite-difference time-domain analysis of spontaneous emission in a microdisk cavity. *Phys. Rev. A*, 61:33808–1–10, 2000.
- [84] R. P. Wang and M.-M. Dumitrescu. Theory of optical modes in semiconductor microdisk lasers. *J. Appl. Phys.*, 81(8):3391–3396, April 1997.
- [85] M. K. Chin, D. Y. Chu, and S. Ho. Estimation of the spontaneous emission factor for microdisk lasers via the approximation of whispering gallery modes. *J. Appl. Phys.*, 75(7):3302–3307, April 1994.
- [86] N. C. Frateschi and A. F. J. Levi. The spectrum of microdisk lasers. *J. Appl. Phys.*, 80(2):644–653, July 1996.
- [87] M. Heiblum and J. H. Harris. Analysis of curved optical waveguides by conformal transformation. *IEEE J. Quantum Electron.*, 11(2):75–83, February 1975.
- [88] B.-J. Li and P. L. Liu. Numerical Analysis of Microdisk Lasers with Rough Boundaries. *IEEE J. Quant. Electron.*, 33(5):791–795, May 1997.
- [89] J. Vuckovic, O. Painter, Y. Xu, A. Yariv, and A. Scherer. Finite-Difference time-domain calculation of the spontaneous emission coupling factor in optical microcavities. *IEEE J. Quantum Elec.*, 35(8):1168–1175, August 1999.
- [90] A. F. J. Levi, S. L. McCall, S. J. Pearton, and R. A. Logan. Room temperature operation of submicrometer radius disk laser. *Electron. Lett.*, 29(9):1666–1667, September 1993.
- [91] R. Coccioli, M. Boroditsky, K. Kim, Y. Rahmat-Samii, and E. Yablonovitch. What is the Smallest Possible Electromagnetic Mode Volume in a Dielectric Cavity? *IEEE Proc. Optoelectron.*, 145(6):391–397, December 1998.
- [92] T. Harayama, P. Davis, and K. S. Ikeda. Nonlinear Whispering Gallery Modes. *Phys. Rev. Lett.*, 82(19):3803–3806, May 1999.
- [93] A. F. J. Levi, R. E. Slusher, S. L. McCall, S. J. Pearton, and W. S. Hobson. Room-temperature lasing action in In(0.51)Ga(0.49)P/In(0.2)Ga(0.8)As microcylinder laser diodes. *Appl. Phys. Lett.*, 62(17):2021–2023, April 1993.
- [94] K. J. Luo, J. Y. Xu, H. Cao, Y. Ma, S. H. Chang, S. T. Ho, and G. S. Solomon. Ultrafast dynamics of InAs/GaAs quantum-dot microdisk lasers. *Appl. Phys. Lett.*, 78(22):3397–3399, May 2001.
- [95] V. Zwiller, S. Fälth, J. Persson, W. Seiffert, L. Samuelson, and G. Björk. Fabrication and time-resolved studies of visible microdisk lasers. *J. Appl. Phys.*, 93(4):2307–2309, February 2003.

Bibliography

- [96] M. Fujita and T. Baba. Proposal and finite-difference time-domain simulation of whispering gallery mode microgear cavity. *IEEE J. Quant. Elec.*, 37(10):1253–1258, October 2001.
- [97] K. Nozaki, A. Nakagawa, D. Sano, and T. Baba. Ultralow Threshold and Single-Mode Lasing in Microgear Lasers and Its Fusion With Quasi-Periodic Photonic Crystals. *IEEE J. Select. Top. Quantum Electron.*, 9(5):1355–1360, October 2003.
- [98] S. Shi, D. W. Prather, L. Yang, and J. Kolodzey. Influence of support structure on microdisk resonator performance. *Opt. Eng.*, 42(2):383–387, February 2003.

Danksagung

An dieser Stelle möchte ich all denjenigen danken, die zum Gelingen dieser Arbeit direkt oder indirekt beigetragen haben:

- *Prof. Dr. Ortwin Hess* danke ich für das Privileg diese vielseitige Arbeit in seiner Arbeitsgruppe anfertigen zu können, und für sein ununterbrochenes Interesse an deren Fortgang. Er hat die exzellente Computerinfrastruktur und die finanziellen Mittel bedingungslos bereitgestellt.
- *Prof. Dr. Hans Herrman* danke ich für die kurzfristige Übernahme des Zweitberichtes und sein Interesse an dieser Arbeit.
- *Dr. Joachim Hamm* danke ich für unterschiedlichste Hilfestellungen und entscheidende Impulse die diese Arbeit im richtigen Moment vorangebracht haben. Sein weitreichendes Interesse an der Physik und seine Begeisterungsfähigkeit haben die vergangenen fünf Jahre mitgeprägt. Nicht zu unterschlagen sind auch die unvergesslichen Diskussionen über seine Hasen und meine Pflanzen.
- *Klaus Böhringer* danke ich für das sehr gewissenhafte und hilfreiche Korrekturlesen meiner Arbeit (was sicherlich nicht immer angenehm war). Seine fundierte Kritik hat zu vielen wichtigen Verbesserungen geführt.
- *Dr. Stefan Scholz* danke ich für die Hilfestellung bei meinen ersten Schritten in Fortran und seine Mitarbeit beim Schreiben des FDTD Programmes mit UPML Randbedingungen.
- *Dr. Christian Hermann* danke ich für seine Hilfe und Anregung beim Entwickeln des FDTD Programmes und seine sachkundigen Informationen zu Scotches und deren Verköstigung. Auch die morgentlichen “Briefings” und manchmal hitzigen Diskussionen möchte ich nicht missen.
- *Dr. Christian Simmendinger*, dem Meister der Hitachi SR8000 und ehrenamtlichen Berserker, danke ich für seine Hilfestellung beim Optimieren der Programme, so daß die Simulationen auch in vernünftigen Zeitspannen fertig wurden.
- *Dr. Edeltraud Gehrig* danke ich für Ihre organisatorische Arbeit und interessanten Diskussionen über die Halbleiterphysik.

- Ein generelles Dankeschön an alle Mitarbeiter und Gäste der Arbeitsgruppe, *Durga Aryal, Nicoleta Azap, Hui Bian, Klaus Böhringer, Guillermo Carpintero del Barrio, Edeltraud Gehrig, Joachim Hamm, Michael Hartmann, Christian Hermann, Ortwin Hess, Manuel Leonés Sanchez, Heiko Pittner, Dietmar Preisser, Dietmar Reschner, Stefan Scholz, Christian Simmendinger* und *Vasilios Stavrou* für die extrem unkomplizierte Arbeitsatmosphäre, diverse unvergessliche Konferenzzufenthalte und andere ausserwissenschaftliche Aktivitäten.
- Der DFB Laser Teil wurde im Hinblick auf eine Kooperation mit Dr. Riechel und Dr. Lemmer (ehemals Universität München) in einem sehr frühen Stadium, begonnen. Ein besonderer Dank gebührt daher den Kooperationspartnern für ihr entgegengebrachtes Vertrauen in meine Fähigkeiten. Leider konnte ich die Arbeit zu den 2D DFB Laserkavitäten nicht fertigstellen bevor Stefan Riechel seine Doktorarbeit beendete.

Ein Dankeschön geht auch an meine zukünftigen Schwiegereltern welche mir in vielfältiger Weise über die fünf Jahre geholfen haben.

Meinen Eltern möchte ich meinen tiefen Dank ausdrücken für ihre bedingungslose und unermüdete Unterstützung in jeglicher Hinsicht, und für ihren Glauben an mich.

Zum Schluss möchte ich noch Claudia für ihre Liebe zu mir und ihre Geduld mit mir danken. Ohne Deine Kritik, Dein Vertrauen, Deine Unterstützung wäre ich nicht so weit gekommen.